Pulsed Laser Processing of Dielectric Materials

Kiran Gulia

A dissertation submitted for the degree of Doctor of Philosophy

Heriot-Watt University

School of Engineering and Physical Sciences

October 2007

Abstract

The thesis investigates the wavelength dependent laser ablation in dielectric materials used for the fabrication of high density Printed Circuit Boards (PCBs) in the electronics industry. Here the market for consumer and industrial products of ever-rising complexity has led to a demand for increased miniaturisation and low costs of multi-level printed circuit boards (PCBs) interconnected by microvias, which electrically connect the various circuit layers. Laser machining offers a potential solution to this need. The main objective of the research is to investigate the wavelength-dependence of the laser machining/drilling efficiency of two important sets of PCB materials, categorised as *Organics* and *Ceramics* using a carbon dioxide laser which can be tuned across its emission spectrum in the 9μm - 11μm spectral region.. The organics include commercially available electronic materials with trade names such as Kapton, Arlon, FR4 and RCC and the ceramics materials studied are alumina and low temperature co-fired ceramic (LTCC). The aim is to determine the optimum laser wavelength for maximum processing efficiency i.e. to find the wavelength where the laser parameters are best matched to the optical, thermal and mechanical properties of each of the materials. A CO_2 laser machining system was constructed which incorporated a novel laser source developed in the research programmes. The laser source was a MOPA system with a line-tuneable cw oscillator and a five pass power planar waveguide rf discharge-excited power operating in the so-called enhanced power regime to produce maximum peak power. An Acousto-optic modulator between the master oscillator and the amplifier allowed convenient control of pulse amplitude and duration. The system enabled the wavelength dependent studies on the wavelength and pulse energy dependence of the laser ablation properties (e.g. ablation threshold fluence and ablation rates) – to derive the so-called 'ablation spectrum' of the selected materials A comparison is made of the wavelength dependence of ablation with the room temperature absorption spectrum measured for each material using *ellipsometry*. It was observed that the 'ablation spectrum' information does not always appear to match the simple expectations derived from the room temperature 'absorption spectrum' of the material. This disparity in results is likely due to the change of absorption properties of material because of rise in temperature, chemical decomposition or melting of material during ablation. However, the room temperature absorption spectrum (while not adequate alone), did provide a useful guide to the selection of a sub-set of the 40+ lines that would otherwise have to be studied. The results may be of direct application in the electronics industry to increase the efficiency of laser machining.

To my parents

Acknowledgements

Firstly, I would like to thank my supervisor Prof. Denis Hall for giving me an opportunity to work in his group and to start my PhD work at Heriot Watt University. His expertise in the area of lasers and helpful attitude inspite of his ill health and busy schedule were of great aid to me. I also extend thanks to Prof. Howard Baker for insights on the direction of writing thesis and advice on presentation of the results and general encouraging conversations. Special thanks go to Dr. Francisco Villarreal for his tireless help in just about every aspect of the experimental set-ups used in this thesis. I would like to acknowledge and thank my colleagues Gavin Markillie, Joseph Wendland, Colin Moorhouse, Krysztof Nowak, Julio Ramirez Zarate, Fernando Monjardin, Enrique Mendez, Roy McBride, Alberto, Victor, Kristian, Ian, and Natalia, whose contributions, support and help had been invaluable for my work and for maintaining a friendly atmosphere in the photonics laboratories.

I would also like to extend special thanks to Linda Bruce, who has been a friend, a guide and a good listener all through my PhD journey. I would also like to thank Steve Haughey for the technical support in the office and Lab, Jinsong, Aongus McCarthy, Himanshu Suyal for his lengthy discussions on every aspect of science, Prof. Ajoy Kar and Prof. Duncan Hand for the motivation and Paul Harrison for his wise words and lengthy emails that helped me reach a successful finish of the thesis.

I would like to thank Dev, my husband, my Father-in-Law, Mr. O.P. Sharma and my parents for their unconditional love, blessings and belief in me that encouraged me to a successful finish. The research would not have been possible without financial support from Heriot Watt University and the Engineering and Physical Science Research Council (EPSRC).

ACADEMIC REGISTRY
Research Thesis Submission

Name:	KIRAN GULIA		
School/PGI:	EPS		
Version: *(i.e. First, Resubmission, Final)*	FINAL	Degree Sought:	PHD.

Declaration

In accordance with the appropriate regulations I hereby submit my thesis and I declare that:

1) the thesis embodies the results of my own work and has been composed by myself
2) where appropriate, I have made acknowledgement of the work of others and have made reference to work carried out in collaboration with other persons
3) the thesis is the correct version of the thesis for submission*.
4) my thesis for the award referred to, deposited in the Heriot-Watt University Library, should be made available for loan or photocopying, subject to such conditions as the Librarian may require
5) I understand that as a student of the University I am required to abide by the Regulations of the University and to conform to its discipline.

* *Please note that it is the responsibility of the candidate to ensure that the correct version of the thesis is submitted.*

Signature of Candidate:	Kiran Gulia	Date:	08/02/08

Submission

Submitted By *(name in capitals)*:	KIRAN GULIA
Signature of Individual Submitting:	Kiran Gulia
Date Submitted:	08/02/08

For Completion in Academic Registry

Received in the Academic Registry by *(name in capitals)*:	CAROLINE MITCHELL		
Method of Submission *(Handed in to Academic Registry; posted through internal/external mail)*:	BY HAND		
Signature:		Date:	08/02/2008

Table of Contents

List of Publications by the Candidate

1. K. Gulia, G.A.J. Markillie, F.J. Villarreal, H.J. Baker, D.R. Hall, "Motion and fibre ejection in the laser vaporisation of fused quartz", European MRS Conference, Strasbourg (2001)

2. K. Gulia, F. Villarreal, R.J. Ramirez, J. F. Monjardin, H.J. Baker, D.R. Hall, "Tuneable MOPA laser system for micro machining applications", LAMP 2002, paper no. 1235, Osaka, Japan, 21 – 31 May, (2002).

3. K. Gulia, F. Villarreal, R.J. Ramirez, H.J. Baker, D.R. Hall, "High speed Videography of microvia formation and melt ejection in laser drilling of circuit substrates" ICALEO 2002, Scottsdale Arizona, USA, 14-17, October (2002).

4. K. Gulia, F. Villarreal, C J Moorhouse, H.J. Baker, D.R. Hall, "CO_2 Laser ablation spectroscopy of dielectric laminate materials", LPM, Munich, Germany 20 –26 June, (2003).

5. K. Gulia, F. Villarreal, C J Moorhouse, H.J. Baker, D.R. Hall, "Single pulse microvia drilling of resin-coated copper substrates using an enhanced peak power planar waveguide CO_2 Laser " SPIE's Lasers and Applications in Science and Engineering San Jose, Ca, 25-29 January (2004).

Chapter 1

Pulse laser processing of dielectric materials

1.1 Introduction

Description of a directed energy weapon was published almost one hundred years ago [1.1], yet the laser came into existence with Maimaon's publication in 1960, where the application involved laser interactions with solids leading to the ejection of particles. Laser ablation first appeared in the sixties with an archived account, where the ruby laser was used to vaporise and excite atoms from solid surfaces. This began the field of microprobe emission spectroscopy, which was the first real application area of laser ablation. Thereafter, came dozens of publications, which detailed the early experiments on laser ablation. Undoubtedly, the fastest growing applications were driven by the needs of the material sciences. Concurrently, the sophistication of electronics and computers vastly increased the drive for laser ablation in the area of micron and submicron structures and micromachining reached the new size regime and spawned the field of nanotechnology. Now laser ablation is successfully used in many applications in medicine, laser surgery, spectroscopy, electronics and in to computers and general manufacturing industry, as well as in the defence industry.

The demand for increasingly complex consumer and industrial electronics products delivering high functionality and unprecedented miniaturisation at extremely low unit cost and short product cycle time from concept to market is placing severe demands on electronics packaging technology. Some of this pressure is transmitted through to the laser material processing industry and the current and anticipated demand for increased specification and efficiency in this area requires research to formulate the conditions for optimum process performance.

Laser precision processing of materials is a laser assisted technological process for precise treatment, modification, and synthesis of materials in the domain of micrometer sizes. This area of laser technology has effective application in precision micro processing of small passive and active elements and components of microelectronics, optics, optoelectronic, and micromechanics. The application of laser micro technology is in various areas of the device building industry and when high precision, spatial resolution and reliability are required. Typical areas of laser

micro technology are micromachining of thin films, micro processing and modification of materials, laser micro patterning and laser assisted synthesis of polycomponent thin film systems.

All laser micromachining techniques use the process of laser ablation, where the interaction of the laser energy with the sample leads to material removal. Therefore to increase the efficiency of laser precision processing of materials, it is imperative to understand the key parameters of laser and optimise these with respect to the material parameters in order to obtain efficient laser material/interaction. Laser ablation usually relies on the strong absorption of laser photons by the sample material, which means that the wavelength of the laser has to be chosen carefully for maximum absorption. This will help ensure a high-energy deposition in a small volume for rapid and complete ablation. The second parameter is short pulse duration to maximize peak power and to minimize thermal conduction to the surrounding work material. The third parameter is the pulse repetition rate. If the rate is too low, all of the energy which was not used for ablation will leave the ablation zone allowing cooling. If the residual heat can be retained, thus limiting the time for conduction, by a rapid pulse repetition rate, the ablation will be more efficient. More of the incident energy will go toward ablation and less will be lost to the surrounding work material and the environment. The fourth parameter is the beam quality. Beam quality is measured by the irradiance, the focussability, and the homogeneity. Further, if the beam is not of a controlled size, the ablation region may be larger than desired with excessive slope in the sidewalls. Hence, the motivation for the research is to obtain low cost technological equipment with unique capabilities of laser assisted technological methods.

CO_2 lasers are frequently used in electronics manufacturing applications because of their ultra compact, sealed construction, excellent beam quality, pulsed operation at high repetition rates and ease of computer control. However, they are restricted to low pulse powers and long pulse duration, thus we intend to use new enhanced - pulse planar waveguide CO_2 laser for the machining of electronic PCB substrate materials. The literature reports a number of studies of laser processing of materials using the pulsed infrared IR CO_2 laser [1.2-1.6] but in spite of there previous laser drilling investigations, the relationship between process parameters (laser and material

characteristics) and final quality of hole to produce at high process rates is not well understood. Such an understanding can reduce the time spent on expensive *trial and error* methodology currently used to determine the correct process parameters for the desired applications of various materials.

The investigation in the thesis would facilitate optimisation for laser/material interaction parameters, leading to more widespread and efficient usage of results. In addition, the work presented in this thesis analyses the complex physical process underlying the ablation phenomenon in materials to determine the relative depth of the understanding of the physics underpinning the mechanisms.

1.2 Objectives of the Research

The main objectives of the research are to optimise the efficiency of laser processing of selected PCB materials by matching the laser beam parameters (wavelengths, peak power, pulse durations and fluences) to the optical and thermal properties of the materials. In particular, the research focussed on two sets of substrate materials: *Organics* and *Ceramics*. The set of organic materials included commercially available materials with the trade names Kapton, Arlon, RCC (Resin Coated Copper) and FR4. Ceramics consisted of commercially available Alumina and LTCC samples from DuPont and Ferro Inc.

The objective of the research work is to determine the laser wavelength and laser pulse conditions, which are optimum in terms of ablation machining efficiency for each material. This involved a determination of the absorption spectrum of each material in the relevant wavelength region (i.e. corresponding to the CO_2 laser emission spectrum). This is used as a guide to selecting the appropriate laser wavelengths to conduct the ablation experiments. The ablation efficiency was determined as a function of wavelength (in the chosen range) and later compared with the corresponding absorption spectrum. During the experiments, the ablation mechanisms are studied and reported as a function of fluence and wavelength.

1.3 Layout of the thesis

This thesis consists of seven chapters. Leading on from the introduction are two review chapters. Chapter 2 aims to familiarise the reader with the need of material

processing of dielectric materials for printed circuit boards. Many materials are available commercially for the manufacture of printed circuit boards but the materials investigated in this thesis are classified in two main categories based on their compositions. These groups are *Organics* and *Ceramics* and each category includes materials of trade names used in the electronic industry. Each material is discussed to familiarise the reader with the thermal, mechanical and optical properties, relevant to laser processing of material. Organics categorise materials with trade names such as kapton, arlon, and proprietary resin from resin-coated copper and FR4. The ceramics material studied are restricted to alumina and low temperature cofired ceramics.

Further the chapter discusses microvias as an important technique for making connections in the board between different components on different layers and its significance to electronic industries and the methods with which these can be drilled in circuit boards. Techniques of drilling vias are categorised as 'conventional drilling and ablation drilling', where conventional technique include mechanical drilling and ablation consists of photo defined, plasma, and laser drilling. Each method has its advantage and disadvantages in terms of via shape, size, quality, and cost of the method. Laser drilling is emphasised for its advantages and ease of use for drilling vias compared to other methods. Finally, a brief discussion is presented on the lasers, which are available commercially for application of drilling holes in circuit board material.

Chapter 3 discusses the physics underlying the laser/material interaction phenomena. Laser/material interaction produces significant changes to the surface morphology due to heating or ablation and the chapter discusses the dynamics of the interaction process detecting the key laser and material parameters. For surface modification or effective laser machining process, high absorption of the laser beam in the materials is required to heat, vaporise and ablate the material. Materials of varied compositions respond significantly differently with the same laser due to the underlying phenomenon of material interaction, which is a function of the laser and material parameters. The CO_2 laser is reported to ablate thermally but the section summarises other types of ablation phenomenon relevant to understanding of the material response. In addition, attention is directed to the surface quality of the material after

ablation, to analyse the effect of IR radiation on the material in terms of quality finish after ablation.

Chapter 4 describes the precision machining system used in the experiments described in Chapters 5 and 6. The overall system consists of a laser source, beam transformation and delivery system and a suitable mechanical translation system on which the substrate under investigation is mounted. The beam train also includes an acousto optic modulator to provide options of pulse duration, amplitude, and repetition rate. The laser source is a MOPA system consisting of a line-tuneable cw CO_2 laser and a multipass planar waveguide power amplifier which could be operated in the so-called "enhanced pulse mode" to achieve the necessary peak power to machine the materials. As a prelude to the material processing studies, the Chapter also presents the result of an investigation of the gain and power amplification characteristics of the MOPA format planar waveguide CO_2 laser amplifier system. Small signal gain measurements are presented and amplification in 5-pass configuration is reported for a range of operational conditions.

Chapter 5 examines the experimental results for laser ablation drilling of *organic* materials, presenting experimental investigations of machining threshold in these materials as a function of wavelength, pulse length, and fluence. Efforts are made to correlate with the recorded absorption spectra of the materials measured by an IR ellipsometer. The ellipsometer is introduced and a brief discussion is made on the measurement technique for recording absorption spectrum of a given material. Finally, an ablation spectrum of each material is produced in the IR processing window, which leads to selection of optimal laser wavelength and process parameters that assures low machining threshold and low fluence for drilling holes in materials. A comparison of absorption and ablation spectra provides information on the wavelength absorption and spectral absorptivity of a material.

Chapter 6 report the experimental results of the ablation in ceramics – alumina and LTCC samples. The pattern of the chapter follows that of Chapter 5. It starts with the measuring of spectral absorption of the material using the ellipsometer data, to distinguish the IR absorption window of the materials. Thereafter, ablation rate is measured as a function of fluence and pulse duration at key wavelengths, which

generates the ablation spectra of materials in the IR spectrum. The influence of wavelength, pulse length and fluence on ablation threshold is reported for each material. The chapter summarises with a discussion of the morphology of the drilled holes and comparison of ablation curves in both the samples of LTCC and comparison of LTCC with alumina. Based on experiments, ablation spectrum enables selection of the most appropriate wavelength for ablating the material with minimum laser fluence.

Finally in Chapter 7, conclusions are drawn from the investigations of the ablation of these materials within the IR processing window based on the key factors like threshold of ablation, influence of the irradiation wavelength on the ablation process and substrate, pulse duration and fluence for drilling a via in material. Results lie in direct interest of electronic industry in laser applications. In addition, proposals are made for the future work.

1.4 References

[1.1] J.C. Miller, "*History, Scope and Future of Laser Ablation*", Laser ablation - Principles and Applications, pp. 1-9, Springer Series (1994)

[1.2] R. E. Russo, *"Laser Ablation,"* Appl. Spectros. **49**, 14A (1995)

[1.3] D. Bauerle, "*Laser Processing and Chemistry*" (Springer, 1996)

[1.4] R. Srinivasan, *"Ablation of polymethyl methacrylate films by pulsed (ns) ultraviolet and infrared (9.17 μm) lasers: A comparative study by ultrafast imaging"* J. Appl. Phys. **73**, 2743 (1993)

[1.5] P. E. Dyer, D. M. Karnakis, G.A. Oldershaw, G.C. Roberts, *"TEA CO_2 laser ablation of Upilex polyimide"* J. Appl. Phys. **29**,2554 (1996)

[1.6] D. W. Zeng, K.C. Yung, "*XPS investigation on Upilex-S polyimide ablated by pulse TEA CO_2 laser,"* Appl. Surf. Sci. **180**, 280 (2001)

Chapter 2

Review of Laser processing of dielectric laminate materials for electronic applications

2.0 Introduction

This chapter presents a review of dielectric laminate materials used for printed circuit boards (PCBs) relevant to the electronic printed circuit board industry and the processing techniques of the boards for high volume. It begins with a discussion of modern printed circuit boards (PCB) dielectric laminate materials, their key optical/thermal properties and goes on to examine the role of microvias for high volume circuitry. Different methods of making microvias in these materials are also discussed with an emphasis on laser processing of microvias.

New applications and products in the electronics industry are driven by increasingly sophisticated markets demanding light, portable systems with many more features and functions at low cost. These new features are provided by the relevant electronic components mounted on PCBs. A printed circuit board, or PCB, is a self-contained module of interconnected electronic components found in devices ranging from common beepers or pagers, and radios to sophisticated radar and computer systems. The circuits are formed by a thin layer of conducting material deposited or "printed" on the surface of an insulating board known as the substrate. Individual electronic components are placed on the surface of the substrate and soldered to the interconnecting circuits. The purpose of the PCB is to keep electronic components mounted in place and to provide electrical connections between them. A printed circuit board may have circuits that perform a single function, such as a signal amplifier, or multiple functions. As electronic systems have become more complex and require more components, the PCB has become more densely populated with components and inter-connects. The increasing demands for additional system functionality are forcing electronic packaging designers and manufacturers to generate new interconnection methods and technologies [2.1].

Printed circuit boards are classified either according to board formation techniques or board wiring standards. According to the printed circuit board formation technique, it is further classified as: rigid printed circuit boards or flexible printed circuit boards.

Industrial examples of rigid printed circuit boards are: the motherboard or a peripheral card of a computer, a communication product, such as a board of a mobile phone, or a board of a consumer product. A base material for flexible PCBs is an integral laminate composed of an insulating base film having high heat resistance and excellent electrical and mechanical characteristics and a metal foil bonded with an adhesive. Because the flexible printed circuit board has properties of lightness, thinness, size, ductility, flexibility and high wiring density, the flexible printed circuit board can be three-dimensionally wired and the shape of the flexible printed circuit board can be changed according to space limitations. The flexible printed circuit board is therefore typically applied in small products, such as notebook (NB), mobile phones, personal digital assistant (PDA) and information appliances (IA). A third category is multilayer printed circuit boards, which have a different thicknesses in each portion, is known as a rigid-flexible printed circuit board. The rigid-flexible printed circuit board is composed of a rigid board portion and a flexible board portion. A multilayer PCB provides a plurality of electrically conductive layers separated by insulating dielectric layers.

Based on the number of board wiring circuit surfaces used, printed circuit boards are also classified as single-sided PCBs, double-sided PCBs and multi-layer PCBs. Most basic PCBs have components mounted on one side and a conductor pattern on the opposite side of board, hence the term *single sided.* The electrical characteristic of the printed circuit board used to physically mount and connect extra circuit components needs a larger capacity and therefore more complex circuit. Thus *double sided* boards are used which have conductor patterns on both sides of the boards [2.2]. The third type, a *multi-layered* board, has a substrate made up of layers of printed circuits separated by layers of insulation. The components on the surface connect down to the appropriate circuit layer. This greatly simplifies the circuit pattern. The configuration in which electronic circuit elements are located and the routing of conductor paths between the circuit elements establish the precise circuit pattern. Having two or more separate conductor patterns requires an electrical bridge or connection between the conductor patterns called a *Via,* which is a simple hole in the board that is filled or plated with metal and contacts the conductor pattern to set up the electrical connection. The use of vias in dielectric laminate materials is imperative because it reduces size and weight of the product and

improves the electrical performance of the system. However, the demand for dense circuits has pushed the board fabrication industry to re-examine techniques for creating smaller vias in denser patterns [2.3]. Many processes include revised methods of creating the holes such as mass etching, micro punching, laser drilling and new methods for additively creating dielectric holes using photosensitive dielectric materials. Overall, the best via formation techniques will be those that combine cost saving and flexibility with speed of mass via formation and reduction in consumable cost [2.4].

Previous studies [2.5] show that laser drilling offers some distinct advantages over conventional drilling methods in terms of speed, flexibility of operation as well as cost reduction. Lasers are not only non-contact tools, with no tool wear, but also can drill very small holes, where mechanical drilling may fail. Although, holes as small as 40μm can be produced with mechanical drills but this only applies to through holes. Moreover, lasers can provide high production rates as compared to other methods as is discussed in details in following sections.

2.1 Base materials of Printed Circuit Board

Printed circuit boards (PCBs) can be divided in to the following types:

(1) Rigid boards that are widely used as single-sided, double-sided, or multilayer boards

(2) Flexible and rigid-flex boards

Over time PCBs have evolved from single-sided (all interconnections on one side) to double-sided and multi-layer boards to meet the demand of higher performance systems requiring higher packaging density and faster propagation speeds. Printed circuit boards are typically commercially available in the form of copper-clad laminates consisting of three principal components: a base or reinforcing material, a resin system or matrix and copper foil. Commonly employed base materials include paper, glass matte, woven glass cloth, quartz, and aramid material. In the typical process for manufacturing the laminated PCB, the base material is impregnated or coated with a resin.

According to Ritchey [2.1], two major applications define the selection of dielectric materials for printed circuit boards, namely *RF analog and digital circuitry*. The major difference between the two areas is in the complexity of the circuitry. From the standpoint of electronic circuit usage, the key laminate properties include the relative dielectric constant, glass transition temperature, loss tangent, dielectric breakdown voltage, and moisture absorption characteristics [2.6]. On the other hand, digital circuits are usually very complex and require multiple layers to accommodate them, which puts the priority on material characteristics such as ease of lamination, ease of drilling and other processing steps. The need for many layers makes PCBs relatively thick and soldering or reworking these thick PCBs may put significant thermal stress on the vias and other plated-through holes on a PCB. As a result, the basic cost of the raw laminate as well as the processing cost places an additional demand on the choice of laminate materials to be used.

From the wide variety of materials available in electronic industries for PCBs, several key materials that are listed in Table 2.1 have been chosen to study the basic laser/material interaction processes. Based on the type of mechanical reinforcement, the materials can be divided into two major classes –*reinforced and non-reinforcements*. Arlon and FR4 are examples of reinforced materials since they may be fabricated by including materials of different characteristics for example glass fibers and the rest come under non – reinforced materials. However, for convenience, materials have been divided in two major classes, on the basis of their compositions as – *Organics and Ceramics*.

Table 2.1: Materials studied in the thesis, classified based on composition

Categories of materials	Trade names of materials
Organics	Arlon Polyimide-Kapton FR4 RCC – Resin Coated Copper
Ceramics	Alumina LTCC – Low temperature co-fired ceramics

2.1.1 Organic materials

(a) Polyimide – Kapton

Polyimide is the generic term given to plastics of the *'imide'* family. The engineering materials known as plastics are more correctly referred to as *Polymers*. This term comes from Greek word Poly, which means 'many' and meros, which means 'part. Polymers are substances composed of long chains repeating molecules (mers). In most cases the elemental carbon forms the backbone of the chain (an organic material). These long chains intertwine to form the bulk of the plastic. The nature by which the chains intertwine determine the plastic's macroscopic properties.

Typically, the polymer chain orientations are random and give the plastic an *amorphous* structure. Amorphous plastics have good impact strength and toughness. Examples include acrylonitrile-butadiene-styrene (ABS), styrene-acrylonitrile copolymer (SAN), polyvinyl chloride (PVC), polycarbonate (PC), and polystyrene (PS). If instead the polymer chains take an orderly, densely packed arrangement, the plastic is said to be *crystalline*. Such plastics share many properties with crystals, and typically will have lower elongation and flexibility than amorphous plastics. Examples of crystalline plastics include acetal, polyamide (PA; nylon), polyethylene (PE), polypropylene (PP), polyester (PET, PBT), and polyphenylene sulphide (PPS). Polymers are basically classified as two types – *Thermoplastic and Thermoset polymers*. Linear polymers that melt upon heating are called thermoplastic polymers whereas thermoset polymers do not melt upon heating and the capacity to make a 3-D structure is the characteristic of this type of polymers. In thermoplastics the polymer chains are only weakly bonded (van der Waals forces). The chains are free to slide past one another when sufficient thermal energy is applied. In addition many polymers soften on moderate temperatures, which are generally, not useful for high temperatures applications.

Kapton is a thermoset plastic which is suitable for PCB applications due to its high dielectric strength and high resistance and high stability properties. Kapton is a trademark of the *DuPont company* is also known by its trade name *vespel*. It is a homogeneous and flexible material made of epoxy resin. Epoxy resin is a thermoset adhesive and has been in production since 1946. It is air curable, highly fillable,

possesses low shrinkage and low susceptibility to stress formation and has good adhesion to almost all materials. The key thermal properties of Kapton film of thickness of 25μm are listed in the Table 2.2. The Kapton film used in the thesis for experiments is 125μm thick and is commercial available. Kapton polyimide films are also called flex circuits industrially and are suitable for laser drilling since these retain their physical properties over a wide temperature range and of all its outstanding properties, it is best known for its ability to withstand heat.

Table 2.2: Thermal Properties of Kapton® Type 100 HN Film, 25 μm (1 mil)

Thermal Conductivity, k	0.12 $Wm^{-1}K^{-1}$
Glass Transition Temperature, T_g	360 – 410 °C
Specific heat capacity, C_s	1.09 $Jkg^{-1}K^{-1}$
Density, ρ	1.42 g/cm^3

(b) Organic material - Arlon

Arlon is another example of composite of epoxy resin with reinforced non-woven aramid fibers in it. An aramid fibre is a generic name for a high-strength, flame-resistant synthetic fabric and is an organic fibre in the aromatic polyamide family. The epoxy shows good adhesion to maintain high tensile and vibrational strength. It possesses high heat resistance, high heat deformation resistance, and high chemical attack resistance. Selection of Arlon for any application is determined by its fibrillation i.e. depending on aramid fibre length and degree of "hairiness" or fibrillation in substrate. The fibrils are slender fibers branching from a "parent" root, where the degree of branching influences the interlocking of these extremely strong fibers giving high degree of reinforcement to the cured film. Figure 2.1 illustrates the fibrillation of aramid in the arlon material. The unique and highly oriented structure creates fibers with extremely high tensile strength, six times stronger than steel on a pound for pound basis. The network of fibers rapidly disperses forces applied to the coating system thus improving flexural strength. Additions of aramid fibers have been shown to increase tensile and tear strengths by factors of up to five times. Wear resistance, which is related to toughness and tensile strength, is also improved several fold, thus making arlon a good PCB material. Laser

ablation of arlon observes different thresholds to aramid and resin. Aramid has high fluence threshold as compared to resin hence optical parameters that can ablate both materials equally generating clean holes is highly desirable industrially. Details of laser ablation of the Arlon will follow in Chapter Five. The key thermal properties of Arlon are listed in Table 2.3.

Table 2.3: Thermal properties of Arlon

Thermal diffusivity, κ	1.73×10^{-7} m^2s^{-1}
Glass Transition Temperature, T_g	275 ^oC
Density, ρ (aramid fibers)	1440 $kg.m^{-3}$
Density, ρ (resin)	1397 $kg.m^{-3}$

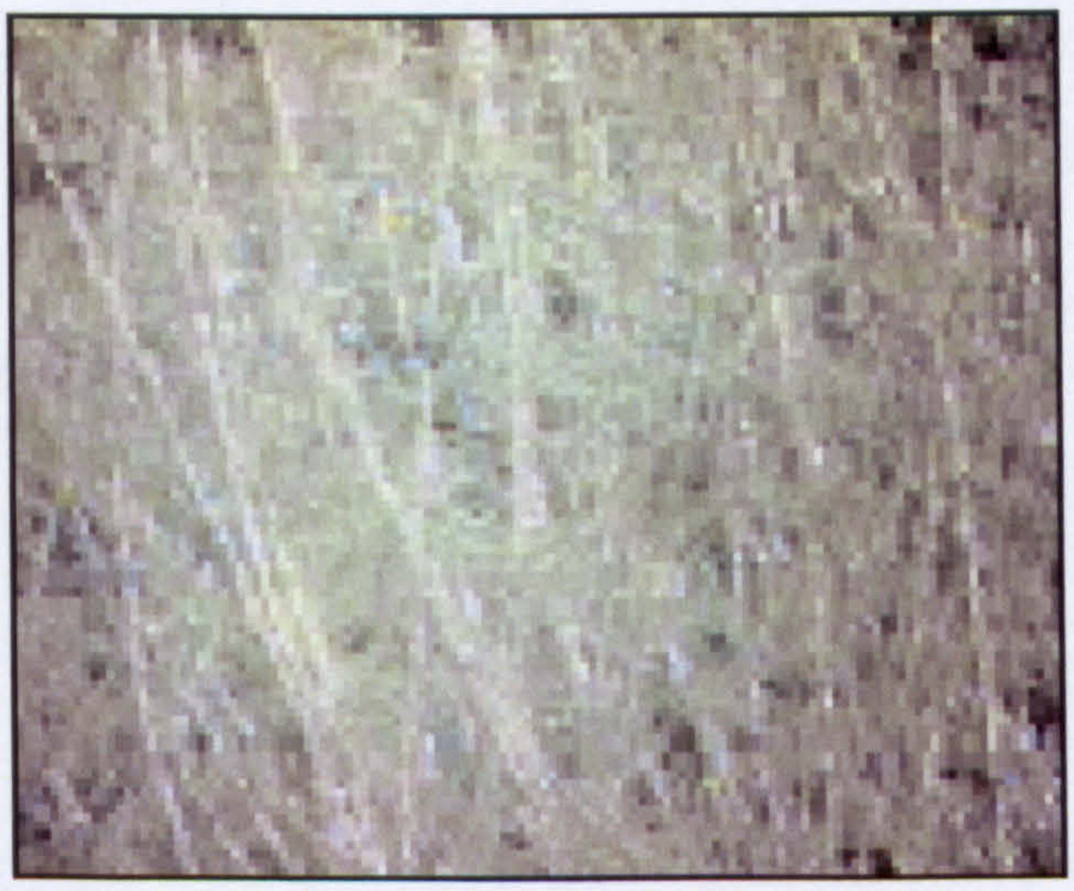

Figure 2.1: Fibrillation of aramid in Arlon film

(c) Epoxy Resin in resin coated copper (RCC)

RCC – resin coated copper, is a dielectric laminate material used for built-up multilayer circuitry. It consists of a uniquely engineered epoxy resin system coated to the copper in a cured/semi cured state [2.7]. RCC is commercially available both as *single layer* and *double layered.* A single layer RCC consists of a coating of resin on a copper layer whereas, a double layered RCC consists of resin/copper/resin configuration as is shown in Figure 2.2. The first coating layer of resin is called *B stage resin* and it is fully cured

high temperature epoxy, whereas second resin coating is *C-stage*, which is semi cured with high temperature epoxy. The function of the C – stage coating is to act like the dielectric, electrically insulating the outer layer copper from the adjacent conductive copper layer. The B- Stage coating acts as the adhesive to bond the copper foil to the inner layer [2.8]. In the present work we have used *double layered* RCC, for experimental investigations. Since the investigation of laser ablation is carried out only in cured resin, the sample was prepared accordingly to expose the resin layer. The surface copper layer is removed by etching in Ferric Chloride solution to expose the heat cured resin layer. This solution is heated with hot water and constantly agitated by shaking the solution to reduce the reaction time. The exposed resin layer is of 60μm thickness sitting on second layer of copper. The thickness of the exposed resin layer is 60 microns, which still rests on the copper layer is shown in Figure 2.3. The thermal properties of the resin are listed in Table 2.4.

Table 2.4: Thermal Properties of proprietary resin of resin coated copper (RCC)

Thermal diffusivity, κ	$1.73 \times 10^{-7}\ m^2 s^{-1}$
Glass Transition Temperature, T_g	140 °C
Thermal conductivity, k	$0.18\ W\ m^{-1}\ K^{-1}$
Density, ρ	$1200\ kg.m^{-3}$
Specific heat capacity, C_s	$1050\ J\ kg^{-1}.K^{-1}$

Figure 2.2: Single layered RCC on left and double layered RCC on right

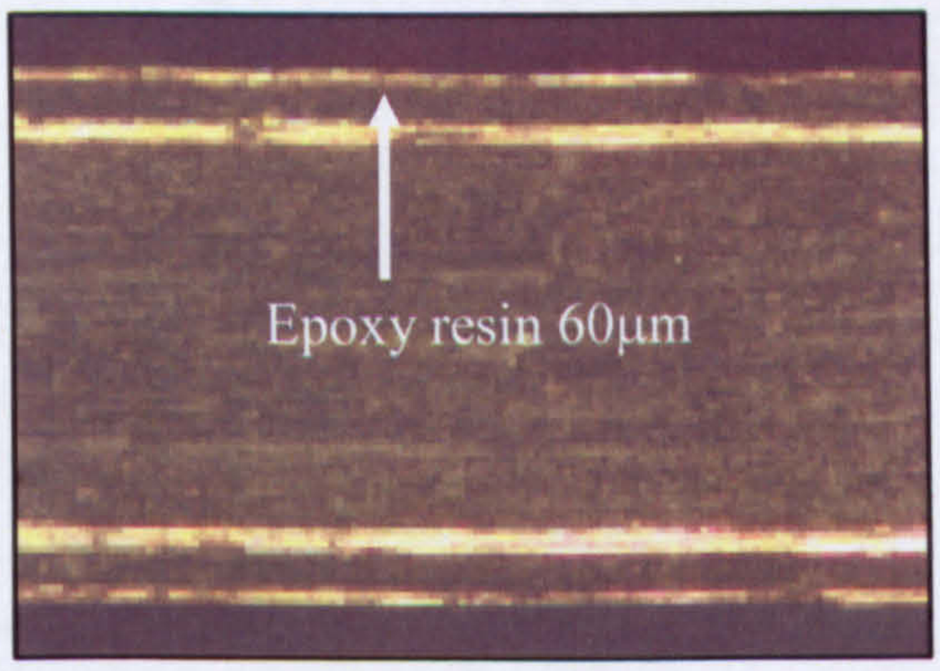

Figure 2.3: 60μm resin used for experimental investigation in RCC. Top layer of copper is etched off to expose resin layer for experiments.

(d) Glass fibre reinforced epoxy resin (FR4)

FR4 is very common and typical board material used for electronic circuits [2.9]. FR4 laminate is the usual base material from which plated-through-hole and multilayer printed circuit boards are constructed. *"FR"* means *Flame Retardant*, and *type "4"* indicates *woven glass reinforced epoxy resin*. The laminate is constructed from glass fabric impregnated with epoxy resin (known as *"pre-preg"*) and may or may not have the copper foil, which is commonly supplied in thicknesses of "half-ounce" (approx. 18 microns) or "one-ounce" (approx.35 microns). Foil is generally formed by electrodeposition ("ED Foil"), with one surface electrochemically roughened to promote

adhesion. A typical 1.6-mm rigid laminate is made by bonding together eight plies of heavyweight pre-preg, with half-ounce copper foil either side, in a hot hydraulic press. In the present thesis, FR4 without the copper foil has been used for the experiments. FR4 laminate displays a reasonable compromise of mechanical, electrical, and thermal properties. Dimensional stability is influenced by construction and resin content. The glass transition temperature (T_g) of FR4, at which the resin changes from a glassy to a plastic state, ranges from 120°C to 180°C depending on resin chemistry. The continuous operating temperature for FR4 is typically 130°C, and it has a resin content of approximately 65% by weight. Also epoxy resin has lower melting and ablation temperature as compared to woven glass. Laser machining of this material requires accurate beam parameters to make vias through both materials (glass and resin) of different thresholds, and to ablate both materials simultaneously. FR4 is available in different forms, based on the woven glass types, thickness of the board, its colours and tight tolerances in the woven grid of glass in the epoxy resin. Figure 2.4 illustrates example of FR4 substrate with standard glass woven in epoxy resin. Figure 2.4 (a) is the actual sample ground to expose glass weaved in resin whereas (b) is the standard glass weave in the substrate. Table 2.5 summarises thermal properties of FR4 with woven glass in its resin.

Table 2.5: Thermal Properties of FR4 with glass

Glass Transition Temperature, T_g	125 - 135 °C
Thermal conductivity, k	0.16 – 0.20 W m^{-1} K^{-1}
Density, ρ	1938 $kg.m^{-3}$
Heat capacity, C_s	1.703 x 10^6 J $m^{-3}.K^{-1}$

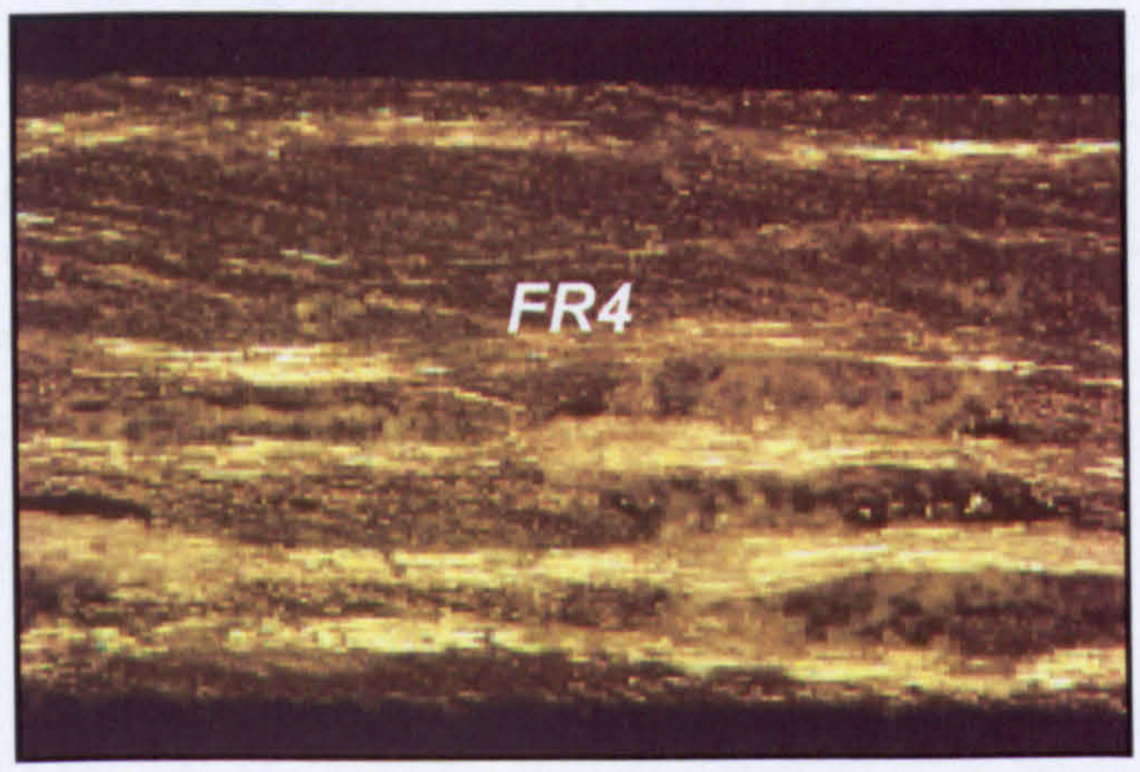

(a)

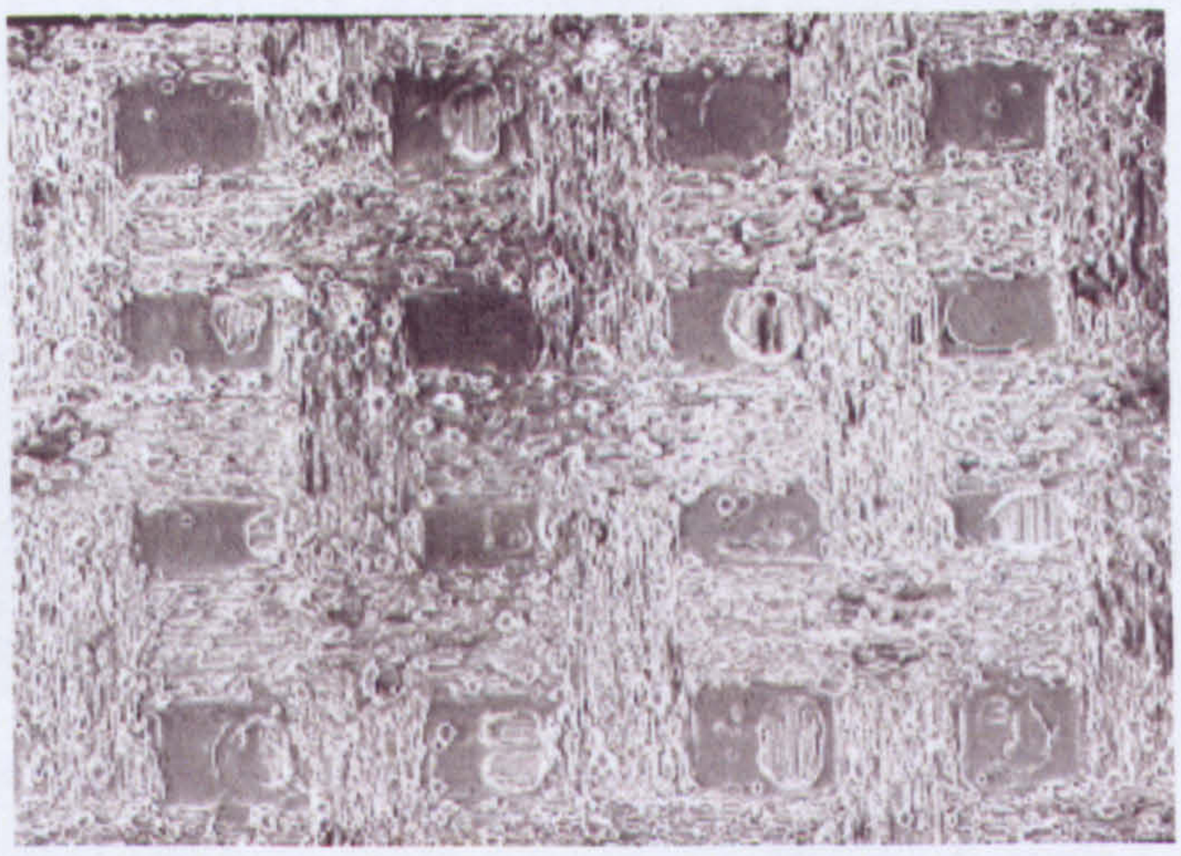

(b)

Figure 2.4: FR4 substrate with standard woven glass reinforced in epoxy resin (a) View of FR4 substrate with glass pattern of sample used in thesis (b) Glass woven patterns in FR4 substrate

2.1.2 Ceramic materials

(a) Alumina

Ceramic is a general term used to describe a broad range of materials that include enamel, concrete, cement, pottery, brick, porcelain, and chinaware. Ceramic can be either crystalline or amorphous, single-phase materials or mixtures of two or more discrete substances. One of the most distinctive features of ceramic is its resistance to being worked or shaped after it is fired. *Alumina (Al_2O_3)* is a dielectric that presents an outstanding combination of low thermal and electric conductivity, high strength, low deformability, high wear resistance and chemical inertness. But alumina is difficult to machine due to the high contraction experienced during sintering process and is impossible to shape or drill accurately using conventional techniques. At high temperature, alumina is transformed from a solid state to liquid state, which is called *Corundum*. To achieve this phase transformation, in an electric arc, fusion at high temperature is performed followed by slow cooling. Thus, corundum represents a family of electro fused aluminas that is classified as follows: *(a) White corundum ("pure" alumina), (b) Brown corundum (aluminas doped at 1.5% or 3% with TiO_2), (c) aluminium oxynitrides (AlON).* The experimental investigations in the thesis are carried out on white or pure alumina and its thermal properties relevant for laser processing are listed in Table 2.6.

Table 2.6: Thermal properties of Alumina

Melting Point	2050 °C
Boiling Point	2977 °C
Density, ρ	3.984 $kg.m^{-3}$
Thermal conductivity, k	33 $W\ m^{-1}\ K^{-1}$
Specific heat, C_s	755 $J\ kg^{-1}.K^{-1}$
Latent heat of fusion	4800 k J kg^{-1}
Latent heat of Vaporisation	24700 k J kg^{-1}

(b) Low temperature cofired ceramic (LTCC)

Low temperature cofired ceramic (LTCC) materials can be defined as a multilayer circuit substrate that is fabricated by laminating single *green sheets* and firing them all together in one step a term for unfired tapes of ceramics. Green Tape is a trade name (of DuPont Company) with printed conductor lines on the surface on top of each other. Three technologies are used to make multilayer circuit substrate structures:

a) Thick Film Multilayer (TFM),

b) High Temperature Cofired Ceramic (HTCC)

c) Low Temperature Cofired Ceramic (LTCC).

In TFM technology, a multilayer is processed serially i.e. layer by layer. Each layer is printed and fired separately at 850 - 1000 °C. In HTCC and LTCC technologies the process is carried out in a parallel way, where all foils are cofired in a single step building a multilayer structure. But the main difference between HTCC and LTCC is in the material of the foil and the firing temperatures. HTCC foils consist of alumina and are fired at 1600 - 1800 °C in a hydrogen atmosphere. Only tungsten and molybdenum can be used as conductor elements due to high firing temperature required for making HTCC foils. In contrast, LTCC foils are made from alumina filled glasses or glass ceramic material and the foils are cofired at 850 - 1000 °C. Higher conductivity metals such as gold, silver or copper replace tungsten or molybdenum used in HTCC foils.

Two types of LTCC are investigated in the thesis, (a) LTCC commercially available from DuPont Inc– Blue in colour and (b) LTCC, white in colour available commercially from Ferro Corporation. Table 2.7 lists the thermal properties of both types (DuPont and Ferro) LTCCs relevant for the laser ablation process.

Table 2.7: Thermal properties of LTCC

	DuPont - Blue	Ferro - white
Boiling Point (Alumina)	2977 °C	2977 °C
Density, ρ	3.1 $g.cm^{-3}$	2.5 $kg.m^{-3}$
Thermal conductivity, k	3 $W\ m^{-1}\ K^{-1}$	2 $W\ m^{-1}\ K^{-1}$

2.2 Microvias

Vias of diameters less than 100μm are termed *microvias* and they have become a critically important capability both for printed circuit board and for fabrication of advanced integrated circuit packages [2.10 -2.12]. There are several types of vias that are drilled, based on the characteristics of the interconnection required in different printed circuit board architecture for varied applications. Figure 2.5 illustrates a cross section view of metalised microvias in industrial Resin coated copper RCC board. The set of important vias with brief descriptions are summarised in Figure 2.6. Microvia holes may be formed in a dielectric layer by several different methods, that include: Mechanical (punching and drilling), Laser (CO_2, YAG and excimer lasers), Photochemical (liquid or dry film resists) and Etching (wet or dry etching).

The mechanical method is also often referred to as the as *conventional technique.* Mechanical manufactured holes by punching or drilling have several disadvantages, since the process is limited by minimal drill bit diameter, high spindle speed, the use of thinner materials and very small dimension of microvias in *high density interconnects (HDI).* The minimum hole diameter for volume production is around 2mm and requires the circuit board of consistent thickness, but the process is still limited by drill bit changes and breakage. The other techniques such as laser drilling and photochemical etching are called *ablation techniques* and offer several advantages for HDI [2.13].

Paste via technology is another category that is widely used to produce via interconnections for commercial applications. Two common technologies in this category are ALIVH™ (Any-Layer Interstitial Via Hole, a trademark of Matsushita Electric Industry,) and B2it™ (Buried Bump Interconnection Technology, a trademark of Toshiba).

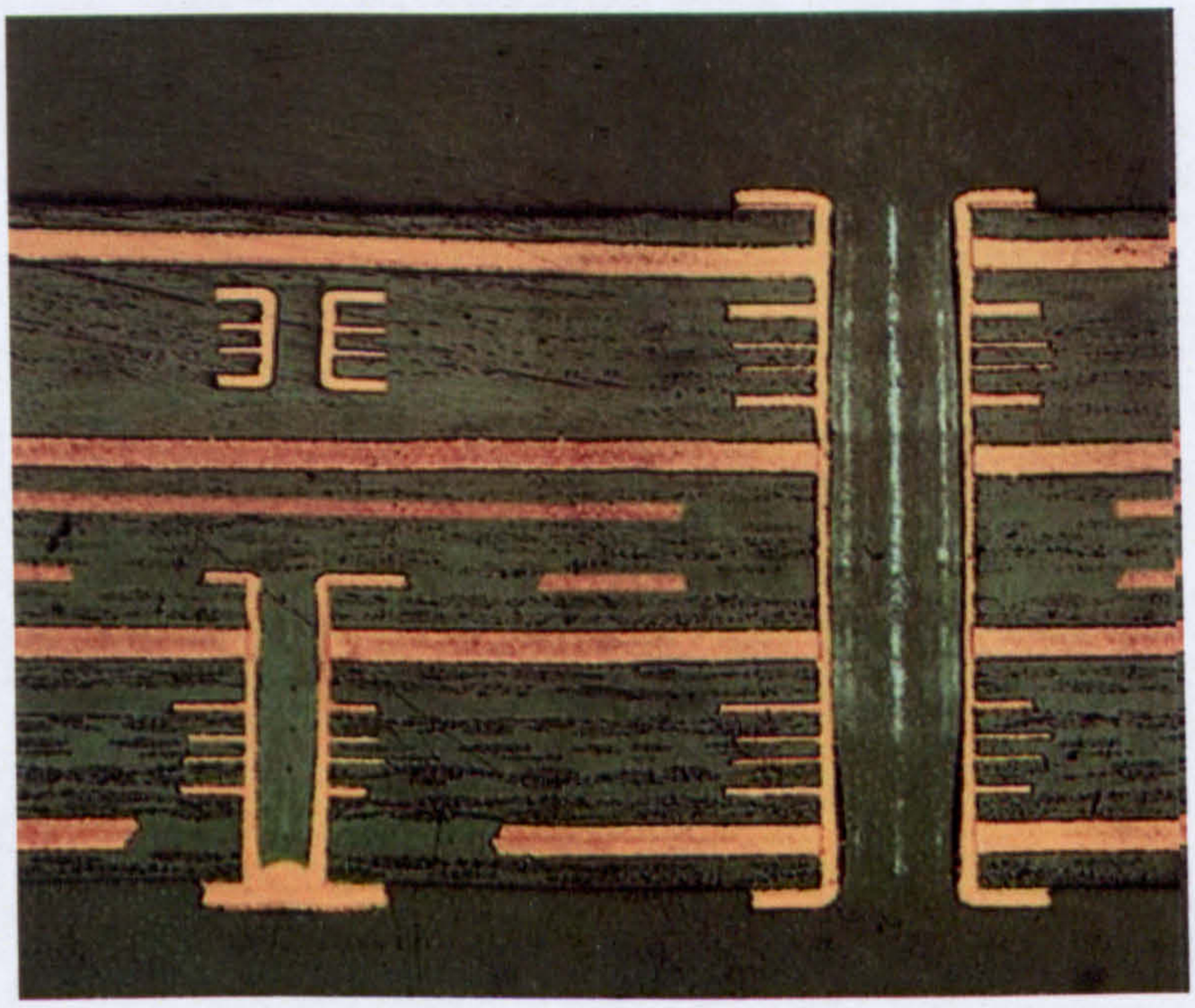

Figure 2.5: Examples of microvias, cross-sectioned of metalised microvias in industrial RCC

BLIND VIA

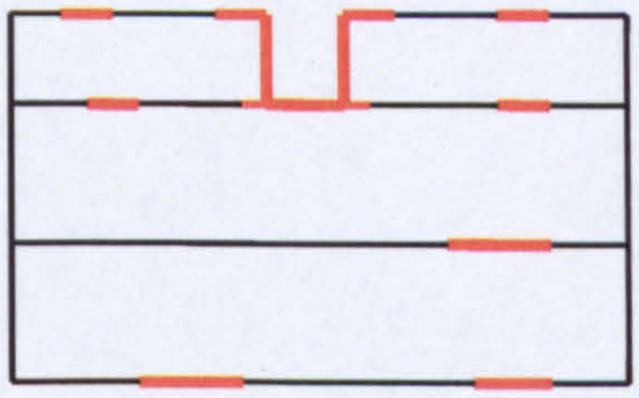

General term for via hole, which interconnects electrically outgoing from soldering or component side not completely up to the opposite outside layer.

BURIED VIA

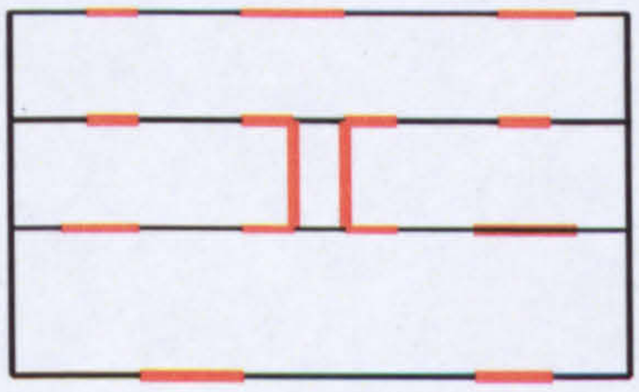

General term for a via hole, which does not contact the outside layers.

STACK VIA

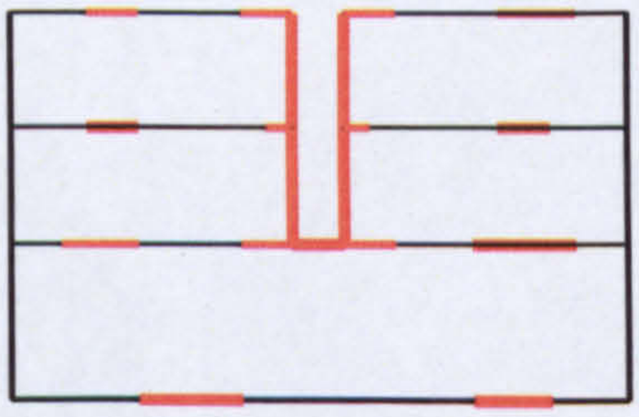

A via which is formed by stacking one or more build-up vias on a build-up via and provides a interlayer connection between three or more conductive layers

HOLE-PLUGGED VIA

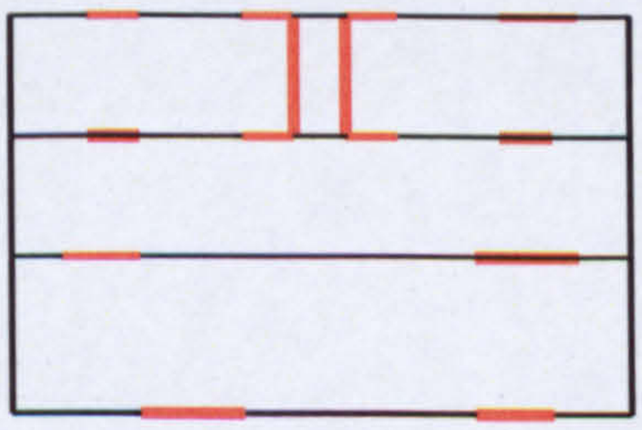

A plated-through via which is formed on the base of a build-up printed board and is filled with a filler in its interior

Fig 2.6: Types of Micro Vias

a) Advantages of Microvias Technology

Microvias offer several distinct advantages [2.15] over their mechanically produced counter-parts from both the aspect of physical features and electrical performance, including the following:

a) Microvias within the substrate allow significantly increased packaging density for assembly with a reduced layer count, greater layout efficiency, and reduce PCB costs.

b) PCBs with conventional through-hole fabrication technology have physical size limitations that cannot support parts with fine line geometry. Microvias are particularly significant here since they enable the incorporation of high density chip packages into the system.

c) PCBs with microvias show better electrical performance and signal integrity due to their physical structure. As the diameter and length of microvias becomes smaller, both the inductance and capacitance decrease, resulting in a reduction in switching noise.

d) RFI/ESD (Radio Frequency Interference/ Electrostatic Discharge) can be improved by effective grounding of a PCB. The microvias-in-pad implementation enables one to utilise more ground or space around the components and increases density of components in given space.

e) Proven microvia technology yields higher reliability because of the significantly lower area aspect ratio (1:1) due to its fabrication in one dielectric layer when compared to a larger drilled through-hole via having a much high aspect ratio (>10:1).

An example of conventionally drilled PCB and microvia drilled PCB is shown in Figure 2.7. The picture on left illustrates an example of the conventional board with original through hole version and the picture on right is 'after' the PCB is microvia drilled in the same board that saves space and increases density of components in given area.

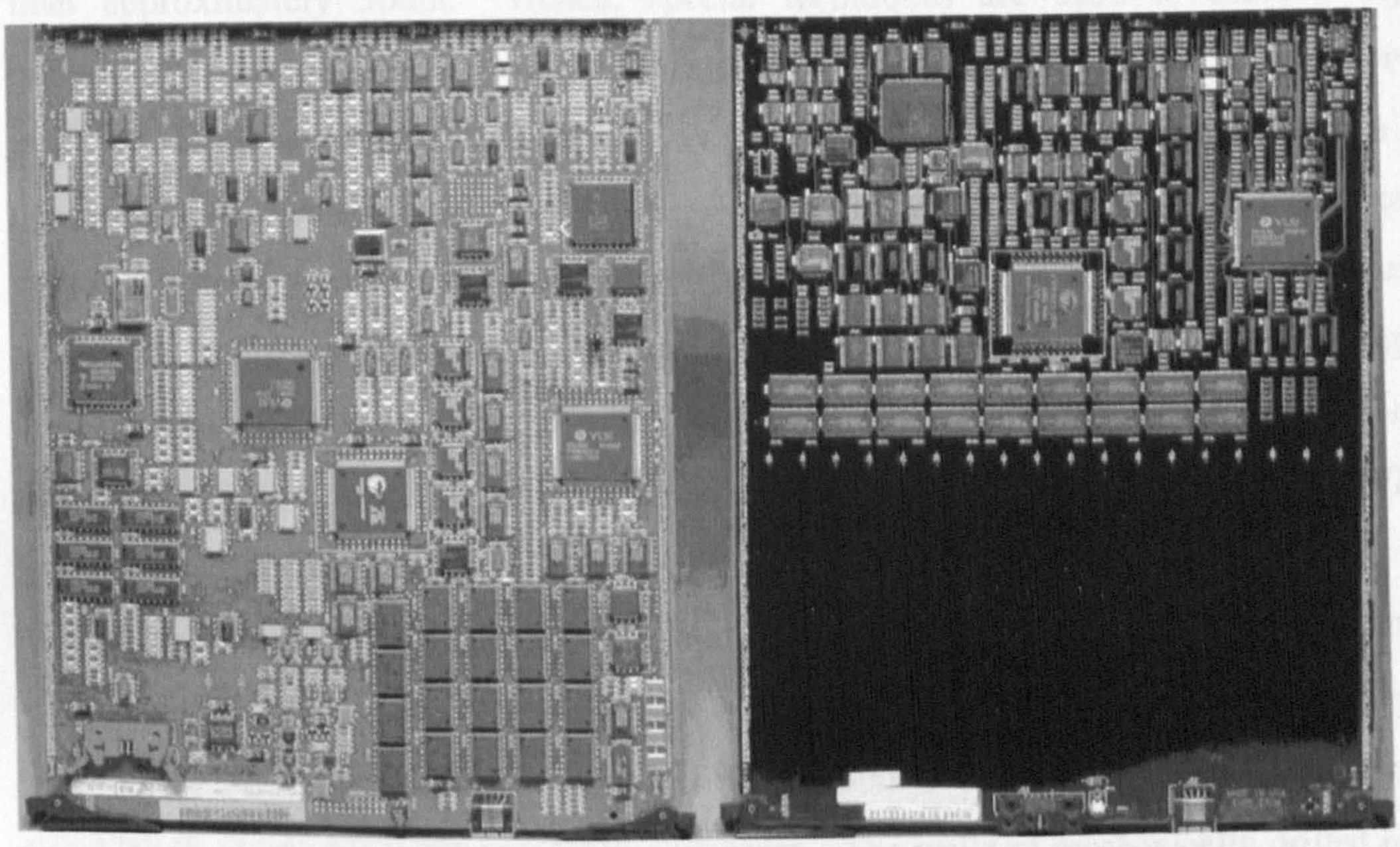

(a) *(b)*

Figure 2.7: Comparison of PCB with conventional through hole technique (a) and microvia drilled technique (b).

2.2.1 Conventional technique for drilling via

2.2.1.1 Mechanically formed microvias

Mechanical drilling has traditionally been the dominant technique for through-vias and large via diameters. Also it is the most cost-effective means of forming a blind via [2.14]. When the panels are drilled, the blind vias are formed by drilling only part way through the board and stopping. But, mechanical drilling is limited to via sizes larger than approximately 50um. Hence, special techniques are used to achieve depth controlled drilling of small via sizes. High-speed spindles are combined with different kinds of depth sensors. For example extremely precise blind via formation can be achieved with Electric Field Sensing (EFS). EFS is based on a simple antenna theory where the pressure is monitored with a low power microwave field. The drill bit is used as an antenna to sense this field and monitor the output signal. The drop of the signal indicates the drill bit touching a metal surface such as a copper surface of the board. From this "ZERO" position, the bit drills with an accuracy of 15um into the board. While the costs are low for large via diameters, but they rise significantly for smaller via diameters, since the drill bits become more expensive and have to be replaced more frequently. There is a significant increase in costs when going down to via diameters of 100 um and even more for via diameters down to 50um. Another unattractive feature of mechanical method is isotropic drilling of holes. The walls of mechanically drilled holes are vertical (straight up and down), making them less desirable for the subsequent plating operations.

2.2.2 Ablation techniques for drilling via

2.2.2.1 Photo defined microvias

Photoimaging techniques have the advantage of forming large number of microvias simultaneously using technology based upon conventional light exposure via a mask, developing, and plating process [2.16]. After exposure with an appropriate light source, the developing process selectively removes the dielectric material creating a via. Photoimaging has been widely used for microvia formation since IBM produced the first microvia boards for its ThinkPad computers in 1990 using processes that incorporated either liquid or dry film photoimagiable dielectric. One limitation of this technique is that microvias with 125 μm and 100 μm diameters are typical, microvias as small as 75

μm are possible, but smaller than this dimension is not practical which is essentially required for high density interconnect in PCBs. Also a new mask is required for any changes in design for making microvias, which further adds to the cost the process.

2.2.2.2 Plasma etched microvias

The plasma technique can be used to make many microvias simultaneously, using print-and-etch steps by creating a via mask and then the plasma etches away dielectric material. Plasma etching can produce microvias with diameters smaller than 100μm on thick polyimide substrates, but the capital equipment costs associated with the process is extremely high. Also plasma etch is an expensive process to maintain, especially in regard to chemical waste treatments and the cost of consumables. Furthermore, it takes significant amount of time to develop new processes that consistently yield reliable microvias, though the advantage of plasma technology is higher reliability and reported yield is of 98 percent in microvias formation. This technique finds niche uses in medical and avionics applications. But this technique is not popular in volume productions also the major limitations lies in vias diameter which is restricted to 75μm.

2.2.2.3 An overview of laser drilling of microvias

Laser drilling is essentially a laser induced material removal process, in which less than 100 μm vias are drilled in materials, by coupling laser light into the material. When the laser pulse strikes the work piece, due to absorption rapid heating occurs that leads to melting and vaporisation resulting in removal of material. This material removal process is also termed as *laser ablation*.

Laser ablation dates back to the 1980's when Srinivasan and co-workers at IBM [2.17] reported ablation of PET (polyethylene terephthalate) at low fluences with the 193nm ArF laser. This pioneering work demonstrated the possibility of unprecedented resolution and at the mechanistic level, an interesting new laser – material interaction phenomenon that Srinivasan termed "*ablative photodecomposition*" [2.18]. Since that time ablation of materials has been developed over the years, for example during the 1980's by Srinivasan [2.19, 2.20]and Yeh [2.21], Srinivasan and Braren [2.22] and Lazare and Granier [2.23] and in the early 1990's by Dyer [2.24] and more recently Yabe

[2.25] has provided an overview of the broad spectrum of scientific applications of laser ablation and processing, covering material removal, surface modification and film deposition [2.26].

Laser drilling of microvias is a straightforward and inexpensive process compared to conventional and other ablation techniques. The capital equipment costs are far less and because a laser is a non-contact tool, there is no expensive hard tooling to replace, as in mechanical drilling. Furthermore, many lasers like modern sealed off CO_2 and UV-diode pumped solid state (DPSS) lasers are of low cost maintenance, minimise downtime and maximise productivity. Due to all these advantages over other methods, lasers compete with other available techniques for drilling microvias [2.27, 2.28]. Lasers are classified primarily by their wavelength and power outputs. The nature of laser emission, for example, the wavelength, fluence (measured in joules per square centimeter), peak power, pulse width, and pulse rate, is different, and therefore different processing and quality is achieved depending on the type of materials considered for ablation. Therefore, drilling applications may require different types of lasers that optimise drilling speed, via hole size, quality, hence there are options available such as excimer, solid state [2.29-2.38] and IR carbon dioxide (CO_2) [2.28-2.33,2.39-2.45] lasers. In the IR spectral range (9 – 11 μm), the two types commonly used CO_2 laser systems are the Sealed RF Excited CO_2 and the TEA CO_2 laser. Both offer high productivity and low cost. The IR CO_2 laser has long wavelength and has natural tendency to be reflected by metallic material, especially copper, therefore these are excellent for drilling non metallic materials especially organic polymers [2.46 – 2.47].

a) CO_2 Laser

The CO_2 lasers oscillate at wavelengths between 9 and 10μm and are advantageous for drilling dielectric PCB materials due to their high absorption in this wavelength region. Industrially there are many types of CO_2 lasers used to drill microvias, but a few basic types are discussed in this section. As an example, TEA CO_2 lasers are capable of high peak powers to a few MW and pulse rates to 600 Hz. To maintain these parameters the system is required to circulate the gas mixture. The other disadvantage is the low quality of the laser, which cannot be focussed to a small spot, therefore conformal masks are

used to project image of the mask on the surface to be drilled. However, the conformal mask method has the problem of higher costs and limitation of resolution in both via and circuits.

Q–switched RF excited CO_2 laser drilling of PCBs such as RCC and FR4 was investigated where the laser can emit pulse lengths of 80 ns, and peak power of 40kW in an initial gain spike followed by a 5μs pulse tail of power <1kW at repetition rates of 100kHz in a burst pulse mode. The high repetition rates of the lasers are advantageous for mass production. However, Q-switched CO_2 laser is not capable of drilling copper due to the initial gain switch spike and the short duration of the high peak power spike which induces plasma screening. In general, Q – switched CO_2 laser systems are expensive with low average power (~50W) hence their use in industry is limited.

Sealed design RF excited slab waveguide CO_2 lasers are of high beam quality (M^2 ~1.1), have high average power of approximately 100 W and require low maintenance. The laser is low cost and can run continuously for 25,000 hours without requiring maintenance. These lasers can be pulsed to frequencies of up to 10 kHz with pulse energies ≥40mj. Due to 50 - 100μs rise times of the pulses requires an external modulation, for example an AOM is used in our system, described in Chapter 4, to shorten the pulse duration.[2.48].

b) UV Lasers

Diode pumped solid state (DPSS) lasers consist of one or more diode laser arrays to continuously pump a rod of Nd:YAG, Nd:YLF or Nd:YVO_4. The fundamental output wavelength of Nd:YAG lasers is in the near-infrared (IR) at 1.064μm. Nd:YAG lasers can be frequency converted to shorter wavelengths by the inclusion of non–linear polarisation crystals. The frequency doubling, tripling and quadrupling emits 532nm, 355nm and 266nm respectively. Both metals and organic materials have far more absorptivity in the UV hence making these lasers more attractive option for laser drilling copper. Frequency doubling to 532nm takes advantage of lower reflectivity of copper and high absorption coefficient. A further advantage of using UV lasers is the different ablation mechanism called the 'cold' photo ablation or more appropriately called photo

chemical ablation. The high energy UV photons break molecular bonds directly at the surface layer of many non-metals resulting in the production of smooth edges and a minimal heat affected zone.

Excimer lasers are also available that can produce short wavelengths in the UV region dependent on the noble gas halogen mixture employed, such as ArF (193nm) and KrF (248nm) and XeCl (308nm). Excimer laser can produce high quality holes and highly accurate ablation features due to photo chemical ablation mechanism. However, the poor beam quality results in excimer lasers being used with projection masks, so their throughput does not depend on via count as it does for Nd:YAG and CO_2 lasers. Nevertheless, the requirement of multiple pulses at low repetition rates with the high running costs, size restrictions of the mask and the missing capability of ablating metals have led to the superior speed and lower cost of CO_2 and Nd:YAG lasers dominating microvia laser drilling [2.49].

c) *Techniques for laser via drilling*

Another major advantage of the use lasers is the capacity to ablate material with high spatial resolution so as to achieve the desired feature sizes. However, there are many issues that need to be addressed in connection with the production of high quality holes by laser drilling. These issues include the production of recast layers that may cause cracks, the taper of the drilled hole may be too large, the shape of the hole may not be satisfactory, high aspect ratios are difficult to achieve, and redeposition around the hole might need post processing etc.

There are four basic techniques [2.50] for laser production of holes, as is illustrated in Figure 2.8:

(a) *Single Pulse drilling*

(b) *Percussion drilling*

(c) *Trepanning*

(d) *Helical drilling*

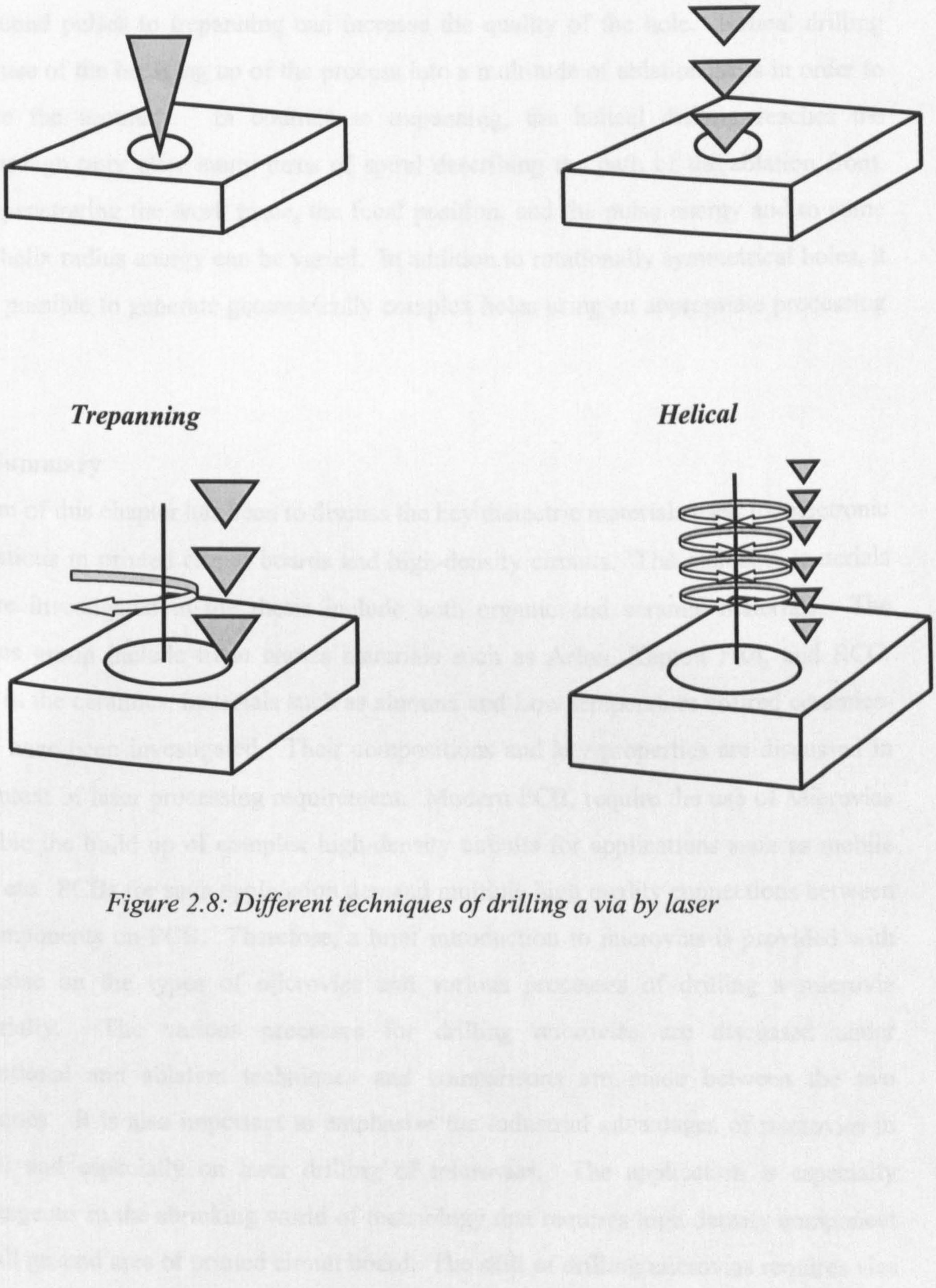

Figure 2.8: Different techniques of drilling a via by laser

In percussion drilling the laser pulse duration is short and is sequentially allowed to fall on the material. This helps reduce the melt of the material. Trepanning is the standard technique for large holes e.g. 500 μm holes in turbine blades. It is essentially a percussion drilling process followed by a cutting procedure. The application of nanosecond pulses to trepanning can increase the quality of the hole. Helical drilling makes use of the breaking up of the process into a multitude of ablation steps in order to enhance the accuracy. In contrast to trepanning, the helical drilling reaches the breakthrough only after many turns of spiral describing the path of the ablation front. While penetrating the work piece, the focal position, and the pulse energy and to some extent helix radius energy can be varied. In addition to rotationally symmetrical holes, it is also possible to generate geometrically complex holes using an appropriate processing energy.

2.3 Summary

The aim of this chapter has been to discuss the key dielectric materials used for electronic applications in printed circuit boards and high-density circuits. The dielectric materials that are investigated in the thesis include both organic and ceramic materials. The organics group include trade names materials such as Arlon, Kapton FR4, and RCC. While in the ceramics, materials such as alumina and Low temperature cofired ceramics-LTCC have been investigated. Their compositions and key properties are discussed in the context of laser processing requirement. Modern PCB, require the use of Microvias to enable the build up of complex high-density circuits for applications such as mobile phone etc. PCBs for such application demand multiple high quality connections between the components on PCB. Therefore, a brief introduction to microvias is provided with emphasise on the types of microvias and various processes of drilling a microvia industrially. The various processes for drilling microvias are discussed under conventional and ablation techniques and comparisons are made between the two techniques. It is also important to emphasise the industrial advantages of microvias in general and especially on laser drilling of microvias. The application is especially advantageous in the shrinking world of technology that requires high density component in small ground area of printed circuit board. The skill of drilling microvias requires vias to be drilled of certain sizes, quality etc as per the application of the PCB. Hence,

different techniques like trepanning, percussion, helical and single pulse drilling are discussed. To generate high quality holes it is necessary to optimise the laser and material parameters. Therefore, the next chapter investigates the underlying physics of laser ablation technique to understand the basic science in order to optimise the laser and material parameters for efficient drilling of microvias.

2.4 References:

[2.1] Lee W. Ritchey *"A Survey and Tutorial of dielectric materials used in the manufacture of Printed circuit Boards"*, Speeding Edge, Circuitree Magazine, Nov. (1999).

[2.2] Norocel-Dragos Codreanu, Paul Svasta, Ciprian Ionescu, Virgil Golumbeanu and Daniel Leonescu *"MOM" Electromagnetic characterization of vias from electronic and microelectronic modules*: "POLITEHNICA" University of Bucharest, Center for Technological Electronics and Interconnection Techniques, (CETTI); Splaiul Independentei **313**, 77206-Bucharest, Romania

[2.3] Jim Paulus and Frank Polakonic *"Integrating High density interconnect microvia technology into the multilayer board mainstream"*. Allied Signal Laminate systems,– Electrochemicals Inc, Maple plain,MW. IPC EXPO , April (1997).

[2.4] James Paulus, Michael Pettit,*"Technical Paper – Microvia Enablers for High density interconnects"*. Allied Signal Laminate Systems,. IPC Printed Circuits Expo 1997, San Jose California, March 9 – 13, (1997).

[2.5] Larry W.Burgess and Fabrizio Pauri, *"Defining the production role of laser technology in PCB fabrication into millennium"*. European printed circuit convention Paris France.,Sep.30, (1998).

[2.6] Dr. Walter Schmidt: "*A revolutionary answer to today's and future interconnect challenges"* Proceedings of third Euro Joint Conference (EIPC) Brussels, Belgium, June (1992).

[2.7] *"Advanced interconnect materials – Oak – mitsui copper foil and aluminum bonded copper products"*. Oak mitsui (2000).

[2.8] *A cost-effective high volume Multi – Layer flex and Rigid Flex technology."* www.parlex.com/dead/tech_papers/palcore.htm September 1, (2001).

[2.9] Larry Lamke:*"Advanced laminate based MCM consortium"* Proceedings. of International Electronics Packaging, Atlanta, GA (1994).

[2.10] .Isaac Tobaly, M.Rotthenhaeusser, *"AOI in Laser drilled microvia production."*, , Printed Circuit Europe ,pp 46,1rst Quarter (2001)

[2.11] *"Blind Vias and Microvias Cranford Circuits PCB Manufacturers Products and services – Blind and Buried"* www.cranford-circuits.co.uk/blind.htm

[2.12] Bob Forcier and Fred Hickman III *"The design and fabrication of HDI interconnects utilizing total integration of fiber reinforced materials"*. Circuitree , March (1999).

[2.13] H. Tourne: *"Laser via Technologies for high density MCM –L fabrication"* MCM Conference, pp. 71-76,(1995).

[2.14] *"High density microvias substrates and applications"* Tech international search Inc, Handbook on microvias (1999).

[2.15] Happy Holden "*Microvias effect on high signal integrity"* Circuit world, Vol 28, Number **3**, pp 10 -12 (2002).

[2.16] N. Watson " *Laser drilling of printed circuit boards'*, Circuit World,pp11, **13**, (1984).

[2.17] R.Srinivasan, V.Mayne-Banton *"Self developing photoetching of Poly (ethylene terephthalate) films by far Ultraviolet excimer laser radiation" Appl. Phys. Lett.* **41,**576 (1982).

[2.18] R. Srinivasan, W.J. Leigh: "*Ablative photodecomposition: action of far-ultraviolet (193 nm) laser radiation on poly(ethylene terephthalate) films* " J. Am. Chem. Soc. **104**, 6784 (1982)

[2.19] R.Srinivasan: In *Photophysics and Photochemistry above* 6ed. By F.Lahmani (Elsevier, Amsterdam 1985)

[2.20] R.Srinivasan: "Ablation of polymer and biological tissue with ultraviolet leaser" Science **234,** 559 (1986).

[2.21] J.C. Yeh:*"Laser ablation of polymers "* J. Vac. Sci. Technol. A4, 653 (1986).

[2.22] R. Srinivasan, B. Braren: *"Ultraviolet laser ablation of organic polymers* "Chem. Rev. **89,** 1303 (1989)]

[2.23] S. Lazare, V. Granier "*Ultraviolet laser photoablation of polymers- a review and recent results*": Laser Chem. **10**,25 (1989).

[2.24] P.E. Dyer: Laser Ablation of Polymers, in *Photochemical Processing of Electronic Materials,* ed. By I.W. Boyd, R.B. Jackman (Academic, London 1992)

[2.25] A. Yabe: Laser Processing of Polymers, in *Macromolecular Science and Engineering: New Aspects,* ed. by Y. Tanabe (Springer, Berlin 1999)]

[2.26] P.E. Dyer "*Excimer laser polymer ablation – twenty years on*" Appl. Phys. **A77,** 167-173 (2003).

[2.27] P.E. Dyer and J. Sidhu, "*Excimer laser ablation and thermal coupling efficiency to polymer* " J. Appl. Physics **57** (4) (1985).

[2.28] J. H. Brannon and J. R. Lankard, *"Pulsed CO_2 laser etching of polyimide"* Appl. Phys. Lett. **48**(18) May (1986).

[2.29] R. Srinivasan, B. Braren, R. W. Dreyfus –" *Ultraviolet laser ablation of polyimide films* " **J.** Appl. Phys. **61** (1) Jan (1987).

[2.30] R. Braun, R. Nowak, P. Hess *"Photoablation of polyimide with IR and UV laser radiation* " Applied Surface Science **43** pp 352- 357 (1989).

[2.31] "*Ultrafast Imaging of UV photo Ablation"* Lambda highlights no.**21,** Lambda Physik Feb (1990).

[2.32] R. Srinivasan *"Ablation of polymethyl methacrylate films by pulsed (ns) ultraviolet and infrared (9.17 μm) lasers: A comparative study by ultrafast imaging"* J. Appl. Phys. **73** (6) March (1993).

[2.33] P. E. Dyer, D. M. Karnakis, G. A. Oldershaw, G.C. Roberts *"TEA laser ablation of Upilex polyimide*" J.Phys.D: Appl. Phys. **29** 2554- 2563 (1996).

[2.34] W.Y.Y. Wong, T. M. Wong, H. Hiraoka "*Polymer segmental alignment in polarized pulsed laser-induced periodic surface structures* " Appl. Physics A **65,** 519- 523 (1997).

[2.35] K. Piglmayer, E. Arenholz, C. Ortwein, N. Arnold, D. Bauerle – *"Single-pulse ultraviolet laser-induced surface modification and ablation of polyimide"*Appl. Physics Letters, vol. **73** no. 6, (1998)

[2.36] J. Wambach, T. Kunz, B. Schnyder, R. Kotz, A. Wokaun: *"XPS Investigations on the UV – Laser ablation mechanism of Kapton"* AnnexV, **37.** PSI Annual Report (1997).

[2.37] *"Technical aspects of ablative photo- decomposition"* Lambda Highlights no. **3,** Lambda Physik (2001).

[2.38] Robert J. Harrach *"Analytical solutions for laser heating and burnthrough of opaque solid slabs"*Journal of Appl. Physics, Vol. **48**, no. 6, June (1977).

[2.39] *Laser Microprocessing at photonics Research Ontario*". ICALEO Laser microfabrication conference , Laser Institute of America, Vol. **88**, (1999).

[2.40] Malcolm C Gower *"Industrial applications of Pulsed Lasers to Materials Microproces*sing". Exitech Ltd. SPIE symposium on High Power Laser Ablation

[2.41] Sri Venkat *"Laser processing of flex"* PC fab Cicuitree, Jan ,(2001).

[2.42] F. Villarreal, P.R.Murray, H.J.Baker, G.A.J. Markillie, R.J.Ramirez, Q.Cao, D.R.Hall l. *"High Peak powers CO_2 planar waveguide lasers for direct high resolution machining."* Proc SPIE **4184**, 258 (2001).

[2.43] Dutov, Motovilov et al *"Slab waveguide high power pulsed RF – excited CO_2 laser"* pp. 23-30,Vol. **2773**, Proceedings of SPIE.

[2.44] C J Moorhouse, F Villarreal, J J Wendland, H J Baker, D R Hall D P Hand, *"Single pulse microvia drilling of resin-coated -copper substrates using an enhanced peak power planar waveguide CO2 laser"*, SPIE-Int Soc Optical Engineering,.5339:276-283 January, (2004).

[2.45] A.I. Dutov, A. A. Kuleshov, N.A. Novoselov, V.N. Sokolov. *"Slab waveguide RF - excited CO_2 laser for material processing"*. Proc. SPIE.. Vol. **2713**. Pp. 51-57 (1995).

[2.46] Happy Holden, *"Microvia: The next generation of substrates and packages"* IEEE Micro Magazine, July-August Pp. 1-8, (1998).

[2.47] Harvey Miller,*"Microvia Decision Time is nearing : A report on 8 approaches."* Chip Scale Review, Edition March – April (1999).

[2.48] C.J. Moorhouse, F. Villarreal, H.J.Baker, D.R. Hall " *Single pulse microvia drilling of resin coated copper substrates using enhanced peak power planar waveguide CO_2 laser.*" SPIE Proceedings, **5339**, p.276-283, (2004).

[2.49] James Paulus and Dr. Michael Petti *"Coated copper foils for high density interconnects"*. IPC Circuits Expo, San Jose, CA March 9-13,(1997).

[2.50] Sudhakar Raman:"*Implementation of laser technology in new applications on PCB"* IPC EXPO, (2001).

Chapter 3

Basics of laser material interaction

3.0 Introduction

Considerable previous work has been reported [3.1-3.6] in the literature where lasers are used for a range of different applications based upon the interaction of a laser beam with the surface of a material. Such interactions may produce significant changes to the surface morphology, for example due to heating or ablation, resulting in surface modification or material removal. The details of the effects produced depend on the dynamics of the laser/material interaction, so that a complete analysis of the interaction process requires information on *both* the parameters of the laser beam and on the thermal, mechanical, and other properties of the material being irradiated.

The previous chapter emphasised on microvias and different techniques of making vias with laser. In this chapter, basic physics underpinning the laser ablation is outlined in order to provide the necessary background to understand the basic process and to enable where possible, the experiments described in Chapters 5 and 6 to be interpreted quantitatively. The analysis considers the key parameters describing the incident laser beam and the optical, thermal and mechanical aspects of the interaction with the substrate. The chapter starts with an analysis of the incident beam on substrate, which is partly absorbed and partly reflected at the surface. This absorbed beam may produce temperature gradients in the substrate, thereby leading to melting or vaporisation of substrate material and plasma formation.

3.1 Laser material interaction

3.1.1 Reflection and Absorption

When laser light is incident on a material the light may be reflected, transmitted or absorbed and in reality, all three processes occur to some degree as illustrated in Figure 3.1. In order to achieve effective laser machining, it is highly desirable that the material absorbs a large fraction of the laser light, so that in general reflected and transmitted light

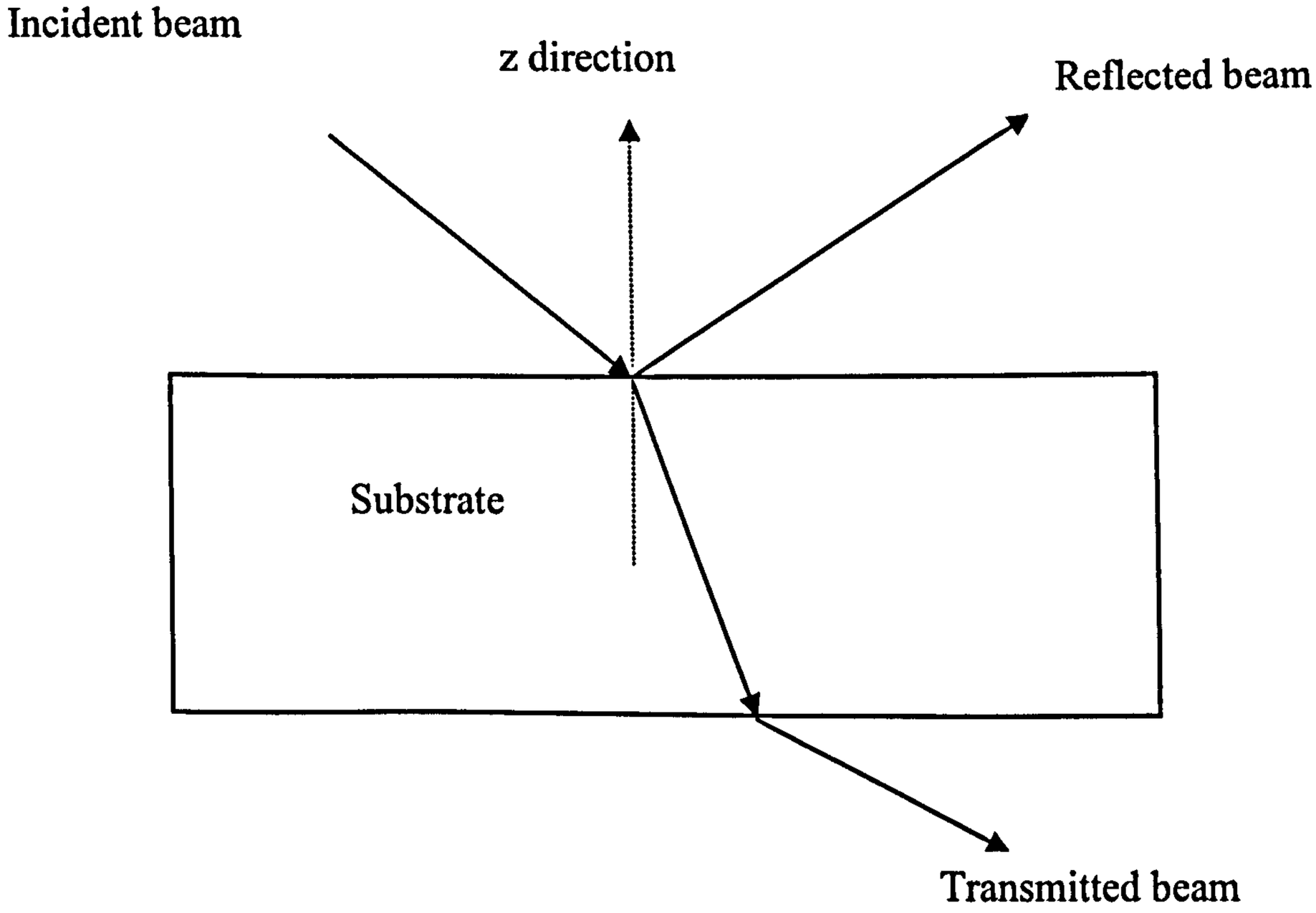

Figure.3.1: Reflection, absorption and transmission of a laser beam incident normal at the material.

represents a loss to the laser machining process. In practice for most cases (negligible transmission) the reflection and absorption of the incident light are related by:

$$A = 1 - R \qquad (3.1)$$

where R is the reflectance and A is the absorptance by the material. The reflectance is given as the ratio between the reflected and incident intensity. In the case of normal angles of incidence of a light beam on a flat substrate surface in air R can be written in terms of well-known Fresnel expression [3.4]

$$R = \frac{(n-1)^2 + k_i^{\,2}}{(n+1)^2 + k_i^{\,2}} \qquad (3.2)$$

where, n is the real part of the refractive index, k_i, is the imaginary part of the refractive index, also called the extinction coefficient. The electric field, E, and magnetic field, H, are given by following expressions [3.1]

$$E = E_0 e^{i(2\pi z/\lambda - \omega t)} \qquad (3.3)$$

$$H = H_0 e^{i(2\pi z/\lambda - \omega t)} \qquad (3.4)$$

where z is the depth of light absorbed in the substrate, λ is the wavelength of incident light, ω is the angular frequency. The energy flux per unit area or intensity, I, of the wave is given by the following expression:

$$I = |E \times H| = E_0 H_0 e^{i(4\pi z/\lambda - 2\omega t)} \qquad (3.5)$$

$$I(z) = I_0 e^{i(4\pi z/\lambda - 2\omega t)} \qquad (3.6)$$

where I_0 is the intensity of the incident laser beam. Now, the absorption coefficient α is defined as:

$$\alpha = -\frac{1}{I}\frac{\partial I}{\partial z} \qquad (3.7)$$

and that becomes:

$$\alpha = \frac{4\pi k_i}{\lambda} \tag{3.8}$$

Now, including the reflection loss at the surface *(1-R)* in equation (3.6) modifies expression to give:

$$I(z) = (1-R)I_0 e^{-\alpha z} \tag{3.9}$$

This is called Beer's law, which defines the variation of the intensity of light within the substrate, *I(z)*, with depth into the material, *z*, where in general the absorption coefficient, α is a function of wavelength, $\alpha(\lambda)$.

3.1.2 Absorption coefficient

As is obvious from equation (3.8), high absorption coefficient is associated with a high value of the imaginary part of the refractive index and high reflectivity is obtained for large values of the real part of the refractive index. The optical response of the material when laser irradiated is determined by the variation of the optical properties, n, and k_i, with wavelength. Hence, the values for these parameters are obtained from equations (3.2) and (3.8) are important to calculate the magnitude of the absorbed light. The absorption coefficient of many materials varies widely with wavelengths and the examples of this are plotted in absorption spectra of materials investigated in Chapters 5 and 6. The significance of this statement is that the laser wavelengths that operate closest to the maximum in absorption of a given material are preferred. For example, the laser used in the thesis can be operated at multiple wavelengths, emitting more than 40 lines in the wavelength region 9-11μm corresponding to the CO_2 molecular emission spectrum, details of which are given in Chapter 4. Not all wavelengths are high absorbed by the material hence; wavelengths were selected that had high absorption coefficient to perform the experiments. Details of wavelength selection are given in Chapter 5.

The absorption properties of materials are also highly temperature dependent. In general this statement is true for dielectrics, and a higher bulk temperature will result in fewer photons being required to excite electrons. This phenomenon is also very well observed

in the ablation experiments performed with dielectric materials, details of which will follow in Chapter 5 and 6, where the removal rate of materials is observed to increase non – linearly at higher fluences.

3.1.3 Temperature distribution in the material

The fraction of the beam that is absorbed in the substrate provides thermal energy to the substrate, which is transferred to greater depths in the bulk of material by thermal diffusion. This transfer of energy generates a thermal gradient in the bulk of the material, thereby increasing the temperature of the part of the substrate. At a microscopic level, the absorbed laser light provides energy to bound electrons, as excitation energy, to free electrons as kinetic energy and lattice vibration produces phonons, leading to random motion of the excited particles. This degrades the localised primary excitation energy into thermal energy. The thermal energy is then equipartitioned via several energy transfer mechanisms involved, with characteristic time constants and different energy relaxation channels. When laser energy is converted to heat, the increase in temperature ΔT is given using the energy balance equation [3.1]:

$$E_v = \rho C \Delta T \tag{3.10}$$

where ρ is the density and C is the specific heat and the product of both is called the v*olume specific heat.* Using equation (3.10), in equation (3.9), the temperature rise is calculated as:

$$\Delta T = \frac{(1-R)\alpha F e^{-\alpha z}}{\rho C} \tag{3.11}$$

where F is the fluence of laser pulse J/cm^2. This equation is frequently used in experiments in Chapters 5 and 6 to obtain the temperature rise in the material and to determine the onset of ablation. The characteristic length over which the heat penetrates in the material for a given laser pulse duration, is called the *Depth of Heat Penetration or diffusion length* that is given as:

$$D = \sqrt{4K\tau} \tag{3.12}$$

where, D is the depth of heat penetration, K is the diffusivity of materials, τ is the pulse duration. The *optical absorption length L or penetration depth of light* intensity in the material is given as $L = 1/\alpha$.

It is important to discuss here the parameter δ that characterises the temperature profile in the substrate in the z-direction, along which the laser irradiates the substrate. This parameter is defined as the ratio between the diffusion length D and the optical absorption length L given as:

$$\delta = \frac{D}{L} = \frac{\sqrt{K\tau}}{1/\alpha} = \alpha\sqrt{K\tau} \qquad (3.13)$$

This is a very crucial parameter for the study in the thesis. The importance of this parameter is that it exhibits the relation between the fluence and corresponding increase in temperature of the substrate. In most laser machining applications the temperature of the substrate should be kept in narrow limits to ensure desired results. This is also a function of absorption phenomenon and heat flow in the material. The temperature profile in substrate along which the laser irradiates the substrate distinguishes two cases, depending on the type of material [3.1].

(a) If $L>>D$, i.e. δ ($\delta<<1$), this corresponds to an exponentially decaying temperature profile with characteristic length L in the substrate, illustrated in Figure 3.2. In this case, clearly the behaviour of α as a function of temperature or fluence is crucial. This condition is known as *adiabatic condition* and applies to materials with low conductivity like insulators e.g. polymers and glasses. Hence is applicable to materials such as Kapton, Arlon, FR4 and proprietary resin from RCC as will seen in Chapter 5. The temperature rise in the substrate can be calculated using equation (3.11). The temperature distribution in the material is one dimensional and lateral heat flow can be ignored.

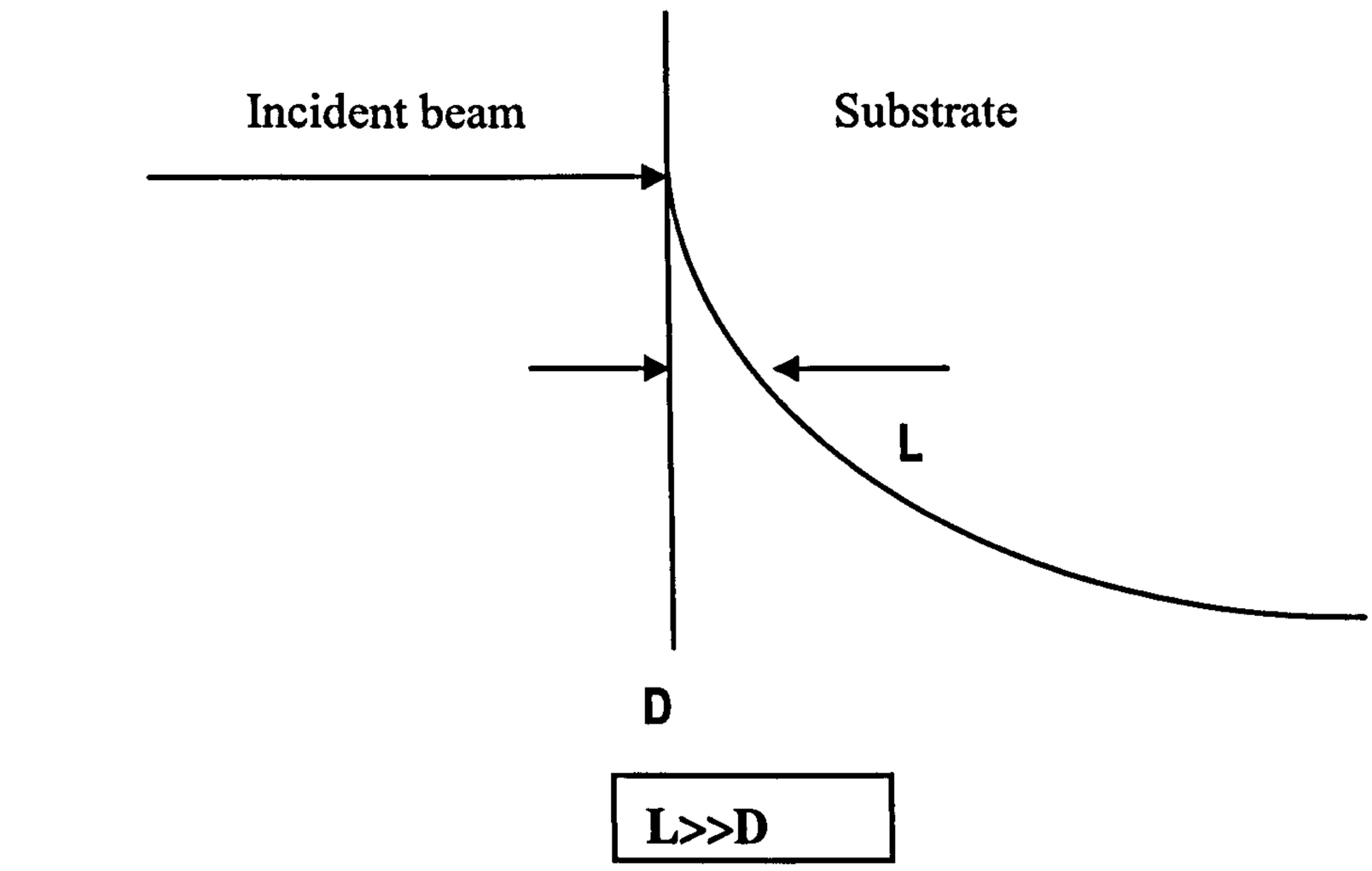

Figure 3.2: Laser target heating corresponding to negligible heat flow in adiabatic condition

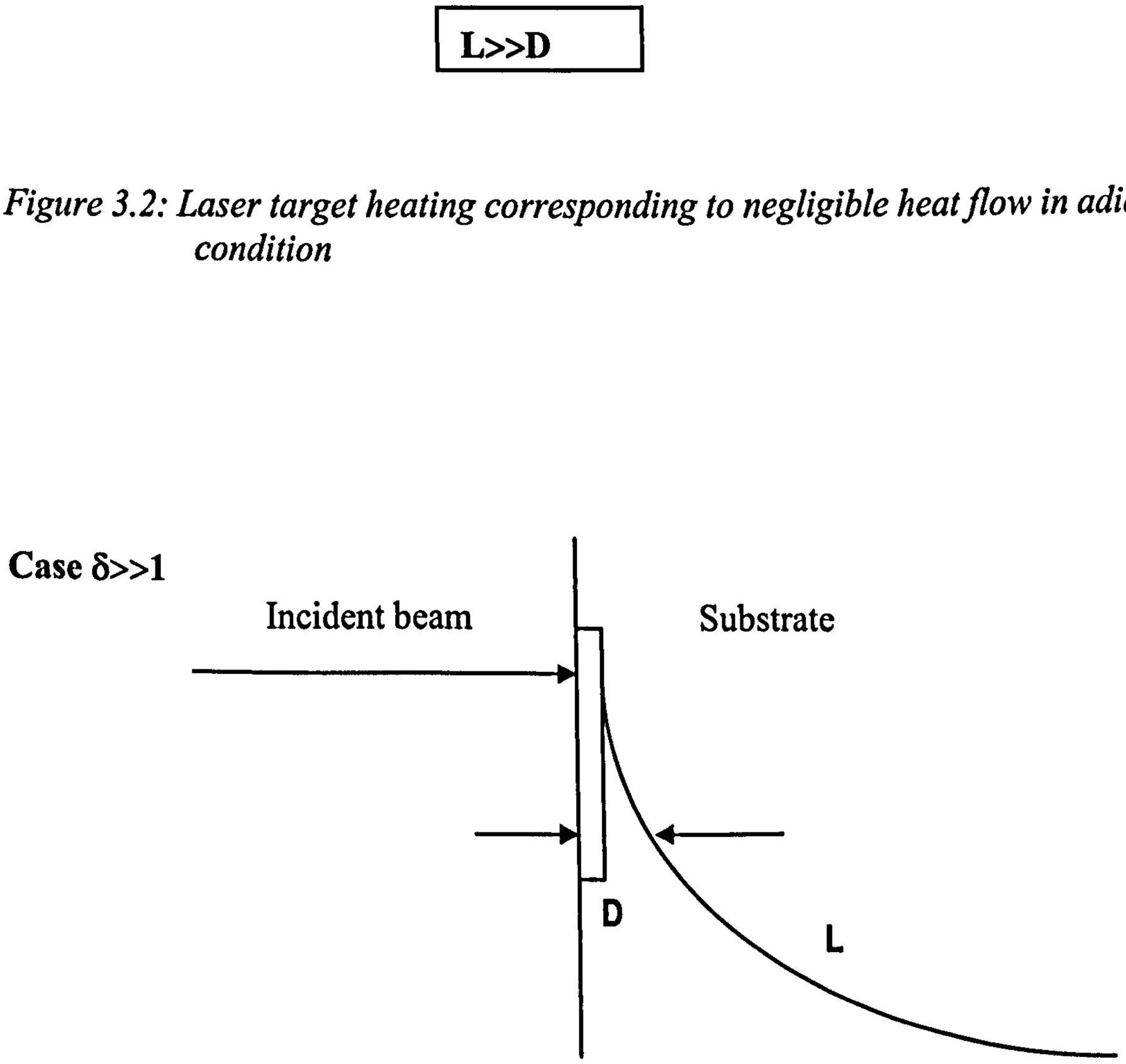

Figure3.3: Laser target heating in diffusive case where heat flow dominates

(b) If $L<<D$, i.e. in laser target heating $\delta>>1$, then the absorption length is much smaller than thermal diffusion length. This is termed the *diffusive case*, where heat flow dominates in the substrate. The absorbed laser power is used to heat the layer of a small thickness of the substrate, which applies to case of metals as is illustrated in Figure 3.3. The propagation of heat in this condition can be considered three-dimensional.

If the losses via heat conduction or diffusion are not too strong, then as the applied laser fluence increases the surface temperature may reach the melting point. In many cases, surface melting of the substrate results in surface deformations of the substrate as is the case with alumina and LTCC, which is described in Chapter 6. The thermal expansion of the material and the surface tension of the liquid formed by melting determine the final shape of the surface deformation. The laser induced phase transition from solid to liquid is utilised in many industrial applications such as surface hardening, surface alloying, welding etc.

3.1.4 Vaporisation and plasma formation

When the laser intensity is high enough, it may induce material evaporation, a transition from the liquid state to the gas state i.e. vapours. The vapours may consist of clusters, ions, molecules and ions etc. The species that leave the surface of the material take away internal and kinetic energy. The species leaving the surface of material generate a recoil pressure on the substrate. In the presence of molten surface layer and laser beam irradiation, the recoil pressure may expel the liquid, details of which are mentioned later in the section. The ablated material may also generate a shock. With high fluence or for long pulse durations as is the case with CO_2 laser, the evaporated material may form a plume above the surface. High temperature and strong pressure gradients in the axial direction of vapour plume compared to corresponding gradients in the lateral direction causes the plume to have strong forward directionality.

There are two modes of evaporation from melt under laser irradiation:

a) Surface Evaporation

b) Volume Evaporation

Surface evaporation is dominant in metal processing and occurs for intensities of typically $\leq 10^9$ W/cm^2. This generally holds when the absorption length α^{-1} is small compared to the heat penetration depth D. Volume evaporation occurs for weakly absorbing materials. In this case, the laser heats the volume whereas evaporation cools the surface of material, but the temperature maxima develops within the material. This super heats the material and increases with the absorption length. It usually results in explosive removal of the superheated region before it is fully vaporised. Large change in the density causes violent expansion of the superheated liquid, hence causing vapour explosion. In this case, the heating is fast enough that boiling of the liquid is avoided. Therefore, a third condition can occur when material absorbs strongly and slow evaporation takes place. It induces 'boiling' within a thin surface layer. This condition is also considered a limiting case of volume evaporation. Boiling requires significant superheating of the melt and pulses long enough to allow bubble nucleation. Melt ejection by boiling strongly depends on the absorption length.

If the laser light intensity is high enough to induce significant material vaporisation, a dense vapour plume above the surface consisting of clusters, molecules, atoms, ions, and electrons is formed. The vaporisation pressure builds up enough to overcome the surface tension of the surrounding molten layer, and hence cause the molten material to flow up the sidewalls and out of the entrance of the hole in the direction of the laser leading to melt ejection. The escaping vapours exert a large recoil force on the surrounding molten material ejecting it from the hole

If the laser pulse duration τ is larger than ($\tau > t_p$) where t_p is the time after which the laser – vapour plume interactions become relevant, screening of the incident laser light by absorption and scattering within the vapour plume diminishes the beam intensity that reaches the substrate. With increasing intensity, an increasing fraction of atoms/molecules become ionized when the vapour becomes substantially ionized, it is called *plasma*. With the formation of the plasma plume, the laser radiation is strongly absorbed and shields the substrate, which may hinder the drilling process by absorbing a significant proportion of the pulse energy. The plasma can expand and heat the surface

around the hole, causing unwanted surface damage. Thus in most drilling applications the beam parameters are selected to avoid plasma generation. When the laser intensity is increased, the plasma plume may expand in volume and its forward direction becomes more pronounced. If the intensity is even further increased, the plasma may decouple from the substrate and propagate towards the incident beam. Such plasma is called Laser – supported absorption wave (LSAW). If LSAW propagates towards the laser beam with subsonic velocity, it is termed as Laser-supported combustion wave (LSCW). The propagation velocity of this wave increases with laser light intensity and reaches the velocity of sound. The LSAW then propagates with supersonic velocity as is described as Laser-supported detonation waves (LSDW).

3.1.5 Liquid phase expulsion

Due to momentum conservation, the species evaporated from the surface causes a recoil pressure, which acts on the non-ablated material, which is of the order of saturated vapour pressure. With focused laser irradiation, the recoil pressure squeezes the liquid out of the irradiated spot, mainly near its edges. This is called liquid phase expulsion. The thickness of the molten layer decreases with increasing laser intensity, mainly due to the increase in recoil pressure. This is observed to occur at low laser power, whereas at high laser powers vaporisation dominates.

A simple model to aid the concept is the so-called 'Piston' mechanism. The evaporating surface is visualised as a piston that exerts the pressure on the melt, squirting it out of the hole radially. The melt is treated as a non-viscous and incompressible fluid. However, the melt can be ejected out only when the radial pressure force overcomes the surface tension of the melt. Hence, this suggests a threshold for the melt ejection mechanism. This mechanism may be applied to explain the possible ablation process of organic resins and ceramics in Chapters 5 and 6 respectively.

Industrially, a gas jet is used to expel the liquefied material from the surface of the substrate. The molten material accumulates near the bottom of the hole drilled on the substrate, due to surface tension, which retards the liquefied material from leaving the hole. The gas jet may be used to expel the liquid droplets or the liquid-phase expulsion

[3.4]. The liquid droplets ejected may recondense within the area being processed; thereby effecting the ablation of the material.

3.2 Phenomenon of laser ablation

Laser ablation is the term used to describe the phenomena involved in the removal of material from a surface by pulsed laser irradiation. Usually, the material must undergo a change of the fundamental state of aggregation and transforms into some volatile phase e.g. a stream of particles, a gas or plasma [3.1-3.6]. Laser ablation may be described in terms of the underlying mechanisms involved in removing the material. Hence, ablation may be classified as

(a) Photothermal ablation

(b) Photochemical ablation

(c) Photophysical ablation.

3.2.1 Photothermal ablation

Photothermal ablation is a heating and vaporisation process and is generally accomplished by using a laser that operates in the visible or infrared (IR) spectrum, between 500 and 10,600nm [3.2, 3.3, 3.19, 3.20]. There are two possibilities of ablation of material.

1) **Ablation due to Vaporisation:** The laser irradiation is absorbed by material and on microscopic level excites the material. The excitation energy is instantaneously transformed to heat that increases the temperature of substrate and hence changes the optical properties of material. The temperature rise can result in (thermal) material ablation (vaporisation) with or without surface melting.

2) **Explosive type ablation:** This is another channel which may induce ablation. The temperature rise can induce stresses, which can be so high that explosive – type ablation, or, thin films on thick substrates, can "pop-off." Stresses also change the optical properties of the material and thereby influence the laser induced temperature rise. Refined heating models as those described in [3.21] and [3.22]

are often used to estimate the temperature rise produced at the surface of a material with absorption coefficient α when it is exposed at the experimentally determined threshold fluence F_{th}. In this way, it is found that typically $T \geq 800 - 1000\ K$ at threshold of a polymer and under this relatively extreme condition, material can be expected to undergo rapid thermolysis i.e. decomposition of material due to thermal energy.

3.2.2 Photochemical ablation

If the photon energy is high enough, laser light excitation can result in direct bond breaking, because of which, single atoms, molecules, clusters or fragments are removed from the surface. This process is seen with laser wavelengths in the UV spectrum below 400nm [3.6-3.8]. Besides this direct effect, again an indirect channel may lead to photochemical ablation. Light induced defects for example, photochemically dissociate bonds and can build stress which result in (mechanical) ablation. Both these direct and indirect channels can take place, in principle, without change in surface temperature, hence for this reason this process is termed photochemical ablation and for this reason, the process is sometimes also referred to as "cold" ablation due to the avoidance of thermal damage. Energy absorbed in the bond breaking process restricts the temperature rise and the extent of thermal damage to the substrate [3.9]. The photochemical ablation is also termed as '*ablative photodecomposition* in which decomposition reactions would take place mainly from electronically excited states and repulsive forces between species which would lead to their rapid expulsion from the surface of the material. In the literature, purely photochemical models of ablation have met with limited success in their application for analysing laser interactions either because they fail to confirm the dominance of a fluence rather than irradiance threshold [3.10] or because they lack quantified 'ablation thresholds' to compare with experiment [3.11]. Comparative studies of laser ablation of materials with IR and UV lasers show that IR laser ablation process has thermal ablation, whereas UV lasers show bond breaking and show dominance of photochemical ablation [3.12-3.18].

3.2.3 Photophysical ablation

Photophysical ablation is a process in which both thermal and non-thermal mechanisms contribute to the overall ablation rate. An example would be a system in which the lifetime of electronically excited species or of broken bonds is so long that species desorbs from the surface before the total excitation energy is dissipated into heat. The material removal process is enhanced by the temperature rise. Thermally or non-thermally generated defects, stresses and volume changes may again influence the overall process. Thermal ablation and photochemical ablation can be considered as *limiting* cases of Photophysical mechanism [3.4]. Figure 3.4 summarises different channels of pulsed laser ablation. However, different mechanisms included in the figure are by no means complete and additional mechanisms such as for example plasma formation may be involved.

3.3 Ablation characterisation

The key to efficient laser ablation is strong absorption in the target materials at the irradiated laser wavelength. An evaluation of the ablation characteristic of a material can be performed by measuring the depth of material removed or ablated from the surface of material by single laser pulse. This is called *ablation rate per pulse*, and is illustrated by the "typical" ablation curve as is shown in Figure 3.5. This curve is plotted by measuring the depth x of the ablated crater/hole produced by single shot/pulse of laser, measuring ablated hole's depth and plotting the depth versus applied axial fluence. Measurements of crater depth versus axial fluence for many materials yield the machining curves of characteristic shapes as in Figure 3.5. The ablation curve in general consists of three main sections.

I Where essentially no material removal occurs, also called the neutral section. The fluence is below the threshold for removing material.

II Where the curve is nonlinear and signifies the onset of ablation.

III Where the curve has a linear part that has a constant gradient.

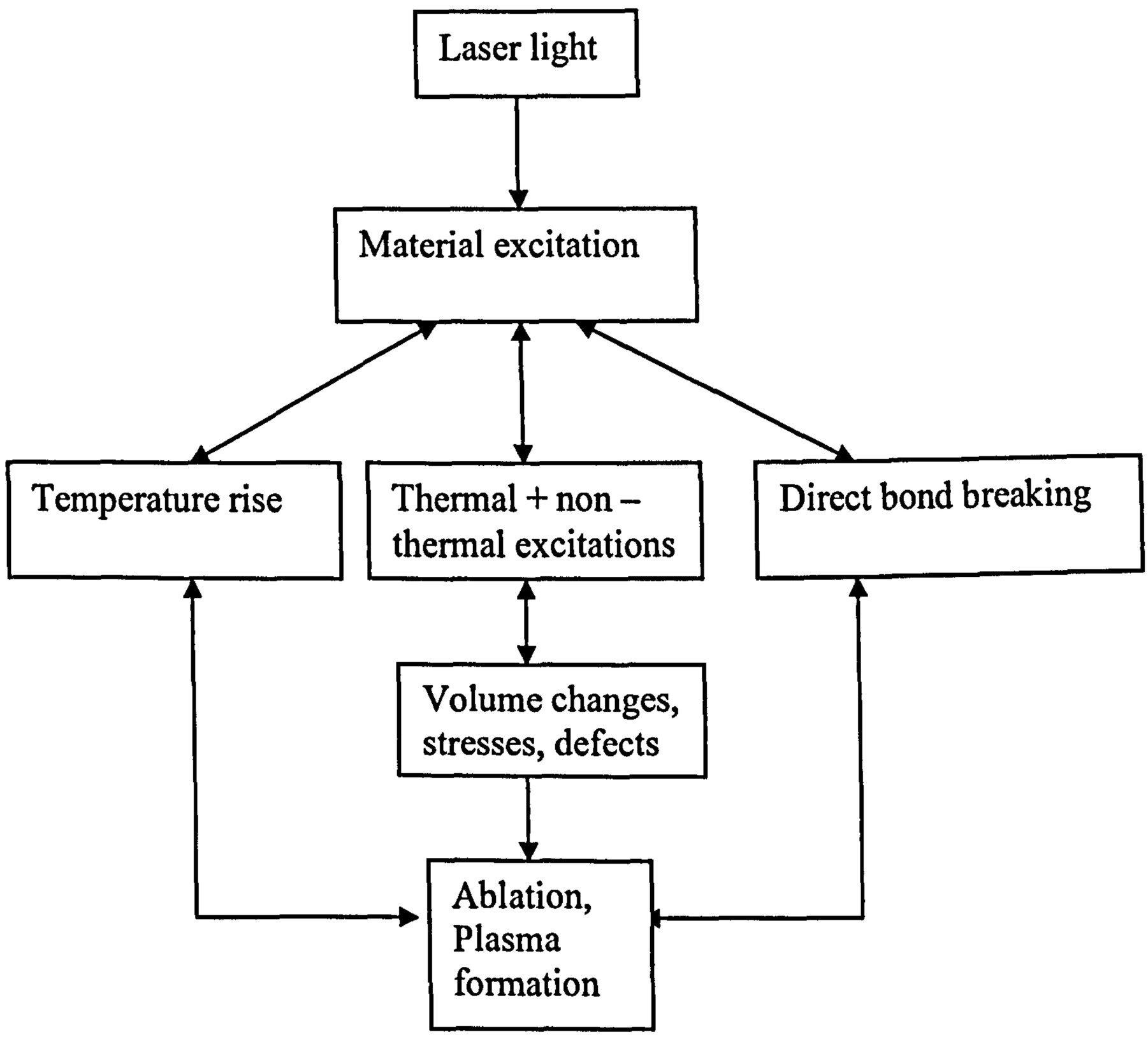

Figure 3.4: Mechanisms and channels involved in pulsed laser ablation. Ablation can be based on thermal activation only (left path), on direct bond breaking (right path) or on a combination of both i.e. Photophysical ablation (intermediate path)

This technique of ablation curve is sensitive and is used to determine depth removal of material from pulse to pulse [3.23].

Using the Beer's law for fluence

$$F(x) = (1-R)F_0 e^{-\alpha x} \tag{3.14}$$

Using equation (3.11)

$$e^{\alpha x} = \frac{(1-R)F\alpha}{\rho c(T_t - T_0)} \tag{3.15}$$

$$\alpha x = \ln\left[\frac{(1-R)F\alpha}{\rho c(T_t - T_0)}\right] = \ln\left[\frac{F}{F_{th}}\right] \tag{3.16}$$

The linear region of plot of ablated depth x per pulse can be fitted with the simple equation

$$x = \frac{1}{\alpha}\ln\left[\frac{F}{F_{th}}\right] \tag{3.17}$$

where

$$F_{th} = \frac{\rho c(T_t - T_0)}{\alpha(1-R)} \tag{3.18}$$

where, F_{th} is threshold fluence at which the ablation is first observed, α is the absorption coefficient of the material at the laser wavelength.

The important question is whether ablation exhibits a true physical threshold. The threshold concept was originally put forward as a convenient practical indication of the fluence at which significant material removal occurs, though it was recognized that some degree of ablation could occur below F_{th} [3.24]. Ceramics are good example of this observation in which there exists a melt or damage threshold within the neutral section of the ablation curve. This aspect of material desorption below the ablation threshold is

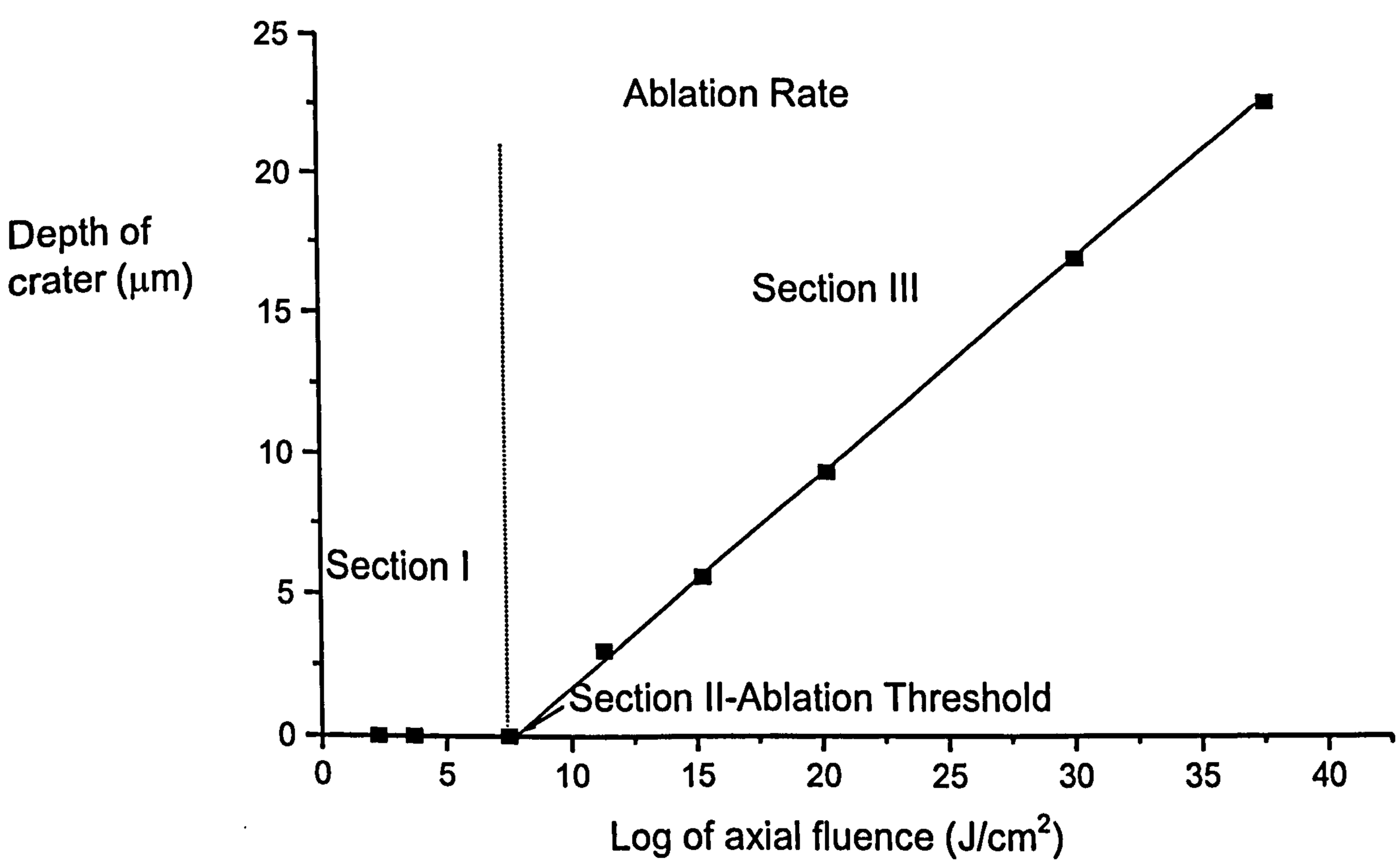

Fig 3.5: Typical Ablation Curve – Depth of crater vs. Log of axial fluence

confirmed in various reports in which sensitive measurement techniques have been used to study removal in the vicinity of threshold. Hence, ablation below the threshold can be summed as the irradiation of the substrates with laser fluences below threshold, which may result in changes in surface morphology and structure on a microscopic level, the generation of defects and the depletion of one of the several components of the material. This is also referred to as the 'damage threshold' in Chapter 5 and Chapter 6. The accuracy of such measurements depends on the experimental technique and on the extent of surface morphology changes due to roughening and the development of surface instabilities.

The detailed investigation of the material damage, material removal threshold and effects of higher fluence on the material above threshold region of a material are incorporated in producing plots of *ablation rate - fluence curves*, which has become generally accepted as a consistent way of characterising a laser/material interaction.

The method used for performing measurements of the optical surface damage affects the measured value of the threshold. The measured damage threshold can be influenced by: the laser pulse width and shape, the size of illuminated area, random variation from site to site in the surface uniformity and the number of laser pulses used. The laser pulse duration used is revealing since the optical damage threshold is specified as either the fluence or intensity at which damage is first observed. If the peak intensity of the laser pulse determines the threshold fluence, it would be linear with pulse duration and if the fluence were the determining factor, the threshold fluence would be independent of pulse duration.

Damage fluences that vary sub - linearly with the pulse duration could result from a simple process like thermal diffusion, which can determine the maximum temperature reached in the absorbing region of the materials. The material properties that seem to correlate with the optical damage threshold are the refractive index: the higher the refractive index, the lower the damage threshold, where the refractive index is related with other properties such as the bandgap energy and enhancement of the local optical electric field around the defects as mentioned earlier in section (3.1.1).

3.3.1 The threshold fluence

It is found that distinct value of threshold fluence F_{th} must be exceeded for significant material removal to occur. This applies where broad range of laser wavelength spanning the long wavelength infrared [3.19, 3.20] through to the vacuum ultraviolet (VUV). In some cases, it has been found, at least for a limited range of fluences above threshold, that the ablation rate obeys a form consistent with Beer's law [3.21] as shown in equation (3.17). The expression (3.18) was originally obtained from a fit to experimental curves and is only used to derive the ablation parameters, α_{eff} and F_{th} here. This equation is not sensitive to the underlying ablation mechanisms, but used because more advanced models, which describes laser ablation very well with a photothermal mechanism, for example for polyimide [3.25] require knowledge of various material constants such as heat diffusivity, specific heat, heat of vaporization etc, which are not known for many polymers or dielectric materials. Laser ablation allows the controlled removal of the material and not simply one that can be thermally evaporated (i.e. these for which a conventionally surface limited evaporative process applies). Thus, laser ablation is known to be prompt, with material being expelled from the surface with a single shot of laser [3.26].

For finite absorption, F_{th} decreases with an increasing absorption coefficient, and a decrease in F_{th} is expected for thermal and non – thermal ablation mechanisms because the excitation energy will be localised within a smaller volume. Another characteristic feature is a decrease in F_{th} with pulse duration. With shorter pulse duration, the spatial dissipation of the excitation energy is reduced and F_{th} is reached at lower fluences. This observation can be related to heat penetration depth or an increase in absorption coefficient due to multiphoton excitation. Thus, in first approximation, ablation should start always around the same "*threshold temperature*."

When $F > F_{th}$ the depth of material subjected to a fluence exceeding F_{th} is ablated, thus carries away excess fluence $(F - F_{th})$. As a result thermal loading on the material remains clamped at $F_{th}A$ where A is the area of the beam. Experimental findings confirm the validity of this simple view [3.9, 3 10].

If heat loss from the absorption zone is negligible, the product $\alpha F_{th} = H$ is a measure of the ablation enthalpy of the polymer, that is, the minimum volumetric energy density is needed to transform the initially cool solid to volatile products. H is found to be approximately a constant, independent of laser wavelength. Values close to $H = 3 - 4$ $kJcm^{-3}$ are obtained for non- char forming polymers under long pulse CO_2 laser exposure [3.3]. Under this condition it then follows that the ablation threshold is inversely proportional to the absorption coefficient

$$F_{th} = \frac{H}{\alpha}. \tag{3.19}$$

H is ablation enthalpy and α is absorption coefficient. This form is consistent with the simple thermal models, provided differences in the beam penetration depth (α^{-1}) do not significantly affect the heating – cooling cycle, so that the available thermal reaction time remains constant.

3.3.2 Fluence above threshold

In Figure 3.5, the linear region illustrated as section III of the curve is the region of fluence above threshold. In general, the absorbed energy density needed to produce ablation, can be expressed as the product of the threshold fluence F_{th} and the effective absorption coefficientα, which is approximately constant for a material. Thermal coupling experiments done using the pyroelectric calorimetric techniques or miniature thermocouples contacted to polymer films have revealed that in the sub threshold region essentially all absorbed IR laser energy appears as heat. Above threshold, the thermal loading tends to saturate, however, at a given value approximately AF_{th}, where A is the irradiated area, because the ablation products carry away the excess energy. This behaviour is confirmed by the experiments carried out by various groups [3.2, 3.27]. The surface temperature rise at threshold ΔT can be estimated using equation (3.11).

With increasing fluence, the ablated material, forms a thin plume ahead of the ablated surface and retains the same absorption coefficient as the parent polymer [3.24] because of which the curve becomes constant and no further increase in fluence raises the ablation of material. Various models have been attempted to explain the relation between the

ablation curves and the plume effect [3.21, 3.29]. However, the most convincing explanation is that the ablation plume provides shielding of the underlying polymer and reduces the fluence at the substrate [3.22]. The absorption coefficient α is likely to be fluence dependent; it is possible for these ablation curves to move within these extremes, leading to relatively complex variation with fluence. Plume shielding has been studied and has been recognized as an important effect in variable pulse length experiments of ablation [3.26]. The plume consists of the variety of the complex structures in a polymer, which leaves the surface at high speeds. Analysis of the ablation products well reveals the insight of the processes involved, which has been studied by Srinivasan and Braren [3.10, 3.12, 3.13].

3.4 Process optimisation

As is learned from the previous sections of laser material interaction, in order to optimise the processing of a given material with laser irradiation, four key parameters should be carefully selected.

a) Laser Wavelength: Wavelength should be highly absorbed by the material to minimise the fluence required to ablate the material. In general, low depth of penetration is desirable.

b) Pulse Duration: Heat Affected Zone (HAZ) is undesirable during drilling of dielectrics, hence largest allowable HAZ will be determined by the duration of the pulses.

c) Pulse Energy: The optimum pulse energy is required to remove the material efficiently with fast production rates especially during percussion drilling. However, it is important to mention that the peak power of a pulse is also taken in consideration in order that the peak power density on the material is sufficiently large to cause a phase change in material, and hence ablate the material.

d) Pulse Repetition Rate: Industrial mass production requires high processing speed to cut the production time and hence limit the production cost. This directly corresponds to the repetition rate of pulses on the material. CO_2 lasers are a

particularly attractive option for PCB drilling due to high repetition as compared to the other lasers industrially. In addition, dielectric materials have strong absorption in the IR spectrum in the 9-11μm region, which makes high processing speeds viable.

The laser parameters should be optimised with respect to the optical and thermal properties of the given material for efficient and cost effective machining of dielectrics. In general, the optical and thermal properties of materials including the optical absorption, thermal diffusivity, conductivity etc, determine the response of the material to laser irradiation.

Now that the key parameters of both the laser and materials have been identified, appropriate selection of the parameter is necessary for optimum machining efficiently. These should be implied to understand the phenomenon of laser ablation of dielectric materials and in general.

3.5 Introduction to ablation spectrum

The idea of an "ablation spectrum" is a novel concept introduced here probably for the first time. This approach provides information in two categories:

(1) The ablation spectrum readily makes available information of the fluence required to achieve ablation threshold as a function of wavelength and the fluence required to drill a hole of certain depth, for example 30 μm depth (see below) as applied for organic materials in Chapter 5.

(2) The ablation spectrum can be readily compared to the absorption spectrum of the material, providing a comparison of the change in absorption coefficient of a material with wavelength and the change in material properties due to phase change (ablation) with wavelength. Similarly, ablation spectrum displays the information of change in absorption coefficient as a function of increasing fluence and changing material properties.

The above points are further explained via the example illustrated in Figure 3.6. The figure shows the ablation spectrum of polyimide – Kapton film used in the experiments described in Chapter 5. Figure 3.6 shows comparison of the ablation spectrum obtained from the experiments and the absorption spectrum, which was obtained from the ellipsometer measurements. Details of the measurement techniques and result analysis are made in Chapter 5. This example is quoted to signify the above made points. Ablation spectrum is demonstrated with two sets of fluence values for each wavelength. For example, 10.24 μm has a fluence threshold of 1.3 J/cm^2 and requires 18 J/cm^2 to drill a 30 μm deep hole. Now comparing this wavelength with all the other wavelengths suggests a high value of the absorption coefficient. However, examination of the absorption spectrum shows that 10.24μm is *not* the highest absorbed wavelength in the spectrum, hence suggesting a possible deviation in the absorption coefficient from the room temperature value. Similarly, comparison can be readily done for all wavelengths hence suggesting relative ease of the result presenting format.

3.6 Surface quality after ablation

Following the termination of laser pulse irradiating the material, the cooling of the ablation site takes place by conduction of thermal energy into the underlying material bulk and this occurs on a timescale given by $t = (4K\alpha^2)^{-1}$, where K is the thermal diffusivity. Any radiation damage will clearly be limited to the depth of order of α^{-1}. This clearly shows distinct advantages in having a large absorption coefficient α, since this reduces the thermal loading on the material ($F_{th} \propto \alpha^{-1}$). The initial depth α^{-1} heated to a high temperature is small, as is any radiation damage zone conduction cooling to the bulk material is fast, since $t \propto \alpha^{-2}$. However, in polyimide and ceramics, the surface after ablation is seen to have deposited particulates or resolidified melt/residues due to cooling. This reduces the surface quality after machining and poses a big problem for high quality machining of material. For example in polyimide ablation such particulates are seen scattered along the periphery of the drilled holes and are chemically found to be carbonised species of ablated material [3.10, 3.13]. These particulate can also probably be formed by condensation of small fragments in the plume [3.14, 3.30] or by secondary reactions with the ambient oxygen in cooling process [3.31]. Redeposition apparently

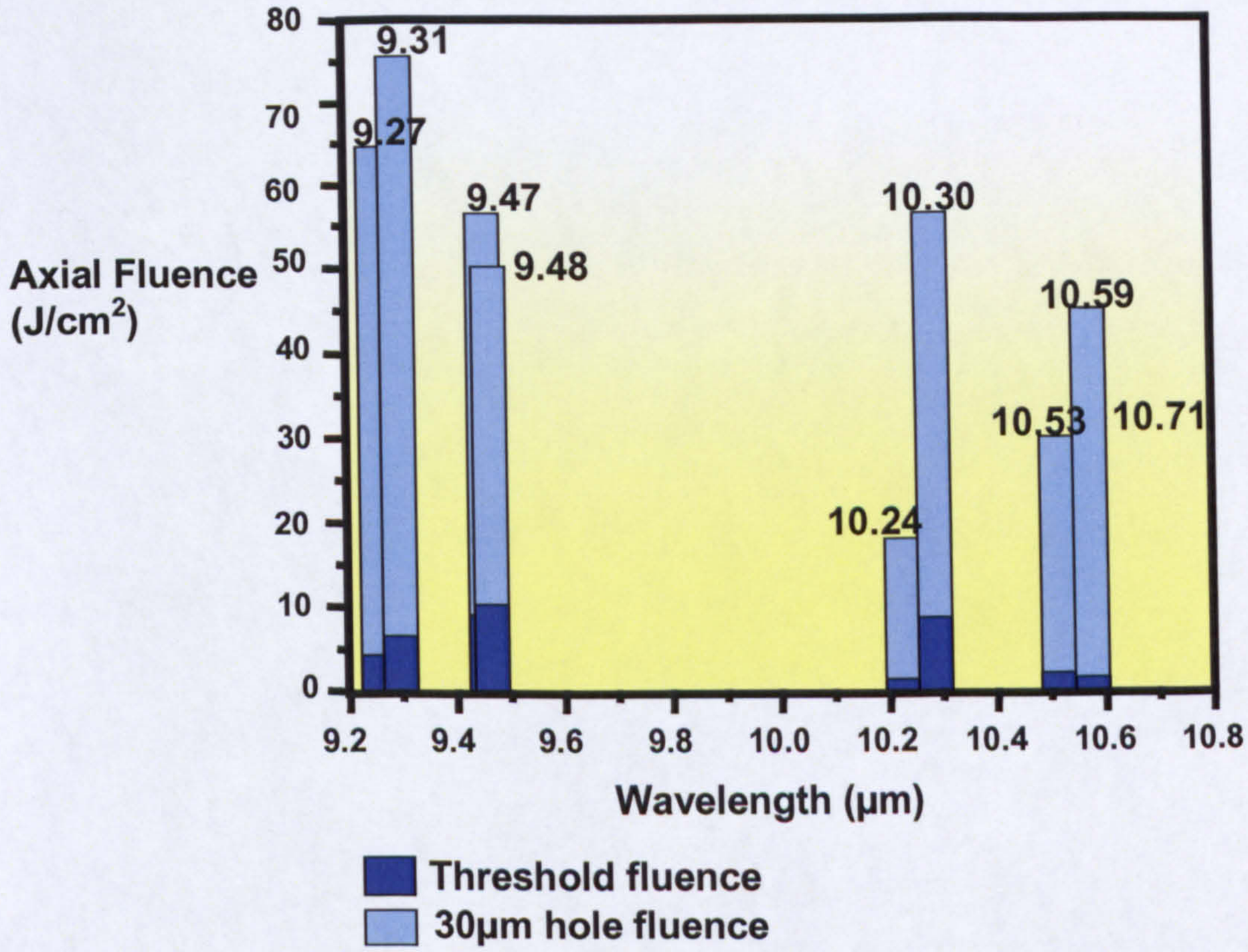

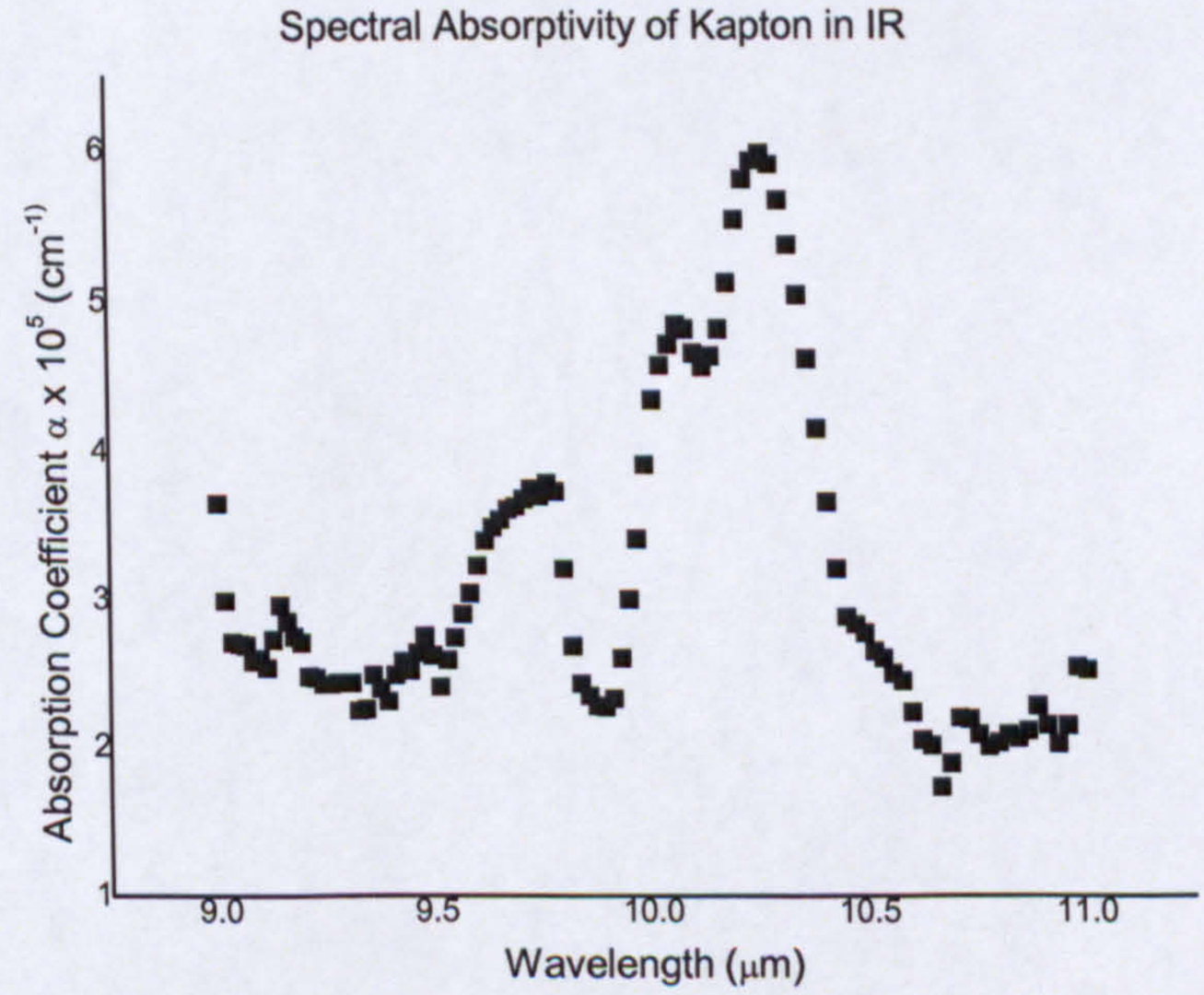

Figure 3.6: Demonstration of format of Ablation spectrum of Polyimide – Kapton, compared with the Absorption spectrum

occurs because ablation leads to formation of a density cavity in the plume, which on cooling causes a net flow of material, including particulates, back to the surface [3.32].

Industrially, redeposition of the ablation product is a common problem and is not only associated with the magnitude of ablating materials like polymers, glasses and ceramics but also the processing environment (gas, vacuum), ablation fluence and the wavelength. Therefore, gas dynamic models have been developed which relate plume expansion to the redeposited debris patterns [3.14, 3.30], and the potential benefit for using gas jets have been explored. Lasers can also be used for removal of deposited material without causing an effect on the already ablated feature on the material surface [3.33]. However, industrially it is important to avoid redeposition of such particulates hence various methods like electrostated collection of the ablated material [3.13] and control of redeposition using flowing gases [3.34] have also been employed to generate clean surface quality of materials.

3.7 Summary

This chapter summarises the underlying physics in the laser material interaction, which provides necessary background for the quantitative analysis of the experimental chapters ahead. The basic characteristics of IR heat treatment to the material surface have been discussed. The interaction mechanisms between the laser pulse and the material and the dependencies on the parameters of laser beam and physical, chemical properties of the material. Laser parameters are wavelength, pulse duration, pulse energy and repetition rate that are identified to be optimised with material parameters for efficient laser ablation. The material is characterised by its chemical composition and microstructure. Conventionally, the IR laser light when irradiated on material is absorbed which can excite free electrons in metals, vibrations in insulator and both in semiconductors. The excitation energy is dissipated as heat, consequently, the laser beam acts as a heat source and induces a temperature rise on surface and within the bulk of the material. The temperature distribution is determined by optical and thermal properties of the material and transformation energies for melting, boiling etc. When the intensity is high enough, it causes material vaporisation. A vapour plume above the material surface is formed. With increasing intensity, the number of species within the plume increases and interactions between laser light and plume dominates, that may cause plasma. Because of

the non linearity in this interaction, small changes in laser properties may cause strong changes in processing results. Therefore, a process optimisation is required to avoid this condition. Melt can be expelled without being vaporised but by recoil pressure of the vapour hence described as liquid phase expulsion. Either of these mechanisms results in laser ablation. The mechanism of ablation varies with wavelengths, hence three phenomena: photothermal, photochemical and photophysical are discussed. If laser processing is thermally activated, it is described by temperature and hence is photothermal ablation as is dominant in CO_2 laser processing. The latter phenomenon is relevant only if phase changes or chemical reaction take place.

For quantitative analysis and optimisation of the laser ablation process, the ablation curve or the ablation rate is conventionally used for comparison. This is plotted as ablation depth as a function of axial fluence. The regimes of fluences *below, at* and *above* the threshold value are discussed and linked with relative changes in material properties. The idea of the ablation spectrum has been introduced, which is a plot of wavelength-dependent ablation in the 9-10 μm spectral region. This analysis is important to assess a direct comparison with absorption spectrum of material. This technique is of significance in Chapters 5 and 6 to determine the effect of wavelength and absorption in a given material. Though it is important to optimise the process for efficient ablation, it is also important to ensure the quality of the surface after ablation, which adds significantly to the cost effectiveness of an industrial process. Therefore, the causes of reasons for debris deposition and possible removal techniques are discussed in the last section.

3.8 References

[3.1] M.V. Allmen and A. Blatter "*Laser beam interactions with materials*" 2nd edition, Springer Verlag (1994).

[3.2] P.E. Dyer: Laser Ablation of Polymers, in "*Photochemical processing of electronic Materials*", ed. By I.W. Boyd, R.B. Jackman (Academic, London, 1992)

[3.3] J.E. Andrew, P.E. Dyer, D. Forster, and P.H. Key *"Direct etching of polymeric materials using a XeCl laser"* Appl.Phys. Lett. **43**, 717 (1983)

[3.4] D Bauerele "*Laser Processing and Chemistry*" 3rd edition Springer Verlag (2000)

[3.5] K. Piglmayer, E. Arenholz, C. Ortwein, N.Arnold, D. Bauerle *"Single-pulse ultraviolet laser-induced surface modification and ablation of polyimide"* Appl. Phys. Lett. **73**,847 (1998)

[3.6] R. Srinivasan *"Ablation of polymethyl methacrylate films by pulsed (ns) ultraviolet and infrared (9.17 μm) lasers: A comparative study by ultrafast imaging* " J.Appl. Phys. **6,73,** p 2743-2750 (1993)

[3.7] H.H.G. Jellinek, R. Srinivasan *"Theory of Etching of Polymers by Far-Ultraviolet, High-Intensity Pulsed Laser and Long-Term Irradiation"* J. Chem. Phys. **88**, 3048 (1984)

[3.8] E. Sutcliffe, R. Srinivasan *"Dynamics of UV laser ablation of organic polymer surfaces"* J. Appl. Phys. **60**, 9, 3315-3322 (1986)

[3.9] P. Klopotek, B. Burghardt and W. Muckenheim, *"Short pulses from excimer lasers"* J. Phys. **E20**, 1269 (1987)

[3.10] R.Srinivasan, K.G. Casey, B. Braren, and M. Yeh, *"The significance of a fluence threshold for ultraviolet laser ablation and etching of polymers"* J. Appl. Phys. **67**, 1604 (1990)

[3.11] P. Simon, *"Time-resolved ablation-site photography of XeCl-laser irradiated polyimide"* Appl. Phys. **B48**, 253, (1989)

[3.12] R. Srinivasan, B. Braren, K.G. Casey, M.Yeh, *"Ultrafast imaging of ultraviolet laser ablation and etching of polymethylmethacrylate"* Appl. Phys. Lett. **55,** 2790,(1989)

[3.13] R. Srinivasan, R.J. von Gutfeld, (IBM, Yorktown Heights, NY, USA) *"Efficient electrostatic collection of debris resulting from 193-nm laser etching of polyimide"* Optical Soc of America, p 282, 1987.

[3.14] P.E.Dyer and R. Srinivasan, *"Nanosecond photoacoustic studies on ultraviolet laser ablation of organic polymers"*. Appl. Phys, Lett. **48**,445 (1986)

[3.15] R. Srinivasan, B. Braren, *"Influence of pulse width on ultraviolet laser ablation of poly(methyl methacrylate)*" Appl. Phys. Lett. **53**, 1233,(1988)

[3.16] R. Srinivasan, B. Braren, *"Ultraviolet Laser Ablation of Organic Polymers"* Chem. Rev. **89**, 1303 (1989)

[3.17] R. Srinivasan, B. Braren, R.W. Dreyfus, "*Ultraviolet laser ablation of polyimide films*" J. Appl. Phys. **61**, 372 (1987)

[3.18] P. E. Dyer, R. Srinivasan, "*Pyroelectric detection of ultraviolet laser ablation products from polymers*" J. Appl. Phys. **66**, 2608 (1989)

[3.19] G.Gorodetsky, T.G. Kazyaka, R. Srinivasan "*Calorimetric and acoustic study of ultraviolet laser ablation of polymers*" Appl. Phys. Lett. **46**, 828 (1985)

[3.20] B. Danielzik, N. Fabricus, D. von der Linde, *"Velocity distribution of molecular fragments from polymethylmethacrylate irradiated with UV laser pulses"* Appl. Phys. Lett.**48**, 21, (1986)

[3.21] G. Koren and J. Yeh, "*Emission spectra and etching of polymers and graphite irradiated by excimer lasers*" J. Appl. Phys. **56**, 2120 (1984)

[3.22] J. Meyer, J. Kutzner, D. Feldmann and K.H. Welge, "*Time-resolved experiments on the photoablation of polystyrene and PMMA by ArF-laser radiation*" Appl. Phys. **B45**, 7, (1988)

[3.23] P. E. Dyer and J. Sidhu, "*Excimer laser ablation and thermal coupling efficiency to polymer films*" J. Appl. Phys. **57**, 1420 (1985)

[3.24] R. Braun , Nowak and Hess "*Photoablation of polyimide with IR and UV laser radiation*": Applied Surface Science **43**, 352 (1989)

[3.25] L.B. Kiss, P. Simon: "*Statistical Model for the UV Laser Ablation Mechanism of Polymers*" Solid State Commun. **65**, 1253 (1988)

[3.26] R.F. Cozzens, R.B. Fox: "*Infrared laser ablation of polymers*" Polym. Eng. Sci. **18**, 900 (1978)

[3.27] K. Piglmayer, E. Arenholz, C. Ortwein, N.Arnold, D. Bauerle: *"Single-pulse ultraviolet laser-induced surface modification and ablation of polyimide"* Appl. Phys. Lett. **73**,847 (1998)

[3.28] J.E. Andrew, P.E. Dyer, D. Forster, and P.H. Key: *"Direct etching of polymeric materials using a XeCl laser"* Appl.Phys. Lett. **43**, 717 (1983)

[3.29] H.H.G. Jellinek, R. Srinivasan: "*Theory of Etching of Polymers by Far-Ultraviolet, High-Intensity Pulsed Laser and Long-Term Irradiation*" J. Chem. Phys. **88**, 3048 (1984)

[3.30] P.E. Dyer, in "*Photoacoustic and Photothermal Phenomena*" (ed. P. Hess and J. Pelzl), p.164 (Springer – Verlag, Berlin, 1988)

[3.31] E. Sutcliffe and R. Srinivasan, "*Dynamics of UV laser ablation of organic polymer surfaces*" J. Appl. Phys. **B60**, 3315 (1986)

[3.32] V. Srinivasan, M.A. Smrtic and S.V. Babu, "*Excimer laser etching of polymers*" J. Appl. Phys. **59**, 3861 (9186)

[3.33] G.D. Mahan, H.S. Cole, Y.S. Liu H.R. Phillip: *"Theory of polymer ablation"* Appl. Phys. Lett. **53**, 2377,(1988)

[3.34] R. Sauerbrey and G.H. Pettit, "*Pulsed ultraviolet laser ablation*" Appl. Phys. A – Material Science and Processing. **56**, 1 (1993)

Chapter 4

Laser processing system

4.1 Introduction

This chapter describes the machining station developed for CO_2 laser ablation experiments on selected PCB materials which are mentioned in Chapter 2. The laser ablation experiments aim to investigate the optimum regime of ablating the material in terms of laser and material parameters. Therefore, there exists a need for a system that produces enough peak power to ablate the dielectric materials to be investigated and which has tuneability in the 9-11μm IR spectral range. It also needs a degree of flexibility in selection of pulse duration with the capability to operate in a stable fashion while permitting control over all these features in almost real time. Therefore, a system should be able to deliver the following set of parameters in a defined range for some, which is configured to be essential for the experiments with chosen PCB materials:

Parameters	**Value range**
Wavelength (λ)	9-11 μm
Fluence (F)	1-50 J/cm^2
Pulse duration (τ)	1-100 μs
Peak power (P)	10-100 W
Repetition rate (PRF)	5 kHz
Near diffraction limited beam quality	

CO_2 lasers that emit in 9-11μm are available commercially either DC or RF excited or pulsed mode as TEA lasers (Transverse Excited Atmospheric). Commercial, CO_2 lasers provide good beam quality, high average power, high repetition rate pulsing from about 100W to 4 kW [4.1] but are limited to pulse duration above ~ 100 μs at kHz repetition rates. The CO_2 TEA lasers readily produce shorter pulse durations of 0.1-2.0 μs pulses with very high peak power levels, but at low pulse repetition rates and usually with poor beam quality. Since, hole drilling in circuit boards requires a combination of shorter pulses and higher peak power and line tuneability to access the wavelengths of strong material absorption than offered by current commercial technology. At this time there is no such system available commercially that provides the necessary features of variability of laser parameters to be utilised for ablation experiments of dielectric materials.

It is necessary therefore to consider the development of a custom-designed flexible system to provide the beam properties required for the ablation experiments. The approach selected was a MOPA (Master Oscillator Power Amplifier) configuration, based on a line tuneable cw CO_2 laser as master oscillator and a multipass waveguide power amplifier operated in "enhanced peak" mode. The latter has been designated as USP (ultra super pulse) mode [4.2-4.4]. This approach also provided flexibility in pulse format by utilising an acousto-optic modulator (AOM) to be incorporated in the system to provide control of the pulse duration and repetition rate at the input to the amplifier stage. The waveguide power amplifier used a five-pass configuration that provided significant power gain across the relevant spectrum.

To optimise the system efficiency, an optical beam transfer system was designed to provide efficient beam coupling to the fundamental mode of the waveguide amplifier. Another set of optics was used to circularise the beam at the exit of the amplifier and relay it to the machining station and focus on the sample. The machining station had manually controlled X-Y translation stages to position the sample for ablation experiments. The machining station provided the spatio-temporal synchronisation between arbitrary position of laser spot and firing time of laser to accurately spatially resolve the crater ablated on the PCB materials. It also included the flexibility to incorporate devices used to monitor and characterise the beam in real time at all stages of its travel on the breadboard. The block and functional diagram of designed and built MOPA system is depicted in Figure 4.1. Each component of the machining system is explained in detail in the next section.

4.2 Overall system design

4.2.1 Master oscillator and beam alignment

A commercial cw tuneable low power CO_2 laser (Edinburgh Instruments Ltd Model PL2-L) was used as an oscillator in the MOPA system. The tuning spectral range is 9.1 to 10.9 μm , emitting more than 40 lines over this range. The laser has a manually-controlled diffraction grating for line selection and a piezoelectric transducer mounted output coupler for fine control of the cavity length.

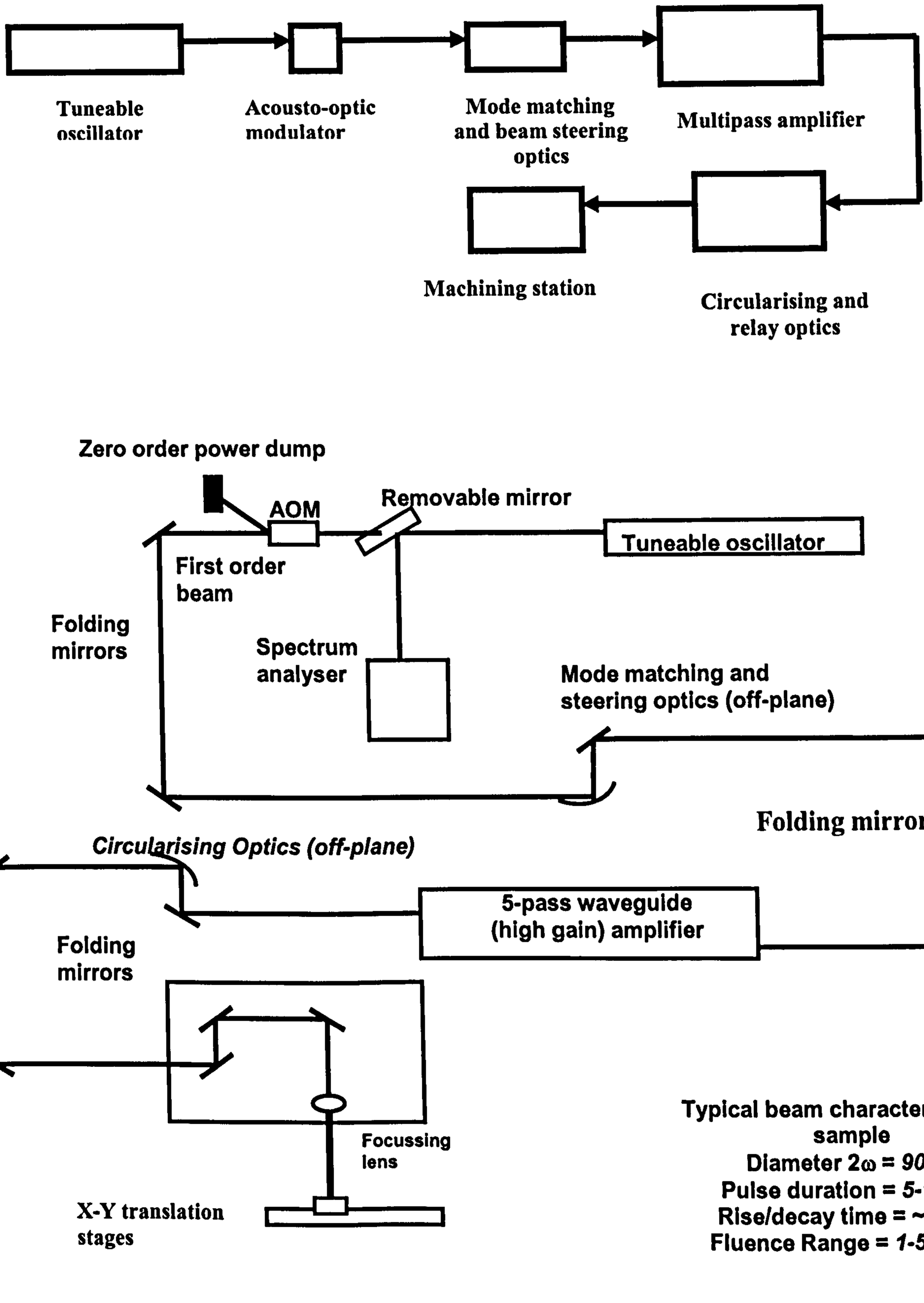

Figure 4.1: Block and functional diagram of machining system with tuneable oscillator high gain amplifier system AOM for pulse slicing and beam launching and circularising optics with machining station.

The resonator is mounted on an invar rod frame to ensure a high degree of passive stability. The laser is water-cooled and the inner walls of the laser tube are specially profiled to suppress off axis oscillations and to ensure that the lowest order transverse mode dominates. The laser beam is vertically polarised and excellent power and frequency stability exists. However, for the experiments described here, the oscillator was physically rotated by 90° to match preferential polarisation of the planar waveguide amplifier. The oscillator produces a (fundamental Gaussian) mode with a measured spot size of 3mm and measured $M^2 = 1.1$. The maximum output power is up to 6watts at peak lines of the emission spectrum of the CO_2 molecule as shown in Figure 4.2. This was measured by placing a spectrum analyser perpendicular to the oscillator to monitor the emission line of the oscillator as shown in Figure 4.1. A replaceable mirror was mounted to relay the beam from the oscillator to the spectrum analyser for line detection and taken off from the path of the beam to allow it to fall on power meter for power measurements.

4.2.2 Acousto optic modulator

To obtain suitable laser pulses from the cw operating mode of the oscillator, an acousto-optic-modulator (AOM - IntraAction Corp. Model 40 series) was incorporated in the system that slices the pulses of desired durations. It also controls the peak power. The AOM consists of a water-cooled germanium crystal with IR antireflective coating for the wavelength range of 9-11μm. The upper limit for the incident power is $5W/mm^2$ or 50W with a beam diameter of 5mm limited by the optical aperture, to prevent the onset of thermal lens or runaway effects in the germanium modulator crystal. It uses a 30-50 MHz RF drive and analogue/digital attenuation control with 40W maximum average input power. The AOM apart from providing pulse duration and peak power control also helps to keep the beam in the system aligned when passing from one wavelength to another. Every wavelength that is selected to pass through the AOM has different angle of deflection from the incident beam. This misaligns the system, hence AOM drive frequency has to be compensated respectively to keep the diffraction angle constant thereby aligning the beam again in the system. The amount of laser light diffracted to the first order beam depends on the amplitude of the acoustic waves or RF control signal to the AOM.

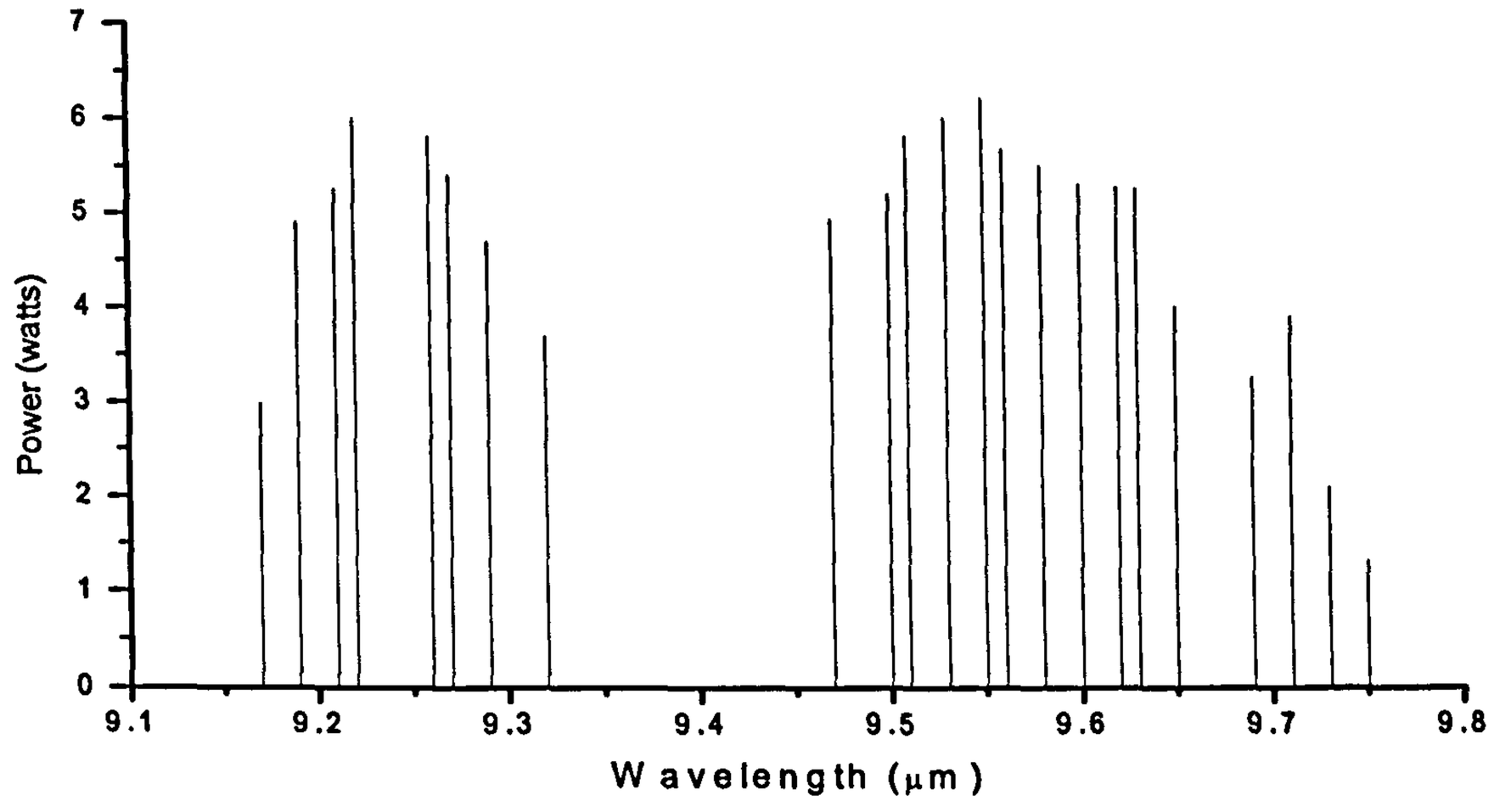

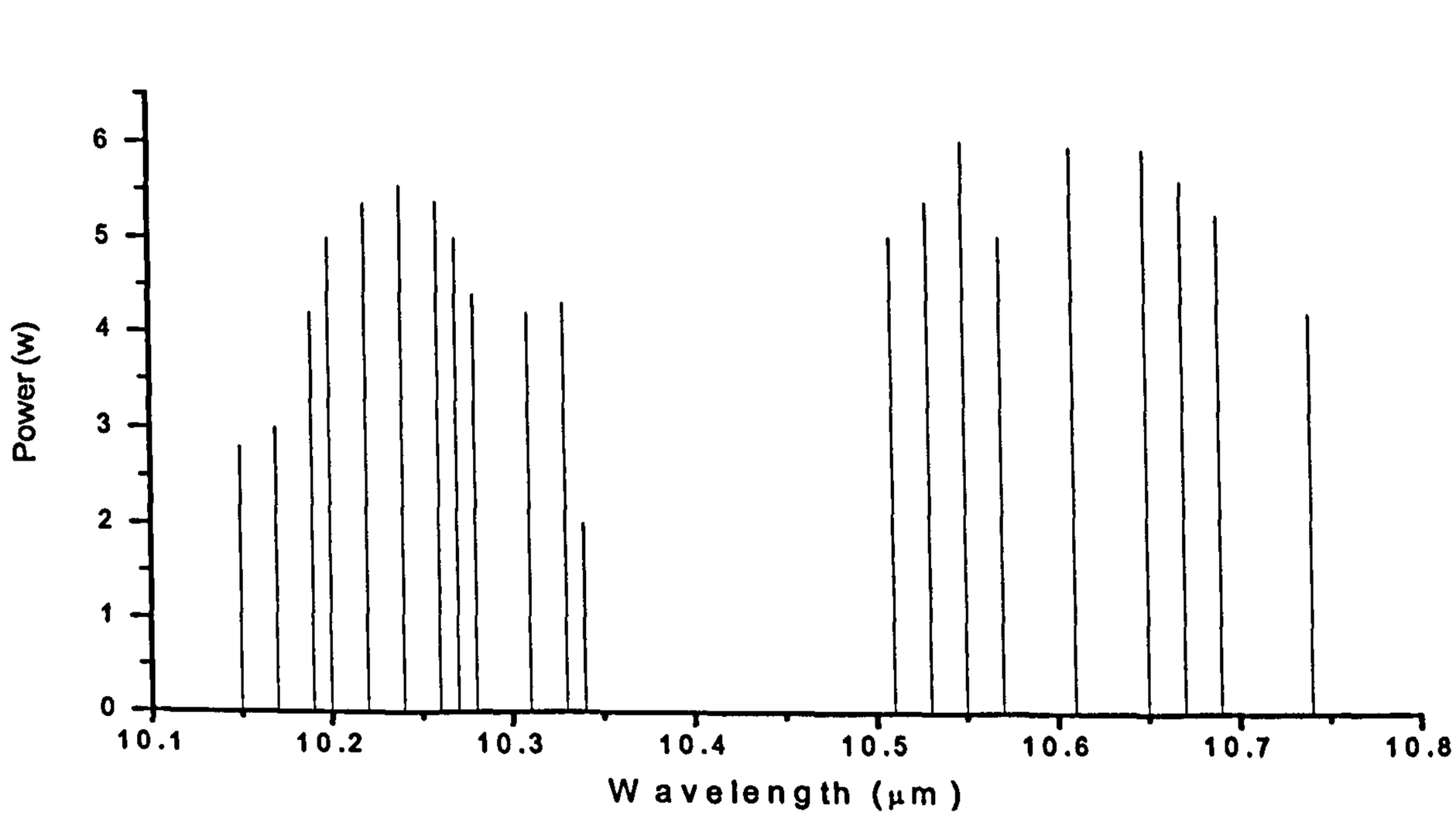

Figure 4.2: Power spectrum of oscillator in 9.1 – 10.9 μm IR spectrum

This is also called the diffraction efficiency which is the percentage of input light power that is diffracted into the desired beam at a specified RF power driving the AOM. The measured value for the AOM used was 81%. The optimum AOM angular position or Bragg angle θ_B as defined by equation (4.1) depends on f (RF drive), λ (wavelength) and speed of sound in crystal [4.5]

$$\sin\theta_B = \frac{\lambda f}{2v_s} \tag{4.1}$$

To further ensure the beam alignment in the system, a He-Ne laser probe beam was aligned collinearly to the oscillator beam that traced the optical path of oscillator beam on the breadboard. When the oscillator was tuned to different emission lines, a phosphorous screen with a UV lamp was used to detect and align the infrared spot of the divergent first order beam from zero order beam exiting AOM, thereby facilitating the alignment process. The AOM slices the pulses in durations of 5-100μs and has 200ns of rise and decay time. Figure 4.3 shows the experimental set-up for pulse slicing using an AOM. Figure 4.4 shows the synchronisation and timing chart of the laser beam triggered from the oscillator, which is synchronised with the AOM and amplifier RF drive signals resulting in the laser pulse out of the AOM. This laser beam after amplification demonstrates the gain. The amplified beam is sliced to produce different pulse durations with time delay and pulse width adjustments. The pulses were made to originate by keeping the peak lobe of the maximum gain in the centre of each sliced pulse.

4.2.3 Mode matching in waveguide and beam steering optics

In our experiments, the concept of mode matching is used to efficiently launch the laser beam from free space into the waveguide of the amplifier. The waveguide supports a number of modes, depending on waveguide geometry and radiation wavelength. Therefore, the input beam is required to match the amplitude and phase profile of the fundamental waveguide mode, with minimum angular and beam offset errors so as to minimise the degree of power coupling to other waveguide modes.

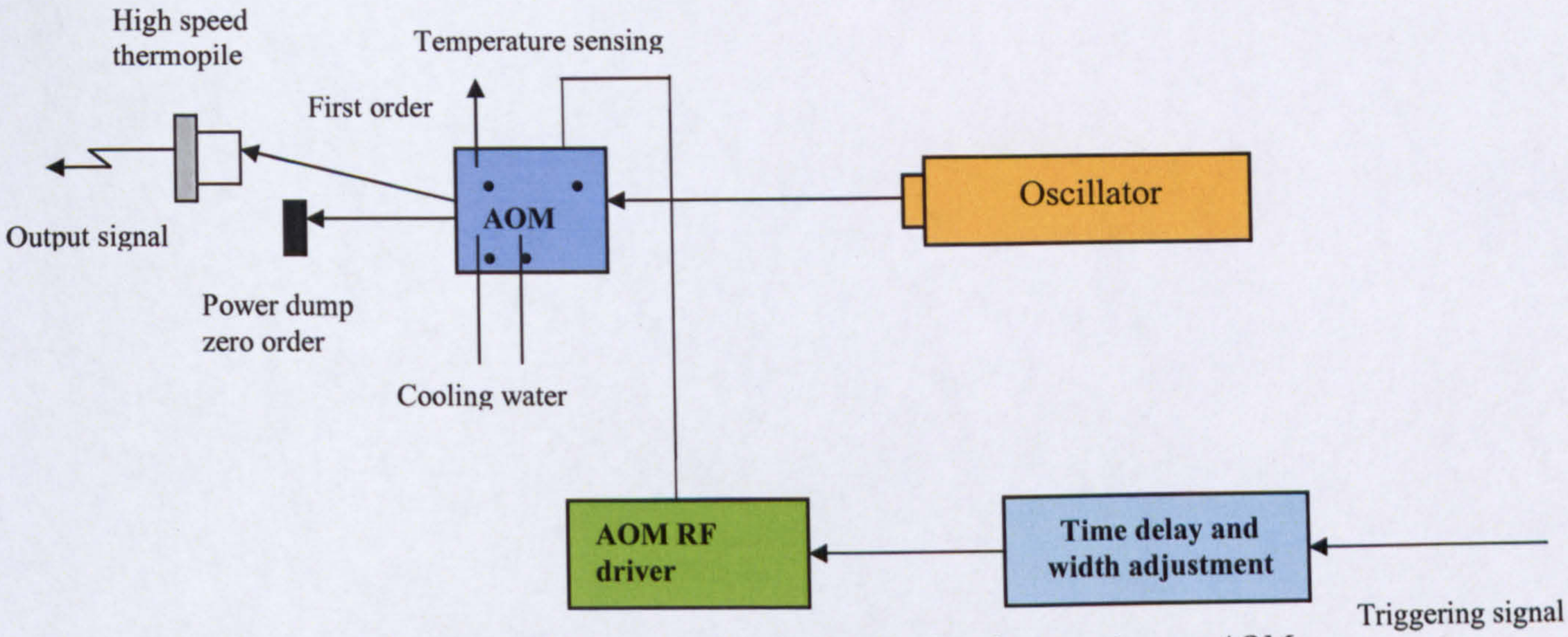

Figure 4.3: Experimental set up and pulse slicing using an AOM

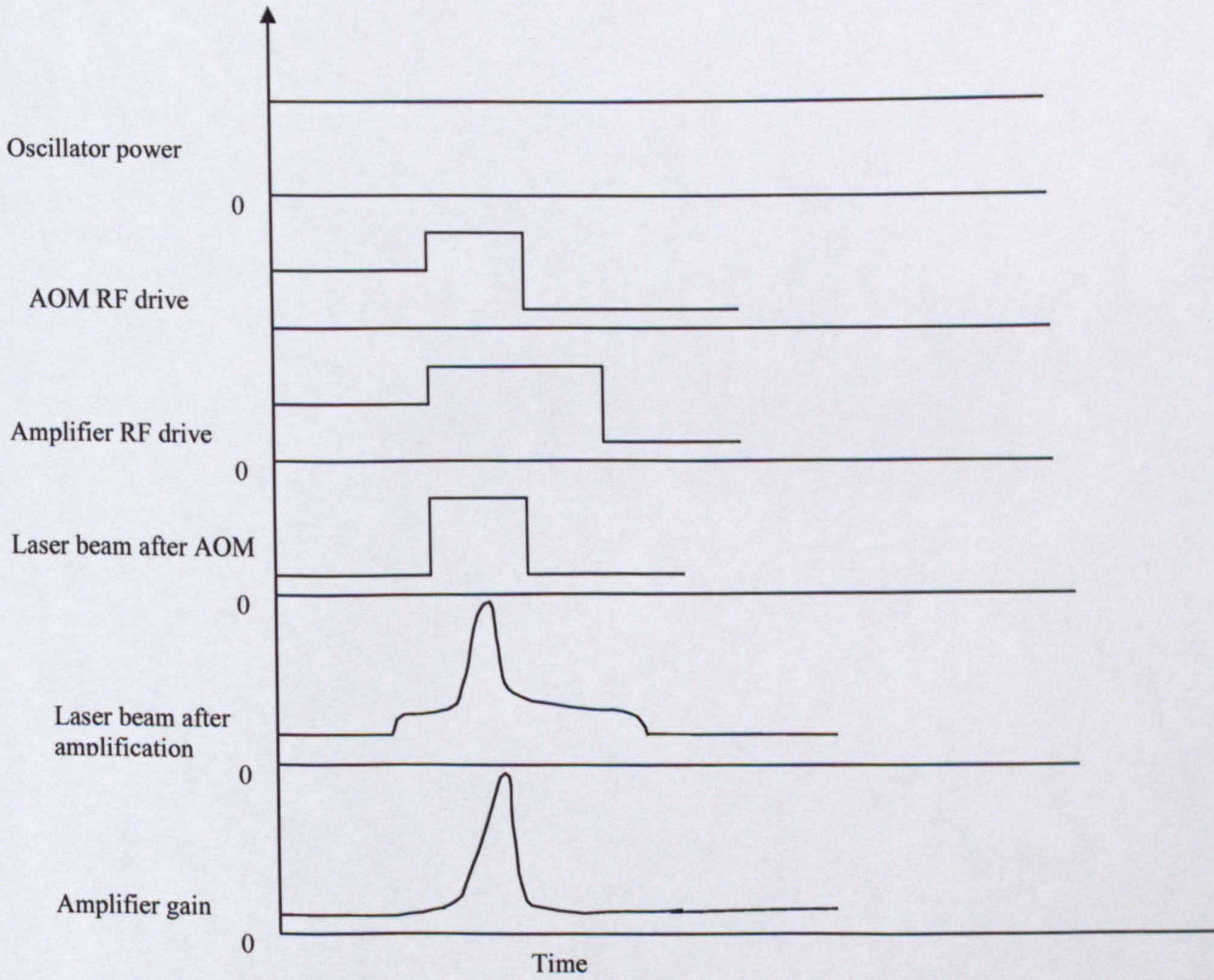

Figure 4.4: Synchronisation and timing sequence

Mode excitation and matching in a waveguide depends on many factors, such as quality of the optical components outside the waveguide, properties of the launched beam and launch conditions etc. For successful transfer of the beam from the oscillator to amplifier, the optical system is required to satisfy the requirement that the beam size from the oscillator is adjustable to match the mode of the amplifier, thereby maximising the excitation of the fundamental waveguide mode. The optimum mode matching condition [4.6] to a rectangular waveguide with a Gaussian beam input can be expressed as $W_y = 0.69a$, where a is the half electrode separation of the waveguide and W_x should have low divergence to be able to fit five passes in the amplifier and is allowed to fall at the entrance of the waveguide. This allowed low truncation loss at the entrance of the amplifier waveguide.

To relay the beam from the oscillator to the amplifier an optical system was designed, making use of the usual Gaussian beam and paraxial *ABCD* matrix techniques [4.7]. An astigmatic optical arrangement of one-mirror relay system as shown in Figure 4.1, maps the oscillator beam onto the amplifier-input plane. The system uses a single off-axis curved mirror, which provides two different focal lengths for vertical and horizontal axis of the beam, allowing the mode match in the waveguide direction and at the same time provide the low divergency in the lateral (free space) propagation direction as is shown in Figure 4.5. The focal lengths of the spherical mirror of radius, R in the plane of the tilt and normal to the plane of the tilt vary with the incident angle θ as described below:

$$\text{Normal to the plane of tilt } f_x = \frac{(R/2)}{\cos\theta} \tag{4.2}$$

$$\text{In the plane of the tilt } f_y = (R/2)\cos\theta \tag{4.3}$$

The advantage of using a single off-axis mirror is that it gives various degrees of freedom and beam parameters may be controlled using variable parameters: R, θ, oscillator to mirror distance, d_{1x} (d_{1y}) and amplifier to mirror distance, d_{2x} (d_{2y}). Also the choice of the mirror radius of curvature R has been aimed at obtaining a system which will fit on a single optical table whilst allowing the space for beam diagnostics devices to be used between the oscillator and amplifier.

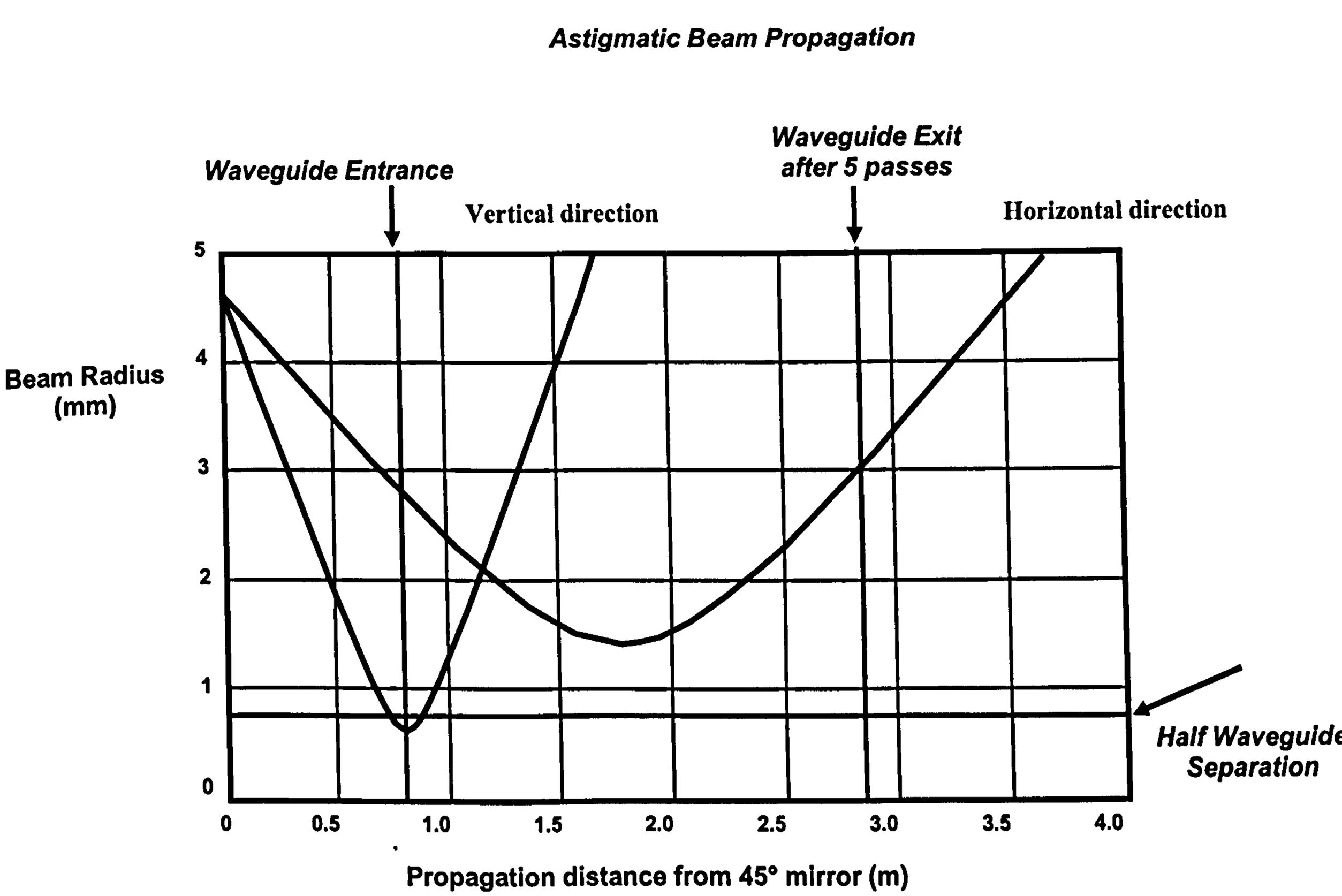

Figure 4.5: Mode matching for planar waveguide amplifier

A numerical calculation was made using MathCAD Plus 5.0 to find the mirror angle and distances from oscillator and amplifier to produce desired beam waists at the amplifier input and in the waveguide for the two orthogonal directions (x, y). Using the well-known ABCD law [4.7] the transformation of the beam is well designed through the optics. In the off-axis curved mirror system, the ABCD matrix is applied in sequence of free space-lens like media-free space and then on the curved mirror for two components of beam in waveguide and free space direction. The basic equation of the one mirror system [4.7] is applied to two orthogonal directions using appropriate focal length of off-axis curved mirror, spot size and beam quality. Results were produced after numerical scanning through values of the distances from the oscillator to mirror and mirror to amplifier, which produced the desired beam waists for the two orthogonal directions.

Finally, after scanning through the values resulting from the calculations a one-mirror system of 2m-ROC was placed at a distance of 230cm from the oscillator and 77cm from the amplifier. This spherical concave mirror was mounted on a vertical section of breadboard at an angle of 45° that relayed the beam to the folding flat mirror. This beam was further led into the waveguide of the amplifier by another flat mirror folding the beam horizontally, ensuring that no beam rotation would occur and without disturbing the pre-set angle of the mode-matching mirror as is shown in Figure 4.1. The astigmatic beam propagation is followed in the amplifier for five passes as indicated in Figure 4.5.

The calculations suggest that the beam waist waveguide direction should be located at the entrance of the amplifier and the free space direction is located between the five bounces in the amplifier. At the waveguide entrance the beam spot size remains 3mm in free space direction whereas it converges in the centre of the amplifier in the third pass to the minimum of 1.5mm. Thereafter, it expands constantly till it reaches the 3mm spot size at the waveguide exit after 5 passes. Figure 4.5 shows that the beam waist for the vertical direction lies at the entrance of the amplifier, whereas the beam waist in horizontal direction lies inside the waveguide between second and third passes. In the vertical direction of the beam is waveguided during the beam 5-passes

propagation. The beam characteristics at the exit of the amplifier are the ones of the fundamental waveguide modes with a measured M^2 of 1.1 [4.8, 4.9].

4.3 Multipass 'USP' power amplifier system

4.3.1 Basic concept

The USP (ultra super pulse) power amplifier is a planar waveguide, five pass RF excited amplifier. This was built targeting the requirement of high peak power and high energy per pulse with shorter pulse durations, which is a major requirement for the hole drilling application in circuit boards. The term 'USP' was coined to distinguish 'ultra super pulse' lasers from 'ultra' and from 'super' pulse lasers. This is illustrated by Figure: 4.6. A super pulse has the duration of less than ~1μs with one energy unit and spike ≤ 15 x cw level, whereas, an ultra pulse has duration of ≤ 100 μs with 3 energy unit and spike ≤ 4 x cw level. An ultra super pulse laser combines the parameters of super and ultra pulses such that it has pulse duration ≤ 10μs , with 3 energy unit and spike ≤ 15 x cw level as is shown in Figure 4.6.

This has been achieved by enhancing power capabilities of planar waveguide CO_2 laser that delivered peak powers up to 30 times the power of a conventional planar waveguide laser with pulses <10μs that of the conventional existing systems. This work has already been reported by our research group [4.3] where powers up to 3.5kW peak were achieved for pulses up to 10 μs and the mentioned technology is known as Ultra Super Pulse Laser (USP laser). The USP technology has shown the capability of operating at repetition rates as high as 20 kHz, at 20 % duty cycle. This characteristic gives the USP systems an advantage over the TEA lasers. Along with this characteristic, the USP technology has proven to be capable of delivering a beam with a beam quality M^2<1.2 which is necessary for hole drilling applications.

For a laser to operate in the USP regime, the main aspect is the ability to control and sustain a stable α-type discharge, which is essential for efficient RF CO_2 laser operation. This can be achieved by correct combination of RF excitation frequency, gas pressure and composition and electrode separation [4.6].

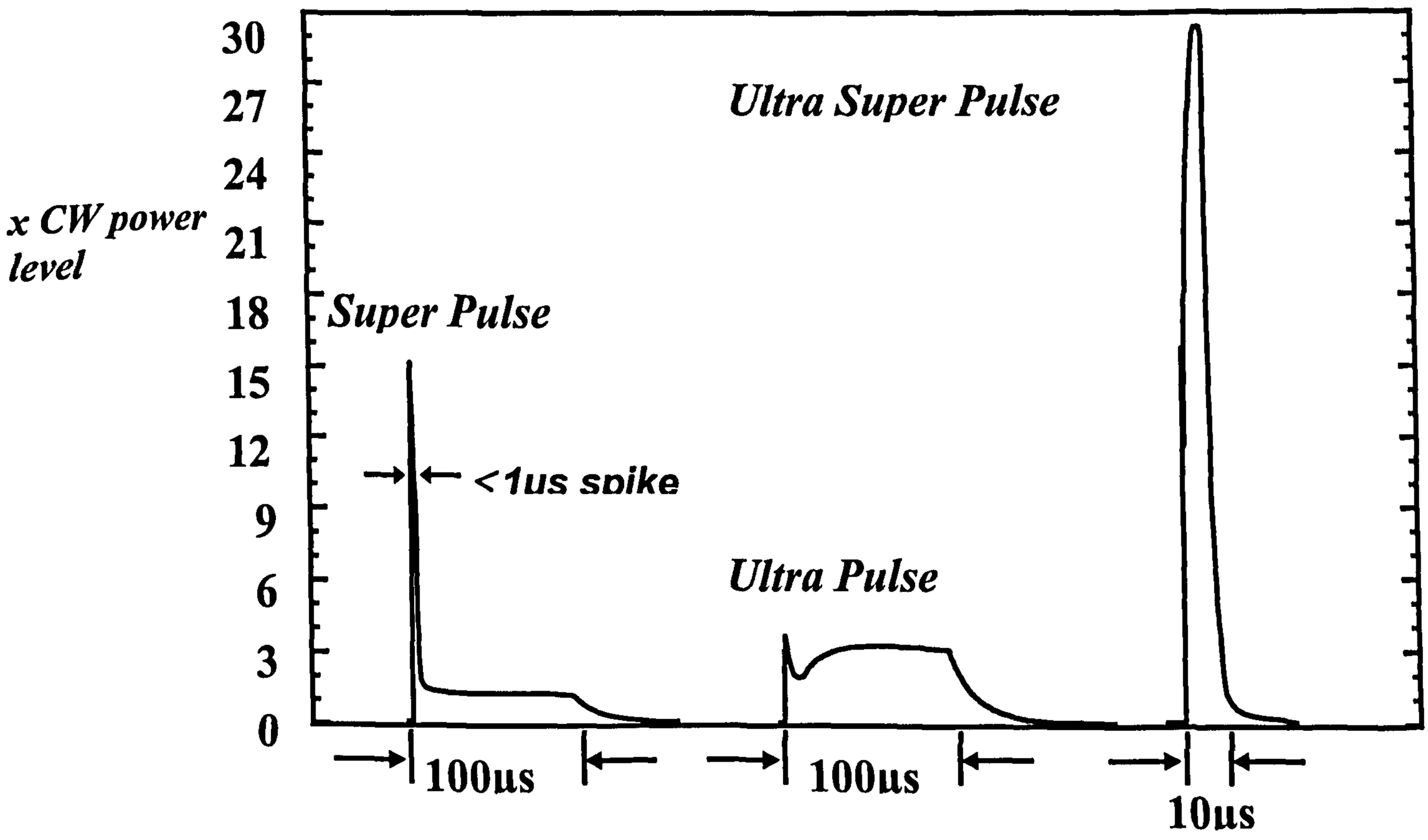

Figure 4.6: USP distinction from super and ultra laser pulses

4.3.2 USP excitation concept

As mentioned in the previous section, the USP power amplifier uses RF excitation to achieve a stable discharge gain medium between the large area parallel electrodes with the electric field direction transverse to the optical axis. Under USP conditions, RF discharges are stable over a relatively narrow range of operating conditions, which must be carefully chosen to achieve optimum conditions for the performance of the laser. Fundamentally, there are two different forms of stable RF discharges i.e. the α discharge and the γ discharge. For CO_2 laser excitation only the α discharge is suitable, while the γ discharge is highly undesirable. In α discharge, two distinct regions are observable from its appearance: the central plasma zone which provides the laser excitation and a pair of bright emission regions adjacent to each electrode, which contain high positive ion concentration referred to as 'sheath' zones. The sheath regions do not contribute directly to the molecular excitation process, though they are essential to the stabilisation of the discharge. Thus is advantageous to operate the discharge under conditions where the sheaths occupy a relatively small fraction of the total discharge volume.

The desired stable α-type discharge is produced when the correct selection of RF excitation frequency is made along with other factors like gas pressure. The combination of RF energy and pulse rate that is applied to the discharge volume is limited by the gas heating, which causes gain and efficiency reduction, while the peak power is limited by discharge instabilities. The α to γ transition results in severe loss of uniformity in the discharge, often followed by damage to the electrodes. Hence maintaining discharge stability and heating limits by adequate excitation frequency, allows laser operation at high power densities required for the USP operating regime before reaching the α-γ transition point. This has been reported in [4.6], which is an extension of the capabilities of the planar waveguide CO_2 lasers.

4.3.3 Amplifier construction

The planar waveguide multipass amplifier module includes two aluminium metal electrodes, separated by 1.75 mm and with drilled internal water cooling channels, giving active area of 44 x 360 mm^2. It can be configured as either a single pass or multifold amplifier. The multipass amplifier has been configured to fit five passes of the laser beam without overlapping using two flat mirrors to fold the beam back and

forth as is shown in Figure 4.7. The electrodes are mounted within the rectangular aluminium vacuum vessel that contains a 40mm diameter invar rod, to which the folding mirrors are mounted independently of the main discharge structure. Antireflective coated zinc selenide windows are mounted on flanges at each end of the amplifier, to permit entry of the launched beam and for the exit of the amplified beam. The whole laser amplifier vessel is filled to the desired gas pressure, with a standard 3:1:1 mixture of helium, nitrogen, and CO_2 plus additional 5% xenon. The planar waveguide is driven by a 81 MHz RF generator, which is connected, to the laser head by a single 50-ohm coaxial cable, via a reactive impedance matching network. With optimised fill up of the active area five passes are enabled and the output beam lateral beam quality is measured to give four times net gain than the conventional laser. In addition, it operates in a pulsed–discharge mode, with a maximum pulse repetition rate of 10 kHz and maximum duty cycle of 20% producing ~ 100W average output power if configured as an oscillator.

4.3.4 Multipass propagation in the amplifier

In the multipass amplifier system the folded beam paths and the beam spot sizes on the amplifier mirrors can be obtained using the *ABCD* matrix using appropriate dimensional offsets of the mirrors. The beam M^2 is 1.2 for the input beam and if the lateral input beam spot size is set to 3mm, then with further calculations, the 5-pass optical beam folding system is easy to produce without beam overlap, while a 7-pass configuration is not possible since the self oscillations were too difficult to be avoided.

In the 5–pass configuration, the shape of the exit beam was found to be similar, irrespective of whether the discharge was on or off. Lateral misalignment of the folding mirrors may produce imperfect exit beams and overlapping of the folded beam may cause interference fringes. No gain saturation effects were observed, indicating that the power levels were not enough to saturate the gain.

There is a combination of losses in the launching and multifold beam path traversing which affect the output power of the amplifier after 5 passes. These losses are thought to be as follows:

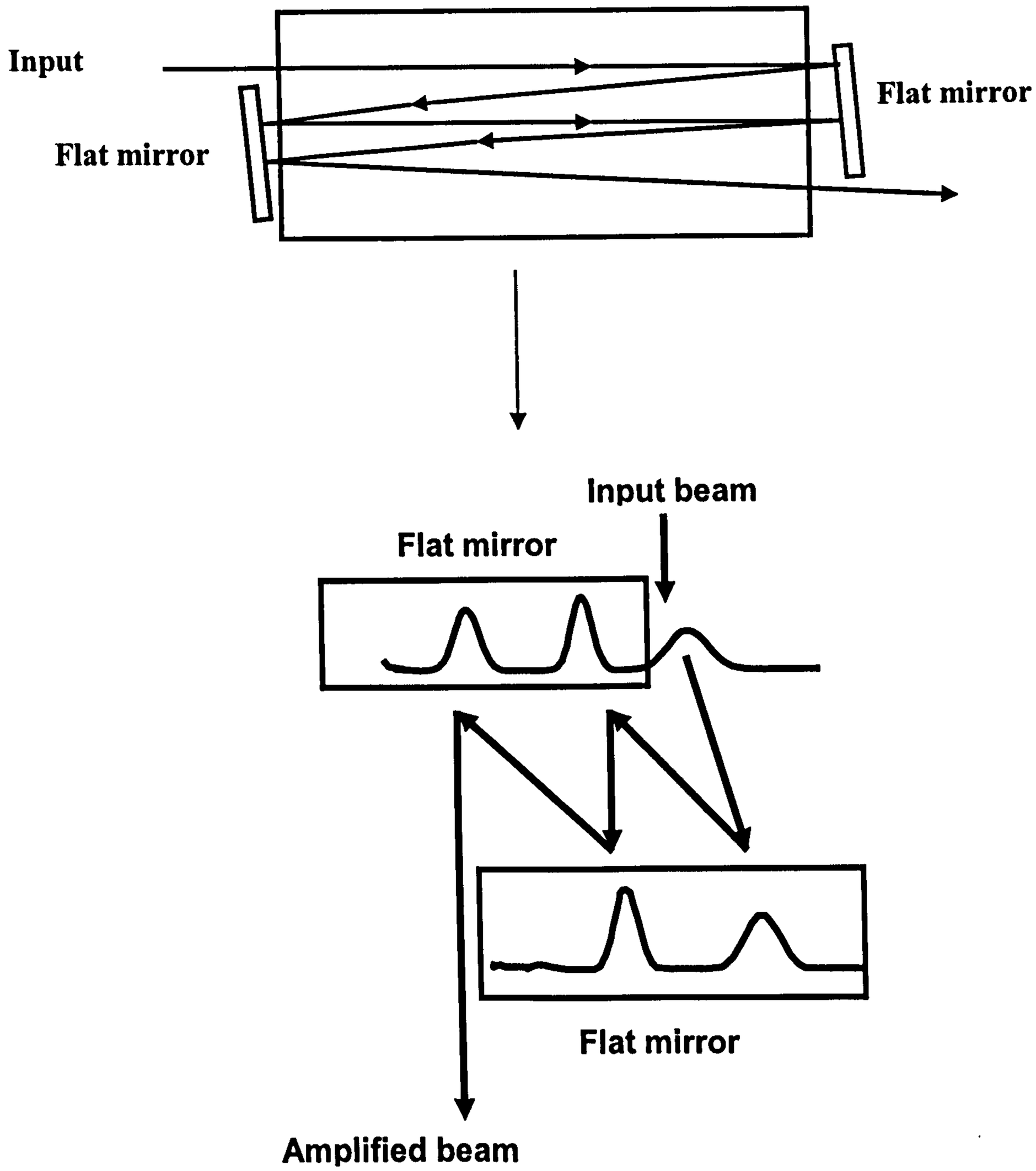

Figure 4.7: Schematic of five passes amplification of laser beam in the amplifier and beam profile on the mirrors

(a) **Launching loss:** The diameter of the input beam was 1.5 mm and the gap of electrodes was 1.75mm, hence, launching beam for the first pass had some low launching losses since input beam size was smaller than that for optimum coupling of fundamental mode.

(b) **Reflection loss**: Reflection losses occur when the input beam after every pass is reflected from the gold coated folding mirrors of the amplifier.

(c) **Coupling Loss:** Between the waveguide and free space sections the repeated coupling losses occur twice per round trip.

(d) **Waveguiding loss:** The waveguiding losses occur depending on the material of the wall of waveguide and on the quality surface finish.

The losses are quantified as: For an input power of 3W the transmission was measured to be 96% for one pass, 76% for 5 passes. These losses may be understood through a combination due to: Beam launching loss for the first pass, reflection losses of ≥ 1% per bounce from the gold-coated folding mirrors and repeated coupling losses occurring twice per round trip between the waveguide and the free space sections, which are estimated to be ~2% per pass. With the mirrors used and gap of electrodes as 1.75mm, the equivalent distributed loss factor combining waveguide, coupling and reflection loss is of the order of ~0.08m^{-1}, while the distributed loss factor for the single pass is of the order of ~0.04m^{-1}, combining the truncation loss at the waveguide entrance.

The calculations of the combination of the losses and equivalent distributed loss factor combining waveguide, coupling, reflection loss in five passes and distributed loss factor for a single pass has been calculated by Cao *et al* [4.6]. Power transmission measurements were also made for the beam traversing the planar waveguide amplifier with the specified folding mirrors.

4.4 Gain measurements and wavelength power spectrum in amplifier

The multi pass amplifier was designed keeping in mind the necessity for a device capable of working in a pulsed mode that delivered net gain up to 33 times the input power of the oscillator, higher than the conventional existing systems. This section discusses the gain measurements of the system that makes it distinctively important along with other features provided by the amplifier. The gain coefficient is a key

parameter to account for actual amplifier system design, scalability and power amplification. The small signal gain coefficient γ_0 was measured for single pass by keeping the discharge of the amplifier on and off when the oscillator beam is allowed to pass through the amplifier. This arrangement of measuring gain is discussed in detail as follows. The advantage of using this treatment is that no exact information on the losses is required. The experimental set-up for gain coefficient measurement and small signal gain measured for enhanced gain–pulsed amplifier and conventional-cw CO_2 laser is shown in Figure 4.8. The incident beam from the oscillator was allowed to pass through power meter (PM_1) to measure the beam power from the oscillator, thereafter this beam is relayed to the amplifier. This beam acted as input to the amplifier. The beam exiting the amplifier was allowed to fall on the second power meter (PM_2). Here the power was measured when the discharge is on and off in the amplifier. If P_1 is the power measured at PM_1, P_{off} and P_{on} is the power measured at PM_2 when the discharge is off/on, then the small signal gain coefficient is given by equation (4.8). The value of P_1-P_{off} was measured and pre – recorded as a convenient means of generating a calibration to permit the reading out of P_{off}, when discharge is on, and to avoid the need for repeatedly switching off the discharge.

The relation used to determine the gain coefficient γ_0 is:

$$\gamma_0 = \frac{1}{L} Ln\left(\frac{P_{on}}{P_{off}}\right) \qquad (4.8)$$

Where, (P_{on}) is the output power at the amplifier on and (P_{off}) that with it off.

The method permits the determination of the net gain coefficient that takes into account the waveguiding loss, power fluctuation or spectral drift of the source laser. It also avoids the problems associated with repeated switching of the RF discharge on and off. The results shown in Figure 4.8 the gain as the function of wavelength under standard and high gain amplifier excitation conditions in emitted lines in 9μm and 10μm emission bands. The results shown in Figure 4.8 illustrate that the high gain pulsed amplifier gain is up to 3 times higher when compared to the conventional cw-long pulse mode CO_2 laser. Some lines specially 10P20 present 10% extra gain attributed to 'hot-band' emission.

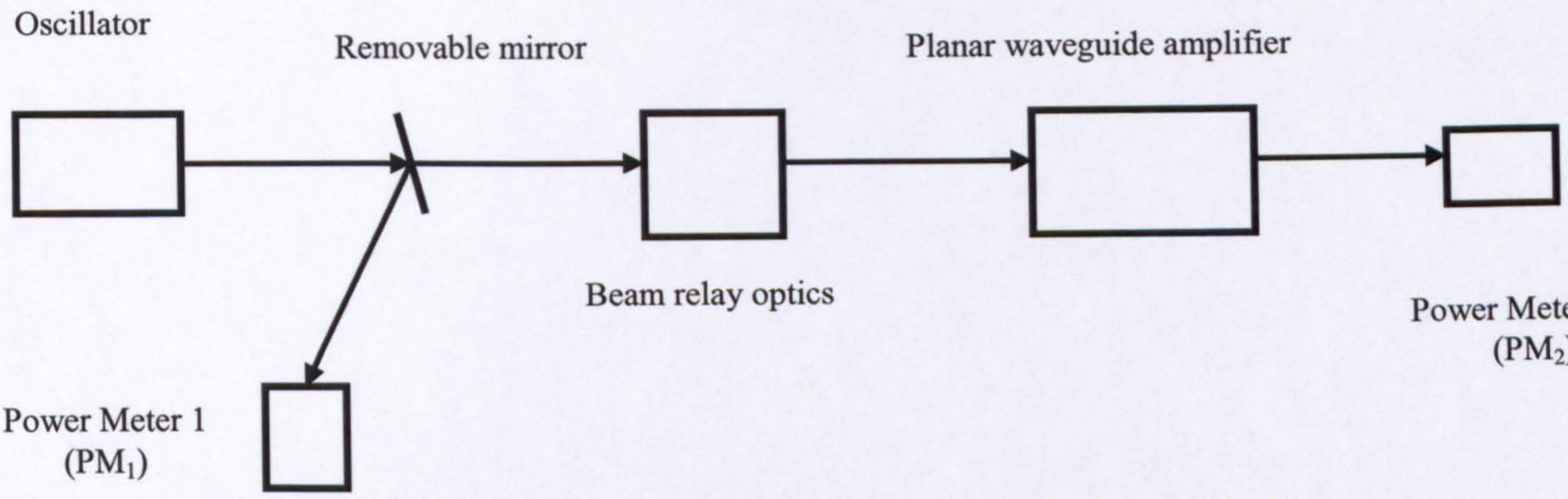

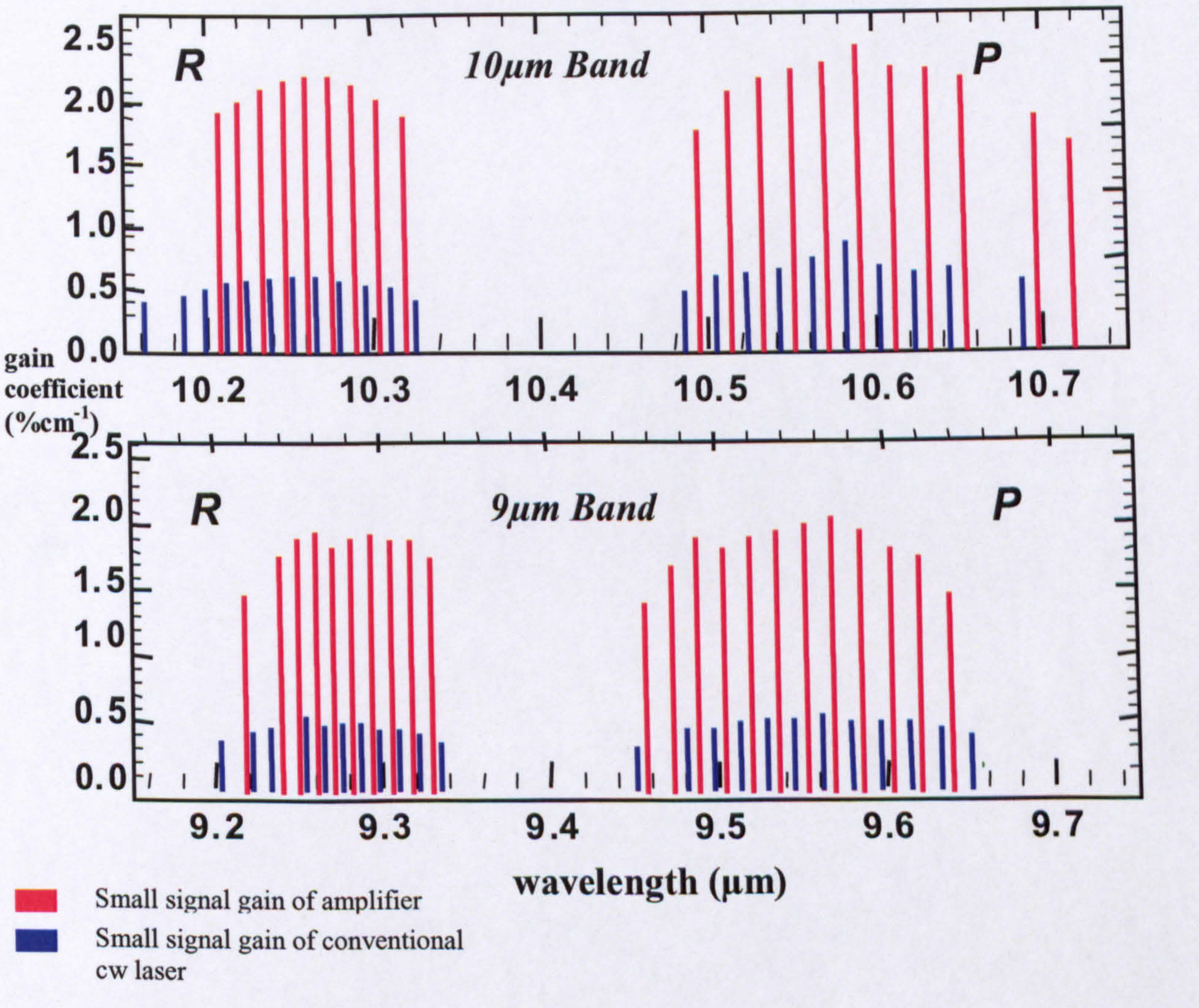

Figure 4.8: Experimental arrangement for gain coefficient measurement and small signal gain measured for enhanced gain –pulsed amplifier and conventional-cw CO_2 laser.

The average power of the oscillator and the peak power were measured and using the Labview software, the net gain was measured in real time. This procedure was repeated for every rotational vibrational line used in 9 μm and 10 μm emission bands. Figure 4.9 illustrates the result for net gain in 9 μm and 10 μm for five passes. Comparing five pass net gain with the single pass standard laser gain, following results are obtained:

- Net gain per pass ≈ 2, in the multipass five passes of amplifier.
- Total net gain increases by up to 33 times the input power from the oscillator.
- More than 20 rotational vibrational lines in the emission bands show peak power greater than 100Watts. Anomalous gain peaks are visible on the 9R16, 9R18, 9R22 lines in the 9 μm band and 10R16, 10P20 lines in the 10μm band of the CO_2 laser.
- High gain amplifier provides full control of pulse output characteristics.

The power amplification or pulse energy gain is shown in Figure 4.10, which is an averaged effect in laser pulse amplification defined as ratio of the unit area output energy to the unit area input energy. The amplified pulse energy is a function of operating conditions. Based on the result [4.6] of dependence of pulse energy on the gas pressure and input energy, the optimum gas pressure maintained was 80 torr and maximum average power from the oscillator was relayed into the amplifier.

The wavelength power spectrum of CO_2 five-pass amplifier in the 9 and 10μm bands is shown in Figure 4.11. In going from 9.1 – 9.8μm, the strongest line observed under the operating conditions mentioned in Section 4.3.3 is at 9.27 and 9.59μm. In going from 10.1 to 10.71μm, the highest gain lines are 10.24 and 10.59μm, with power up to 100 and 131watts respectively, after five passes. The average power of the oscillator of 6 watts at these peak gain lines is amplified to the peak power of 100watts.

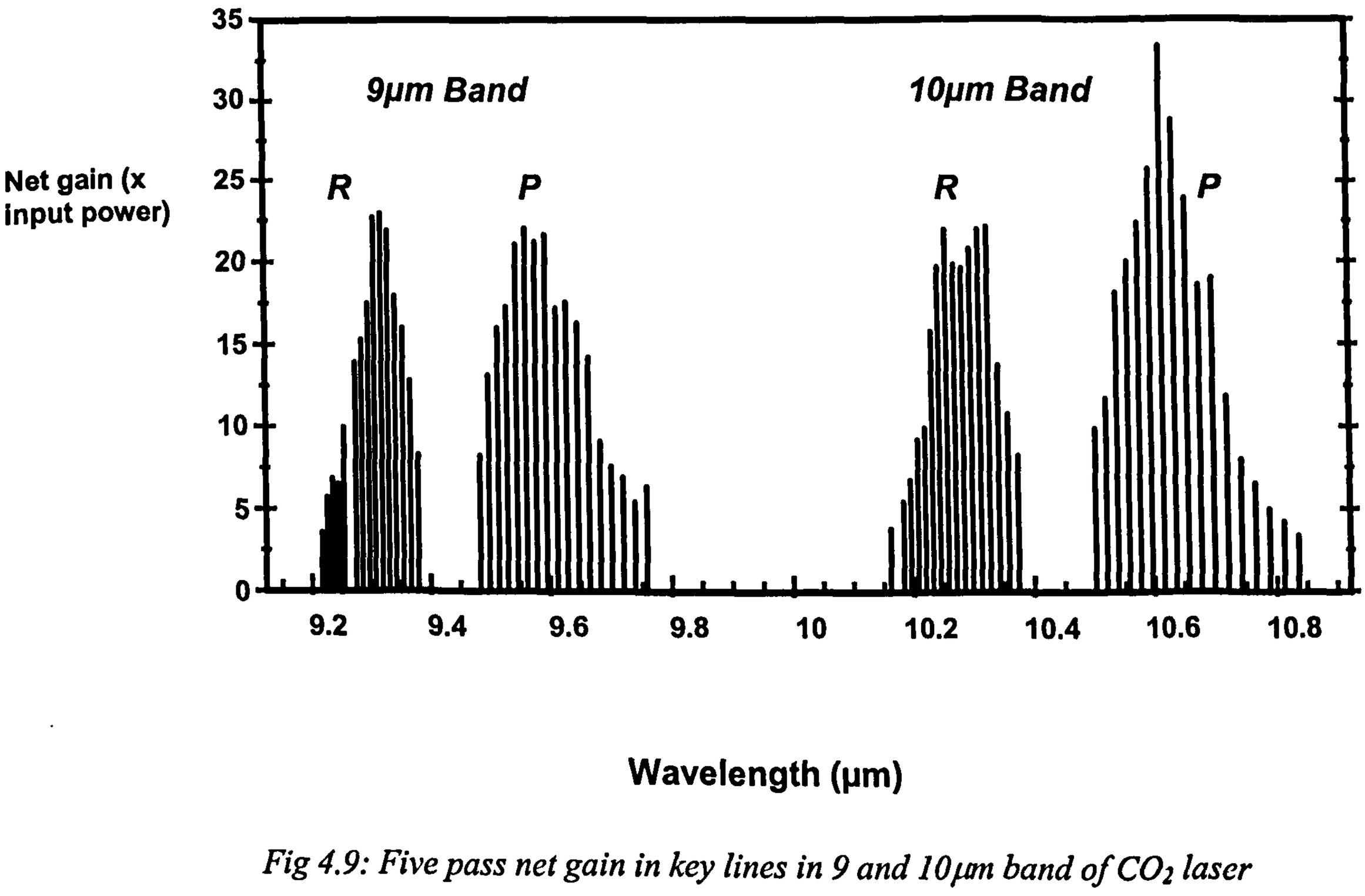

Fig 4.9: Five pass net gain in key lines in 9 and 10μm band of CO_2 laser

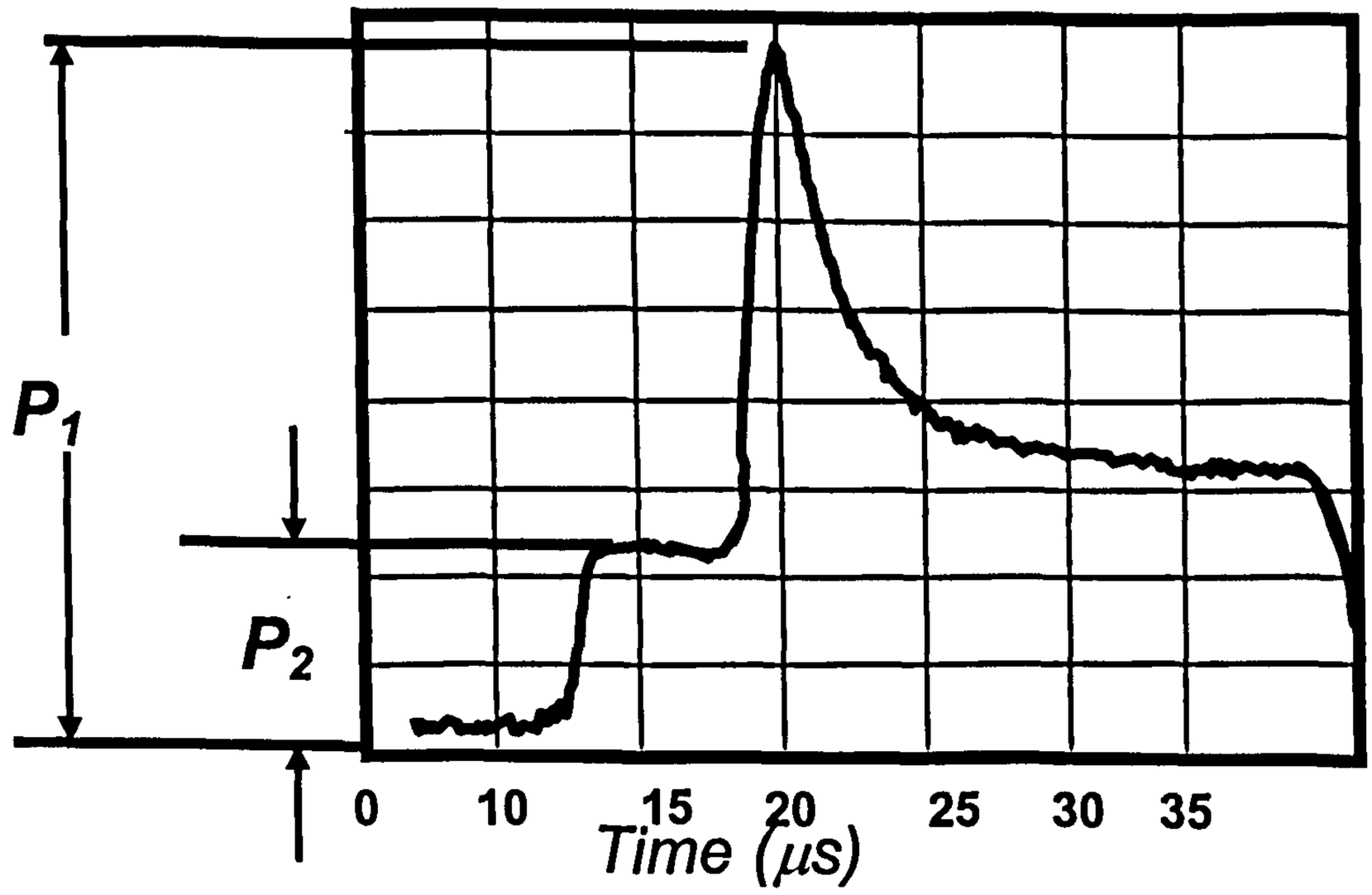

Figure 4.10: Power gain in an amplified pulse: P_2 is the oscillator power signal and P_1 is the amplified power signal

4.5 Circularising optics and machining station

At the exit of the amplifier the waist of the beam was measured and the additional optical set-up was placed to circularise and filter the beam to improve the profile. A carefully adjusted set of a flat and a concave spherical mirror with radii of curvature 1m was used to carry out circularisation as is illustrated in Figure 4.1. The beam was allowed to fall on the pyrocam to view the beam profile in the real time. The circularised beam was folded to fall on the machining station optical set up. The beam was further relayed on to an aspheric *ZnSe* lens of 1" diameter of the focal length of f =1.5" to produce 90 μm minimal diameter $(1/e^2)$ spot on the target placed on the translation stages. The XY translation stages were appropriate for a precision machining station. These were DC motor powered stages, with motion smoothness and jostle free–operation but were manually operated for the ablation experiments. The software executed the sequence of synchronisation between laser firing and instantaneous spot position. The workpiece was fixed on the stack of the travelling stages to avoid accidental change in position during machining. The slide holder held the work piece on the stack of travelling stages through a levelling table. The work piece was usually in the standard format of microscopic slides of 1.2 x 3 cms, which was easier to be accommodated in the slide holder.

4.6 Summary and conclusion

This chapter discussed the hardware of a MOPA machining station and the construction and operating conditions of a high gain five-pass amplifier. The MOPA formatted system demonstrated independent control of wavelength, pulse duration and peak power parameters. The master oscillator was a tuneable source that spanned the wavelengths between 9.1 to 10.9 μm, but had low average power operating in cw mode. A five-pass planar waveguide amplifier was constructed that amplified the low average powers of the oscillator. Gain characteristics and power amplification of the planar waveguide CO_2 laser amplifier was also investigated. The maximum net gain measured was 33 times the input power from the oscillator and the maximum power amplified was 131 watts in 10.59μm line. Optics were designed that mode matched the beam from free space to the waveguide and also provided the flexibility of steering the beam. The objective of building flexible a machining centre was achieved. The experimental results of ablation of key PCB materials using this machining system are presented in the following chapters.

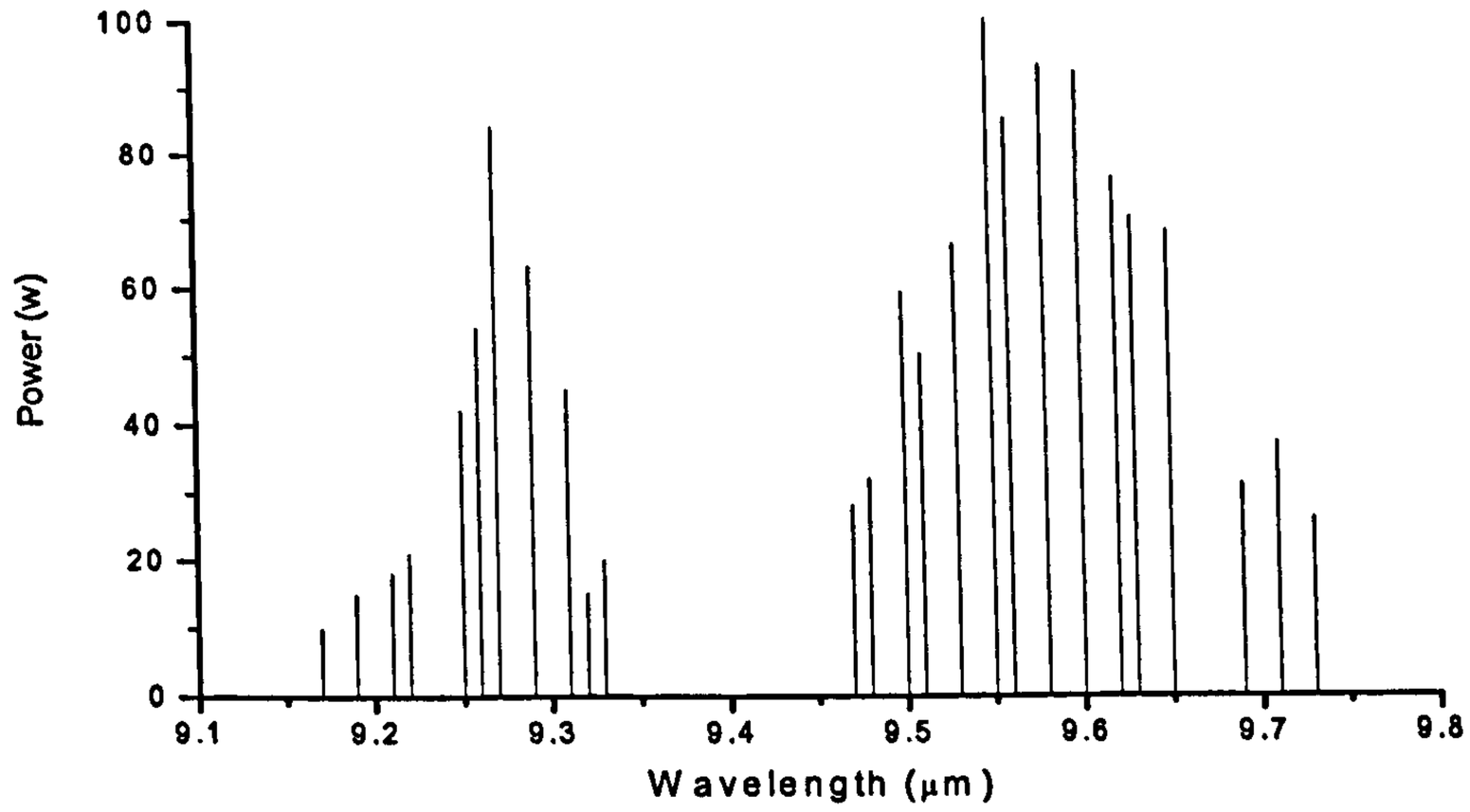

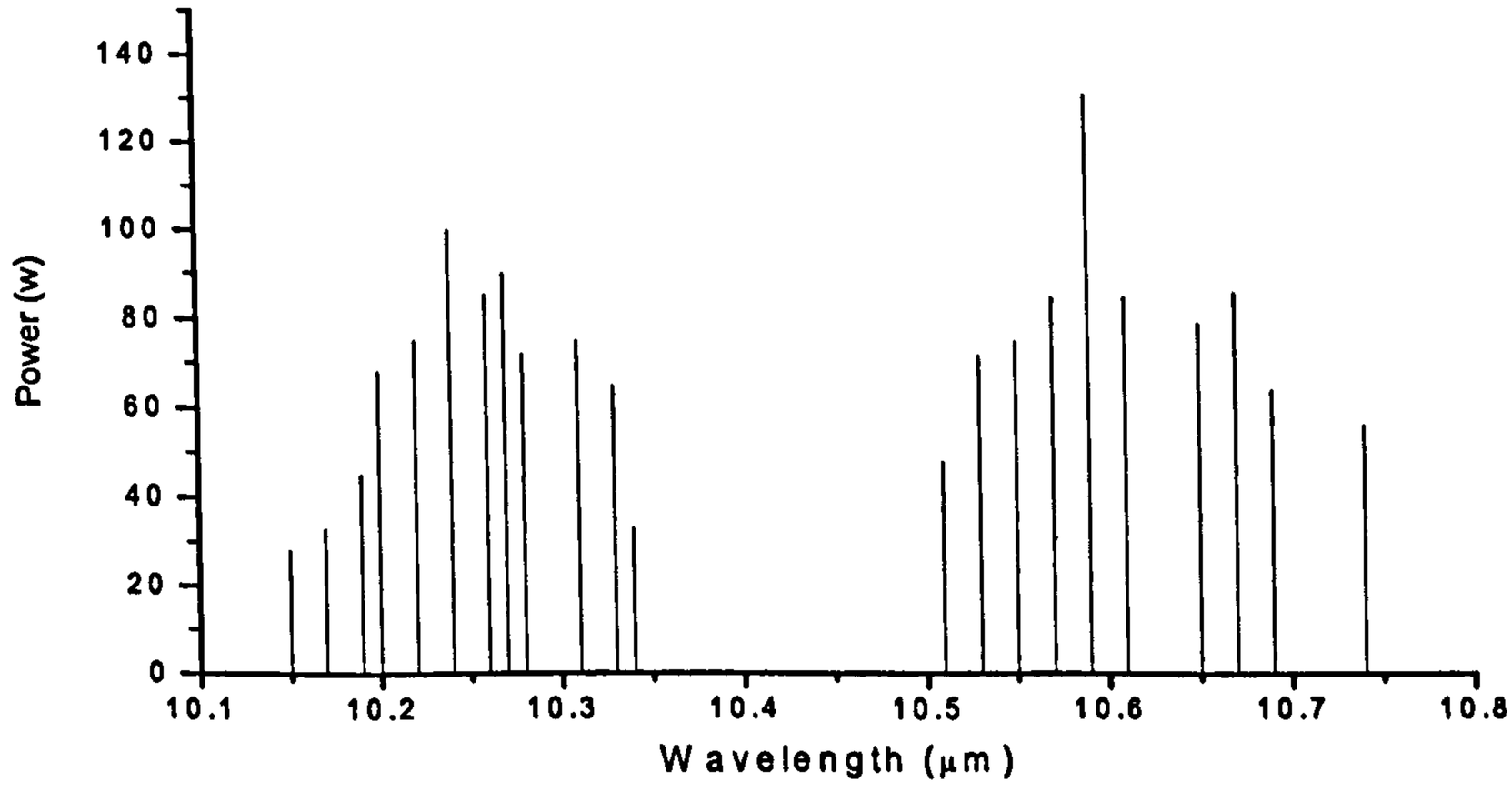

Figure 4.11: Wavelength power spectrum of CO_2 amplifier after five passes in 9 and 10μm emission band

4.7 References:

[4.1] Planar waveguide CO_2 lasers marketed by Coherent Inc (Santa Clara, USA) and Rofin-Sinar Technologies Inc. (Hamburg, Germany and Hull, UK)

[4.2] C. J. Moorhouse, F. Villarreal, J. J. Wendland, H. J. Baker, D. R. Hall, and D. P.Hand, *"Single pulse microvia drilling of resin-coated copper substrates using an enhanced peak power planar waveguide CO laser,"* in Proc. SPIE, vol. **5339**, pp. 276–283 (2004).

[4.3] F. Villarreal, P. R. Murray, H. J. Baker, and D. R. Hall, *"Enhanced peak power and short pulse operation of planar waveguide CO lasers,"* Appl.Phys. Lett., vol. **78**, pp. 2276–2278, (2001).

[4.4] F. Villarreal, Q. Cao, R. J. Ramirez, H. J. Baker, and D. R. Hall, *"High gain and high peak power in planar waveguide lasers,"* in Proc. CLEO Pacific Rim, vol. **1**, pp. 220–221, (2001).

[4.5] R. Adler, *"Interaction between light and sound,"* IEEE Spectrum **4(5)**, pp 42-54, (1967).

[4.6] Q Cao, H. J. Baker, D.R. Hall," *Transverse mode propagation and gain coefficients in a planar waveguide CO_2 laser amplifier"* IEEE Journal of Quantum electronics, Vol. **37**, 3, p376-383, (2001).

[4.7] Amnon Yariv, *"Optical electronics in modern communications."* Fifth edition, Oxford university press 1997,Chapter 2 (1997).

[4.8] A. E. Siegman, M.W. Sasnett, T.F. Johnston, *"Defining and measurements of lasers beam quality: the M^2 factor."* IEEE J. Quantum Electro. pp 1098, 27, April (1991).

[4.9] ISO TC 172 SC 9 WG 1 *"Standard for the Measurement of Beam Width, Beam Divergence, and Beam Propagation Factor."*

CHAPTER 5

Single pulse drilling of organic materials

5.1 Introduction

This chapter reports the ablation rates of selected organic PCB materials at multiple IR wavelengths in the 9μm and 10μm emission bands of the CO_2 laser. The selected organic PCB materials are a proprietary resin of RCC, FR4, Arlon and Kapton. The relevant characteristics and properties of each material were given in Chapter 2 section 2.3. The effect of laser parameters in material interaction is investigated over a wide range of IR wavelengths and pulse durations. The investigation may provide useful practical data, which may contribute to the understanding of the key factors for efficient ablation of materials. Where possible the attempt is made to suggest the optimum material removal regime for the material, which may be of direct application in the electronics industry as it can be used to increase the efficiency of laser machining.

5.2 Design of experiments for single pulse drilling

In Chapter 4, the laser machining system that emits 40 lines in to IR spectral band was described. However, it is not practically possible to investigate the ablation mechanism at *all* the emitted lines for each material. Therefore, some method is needed to restrict the choice of wavelengths to a narrower range based on selecting (where possible) the lines with the highest absorption for that material. Thus, the number of wavelength needs to be assessed in a manner, which is practical but which minimises the chance of losing valuable information. The method selected here has been to base the selection on the *absorption coefficient* data, obtained either from the literature or from our experiments. The first approach is to gather information from the literature and from the material manufacturing companies. The problem encountered here is the relative lack of such information in the literature and the information obtained from manufacturers is non–reliable due to lack of unknown composition or genre of the materials.

Therefore, two sets of experiments have been conducted:

(1) Absorption measurement by ellipsometry (see section 5.3).

The idea of ellipsometery measurements is to determine the absorption coefficient over the relevant wavelength range for each material to be studied, i.e. Kapton, Arlon, RCC, FR4, alumina and LTCC. The principles and the relevant practical details of ellipsometry are discussed in Section 5.3. The technique is used to select a subset of wavelengths for further study by the ablation spectroscopy techniques.

(2) Wavelength dependent ablation measurements (Ablation Spectroscopy).

Each selected wavelength is now used to machine the material and to obtain the ablation or machining curve. An array of craters (10x10) is ablated at varying fluence as a function of the selected wavelengths in 9 and 10 μm IR emission bands. For each material, the ablated holes are studied and recorded using an atomic force microscope (AFM), scanning electron microscope (SEM) and DekTak stylus tip, where appropriate. The recorded ablated depth per pulse is plotted against axial fluence yielding an ablation rate curve. The ablation rates are plotted together for the material to give an 'ablation spectrum'. The aim is then to compare the ablation spectrum to the room temperature 'absorption spectrum' of the material, which is derived from the measurements using an IR Ellipsometer. This is performed to allow analysis and to determine a pattern (if any) of deviation of absorption of peak lines in the material at room temperature and when material changes phase during laser ablation. The ablation mechanism is observed and recorded at each wavelength to understand the underlying material removal processes as a function of wavelength, pulse duration, spot size and peak power. The collective information therefore helps in optimising the key parameters for efficient material removal.

Errors:

It is important to mention here that efforts are made to obtain the results with minimal experimental errors and to determine the errors, which do exist. Each set of experiments was repeated ≥3 times. In each set of experiments, an array of craters (10x10) was ablated for each value of change in fluence. The standard deviation in the measured values (e.g. of threshold fluence) were determined. In general, it was noted that the standard deviation value was <5%. All the measurements were

performed at room temperature. The spot size of the beam is measured at the exit of the amplifier, each time when the oscillator was tuned to a different line for ablation. The peak power is measured every time to check power stability before each set of ablation experiments. The entire process is repeated to check the repeatability of the process.

5.3 Ellipsometry Measurements

Ellipsometry is the measurement of the effect of reflection on the state of polarisation of light. The result of an ellipsometric measurement is to determine the complex refractive index of the reflecting material, or if the reflecting material is film covered, the thickness and optical constants of the material can be determined. Ellipsometry is particularly attractive because it does not perturb the sample being measured and it is extremely sensitive to minute interfacial effects and can be applied to surface having thickness as small as monatomic to as large as several microns. The ellipsometry technique was discovered one hundred years ago but it is only in recent years following the development of advanced electronics and computers that the technique has expanded significantly in many fields, particularly for the determination of absorption coefficient of the materials.

5.3.1 Principle of Ellipsometry

A commercial IR ellipsometer, (Model GESP5 FTIR, Sopra Inc. France), was used to record the absorption spectra of the materials investigated in the thesis. Acknowledgement is made to Dr. Joe Keddie and Dr. Tim Simpson of University of Surrey, U.K., for providing access to the ellipsometer and considerable technical expertise and help in making the measurements. Dr. Keddie and Dr. Simpson provided the programme analysis to produce results for each material.

An ellipsometer essentially consists of a light source and a detector, a polariser and an analyser. The polariser establishes the input polarisation state and the analyser measures output polarisation state. The sample to be measured is always placed in between the polariser and analyser. A schematic diagram is shown in Figure 5.1 of the basic apparatus of the ellipsometer.

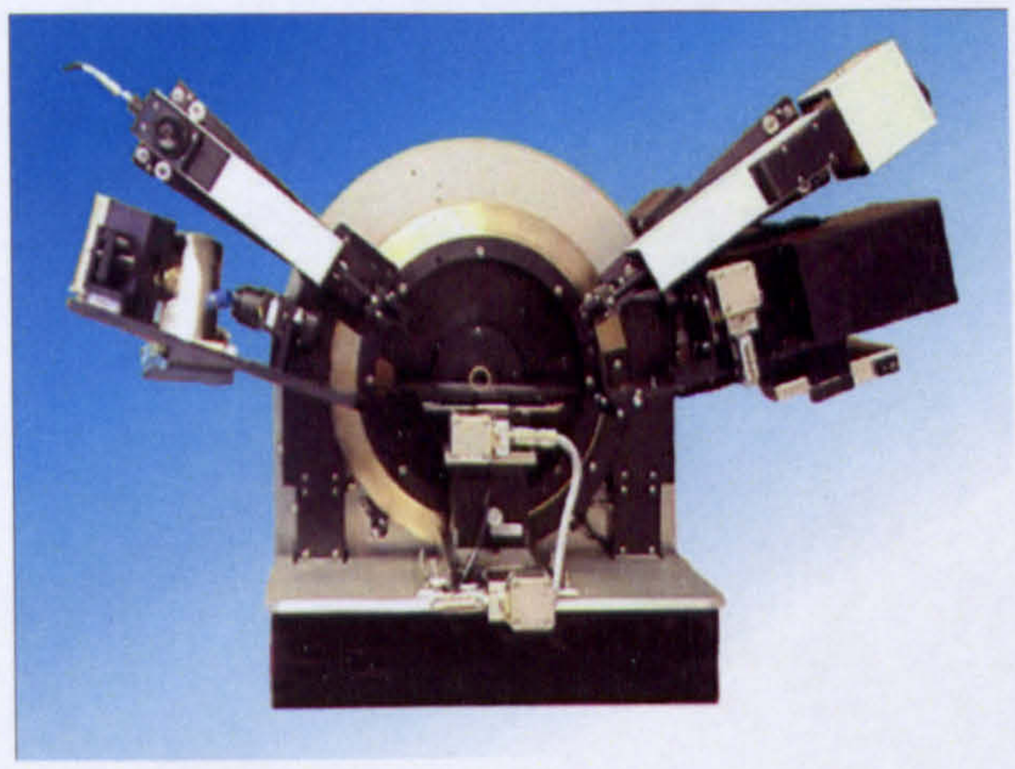

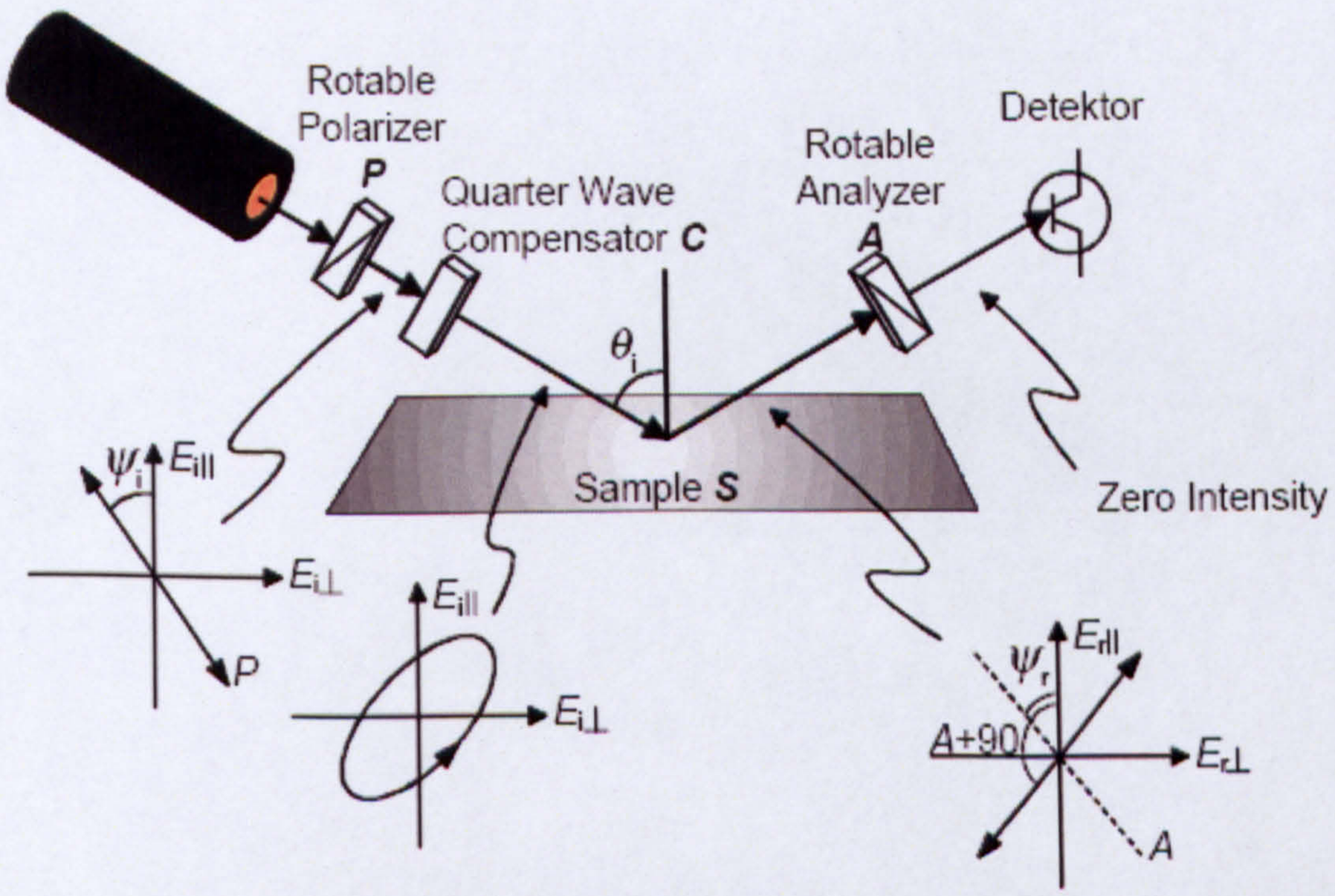

Figure 5.1: Picture of an IR Ellipsometer courtesy Sopra Inc. France, schematic representation of ellipsometer and state of polarisation of incident and reflected beam

Light Source:

The light source required by the ellipsometer can be either a laser or some type of lamp. Ellipsometers that use a laser have the advantage of having a very intense and collimated light beam that allows for a very small spot size. However, the laser light provides just one wavelength whereas spectroscopic ellipsometry (as used for the experiments in the thesis) requires a broad spectrum. This is achieved by using lamps as light source that provide a broad spectrum of wavelengths, most often these being deuterium, halogen, quartz tungsten halogen lamps.

Polariser/analyser:

The most important optical element for making ellipsometric measurements is the polariser. A polariser converts any light beam into linearly polarised light oriented with respect to the transmitting axis. Nearly ideal optical polarisers are commercially available, but must be matched to the wavelength range of the spectroscopic ellipsometer. An analyser detects and measures the polarisation of the beam reflected off the sample.

Compensator:

A compensator converts linearly polarised light to elliptical polarised light. An ideal compensator is an optical retarder that has a retardation of exactly 90° (or 1/4 wave). Retarders are useful but they can be difficult to work with because the exact retardation is a strong function of optical alignment and of the wavelength being used. A rotatable compensator combined with a rotatable polariser can convert unpolarised light into any elliptical polarisation.

The basic principle behind ellipsometry is simple. First, the polarisation state of incoming light is known and this incident light interacts with the sample and reflects from it. The interaction of the light with the sample causes a linear to elliptical polarisation change in the light. This change in the polarisation is then measured by analysing the light from reflected sample. Ellipsometer directly measures two values, ψ and Δ (angles of polariser and analyser), that describe this polarisation change. These values are related to the ratio ρ of Fresnel reflection coefficients, $E_{\parallel}$ and $E_{\perp\square}$ for electric field parallel to the plane of incidence and perpendicular to the plane of incidence respectively, as is shown by equation 5.1 [5.1]. These two values by

themselves are not very useful in characterising a sample but to know parameters like film thickness, optical constants, refractive index, the measured values, ψ and Δ, are used in a complex model with specific equations and algorithms to produce a result that describes the interaction of light with the sample. These two angles provide a measure of the amplitude ratio and the phase difference between the two components of light upon reflection.

So basically ellipsometry gives two angles ψ and Δ

$$\rho = \frac{E_{\perp}}{E_{\mathrm{II}}} = e^{i\Delta}(\tan\Psi) \qquad (5.1)$$

5.3.2 Ellipsometry data for Arlon

While a number of different ellipsometry methods exist for obtaining ψ and Δ, the most common are the nulling, rotating analyser/polariser methods [5.1]. Measurements by an automatic ellipsometer were introduced with the advent of the computers. The model used in the experiments is an example of a rotating polariser ellipsometer. The orientation of the polariser and of the analyser allows one to obtain the ellipsometric parameters of the sample ψ and Δ respectively. An ellipsometer is primarily used to measure film thickness and optical constants n, k where n is the refractive index of a sample that gives the propagation of the speed of the wave through the sample, and k is the extinction coefficient that relates energy of the wave absorbed in a material. For example, measurements of Arlon material (detailed discussion of material given in chapter 2) were made by the GES5-FTIR Sopra ellipsometer and are shown in Figure 5.2. The intensity of light absorbed by the sample can be determined from the plot of extinction coefficient k and Beer's law shows the exponential decay relationship, from where the absorption coefficient α can be determined:

$$I = I_0 e^{-\alpha z} \qquad (5.2)$$

$$\alpha = \frac{4\pi k}{\lambda} \qquad (5.3)$$

where, I is the light intensity absorbed by material, I_o is the initial light intensity, z is the propagation depth, λ is the wavelength of light. Using equation 5.3, a plot of

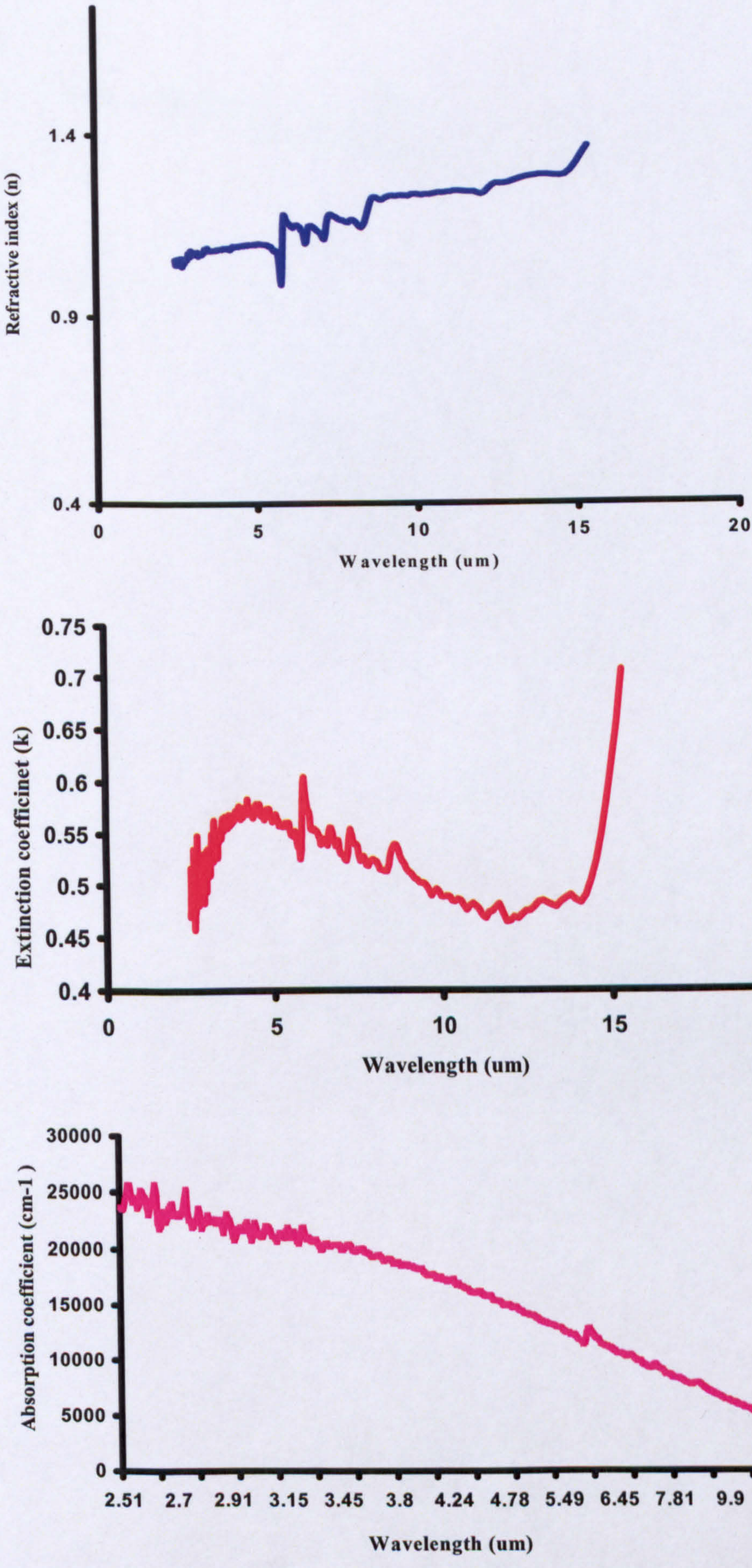

Figure 5.2: Plots of refractive index (n) and extinction coefficient (k) versus wavelength obtained from ellipsometer for arlon and plot of absorption coefficient (α) calculated using equation 5.3.

absorption coefficient is determined for the same material, which readily provides the information on the variation of absorption with wavelengths in the material. The same procedure is repeated to obtain the absorption spectrum for all the materials investigated in the thesis.

5.3.3 Issues with Ellipsometry data

The main objective of the ellipsometer experiments was to select the wavelengths, which are highly absorbed by the materials under study and where little or no reflection takes place at the surface of the material. This will consequently enable the selection of the wavelengths that require less fluence to ablate materials. The wavelength is selected by taking a room temperature absorption spectrum of material and then selecting the lines where the absorption values peak. For example, Figure 5.3 is an IR spectrum of 5.3μm thick polyimide reported by Brannon and Lankard [5.2] demonstrating significant absorption in mid IR region. High absorption is observed in 9μm and 10μm emission band hence selected wavelengths are 9.24μm and 10.6μm that are highly absorbed in the material.

It is important to mention here that there are issues related to the reliability of data measurement with the IR ellipsometer. These issues are mainly due to reflection and transmission of light in the material. The problem encountered is lack of significant absorption peaks in absorption spectrum of materials, as will be seen later in the chapter. Also this problem relates to the roughness of the surface, reflection and transmission issues such as interference fringes, conical illumination and light dispersion effects that add to the errors in measured data. Other contributing factors are the spatial homogeneity of the investigated material over its area, for example arlon has aramid fibres and FR4 has soda lime glass fibers which may add to the reflection and transmission of the probe light that is collected to obtain data of absorption in the material. More ellipsometer data for the materials investigated will be presented later in chapter. Adding to the problem is the characteristic variation of absorption in the material with temperature. This may result in the shift of spectral absorption of the material when it changes phase due to ablation. This statement is very well applied for any material in general since the change in absorption with change in phase of material essentially throws into question the accuracy and reliability of room temperature spectral absorptivity of materials for experiments involving ablation. However, the spectrum obtained from the IR ellipsometer and

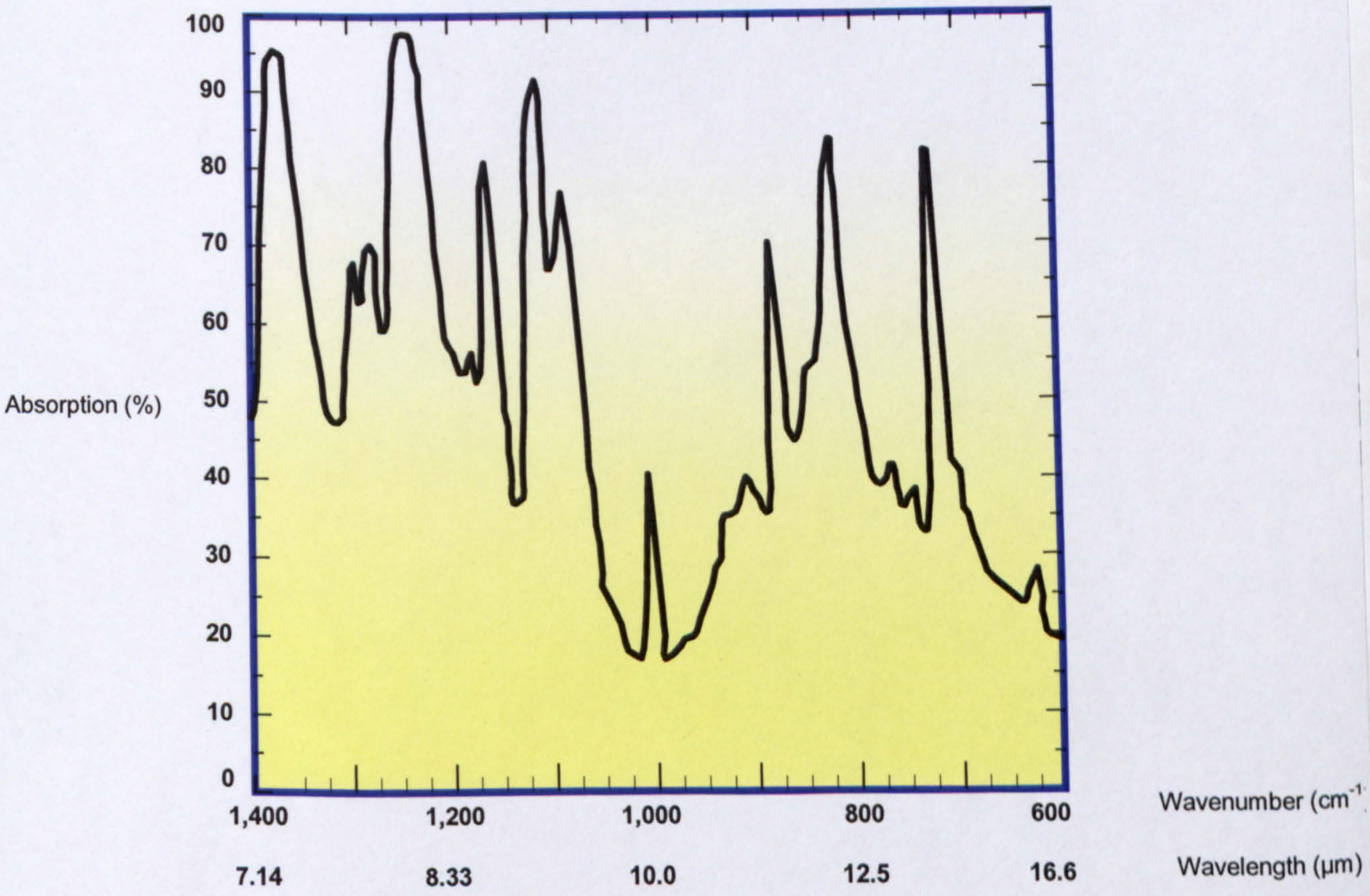

Fig 5.3: Spectral Absorption of Polyimide 5.3µm thick, a reference spectrum courtesy Brannon and Lankard, [5.2]

from other sources may be used as reference, which may provide information on the *approximate* range of wavelengths where absorption is high for a given material.

The solution to the problem of relative unreliability of room temperature spectral absorptivity data is to obtain the spectra of the materials directly when the material is undergoing phase change due to ablation. To do this, the experiments in the thesis are designed such that the so-called 'Ablation Spectrum' of each material is obtained. The significant advantage of using an ablation spectrum is its reliability in demonstrating the optimum laser line absorbed by the material and at not only threshold of ablation but also when the temperature increases and the hole of definite depth is drilled in material. This can be found by plotting ablation rates at constant power and varying pulse width to provide varying pulse energy as a function of wavelength. The ablation rate is then plotted as varying fluence against hole depth. The fluence can be varied by varying either power or pulse widths. However, the range of power values available with this workstation was limited so, pulse energy values were varied by changing the pulse duration. We have chosen to keep peak power constant and vary axial fluence by varying pulse widths because the machining system has a limit to the maximum emitted peak power.

It is also essential to use a combination of acceptable spot size-pulse widths and melt threshold in the material. Melt threshold is predicted using equation 3.15 of Chapter 3 for each material. An example is shown in Figure 5.4, where it is calculated that for pulse widths, less than 100μs with a spot size of 90μm the corresponding fluence is effective to ablate resin to be less than melt threshold region at absorption coefficient of 11.5×10^3 cm^{-1}. The wavelength that requires least fluence in ablating a hole in material will be the choice of wavelength to machine the material. The ablation spectrum may provide the information of parameters like fluence, power, pulse length required to ablate the material and to drill a hole of 30μm depth in the material. This approach may aid in understanding of the machining regime and mechanism dominating the ablation phenomenon hence, a well-informed decision can be made in selecting optimum laser parameters to effectively machine the material.

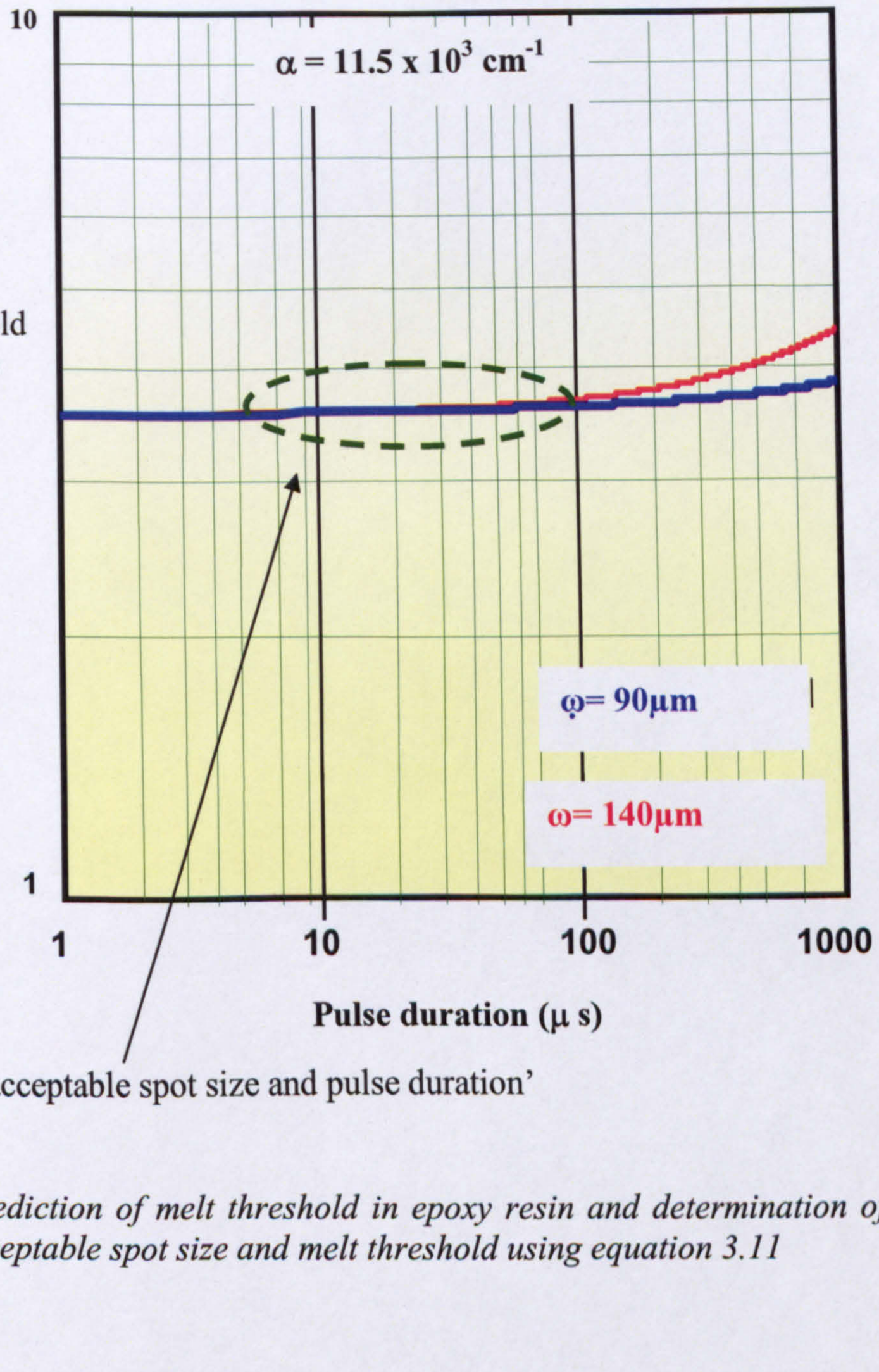

Fig 5.4: Prediction of melt threshold in epoxy resin and determination of region of acceptable spot size and melt threshold using equation 3.11

5.4 Drilling of Kapton

Initial Observation

a) Region below threshold $F \leq F_{th}$

The fluence required to remain in the region below machining threshold of Kapton is measured to be below 4J/cm^2 in the 9μm band and 1J/cm^2 in the 10μm band. It is observed that within the range of fluence below machining threshold there is visible surface damage on the Kapton surface. The SEM analysis of the Kapton surface irradiated with fluence in this region shows volume increase or swelling of the surface. The surface swell shows bubbles of varied sizes that ranged from 3 to 8μm in diameter. Figure 5.5(a) illustrates the sequence of the sub-threshold phenomenon of boiling/foaming in Kapton. Further increasing the fluence by the order of a few millijoules increases the size of the elevated surface. At this stage, the bubbles disappeared and the elevated surface grows homogeneously appearing more like a nucleated blister. Depending on the wavelength, this nucleated blister is seen to rise to a height of 10 - 20μm. This is the first report of bubbling and foaming of Kapton HN film at sub-threshold region ablated by CO_2 laser wavelengths with microsecond pulses. Bauerle et al reported an increase in volume below threshold in UV pulsed laser ablation in Kapton at 302nm wavelength and pulse durations of 140ns to 5μs [5.3, 5.4]. Similarly, Dyer et al [5.5] also reported of the phenomenon with randomly spaced holes at the irradiated site in Upilex Polyimide ablated with TEA CO_2 of pulse lengths of 100ns and at laser wavelength 10.24μm. It is suggested that the cause of swelling is due to gaseous products driven to the surface from the bulk of the material hence increasing the volume. Hence, the phenomenon can be explained as when the Gaussian beam irradiates the surface, due to low heat conduction, the energy absorbed causes the deeper layers of the film to expand faster than the top layers of the film since the top layers cools easily. The thermal energy inside the deeper layers melts or decomposes the material due to strong absorption. The melt depth is estimated to be of the order of optical penetration depth. The decomposition of material releases trapped gases that create the pressure underneath the top layer/s, hence raising the surface of Kapton film. R. Srinivasan et al [5.6] have also reported the phenomenon of release of gases in Kapton due to thermal decomposition.

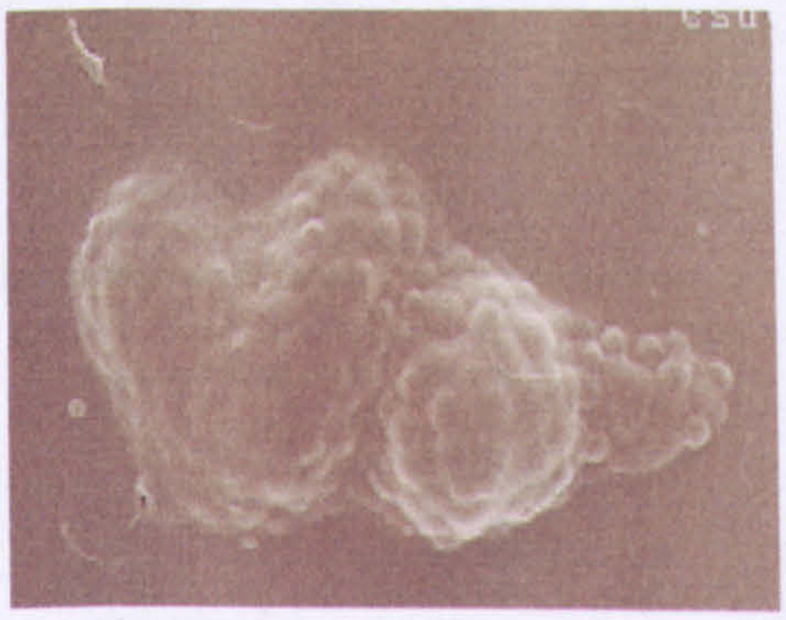

Foaming/boiling of surface

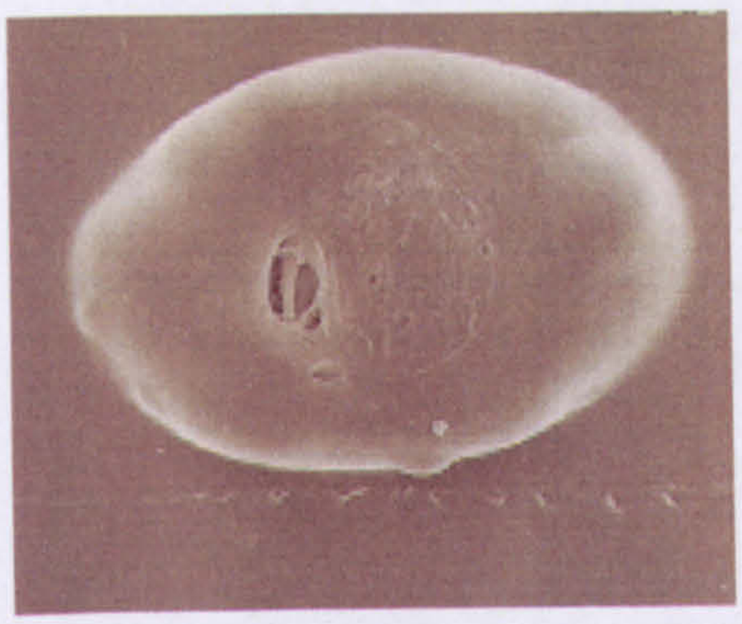

Elevation of surface

(a) Sub threshold fluence range - $F < F_{th}$

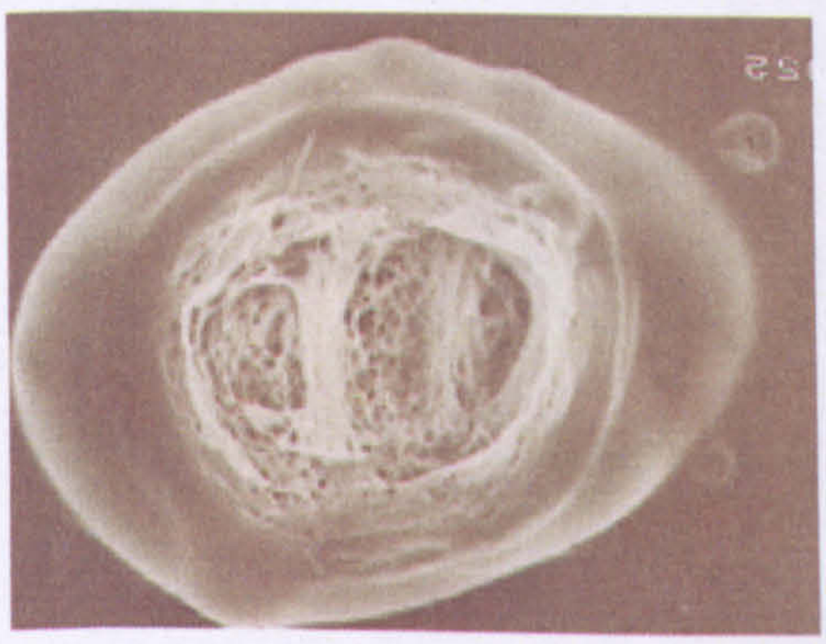

Ruptured cover of elevated surface exposing fibre mesh at bottom – true ablation threshold

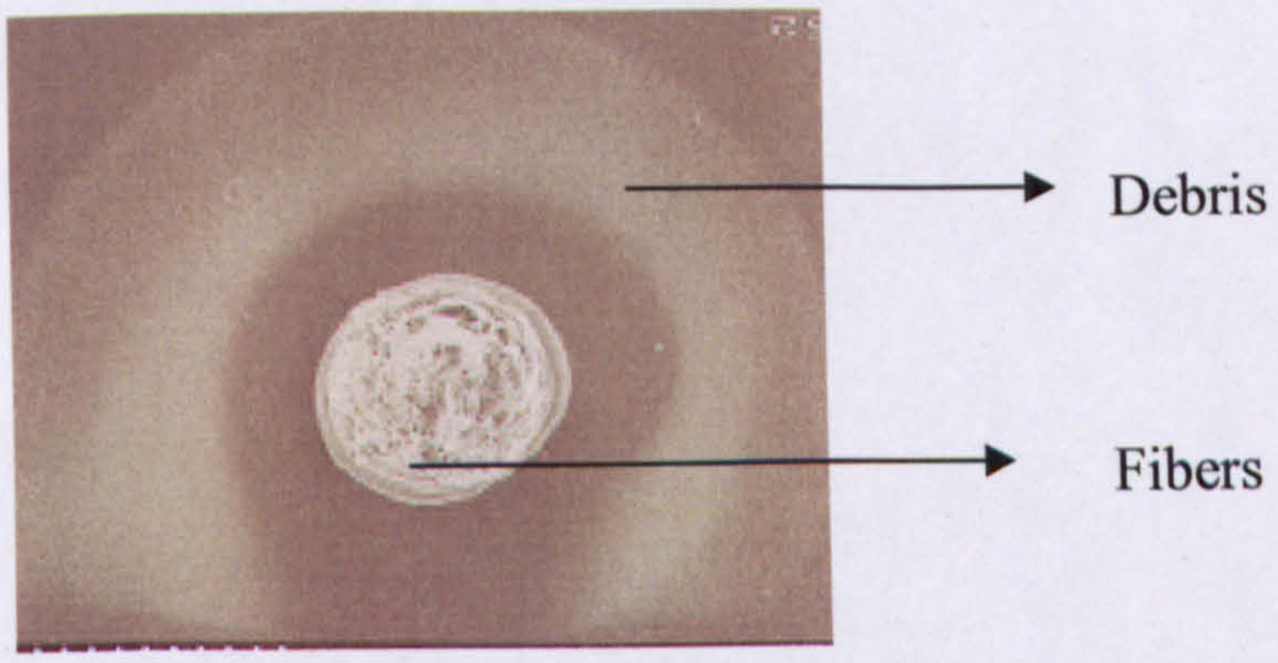

Fibers protruding out of crater, scattered powdered debris – apparent machining threshold

(b) At ablation threshold – $F = F_{th}$

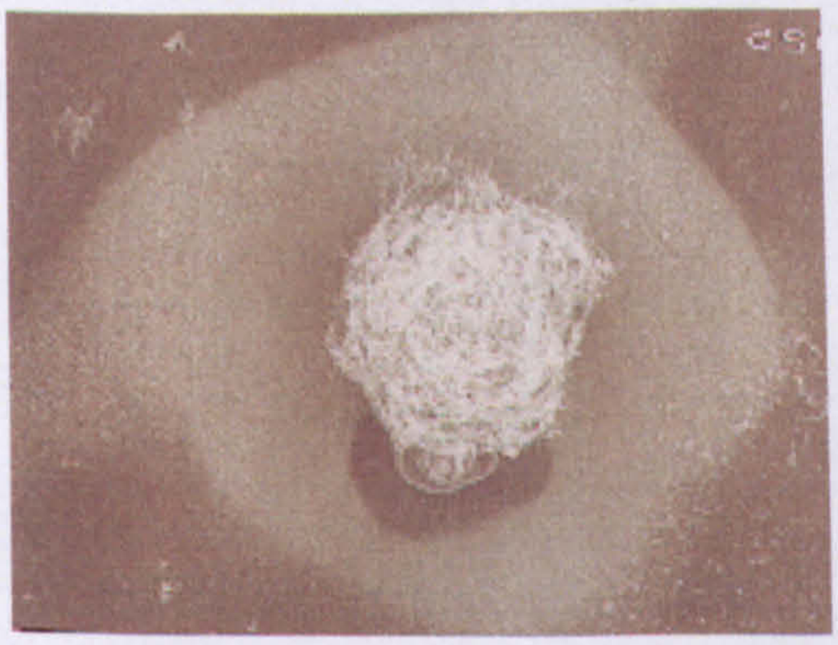

(c) Above ablation threshold - $F > F_{th}$

Figure 5.5: Ablation of Kapton at 10.24μm wavelength (a) In sub threshold regime (b) at threshold, (c) above threshold (pictures not to scale)

b) Region at threshold $F = F_{th}$

According to Bauerle et al [5.4], a material reaches the ablation/machining threshold when the least required fluence causes a dip in the elevated surface / hump as illustrated in Figure 5.6. Following this definition, the sequence of events towards attaining the machining threshold in Kapton is illustrated in Figure 5.6. This sequence of ablation events mirrors the sequence in Figures 5.5(b) and 5.6 (b), which illustrates the actual events near threshold. It is observed that Kapton attains machining threshold when the fluence is high enough to rupture the top layer or film that exposes a fibrous mesh in the volume or where a dip is created in the hump. However, this stage is very difficult to observe or measure and it is not possible to find the mass loss at this stage to establish an ablation or machining threshold. Therefore, to measure the depth of holes, it is required to clean the machined Kapton film ultrasonically in a water bath or by smearing the surface using an acetone soaked Q-tip to clear the decomposed material in and around the holes. The depth of these clean holes is measured to establish an 'apparent'machining threshold and the respective fluence values are presented as threshold fluences. This method is practiced because at the stage where a dip appears in the hump, axial fluence ruptures the film in the centre of the elevated surface as is shown in Figure 5.5 (b) where it just exposes the fibrous mesh. The top film is still tightly intact with the surface and does not clean off with either of the cleaning procedures. Further increasing the fluence by the order of few millijoules from this stage of making dip in hump, the top film melts off and the decomposed fibrous mesh increase in density and erupts out of the machined hole perhaps similar to a volcanic eruption. Increase in fluence raises the pressure under the fibre mesh hence breaking and further erupting the fibres out of the walls of the holes. A powdered debris/soot is seen scattered round the periphery of the holes at this stage. The difference in magnitude of the fluence between the region below threshold and attaining apparent machining threshold is of the order of tens of millijoules. Yet again, this phenomenon of film rupture and the fibre eruption is observed at all wavelengths at threshold fluences. The values of apparent machining threshold fluence measured for the 9 and 10 μm emission band is listed in Tables 5.1 and 5.2. This is believed to be the first report of machining threshold values of Kapton at different wavelengths and varying pulse widths.

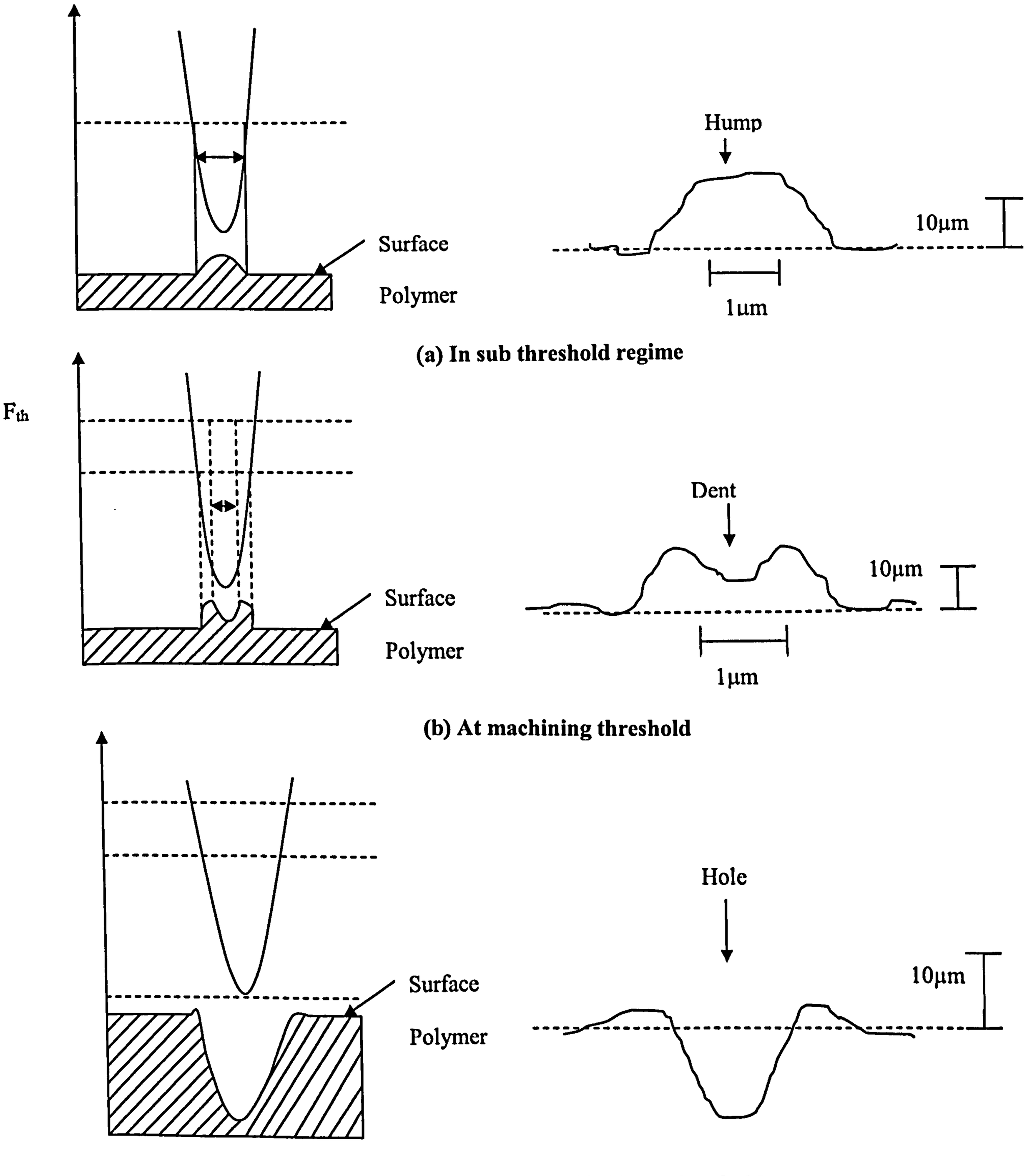

Figure 5.6: A typical sequence of hole machining in kapton at all investigated wavelengths (a) In sub threshold regime (b) at threshold, (c) above threshold

Lowest ablation fluence threshold is observed at 9.27 μm, which is 4.2 J/cm^2, and in 10.24 μm as 1.3 J/cm^2. Wavelength 10.24μm agrees well with absorption spectrum of Kapton at room temperature, illustrated in Figure 5.10, though this is not the case with the value of 9.27μm. The measured value of threshold fluence at 10.6μm is 1.5 J/cm^2, which agrees well with the reported value by Brannon et al [5.2] yet again, it is not the highly-absorbed wavelength in the room temperature absorption spectrum.

c) Region above threshold $F > F_{th}$

Figures 5.7 and 5.8, present the ablation rates for Kapton as a function of the selected wavelengths in the 9 and 10μm IR spectrum. At fluences, higher than the reported machining thresholds, the depth and the diameter of the ablated hole (which becomes spot size limited) increases linearly with fluence. The melt depth is seen to be approximately proportional to the penetration depth in this region. Heat conducts only after an increase in the pulse duration from 50μs and above. Hence, this is a good parameter choice for Kapton ablation. It is also observed that the increase in fluence also increases the density and hence the length of the fibers protruding out of the holes. Close examination of the fibers with SEM shows that the fibers are approximately of 100nm size at fluence 30J/cm^2. There is also an increase in the scattered debris or soot scattered radially around the hole. Zeng et al [5.7] reported an XPS investigation of the decomposition of Kapton with UV laser irradiation where the fibres and solid debris erupted during ablation of Kapton and is suggested due to material charring due to pyrolysis and combusted due to photo thermal ablation. The rapid rise of temperature at the ablation site with fluence possibly decomposes the Kapton and this mechanism release the oxygen and nitrogen gases or volatile species. This explanation also supports the pressure built up under the surface due to these gases, which elevates the surface in region under threshold fluence. The fibre bundles consist mainly of carbon [5.7]. It is suggested that the photo thermal decomposition of Kapton is observed to be enhanced linearly with the increase in fluence. The length of fibres increases on an average of 10μm with the increase of 10μs pulse length. The fibres are observed to be longer in length at rim of hole than in centre of hole. This suggests that the central rise in temperature due to axial fluence further decomposes

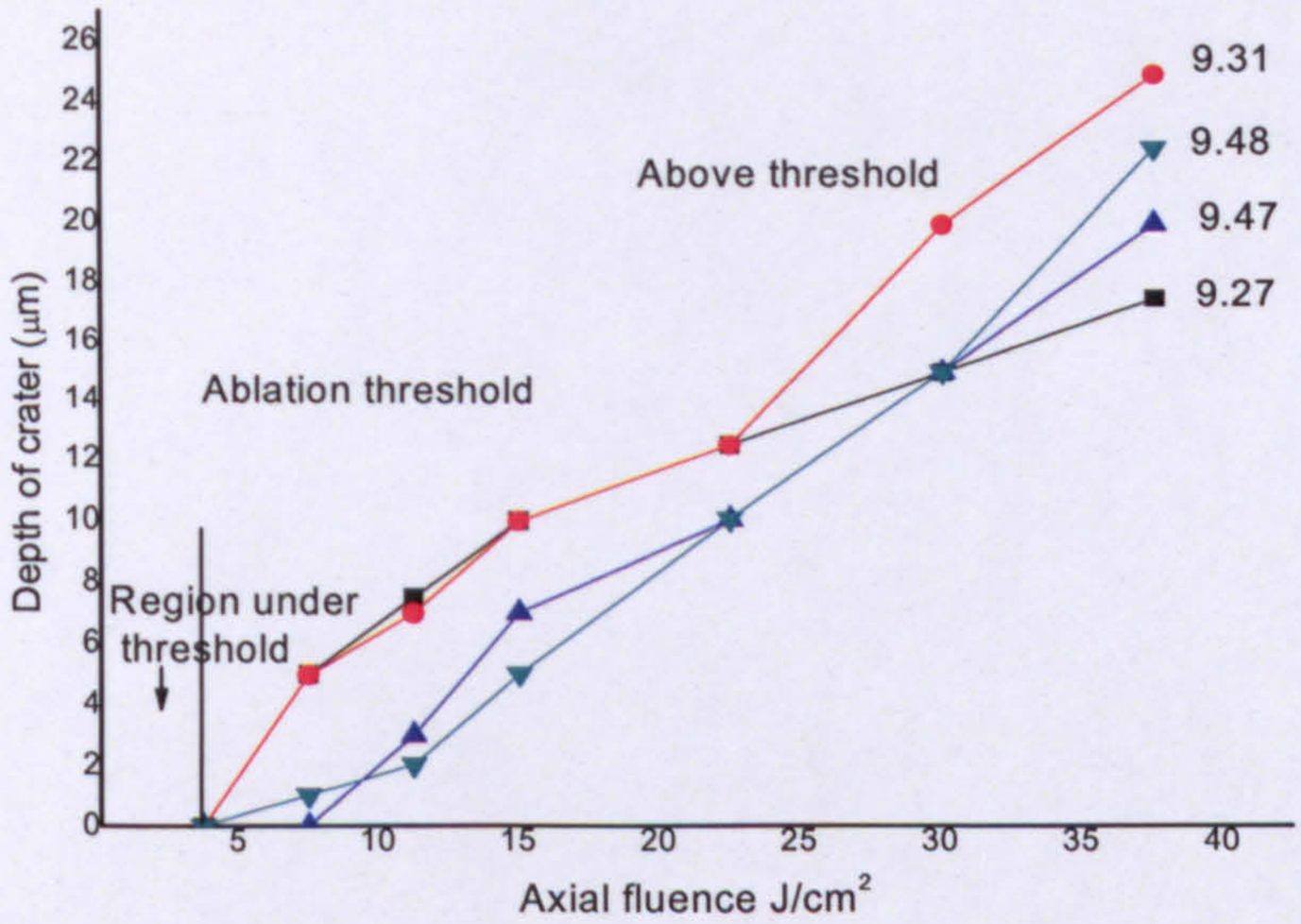

Fig 5.7: Ablation curves of Kapton in 9 μm IR band

	Wavelength (μm)	Threshold Fluence (J/cm^2)
1	9.27	4.2
2	9.31	6.5
3	9.47	9
4	9.48	10.2

Table 5.1: Threshold fluence measured at peak lines in 9μm emission band for Kapton

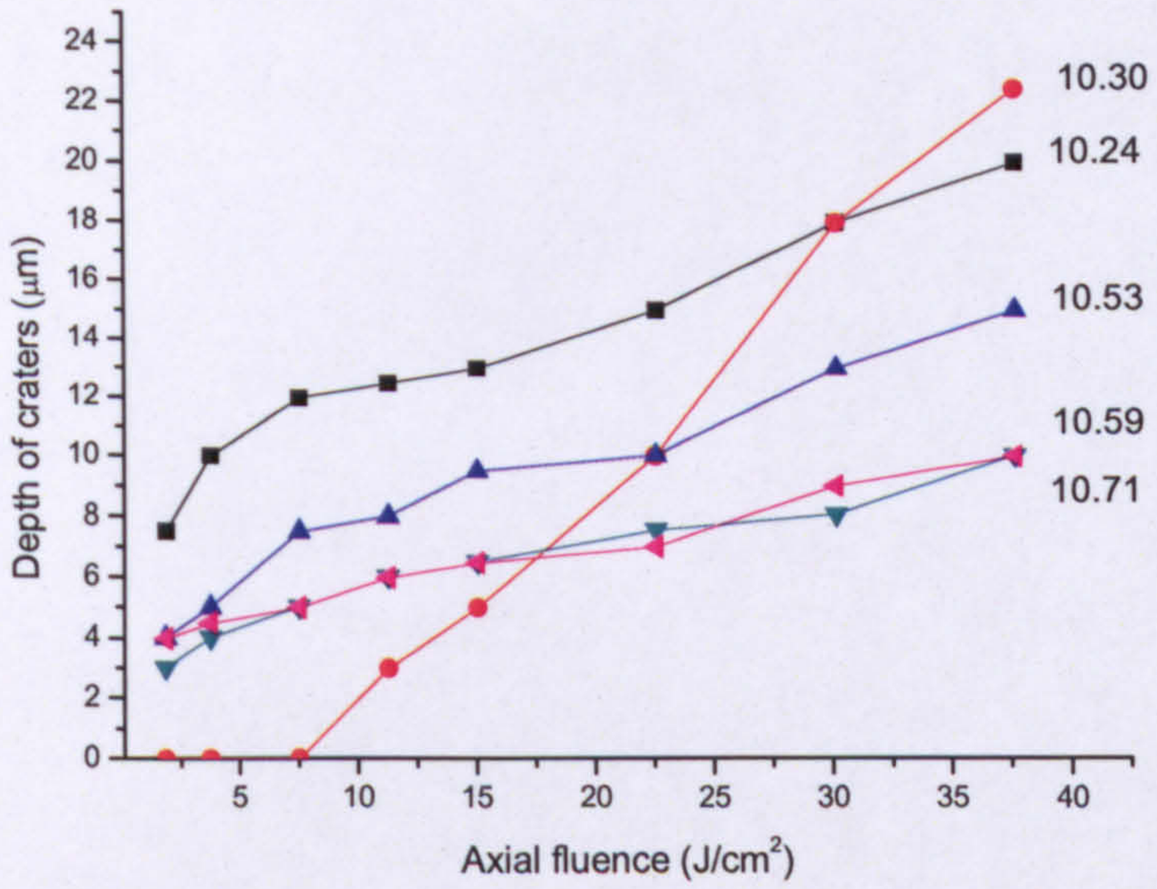

Fig 5.8: Ablation curves of Kapton in 10μm emission band

	Wavelength (μm)	Threshold Fluence (J/cm^2)
1	10.24	1.3
2	10.30	8.6
3	10.53	2
4	10.59	1.5
5	10.71	2.5

Table 5.2: Threshold fluence measured at peak lines in 10μm emission band for Kapton

the fibres and ablates off as nano particles and deposits around the hole radially. The measurement of fibres was recorded using SEM (Scanning Electron Microscopy).

A set of experiments was performed to laser clean the holes by applying multiple shots of constant pulse widths and fluence. Another 2-4 shot of constant fluence at the already single shot ablated hole does not make an apparent effect on the fibres. Another 5-10 shot burns the fibres off in the centre of the holes however the fibres are still intact on the rim of the holes. Multiple shots (~20) creates ripples on the surface of the Kapton and soot is redeposit around the periphery as far as 200μm. Bo Gu et al [5.8] also reported laser cleaning of Kapton with multiple pulses at IR wavelengths in an oxygen gas environment. The advantage of using an atmosphere of pure oxygen is that it causes blackening of the fibrous material, which is reported to be readily oxidised and removed during multiple laser pulse shots.

5.4.1 Comparison of ablation and absorption spectra

Figure 5.9 presents the ablation spectrum of Kapton, which demonstrates the following:

(1) Values of fluence required to attain a machining threshold

(2) Values of fluence required to drill a hole of 30μm depth at each selected wavelength.

Figure 5.10 shows the absorption spectrum of Kapton at room temperature, obtained from the ellipsometer data. Comparing both spectra leads to following conclusions:

1 In 10μm emission band, 10.24μm requires lowest fluence to attain ablation threshold and to drill 30μm deep crater. Absorption spectrum also showed the highest absorption coefficient for 10.24μm where $\alpha = 5.93 \times 10^4$ cm^{-1} hence both the spectra agree well for the 'optimum' wavelength.

2 Wavelength 10.30μm has fairly high absorption ($\alpha = 5.6 \times 10^4$ cm^{-1}) yet requires highest fluence to reach ablation threshold ($F_{th} = 8.6$ J/cm^2) and to drill 30μm deep crater as compared to all other peak lines in 10μm band. This

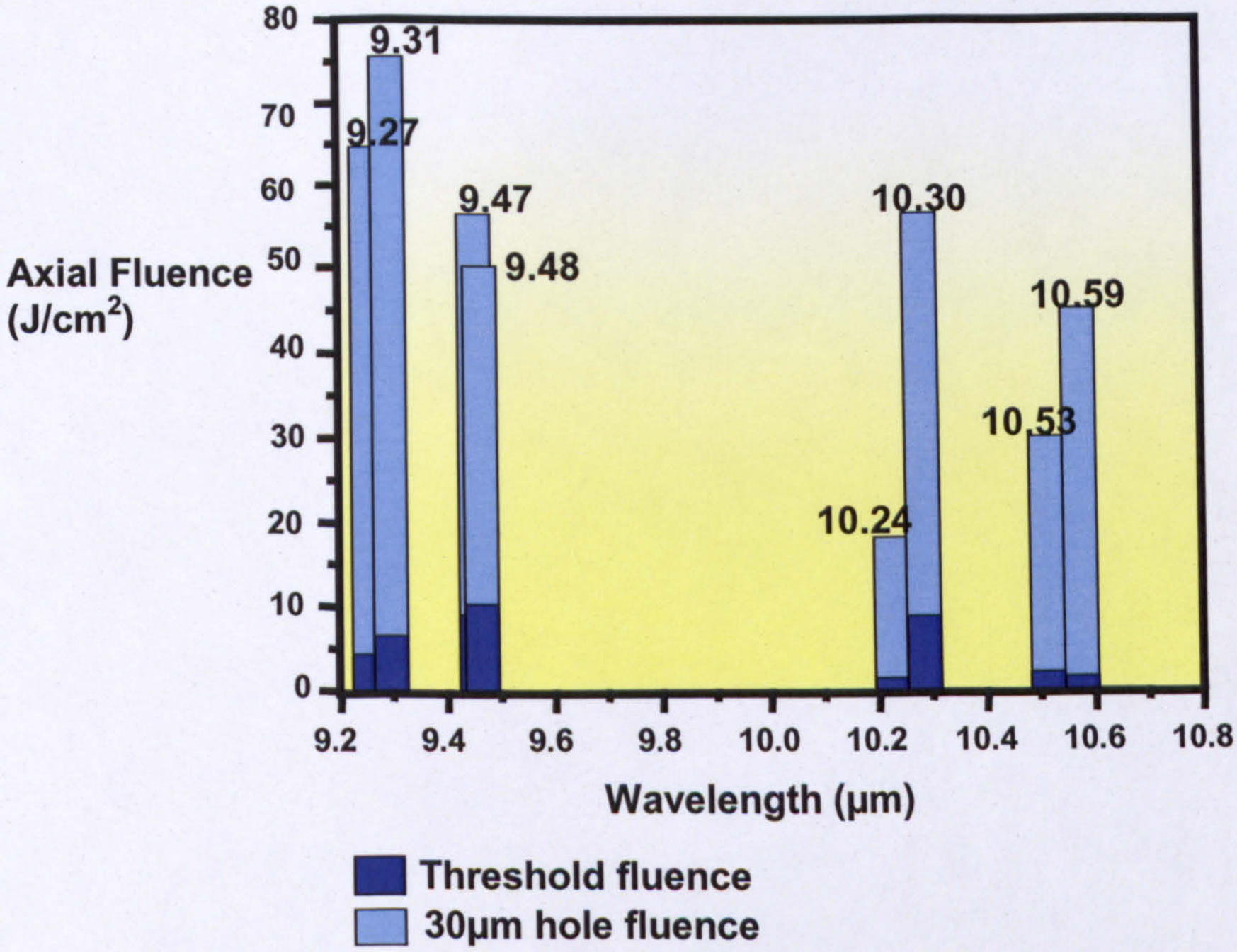

Fig 5.9: Ablation spectrum of Kapton

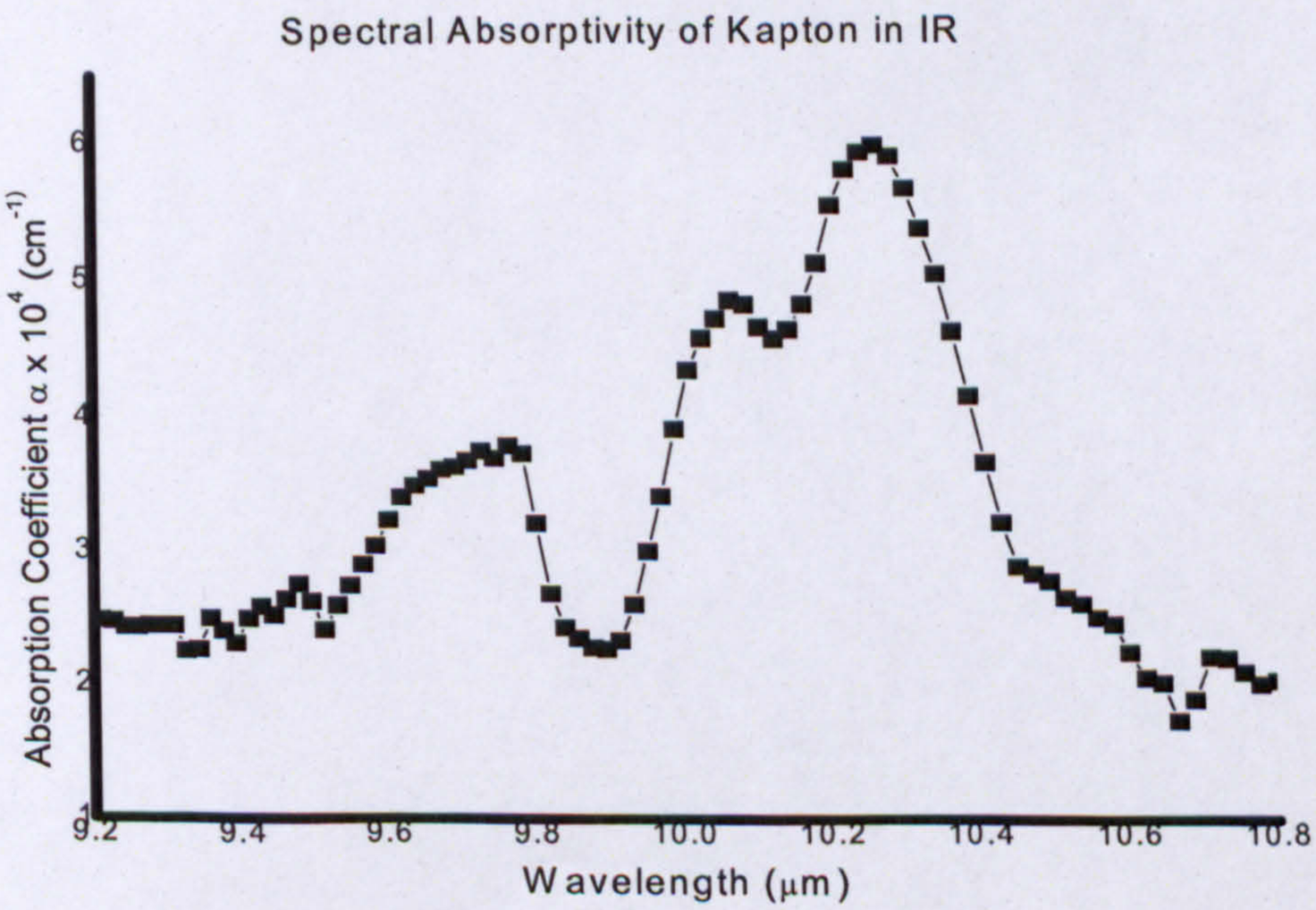

Figure 5.10: Absorption spectrum of Kapton

disparity is not well understood but it could be an example where absorption coefficient may change at higher temperatures.

3 In 9μm emission band, the emission line 9.47μm ($\alpha = 2.75 \times 10^4$ cm^{-1}) is absorbed more than 9.27μm ($\alpha = 2.44 \times 10^4$ cm^{-1}). However, the threshold fluence measured for 9.27μm is $F_{th} = 4.2$ J/cm^2 that is lower than $F_{th} = 9$ J/cm^2 measured for 9.47μm hence suggesting the variation of absorption coefficient with temperature at these peak lines as well.

It is observed that no selected wavelengths were able to machine Kapton with clean holes. The holes were full of fibrous debris and soot scattered around the periphery of the holes. Kapton surface needed post cleaning prior taking measurements for generating ablation curves. It would be a fair statement that IR wavelengths may not be the best to machine Kapton. This is also supported by industrial evidence where microvias in Kapton are ablated using UV lasers due to cleaner hole quality. However, due to economical reasons, wavelengths 10.6 and 9.30μm have been increasingly popular in Microvia drilling in Kapton but using an assist gas in order to help remove ablated material from the hole site.

5.5 Drilling of RCC

Initial Observations

a) Region below Ablation Threshold $F \leq F_{th}$

With the application of axial fluence, less than the fluence required for achieving threshold of ablation ($F \leq F_{th,}$) on the RCC sample, irreversible damage or the onset of marking threshold due to melting is observed. The range of fluence to achieve this effect is less than 1J/cm^2 in the 9μm emission band and less than 5 J/cm^2 in 10μm emission band. However, for this range of fluence values there is no hole formation that could be characterised or measured.

It is known that the thermal decomposition and removal temperature of resin is 671 °C [5.9, 5.10]. It is calculated (using equation 3.11 and using the value of density from Chapter 2), that the temperature rise at the fluence values in the region below

threshold is approximately 150 °C hence confirming the absence of thermal decomposition and removal of resin surface yet at these low fluence values.

b) The threshold fluence ($F=F_{th}$):

As the fluence is increased, the rate of energy deposition in the thin surface exceeds the rate of heat dissipation that occurs due to thermal diffusion and radiation. The temperature increase is calculated to be approximately 680 °C at the point where the resin decomposes and particles and gaseous products leave the surface hence contributing to measurable mass loss. This is where the ablation threshold is attained. The value of fluence required to attain ablation threshold in resin at selected wavelengths in 9-10μm band is listed in Tables 5.3 and 5.4 respectively. These results are discussed later.

c) Interaction above threshold ($F>F_{th}$):

Further increase in fluence above ablation threshold value gives rise to a further increase in temperature in the irradiated area of the resin sample. The temperature calculated at the fluence value is 800 °C, which is higher than the decomposition of resin and removes the material. At this high temperature, the molten resin evaporates and hence contributes in increasing the ablation rate. The depth of ablated holes is measured and plotted against the values of fluence as a function of wavelengths in each emission band to obtain ablation curves. These ablation curves are plotted in Figures 5.11 and 5.12.

In the 9 μm laser emission band, an interesting feature, which is observed during ablation of resin is the ejection of melted resin as solidified stems or fibres. This melt ejection is observed at all wavelengths in this band. At 9.27μm, the fibres are seen attached at a depth of 4-6μm in to the hole whereas at 9.47μm the longest melt ejected fibre is 337μm length and the roots are attached closer to the rim.

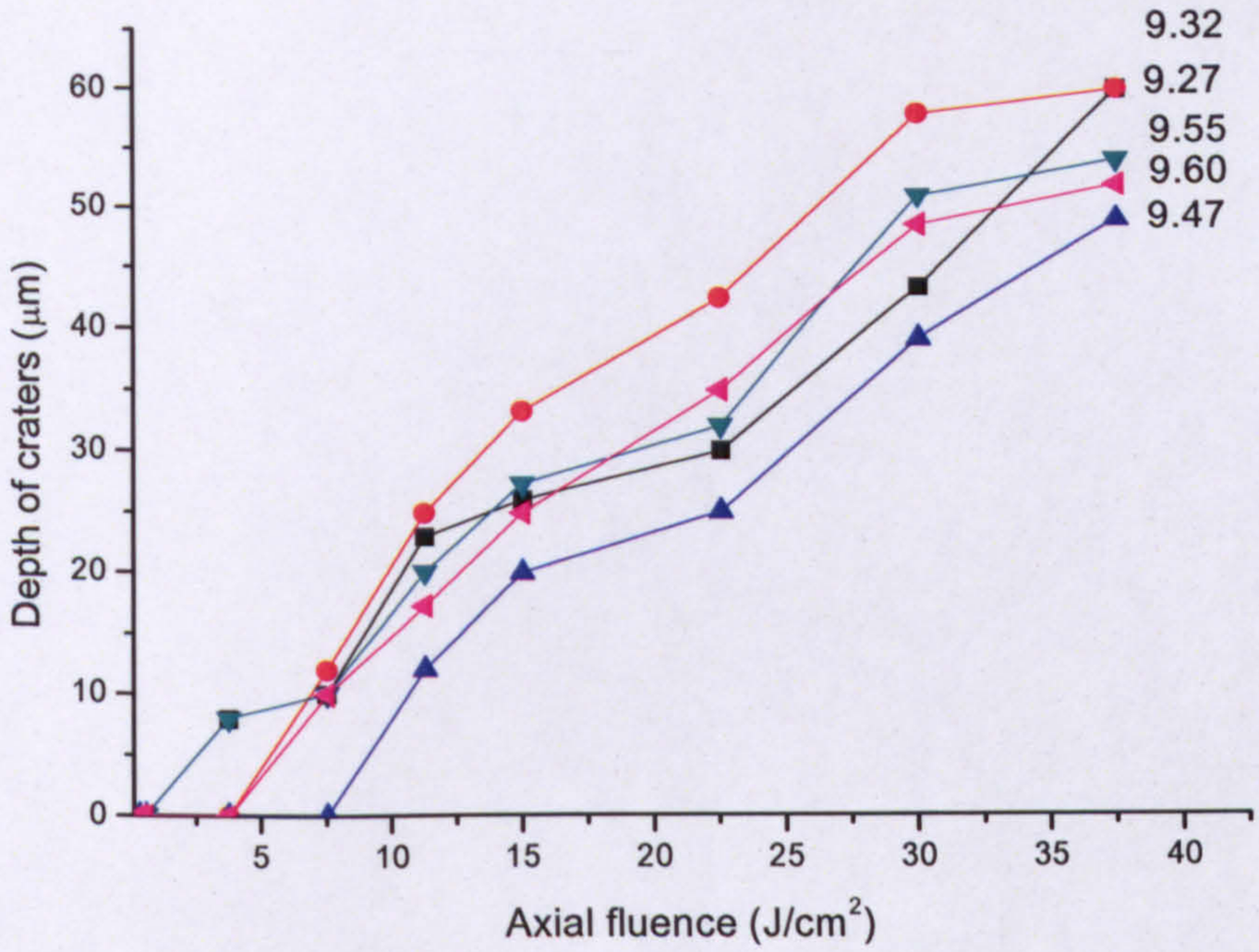

Figure 5.11: Ablation curves in the 9μm band peak lines in resin (RCC)

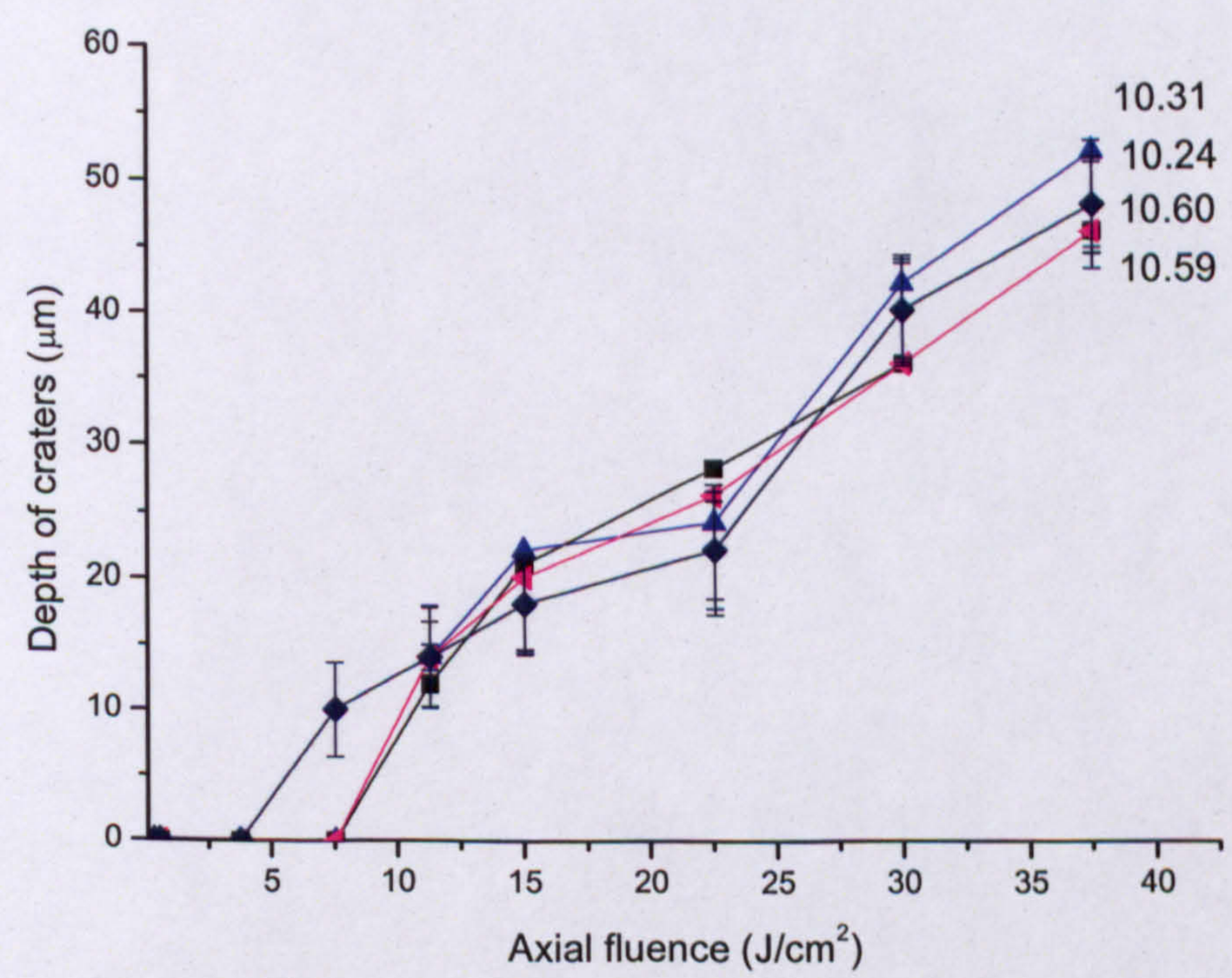

Figure 5.12: Ablation curves at peak lines in the 10μm band in resin (RCC)

	Wavelength (μm)	Threshold Fluence (J/cm^2)
1	9.27	4
2	9.32	2
3	9.47	6.5
4	9.55	6
5	9.60	3.9

Table 5.3 Threshold fluence at peak lines in 9μm band for resin.

	Wavelength (μm)	Threshold Fluence (J/cm^2)
1	10.24	6.2
2	10.31	5.3
3	10.59	7.2
4	10.60	5.8

Table 5.4: Threshold fluence at peak lines in 10μm band for resin.

At wavelengths of 9.55μm and 9.60μm, the fibres are deep rooted in the centre of the holes. This phenomenon is observed typically at the fluence range between 10.J/cm^2 to 35 J/cm^2 between the pulse widths of 30 and 100μs. Interestingly, it is observed that the length of the emitted solidified fibres increases for wavelengths with small absorption coefficient values. For example at 9.47μm (α = 0.94 x 10^3 cm^{-1}), the length of ejected fibres is measured to be as long as ~337μm compared to 9.60μm (α = 3.8 x 10^3 cm^{-1}) where the length of the fibres is 50μm.

In the 10μm the laser emission band, this feature is not observed with wavelengths 10.24 or 10.31μm but for wavelengths 10.59 and 10.60 μm ejected solidified fibres are observed for fluences between 13.8 and 17.29 J/cm^2. There appears to be no data published so far on melt displacement of resin as filaments/fibres as described here. Markillie et al [5.11] reported similar mechanism of fibre formation but in silica, at a given range of pulses and fluences conditions. According to the study, this phenomenon of melt displacement and cooling as solidified stem can be explained assuming that the melt pool at this irradiance level becomes viscous, highly mobile, permitting material removal by melt ejection.

Figure 5.13 (a) shows the fibres ablated at 10.59 μm at fluence 27.69J/cm^{2}and (b) shows the fibres emitted at wavelength 10.49μm at fluence 10.38 J/cm^2. Figure 5.13 (c) suggests the phenomena of creation of fibres during laser ablation of resin. The fibres do not stand erect at the rim of holes, as is the case in silica but lie horizontally on the surface of resin. The length of the fibres was measured using a microscope. The pictures of insitu fibres are not available since the fibres wear off due to movement of the ablated samples. As mentioned in Chapter 2, resin attains a glass transition temperature and changes the solid phase to glassy state corresponding to a hard, rubbery structure with increased polymer chain motion at high temperatures [5.11]. Figure 5.14 shows the typical holes ablated in resin at higher and at threshold fluence at wavelength 10.59μm. Resin retains heat in a small volume where irradiated, hence heat flow in resin is appropriately two dimensional above the threshold region. Though for increased fluence, resin absorbs heat to attain the temperature where it melts and ablation results due to recoil pressure of the molten or gaseous material that is evaporated pushing the resin from the centre of the hole and up the sidewalls. The decomposition of resin

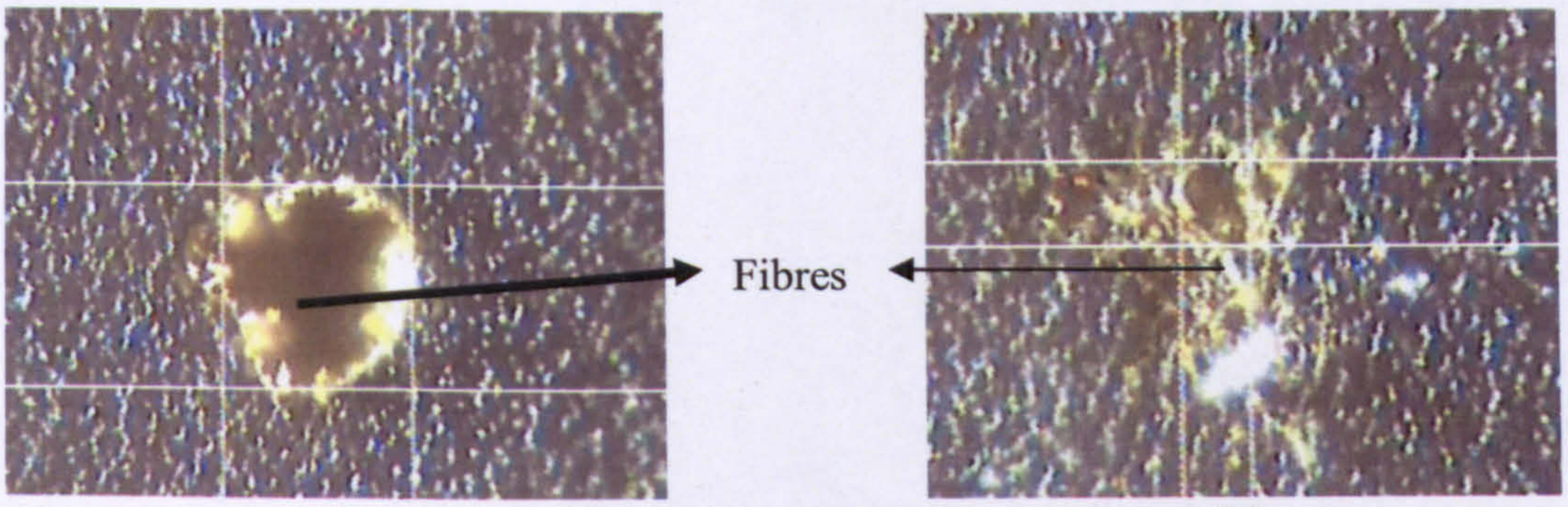

Figure 5.13: Melt ejection of resin as a solidified stem (a) λ - 10.59μm at pulse duration 80μs with axial fluence 27.69 J/cm^2(b) λ-10.49 at pulse duration 30μs with axial fluence 10.38 J/cm^2 (c) Fibre ejection phenomenon

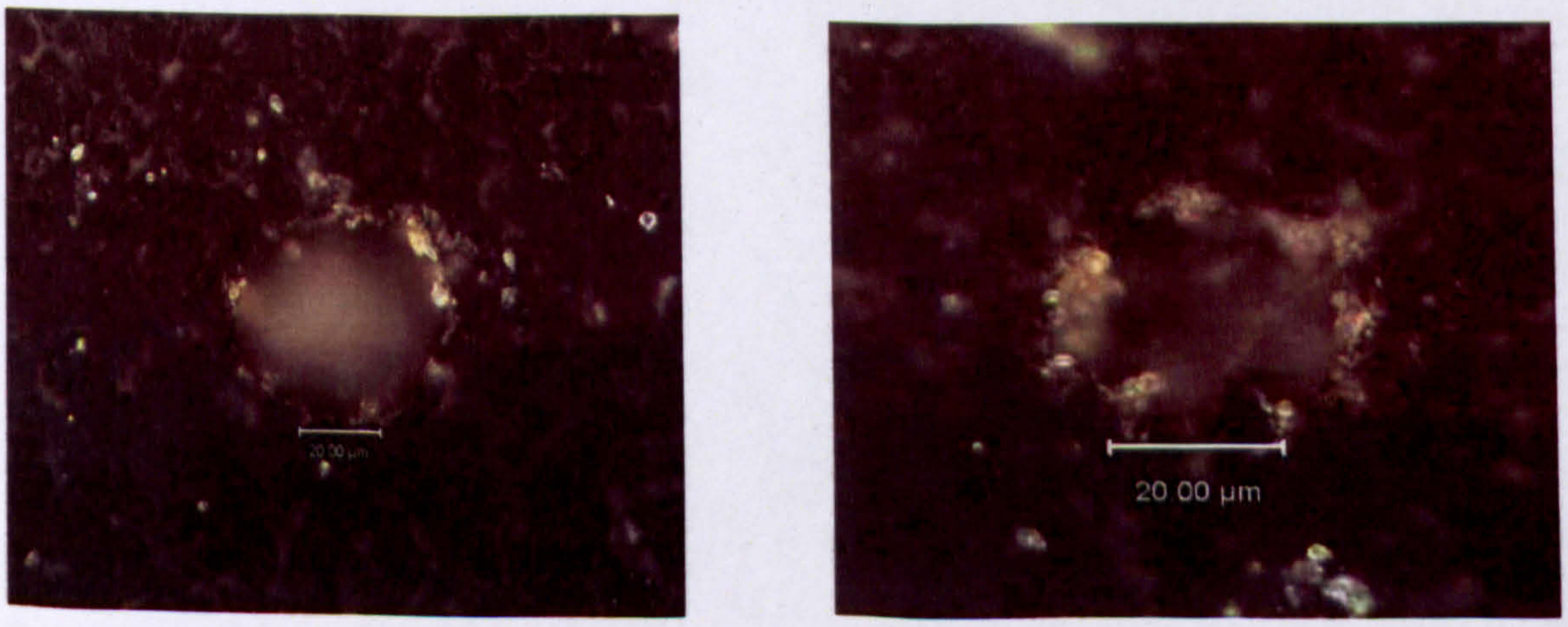

Typical ablated hole in resin

Typical hole ablated at threshold

Figure 5.14 Typical holes ablated in resin at higher fluence and at threshold fluence at constant conditions of spot size 90μm

may also release trapped gases that make an explosive escape from the surface hence leaving the rim of the hole unsymmetrical and ragged in shape.

5.5.1 Comparison of ablation and absorption spectra

Figure 5.15 shows the ablation spectrum for a proprietary resin (Company–DuPont Inc.). Figure 5.16 presents the absorption spectrum at room temperature of resin obtained from the Ellipsometer data. The comparison of the two spectra shows:

1 At a wavelength of 9.47μm the highest fluence is required to achieve ablation threshold but also to drill a hole of 30μm depth as compared to other selected lines in the emission band.

2 Wavelength 9.55μm requires lowest fluence to drill a hole of 30μm depth but requires higher fluence to achieve ablation threshold as compared to wavelength 9.32μm. Comparing the absorption coefficients from the absorption spectrum in Figure 5.16 for wavelengths 9.47 ($\alpha = 2.94 \times 10^3$ cm^{-1}), 9.55 ($\alpha = 2.32 \times 10^3$ cm^{-1}) and 9.32μm ($\alpha = 2.99 \times 10^3$ cm^{-1}), there is no significant difference in the values of the absorption coefficient at each wavelength. However, the ablation spectrum clearly suggests 9.55μm as the optimum wavelength for drilling holes in resin. This suggests that absorption coefficient alone is inadequate to determine the optimum wavelength for machining the sample.

3 In the 10 μm emission band, use of the wavelength 10.59μm ($\alpha = 2.8 \times 10^3$ cm^{-1}) requires the lowest fluence to achieve the ablation threshold but requires higher fluence to drill a 30μm deep hole as compared to the other selected wavelengths. This suggests that the temperature dependent factors of absorption coefficient play a significant role in efficient machining of the substrate and the information cannot be displayed by the room temperature absorption spectrum of the substrate.

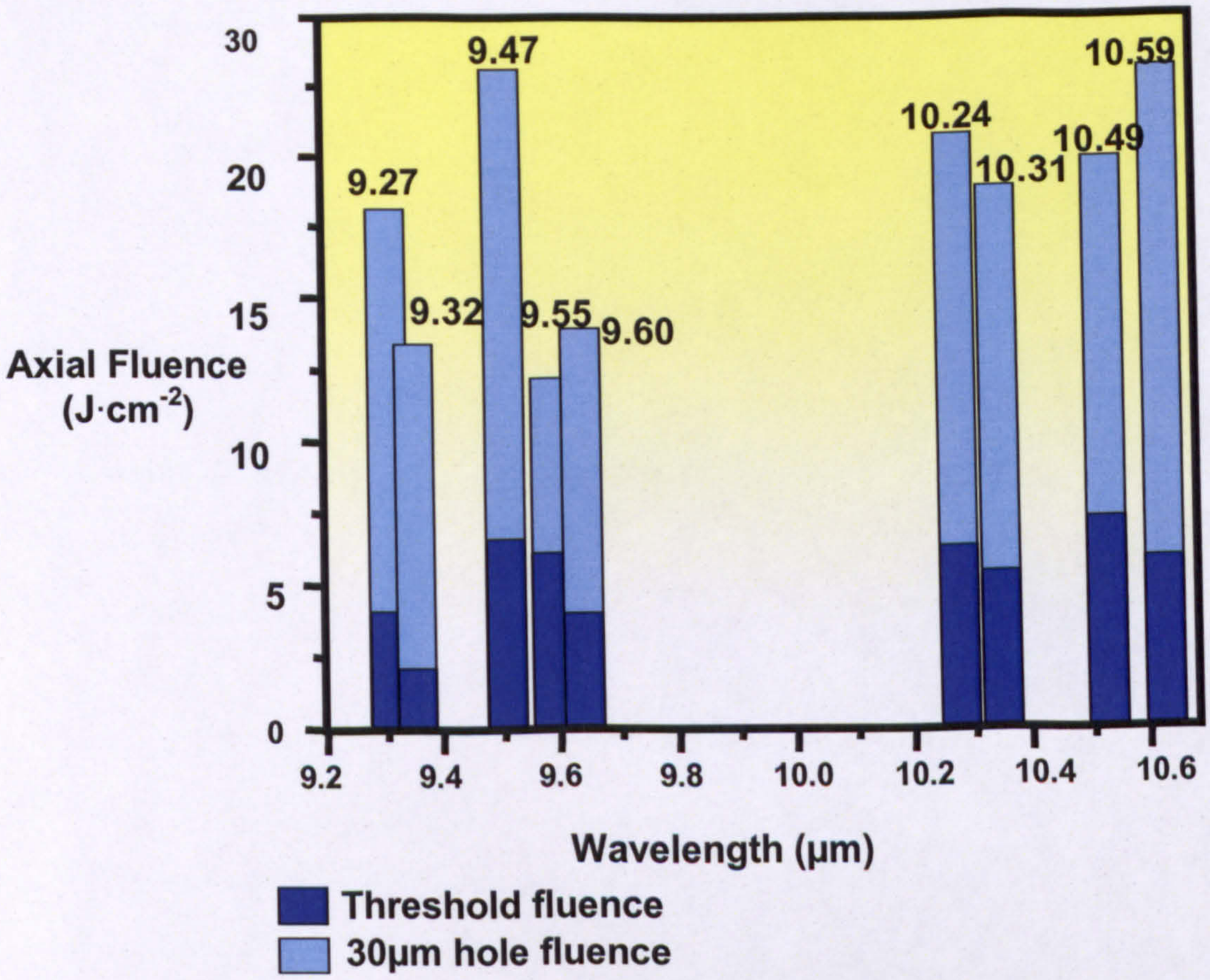

Fig 5.15: Ablation spectrum of resin

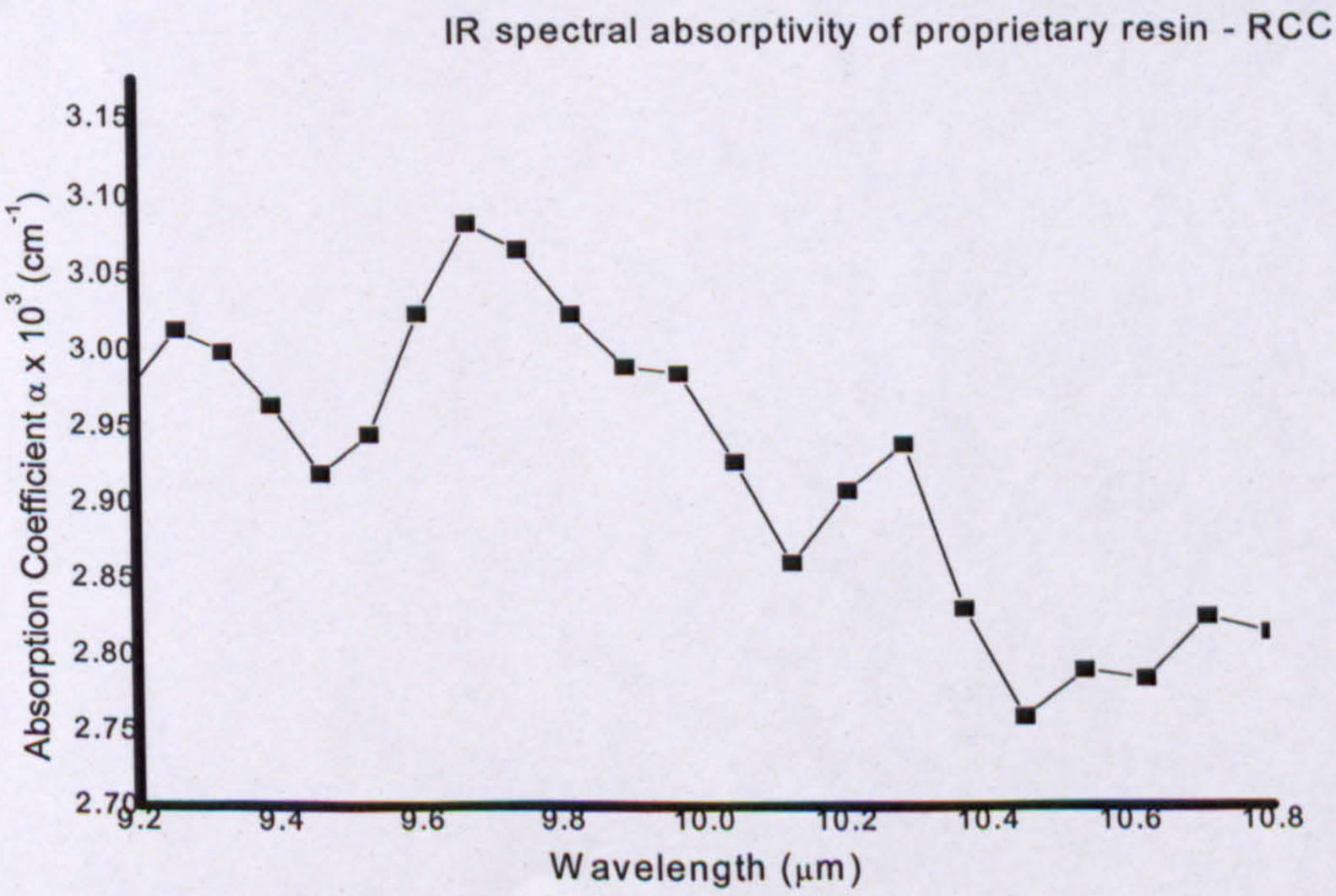

Figure 5.16: Absorption spectrum of resin recorded at room temperature by IR ellipsometer

5.6 Drilling of Arlon

Initial observation

a) Region under threshold $F \leq F_{th}$

Figure 5.17 (a), shows the sequence of surface change in Arlon at regions below threshold, at threshold and above threshold at a wavelength of 9.27μm at peak power level of 10W. The region below threshold is in the fluence range below $5J/cm^2$ whereas for 10μm band the threshold occur at $3J/cm^2$. This fluence limit has been described as the "adiabatic machining threshold" of a material [5.11] where the fluence applied on the surface raises the thermal energy of the surface, where possible thermal desorption of the material might take place thereby ejecting molecules of material off the surface. L.V. Zhigilie et al [5.12] suggest that below the ablation threshold mostly monomers are ejected from the surface. The localised irradiation yields an elevation of Arlon surface forming a hump as shown in Figure 5.17 (b). The maximum height of the hump attains before material is ablated off the surface was measured to be 4μm. This phenomenon is understood to occur due to high pressure build up in the irradiated volume. During pulsed laser irradiation, rapid energy transfer occurs from vibrationally excited molecules which results in rapid thermal energy rise of the material. Consequently, a sharp temperature rise occurs during laser pulse duration. When the heating time is shorter than a characteristic time of the mechanical relaxation, the material is inertially confined i.e. it does not have time to expand and locally, heating takes place at nearly constant volume. This constant volume heating inevitably leads to a higher pressure build-up in the irradiated volume. Hence the high pressure formed within the penetration depth relaxes by expansion of the irradiated material. This relaxation drives a strong compression wave into the direction towards bulk in the cold part of the material, and this internal pressure is additionally built up due to trapped gases within the polymer, causing an observable swelling of the surface [5.3, 5.4].

b) Region at threshold fluence $F = F_{th}$

In the irradiated surface region at a higher fluence levels, the pressure gradient leads to forces driving the acceleration of the top layers in the direction normal to the surface. Thus, ablation is initiated when these forces exceed the strength of the material and

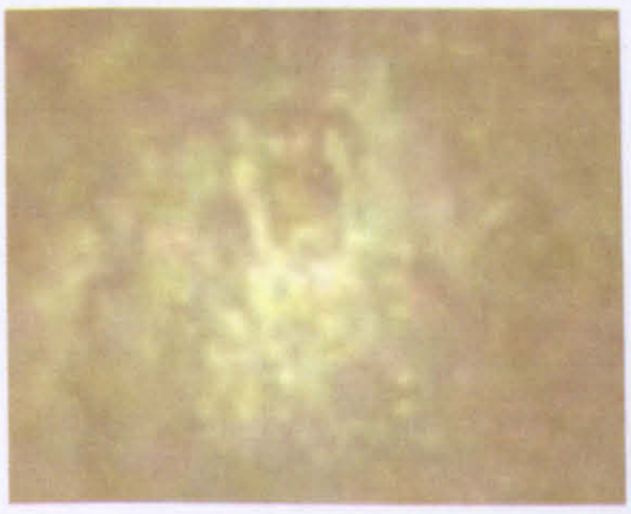

Region below threshold,

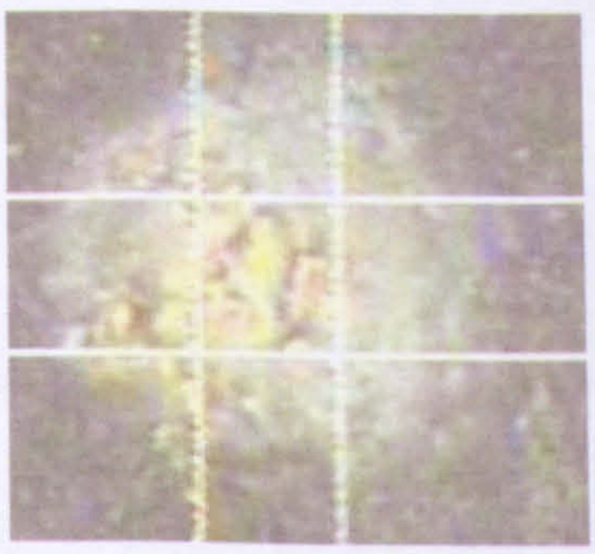

, At threshold

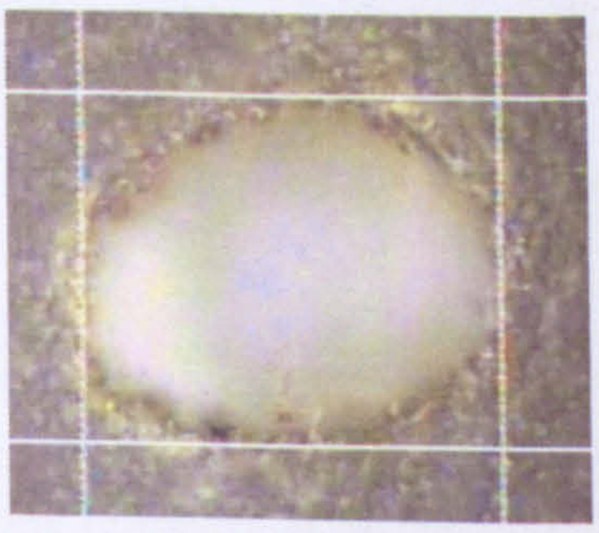

Above threshold

(a)

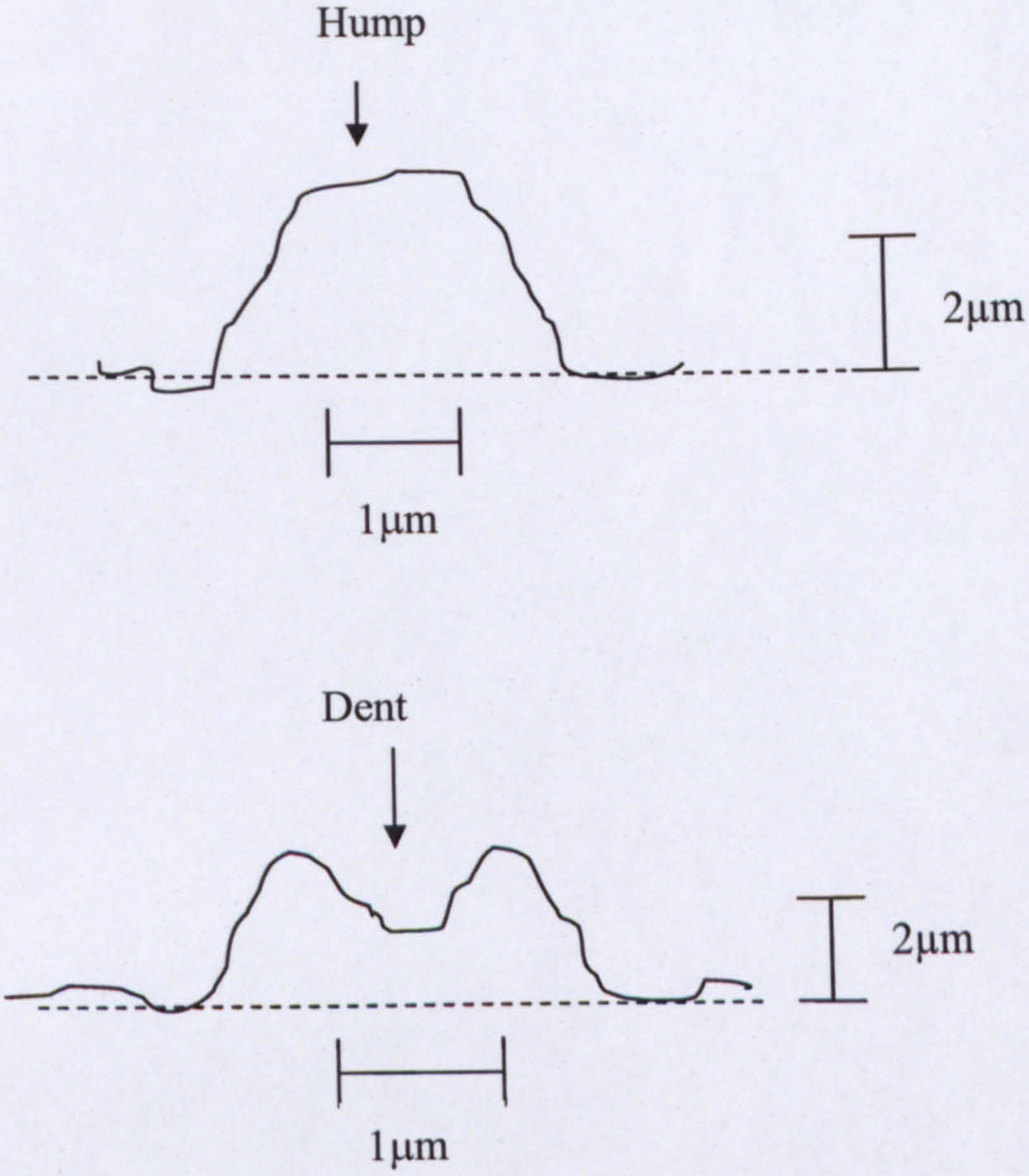

(b)

Fig 5.17: Surface topology sequence during ablation of Arlon at 9.20μm at spot size 90μm (a) Actual sequence of events (b) Schematic representation of actual sequence of events.

cause material fracture and particulate ejection. The threshold is used to describe the onset of a steep increase of the ablated depth with laser fluence. Hence, increase in the fluence from 5J/cm^2 reaches the onset of massive material removal or ablation. The surface topography of the arlon changes at threshold with the formation of a crater in the risen surface/bump that was created in the fluence region of below threshold as illustrated schematically in Figure 5.17 (b). Bauerle et al [5.14] also identify threshold by the average of the lowest fluence at which the dip appears in the center of the hump and the highest fluence for which this dip is absent. Experimentally measured values of threshold fluences for the 9 and 10μm emission bands for Arlon are listed in Tables 5.5 and 5.6. The results are discussed later in the section.

c) Region above threshold $F > F_{th}$

The Figures 5.18 and 5.19 shows that the ablation curves in the 9 and 10μm emission bands do not follow the logarithmic dependence of the equation (3.17). In the linear part of the curve where $F > F_{th}$, the ablation rate is high. The non-linearity of ablation curves of wavelengths 9.47 and 10.24μm could be explained due to presence of strong aramid fibers at the bottom of the crater. The beam is strongly reflected and bounced back internally in the crater due to presence of strong aramid fibers which remain uncut at the low absorbed wavelengths. This effect may show that the resin in Arlon has low absorption coefficient as compared to the aramid fibers and gets ablated easily, whereas, aramid fibers require higher fluence to be ablated. A typical ablated crater has no debris around or in it, but at certain low absorbed wavelengths, uncut aramid fibres are visible hanging at the entrance of the hole. This is understood to have occurred due to high energy density falling on the surface where the ablation of fibers is initiated but abrupt cooling leaves the fibres attached to the rim of crater. This may be possible due to influence of the non-reactive ambient atmosphere, which might enhance the absorptivity of the material but reduces the vaporisation enthalpy. This situation may change if however greater fluences are applied which increases the vaporisation enthalpy and provides enough energy density for the ablated materials to leave the surface either undergoing the carbonisation or thermal combustion. It has

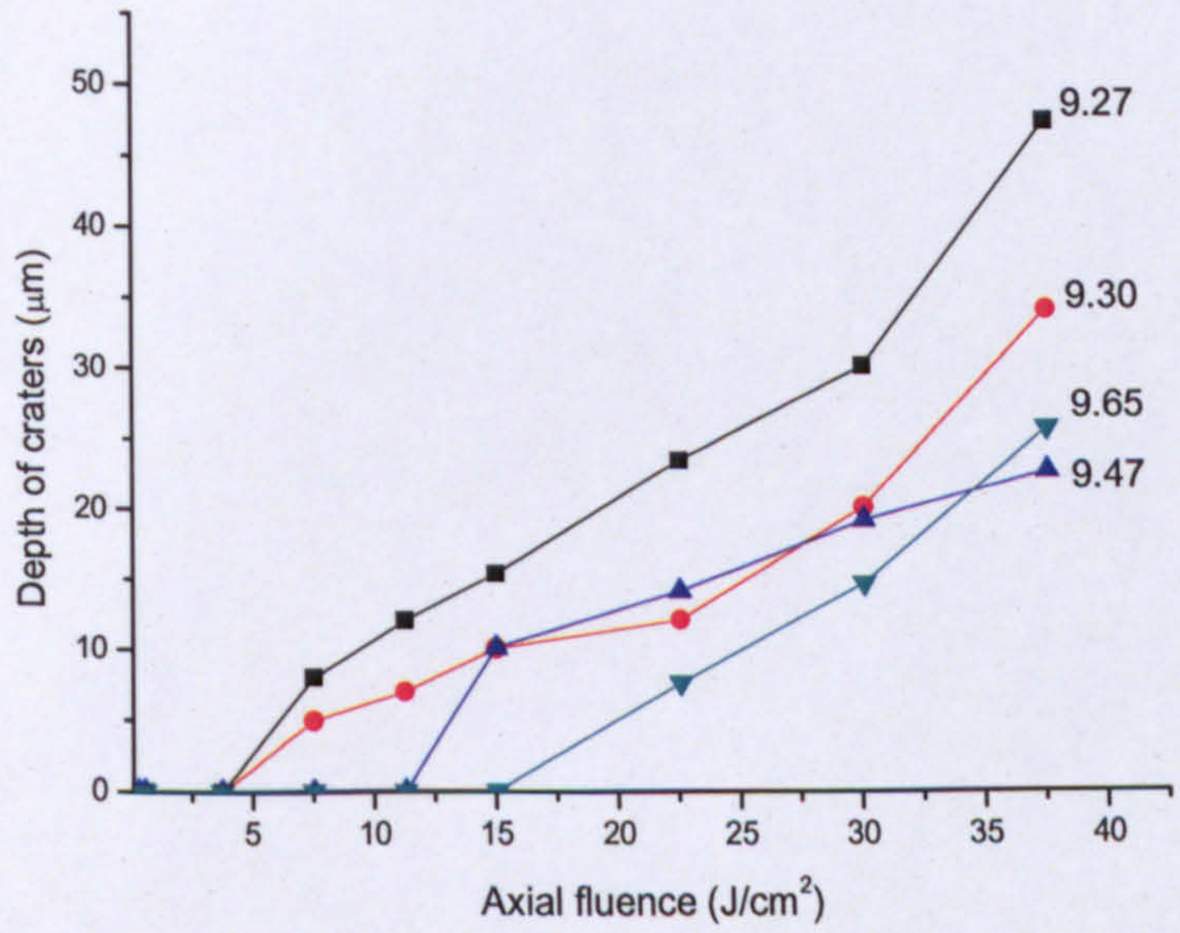

Fig 5.18: Ablation rates of Arlon in the 9 μm band

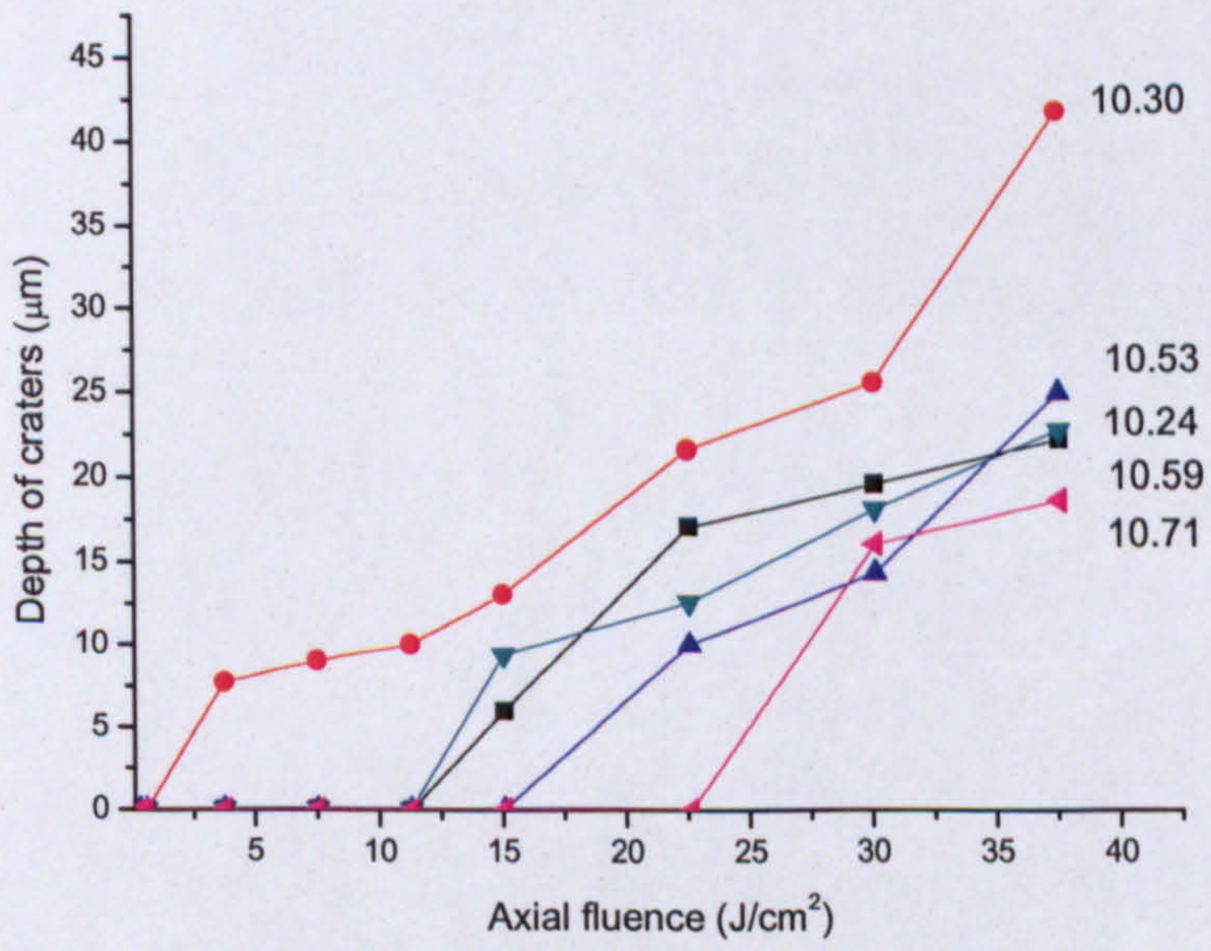

Fig 5.19: Ablation rates of Arlon in the 10 μm band

	Wavelength (μm)	*Threshold Fluence (J/cm^2)*
1	*9.27*	6
2	*9.30*	6.2
3	*9.47*	7.9
4	*9.65*	15

Table 5.5: Data of ablation threshold for the 9 μm band in Arlon.

	Wavelength (μm)	*Ablation Threshold (J/cm^2)*
1	10.24	12.2
2	10.30	3.9
3	10.53	16
4	10.59	12.5
5	10.71	17.5

Table 5.6: Data of ablation threshold in the 10 μm IR band in Arlon.

been observed that higher fluence than 9J/cm^2 cuts off aramid fibers of Arlon, but at a wavelength where absorption is low, fibers are observed to be uncut at the bottom of the crater. This is observed to reduce the depth of the crater by the order of 8-10μm. But with a presence of strong aramid fibre at the bottom of the crater, the light is reflected back which ablates the resin off from the entrance of crater thereby increasing the diameter and depth of the crater. This also might be the reason for the rugged surface of the craters. The holes are clean and no charring or blackening of edges is observed at all fluences used. Hence, optimum-machining conditions for Arlon may be to apply fluences above 9J/cm^2 at highly absorbed wavelengths.

5.6.1 Comparison of ablation and absorption spectra

1 As is observed from the Tables 5.5 and 5.6 the F_{th} is increasing with increasing wavelength. This could be due to the decrease of α with wavelengths as is observed in Figure 5.21, which is absorption spectrum of the Arlon determined from ellipsometry. This goes well in agreement with the threshold fluences at the 9.27μm peak line where the F_{th} = 6J/cm^2 , but the trend shows deviation at 10.30μm where the F_{th} is significantly low 3.9J/cm^2 and at 10.59μm it is 12.5J/cm^2. This is a deviation observed from the room temperature measured absorption spectrum of the arlon. This may be possible because Arlon material highly absorbs the peak line 10.30μm when at higher temperatures; an example of absorption coefficient variation with temperature is discovered in [5. 5]

2 Spectral absorption sensitivity of Arlon varies as a function of temperature. The absorption spectrum measured at room temperature does not go well in agreement with the ablation spectrum of Arlon, which is shown in Figure 5.20.

3 By comparing the absorption spectrum Figure 5.21 of Arlon with its ablation spectrum Figure 5.20, ablation spectra show that wavelengths 9.27μm and 10.30 μm have low ablation thresholds. However, 9.27μm requires low fluence to drill a 30μm deep hole compared to 10.30μm. This shows that it is not important that the wavelength that requires low fluence to reach threshold will necessarily

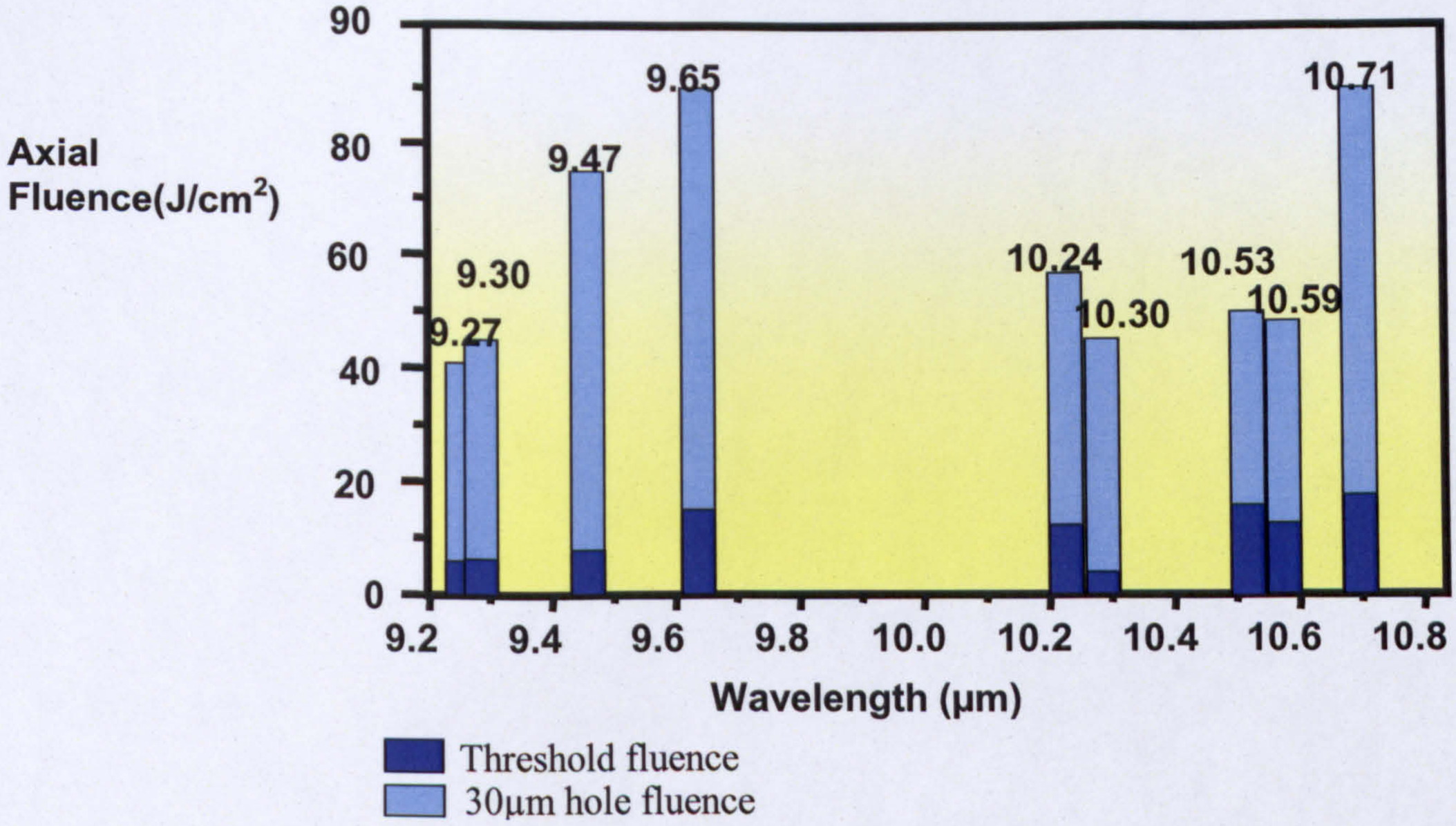

Fig 5.20: Ablation spectra of Arlon

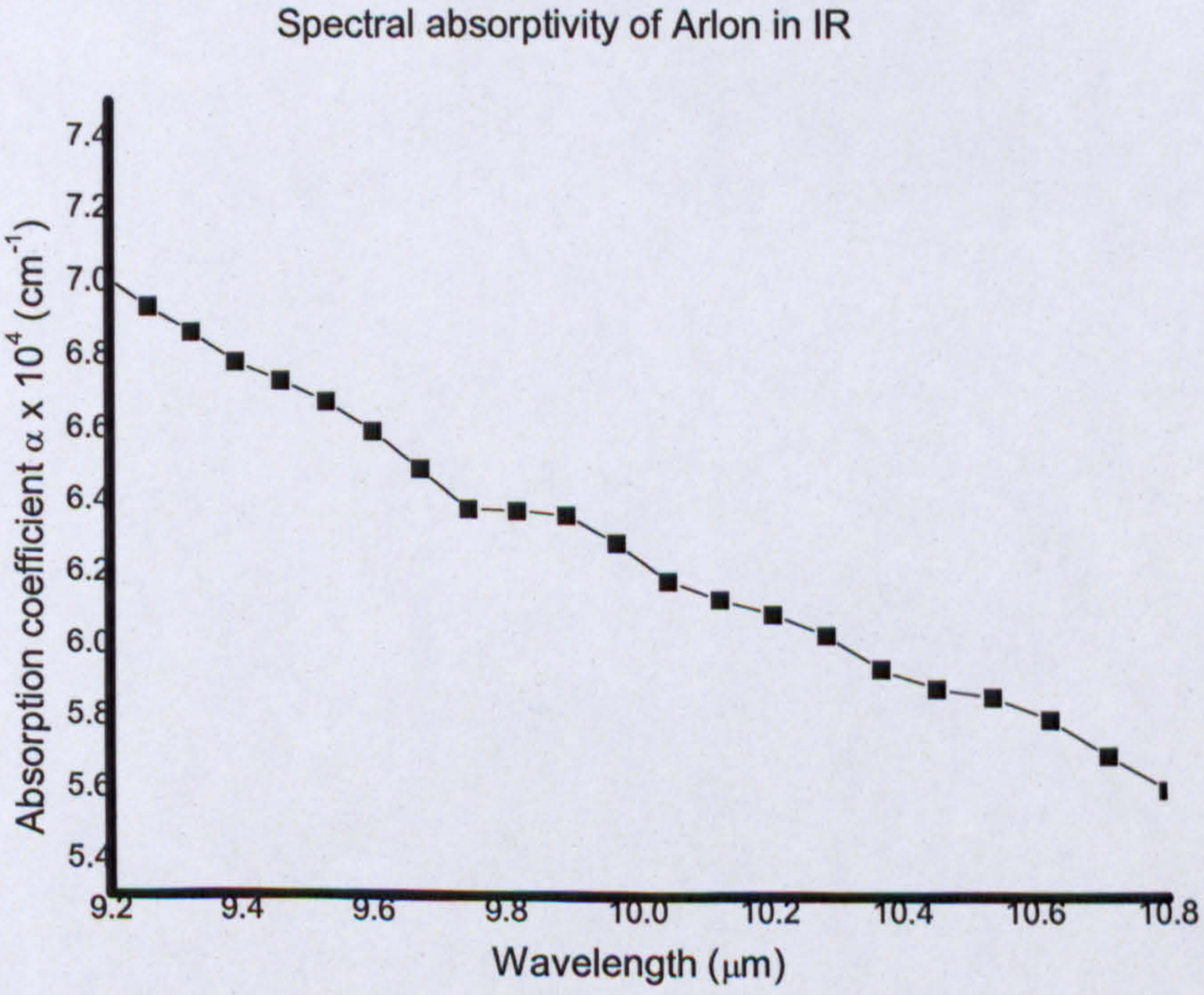

Figure 5.21: Absorption spectra of arlon as calculated from the measured values of ellipsometer

require the low fluence in drilling holes. There are various mechanisms, which effect the ablation of the material that decides the fluence required at a particular wavelength.

5.7 Drilling of FR4

Initial Observation

The FR4 sample used in the experiments is epoxy resin impregnated with homogeneously weaved glass yarn. The thickness of the sample is 1.5mm. Details of the material characteristics and its properties are presented in Chapter 2. FR4 presents laser machining challenges for several reasons. First, the material is highly heterogeneous, particularly with respect to properties governing laser ablation characteristics such as melting and vaporization temperatures. Specifically, the vaporization temperatures of the woven glass reinforcement and the polymer resin matrix differ greatly. Pure soda lime glass has melting and vaporization temperatures of 600 ^{0}C and 800 ^{0}C, respectively, while typical organic resins such as epoxies vaporize at much lower temperatures, on the order of 300 ^{0}C. This disparity makes it difficult to laser-ablate the glass component while avoiding too much ablation of the resin. Secondly, FR4 glass cloth is woven from bundles or "yarns" of individual glass filaments. Filaments in the sample are typically 4 to 7μm in diameter, and yarns range from about 50 μm to several hundred microns in diameter. In the sample, the yarn is woven in an open-weave pattern, resulting in areas of high glass density where yarns cross each other and areas of low or zero glass density, such as between adjacent bundles. Because the locations of holes cannot be selected a priori with respect to the weave pattern, the hole locations will vary in glass density. The matrix of holes ablated on the sample is observed to have the probability of positioning at three common positions that affect the depth, diameter and mechanism of ablation of the holes. Experimentally there are three common positions frequently observed as is shown in Figure 5.22, which are mentioned below:

Location 1 Where no glass fibre is ablated, i.e. only epoxy resin is ablated.

Location 2 Where only a part of the glass bundle or one fiber is present in the ablated area.

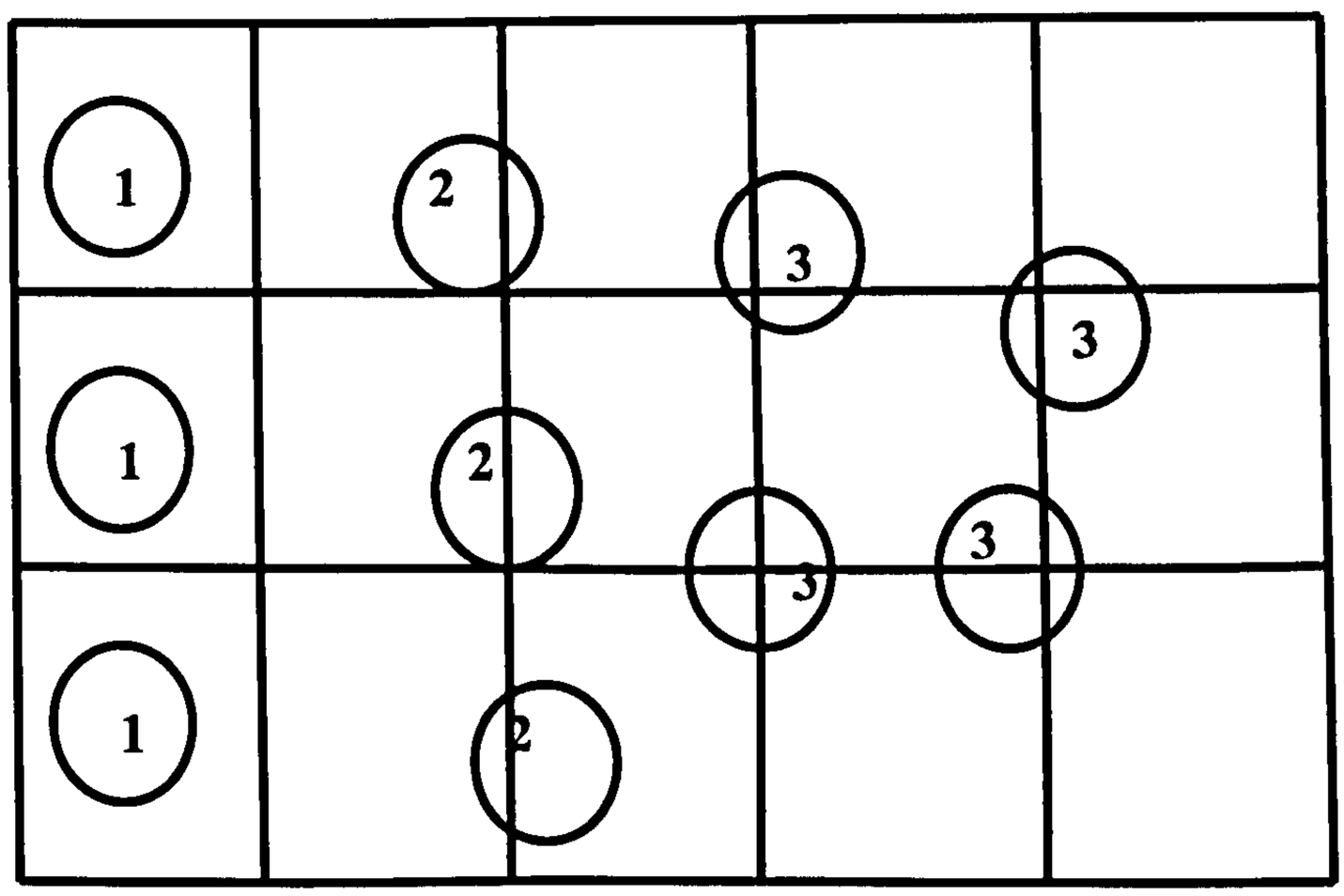

Figure 5.22: Position of the holes on the surface of FR4 with respect to the glass fibre mesh

Location 3 Where two crossing glass fibers/bindle are present in the ablated hole.

It is important to note here that the ablation curves incorporate without a priori destination all the three cases. However, the measured ablation *threshold* fluence values reflect the fact that *only resin is involved* since the glass fibres are located deeper in to the substrate. Thus the laser micromachining process parameters that work equally well in both high and low-glass-density regions of the substrate are desirable. Process conditions are required that are "aggressive" enough to cleanly vaporize all the glass in high-density regions and at the same time are "mild" enough to avoid over-ablation or removing too much resin in low-density regions.

a) Region below and at threshold $F \leq F_{th}$

Location one as illustrated in Figure 5.22 is the dominant case in region below and at threshold where only resin is ablated off. The glass fibers are as low as 20μm in depth from the surface. It is observed that the sub threshold fluences lie less than $5J/cm^2$ in the 9μm band and less than $3J/cm^2$ in the 10μm band. A damage threshold exists in the epoxy resin melts and leaves a visible mark on the surface of FR4. The fluence threshold is observed to increase with wavelengths in the 9μm emission band whereas in the 10μm emission band, 10.31μm has increased the threshold fluence as compared to 10.24μm and 10.49μm. Tables 5.7 and 5.8 illustrate the values of fluence at threshold for FR4 in the 9 and 10μm emission bands respectively.

b) Region above threshold $F \geq F_{th}$

Figure 5.23 shows the typical example of a hole ablated in the 9 μm emission band. The holes at the surface show no melt and visibly very small heat affected zone. At the bottom of the holes there might exist two cases: where the glass fibers may be present or absent. Both the cases is illustrated in Figure 5.23, where holes are ablated at the peak fluence of $23\ J/cm^2$ at 9.30 μm. These are approximately of 30μm depth. Hole (a) is positioned where no glass fibers interfere in its formation, hence the depth of the hole increases by 5-12μm as a function of fluence and wavelength absorption. Hole (b) shows the glass fibers at the bottom of the hole. The glass fibers may run vertically or horizontally or could be layered on top of each other hence decreasing the depth of resin from surface. The presence of glass fibre in the hole makes it very hard to measure the exact depth of the holes. It is observed that the glass fibers reflect

light and hence increase the resin ablation deeper within the holes, hence making a hole much deeper by 20 μm. In unablated glass fibers it is very hard to measure the exact depth of hole especially under the glass fibers. At lower fluences the melt ejection seems to be creating holes. The fluence is high enough to melt resin and spatter the melt out of the holes. The glass fibers have a high sublimation temperature of 2300 °C, the fibers protrude into the crater wall. But the melting point of the glass is 700 °C hence the glass fibers protruding become spherical in shape due to surface tension. The glass fibre projection in the crater wall or at the bottom of the crater is particularly large at the lower fluence [5.16, 5.17]. This is the effect observed for wavelengths 9.55μm and 9.30 μm at fluences less than 60 J/cm^2. The threshold fluence of glass ablation is observed to be 50 – 80 J/cm^2. At higher fluences, the rapid delivery of energy has the effect of driving the local temperature above the higher of the two vaporization points (several thousand Kelvin for glass) very rapidly. The effective ablation process requires vaporisation of both materials quickly and thereby obtains roughly equal amounts of material removal in the two materials despite the differences in their thermal characteristics. The pulse energy delivered at low instantaneous power ablates the epoxy resin that still reaches its vaporization temperature early in the laser pulse while the glass remained solid and unablated. Delivery of such low instantaneous power levels leads to differential material-removal effects. As is observed at 9.30 μm, the fluence above 50 J/cm^2 leaves unvaporised ends of the glass fibers that protrude into the hole. This is because the more aggressive ablation of the resin enlarges the hole diameter relative to the area in which the glass is ablated. This phenomenon is known as "wicking" in the printed wiring board industry. In FR4 via drilling, wicking is more severe with lower-energy laser pulses. Hence, this regime of ablation in FR4 should be avoided for machining. In addition to the observation, it is also seen that the glass is not cleanly vaporised. Instead, the ends melt, are not ejected from the hole, and re-solidify into large spherical knobs at the fiber ends. This is also an unacceptable final geometry for the drilled holes, an example of which is illustrated in Figure 5.23 (c).

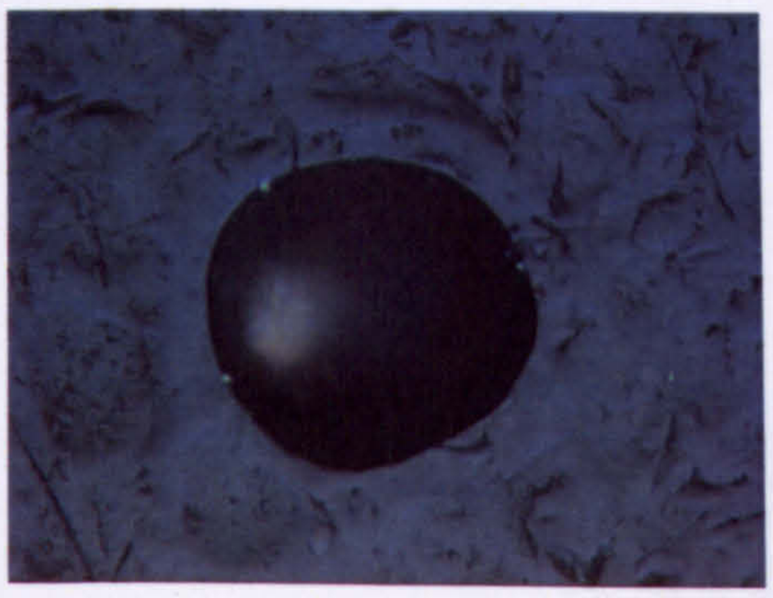

(a) Hole at surface

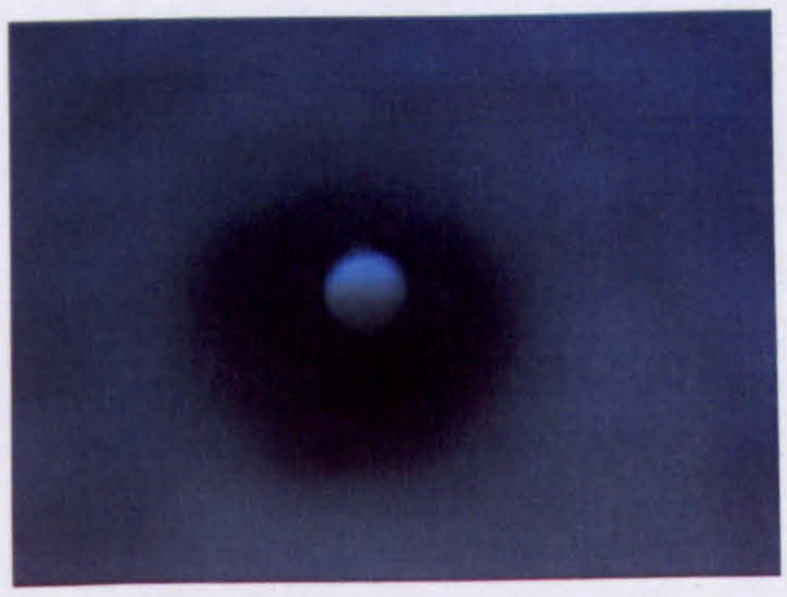

Hole at 30μm depth with no glass fibres

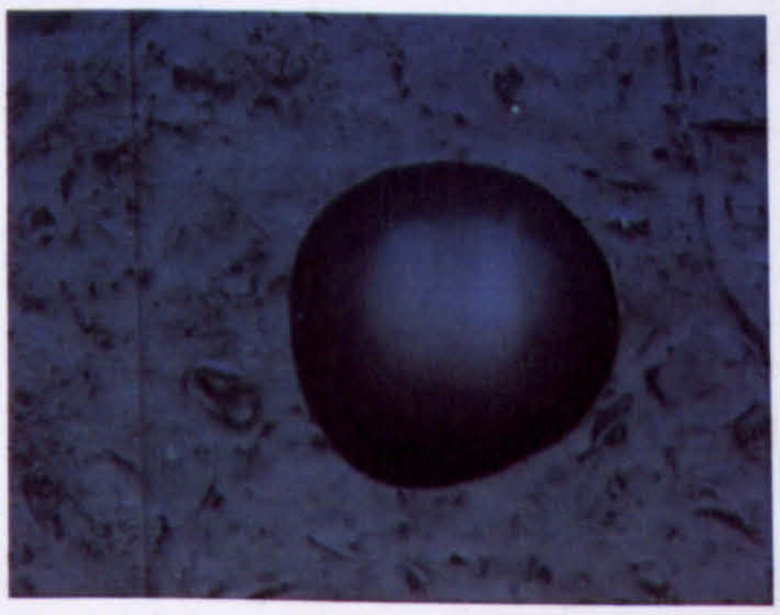

(b) Hole at the surface

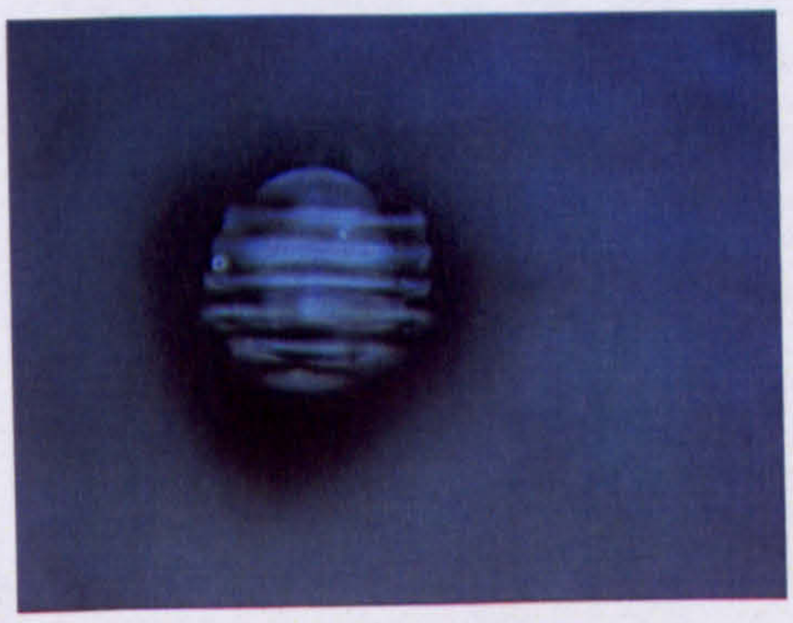

Hole at 30μm depth with glass fibres

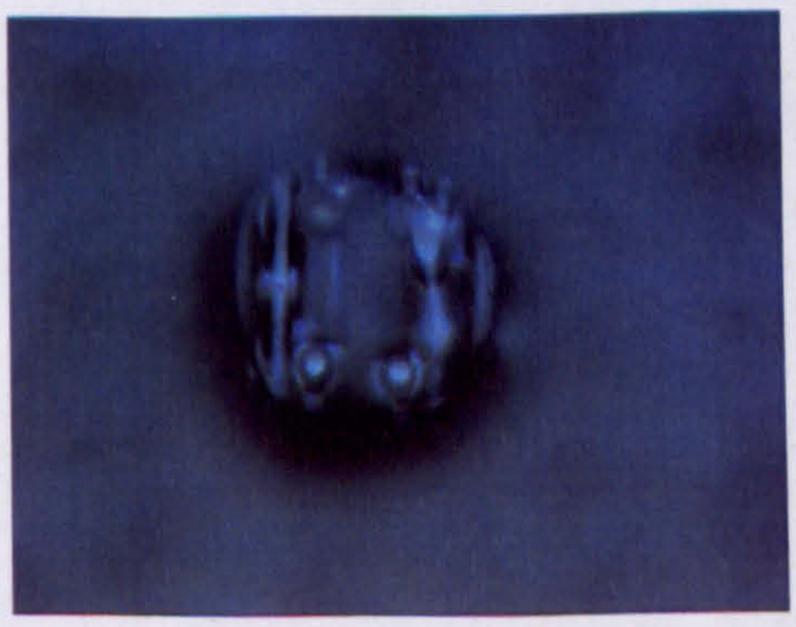

(c) Hole at 30μm depth with glass globules

Figure 5.23: Hole ablated at Fluence 23J/cm^2 (a) Hole with no glass fibre at the surface and in the bottom of the hole(b) Hole at surface with uncut glass fibre at bottom, (c) Hole with cut glass fibre at bottom, formation of glass globules due to surface tension.

In the 10μm emission bands, the melt ejection phenomenon predominates over ablation and at all wavelengths in this band, the droplets of melt are observed to be squirted out of holes. The melt is also seen rolled off at the edges of holes hence creating a sharp radial rim around holes. This could be explained hypothesising, that on application of high fluences, the surface tension plays a role in drilling while melt ejection from deeper holes relies on evaporation pressure. The mechanism of creating holes in FR4 can be understood by the so-called "Piston effect" [5.15]. This is illustrated in Figure 5.24 (a), where the evaporation surface acts as piston that exerts a pressure onto the melt hence squirting it out of the hole radially. This effect is clearly seen in the Figure 5.24 (b) a typical hole created, where the exerted pressure rolls out the melt radially but also drops the melt globules. The ablated holes in this regime also showed melt of resin at the bottom of the craters. The heat affected zones is of the order of 35-40μm around the craters. There is no evidence of ablation of glass until 70 J/cm^2 in the 10 μm emission band. Hence, it also suggests that the spectral absorptivity of silica is higher in the 9μm emission band than in the 10μm. Figures 5.25 and 5.26 illustrate the ablation curves in FR4 in 9μm and 10μm emission band respectively. The steps in the ablation rates in 10μm curves above 20μm crater depth suggest some measurement anomaly for the depth of holes.

5.7.1 Comparison of ablation and absorption spectra

Correlating absorption and ablation spectra of FR4 as shown in Figures 5.27 and 5.28 shows that:

1 There is observed a clear trend in increase in threshold behaviour of optical absorption of wavelengths in 9μm emission band with increase of wavelengths. There is much less melt ejected and smaller heat affected zone (HAZ). The glass fibers are seen cut at fluences 50 – 80 J/cm^2, which is much higher threshold of ablation compared to threshold of resin in FR4. In 9μm emission band, 9.55μm seems to be the best wavelength to machine FR4 in terms of clean quality of holes and clean ablation of resin and glass between 40 – 80 μs pulse lengths. However, 9.27μm emission effectively ablates glass and no melt ejection is observed leaving clean holes however during the ablation process at this wavelength, the

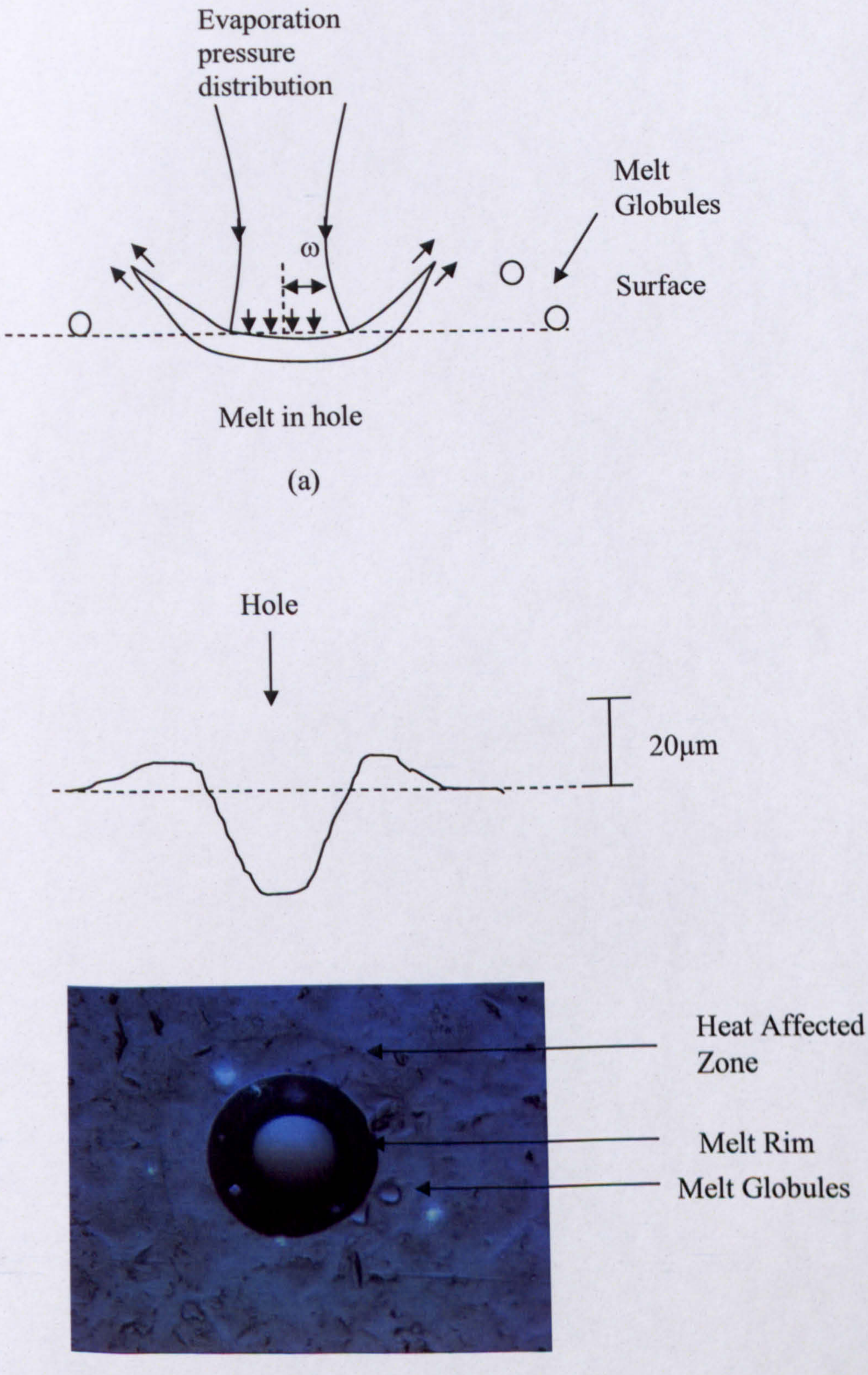

Figure 5.24: (a) "Piston" mechanism of melt ejection by the evaporation recoil pressure in FR4, (b) Hole with melt rim and globules, ablated due to the mechanism

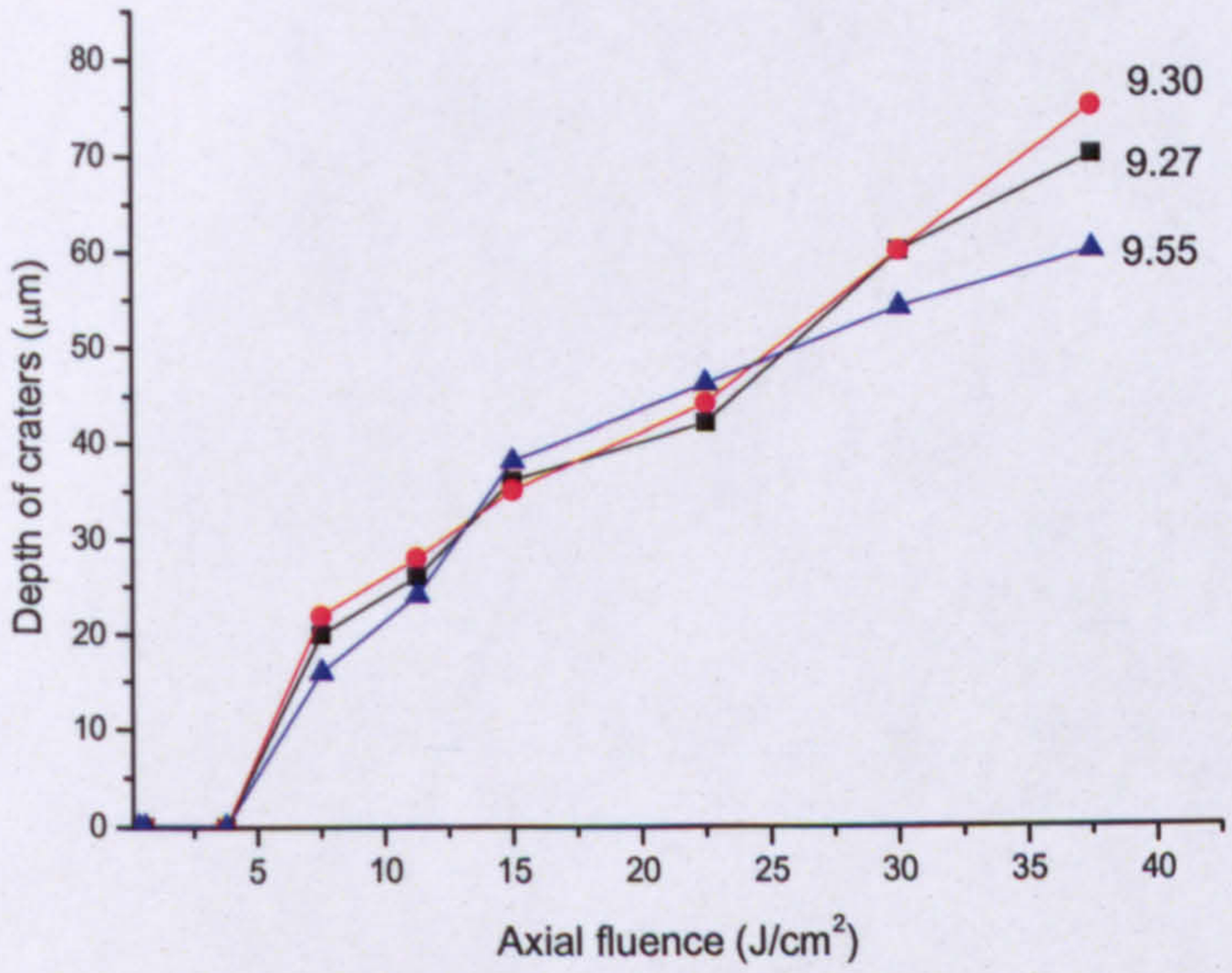

Fig 5.25 Ablation curves of FR4 in 9μm emission band

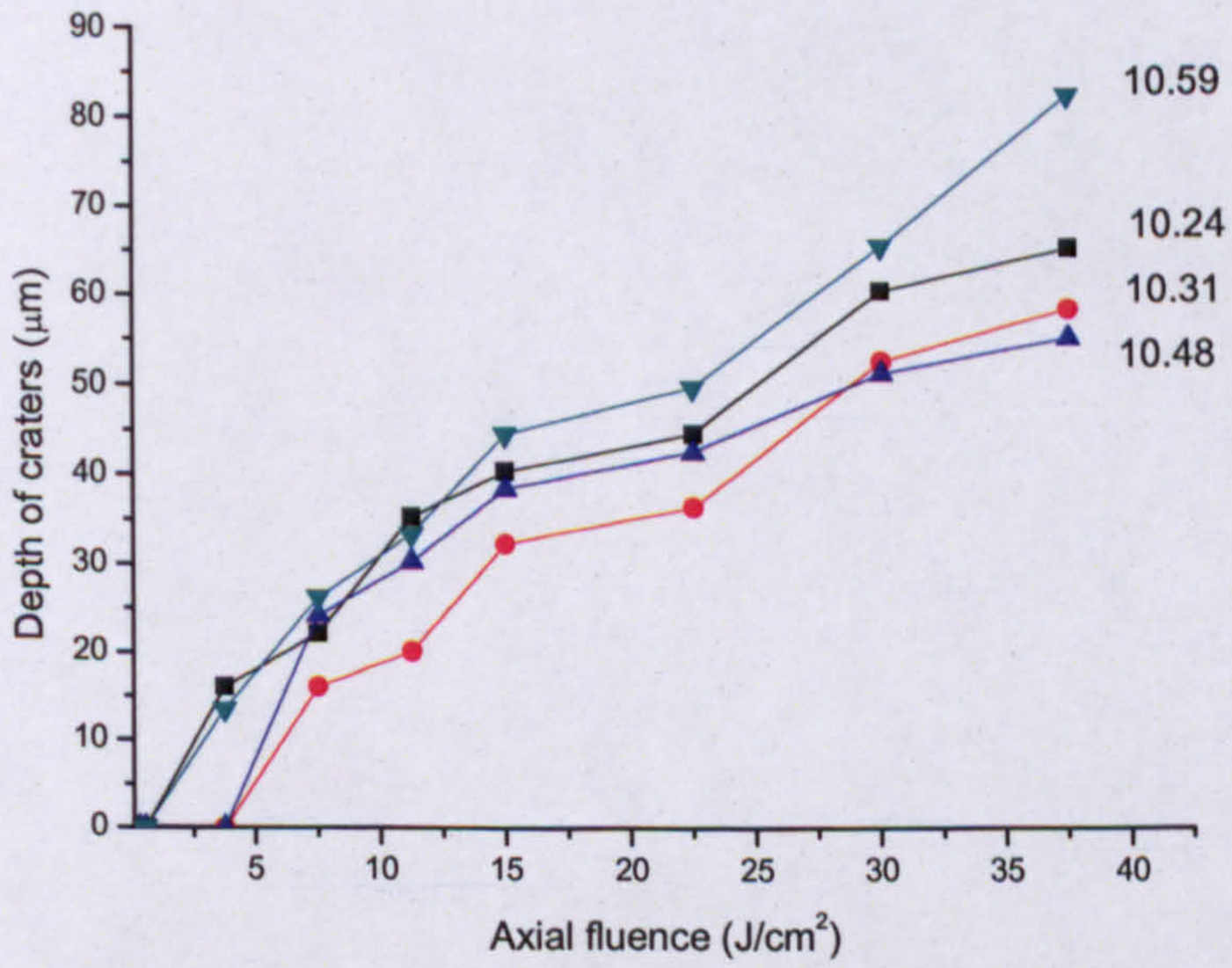

Fig 5.26 Ablation curves of FR4 in 10μm emission band

	Wavelength (μm)	Threshold Fluence (J/cm^2)
1	9.27	5
2	9.30	8
3	9.55	11.5

Table 5.7: Data of thresholds of FR4 in 9-micron band

	Wavelength (μm)	Threshold Fluence (J/cm^2)
1	10.24	5.5
2	10.31	12.5
3	10.49	9.5
4	10.59	3.5

Table 5.8: Data of thresholds of FR4 at 10-micron wavelengths

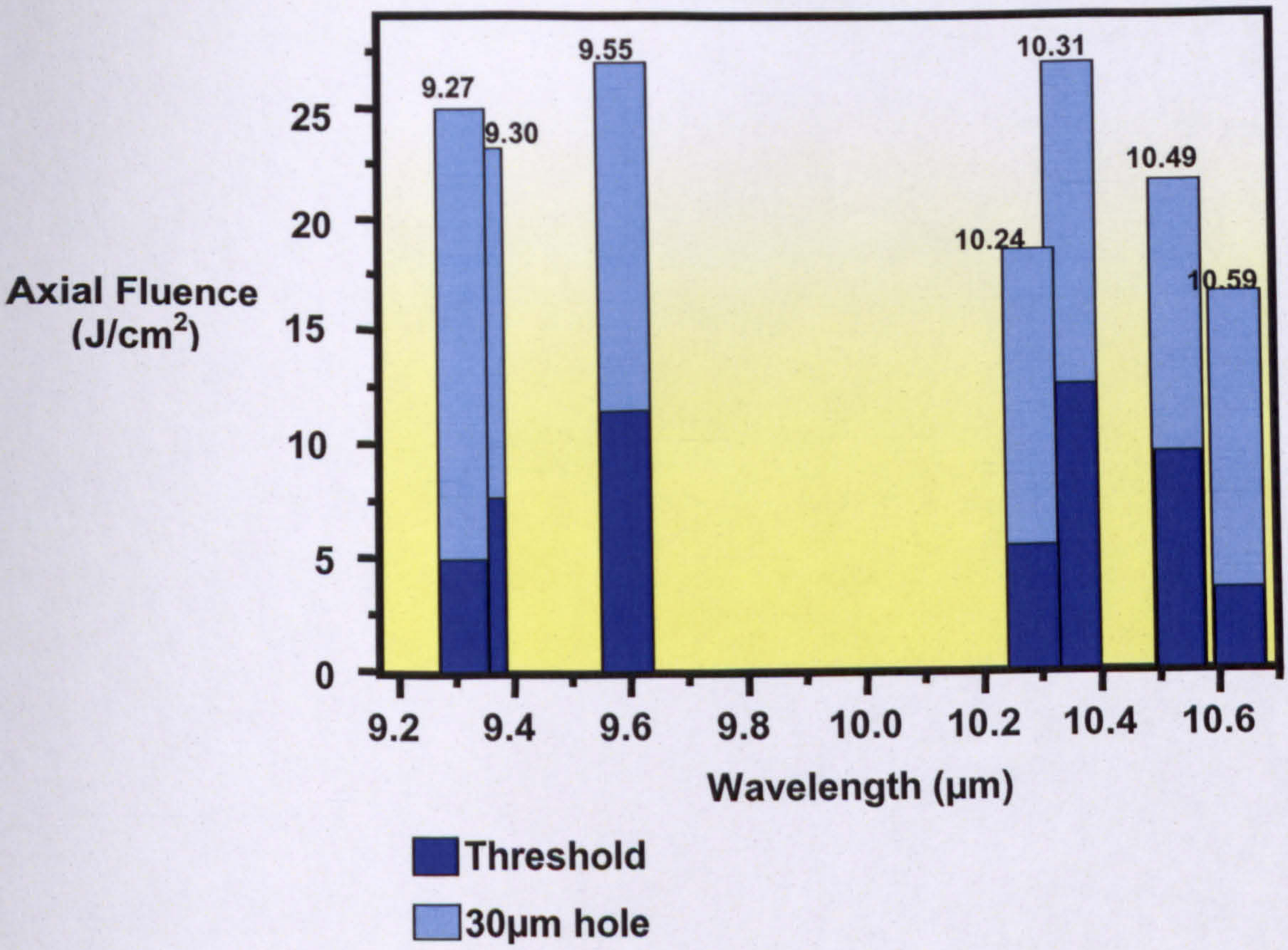

Figure 5.27: Ablation spectra of FR4

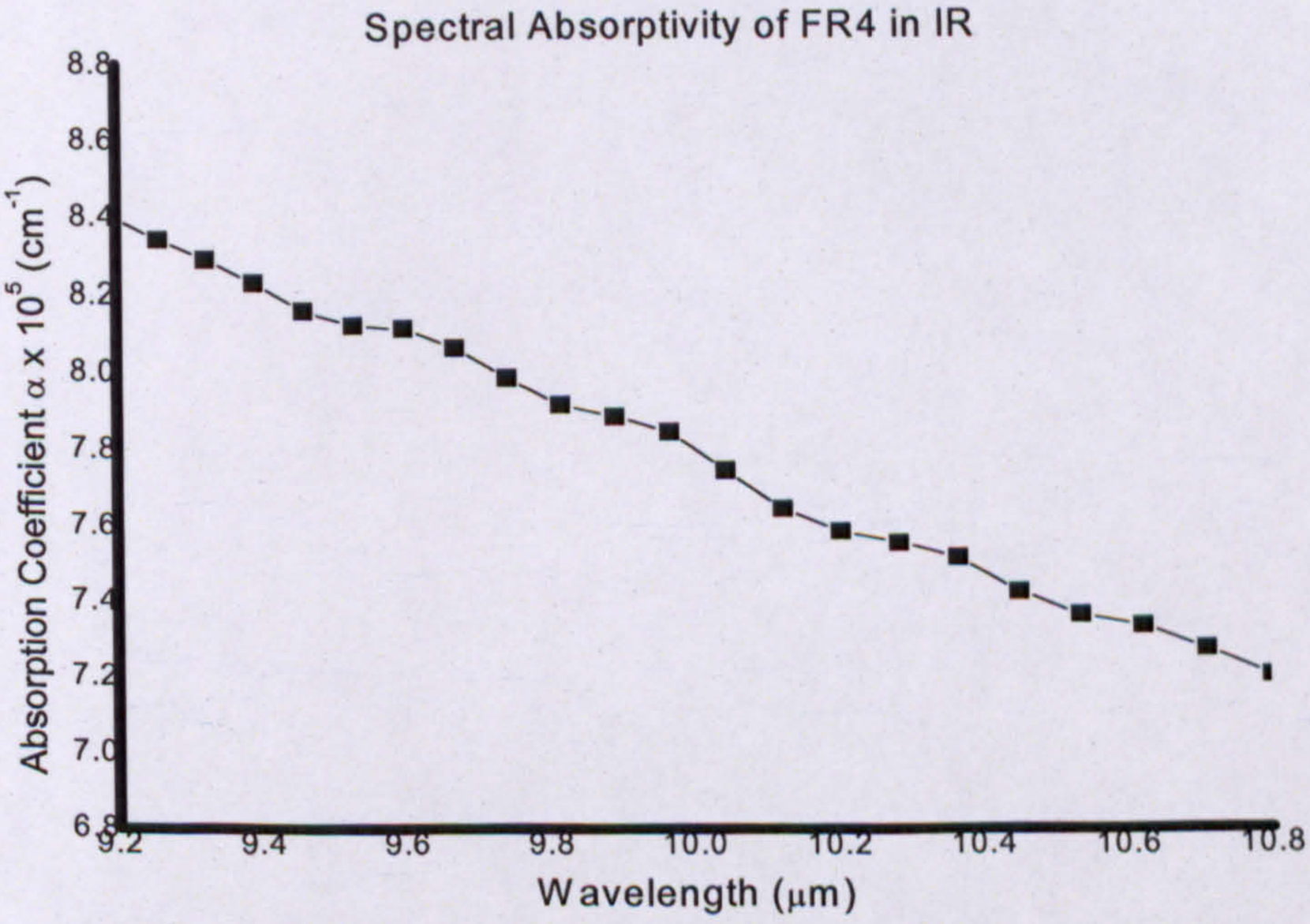

Figure 5.28: Absorption spectrum of FR4 recorded by IR Ellipsometer at room temperature

5.8 References

[5.1] R.M.A. Azzam, N.M. Bashara "*Ellipsometery and Polarised light*" North Holland Physics Publishing, Ed. – 1986, Elsevier Science Publishers

[5.2] J.H. Brannon, J.R. Lankard, " *Pulsed CO_2 laser etching of polyimide"* Appl. Phys. Lett., **48**, 18, (1986).

[5.3] K.Piglmayer, E.Arenholz, C.Ortwein, N.Arnold, D.Bauerle, "*Single pulse ultraviolet laser induced surface modification and ablation of polyimide*": Appl. Physics letters, Volume **73**, No.6, (1998).

[5.4] Himmelbauer, E. Arenholz, D. Bauerle, "*Single shot UV laser ablation of polyimide with variable pulse lengths"* Appl. Physics. A, **63**,87-90, (1996)].

[5.5] P.E. Dyer, D.M. Karnakis, G.A. Oldershaw, G.C. Roberts*"TEA CO_2 laser ablation of upilex polyimide"* J. Phys. D: Appl. Phys. **29**, pp 2554-2583, (1996).

[5.6] R. Srinivasan:" *Ablation of polyimide (kapton) films by pulsed (ns) ultraviolet and infrared (9.17μm) lasers."* Appl. Phys. A **56**, 417-423, (1993)

[5.7] D.W. Zeng et. al.:*"XPS investigation of the chemical characteristics of Kapton films ablated by the pulsed TEA CO_2 laser"* Surface and Coatings Technology, **153**, 210-216 (2002)

[5.8] Kristen Coupland, Peter R Herman, Bo Gu "*Laser cleaning of ablation debris from CO_2-laser-etched vias in polyimide"* Applied Surface Science, **127**,731-737 (1998)]

[5.9] Grassie N and Mc Neill "*Thermal degradation of polymethacrylonitrile* "J. *Polym. Sci.* **39** 211 (1959)

[5.10] Sammon C, Yarwood J, Everall N , *"An FT-IR study of the effect of hydrolytic degradation on the structure of thin PET films"* Polymer Degradation Stability **67**, 149 – 158 (2000)

[5.11] G. Markillie, H. Baker, F. Villarreal, D. Hall*:" Effect of vaporisation and melt ejection on laser machining of silica glass micro – optical components."* Applied Optics, Vol **41**, n 27, Sep (2002).

[5.12] Leonid V.Zhigilei, Barbara J. Garrison, "*Molecular dynamics simulation study of the fluence dependence of particle yield and plume composition in laser desorption and ablation of organics solids"* Appl. Physics letters, Volume **74**, No. 9, (1999).

[5.13] Shozui Takeno, Masaharu Moriyasu, Masaki Kuzumoto *"Laser drilling of epoxy-glass printed circuit boards"* Section **B**- ICALEO (1997).

[5.14] Hirogaki, E. Aoyama, H. Inoue, K.Ogawa, S.Maeda, T.Katayama *"Laser drilling of blind via holes in aramid and glass/epoxy composites for multilayer printed wiring boards"* Composites Part A: Applied science and manufacturing, **32** 963-968, (2001).

[5.15] M.von Allmen and A. Blatter,"*Laser beam interactions with materials"* 2nd ed. (Springer–Verlag), Berlin, Chap. **5**, pp. 115-165, (1995).

CHAPTER 6

Single pulse drilling of alumina and LTCCs

6.1 Introduction

Laser machining is a non-contact, abrasion-less technique, which eliminates tool wear, machine-tool deflections, vibrations and cutting forces, reduces limitations to shape formation, and inflicts less sub-surface damage. Therefore laser machining of ceramics is used extensively in the microelectronics industry for scribing and hole drilling [6.1]. However, laser drilled holes are inherently associated with spatter deposition, due to the incomplete expulsion of ejected material from the drilling site, which subsequently resolidifies and adheres to the material surface around the hole periphery. In addition, due to the brittleness of ceramics, fractures or micro cracks in the bulk phase of the material seem inevitable during laser machining.

The present work seeks to investigate surface ablation and to determine the damage threshold of alumina and LTCC (in the sintered / fired state) for a range of CO_2 laser lines. Issues addressed here are important from the point of view of machining, including the sensitivity of the ablation characteristics to the laser wavelength, the ablation threshold, the dependence on laser pulse duration and the subsequent surface quality in alumina and LTCC. The pulse duration dependence of laser induced damage on ceramics materials is studied for infrared laser pulses in the microsecond range. This chapter presents experimental data on laser ablation rates for alumina and LTCC in the microsecond pulse range with selected IR wavelengths.

6.2 Review of Laser processing of alumina and LTCC

Because of the high absorption of alumina at 10.6 μm [6.2], carbon dioxide lasers have been in common use to drill vias, make slots, and produce scribe snap-lines in Al_2O_3 substrates [6.3,6.4]. In the early work, dc discharge excited lasers were employed, while more recently, more compact and sealed radio frequency (RF) discharge-excited slab lasers with peak/average power levels of 100W have been introduced to overcome the limitations of gas flow lasers. With such lasers, the

combination of peak power levels and high repetition rates result in smaller heat-affected zones and faster material processing.

In 1999 Imen and Allen [6.5] reported using a TEA CO_2 laser to machine LTCC and found air breakdown over the ablation site and plasma screening to be a major problem (due to the high peak power employed). They found that operating at reduced pressures alleviated the problem and a material removal rate of 30–40 μm per pulse at 100 Jcm^{-2} was reported, though large values of fluence (1.2–1.5 kJ cm^{-2}) were required. Nd: YAG lasers at 1.06 μm have been used for drilling 75 to 500 μm diameter holes in LTCC with reasonable quality and at reasonable pulse rates, but the material removal rate and overall machining control are low for an industrial process due to relatively weak absorption at this wavelength.

Nowak et al [6.6] reported cold ablation of *green state* LTCC. The green state LTCC is a composite consisting of alumina particles and glass frit particles that allow a lower sintering temperature, held together by an organic binder. The CO_2 laser is used to ablate green state materials with high speed and high resolution demonstrating a self – cleaning technique.

The laser processing speed and efficiency are clearly issues of considerable importance for overall economic viability in machining ceramics. This chapter presents the results of an investigation to explore the optimisation of laser process efficiency with emphasis on laser wavelength absorption and on laser parameters over a wider range of pulse characteristics to understand the underlying ablation mechanisms than previously explored in both alumina and LTCCs.

6.3 Design of experiments

The sets of experiments are similar to those used to investigate dielectrics in Chapter 5. The peak power is kept constant at 23 watts in alumina and 12 watts in LTCCs and pulse durations are selected in the range of 5 – 100 μs, to vary axial fluence by varying pulse durations. A matrix of holes was ablated in the surface of the substrate as a function of fluence at each selected wavelength. The depth of the ablated holes was plotted as a function of fluence at each wavelength to obtain an ablation or

machining curve. The machining curves at all the selected wavelengths are plotted together. The plot of ablation curves is therefore compared to the absorption spectrum of the material to critically analyse the characteristics of absorption of wavelengths, to establish any pattern of deviation in spectral absorptivity and to understand the cause of the shift if any.

6.3.1 Wavelength selection

The peak lines emitted in the 9 and 10 μm bands are selected to investigate laser machining of alumina and LTCC. The selected lines are 9.2, 9.6, 10.2, 10.6 μm. The criterion for selecting peak lines is derived from the examination of the spectral absorptivity of alumina as is shown in Figure 6.1 and LTCC as shown in Figure 6.9.

6.4 Initial Observation of ablation in Alumina

The ablation curves at selected wavelengths in alumina are plotted in Figure 6.2. It is observed that the ablation curves in alumina and LTCCs exhibit the typical three section form as introduced in section 3.4. There exists a neutral section where no material removal takes place (Section I), the onset of ablation (Section II) and section III is the linear part of constant gradient where considerable increase in ablation is observed. The initial observation of surface changes in alumina in these sections is discussed below:

(a) Fluence less than ablation threshold ($F < F_{th}$) – Section I:

For alumina (Figure 6.2) two distinctive thresholds may be distinguished: a fluence threshold for damage and a fluence threshold for ablation. Ceramics are known to melt at well defined temperatures. For example, alumina is known to melt at ~ 2050 ^{o}C, therefore at the damage threshold; the fluence raises the temperature of the surface to the melting point of alumina. At raising the fluence, the temperature increases to ablate the material off the surface [6.3]. The ablation temperature for alumina is calculated using equation (3.11) of section 3.1.3 of Chapter 3, to be ~ 3000 ^{0}C. At this high temperature, the surface deformations show the characteristic crater shape to the given spot size. However, the melt is not displaced from the surface such that a measurable crater depth is attained. The melted surface cools off and an irreversible deformation is visible on the surface. This surface modification in alumina is shown

in Figure 6.3 (a) at a fluence of 5.5 J/cm^2 at 10.6μm. The amount of fluence absorbed here increases the surface layer temperature to the point where melting or at least softening occurs. This then allows the surface tension driven mass flow of the viscous molten or softened layer, followed by re-solidification of the surface. Reference here to the heating of thin layer is justified since at 10.6μm, the penetration depth of room temperature is very small confined to ~ 5μm, as calculated using equation 3.12 of Chapter Three. The heat conduction is one dimensional in the fluence range and the temperature profile here can be mapped as exponential decaying similar to case shown in Figure 3.2 of Chapter Three. The damage thresholds for different wavelengths are observed to be

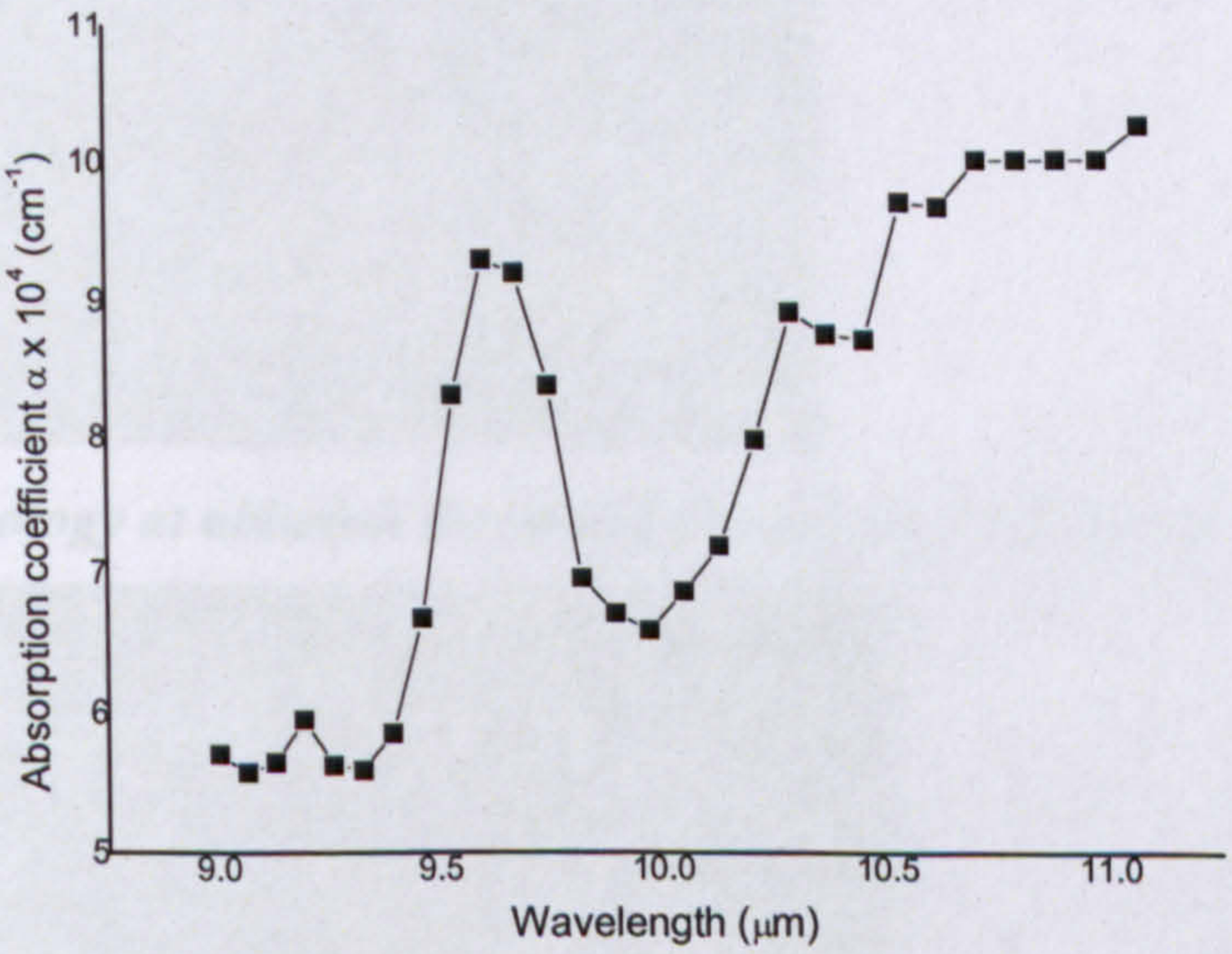

Figure 6.1: Absorption spectrum of alumina from IR ellipsometer

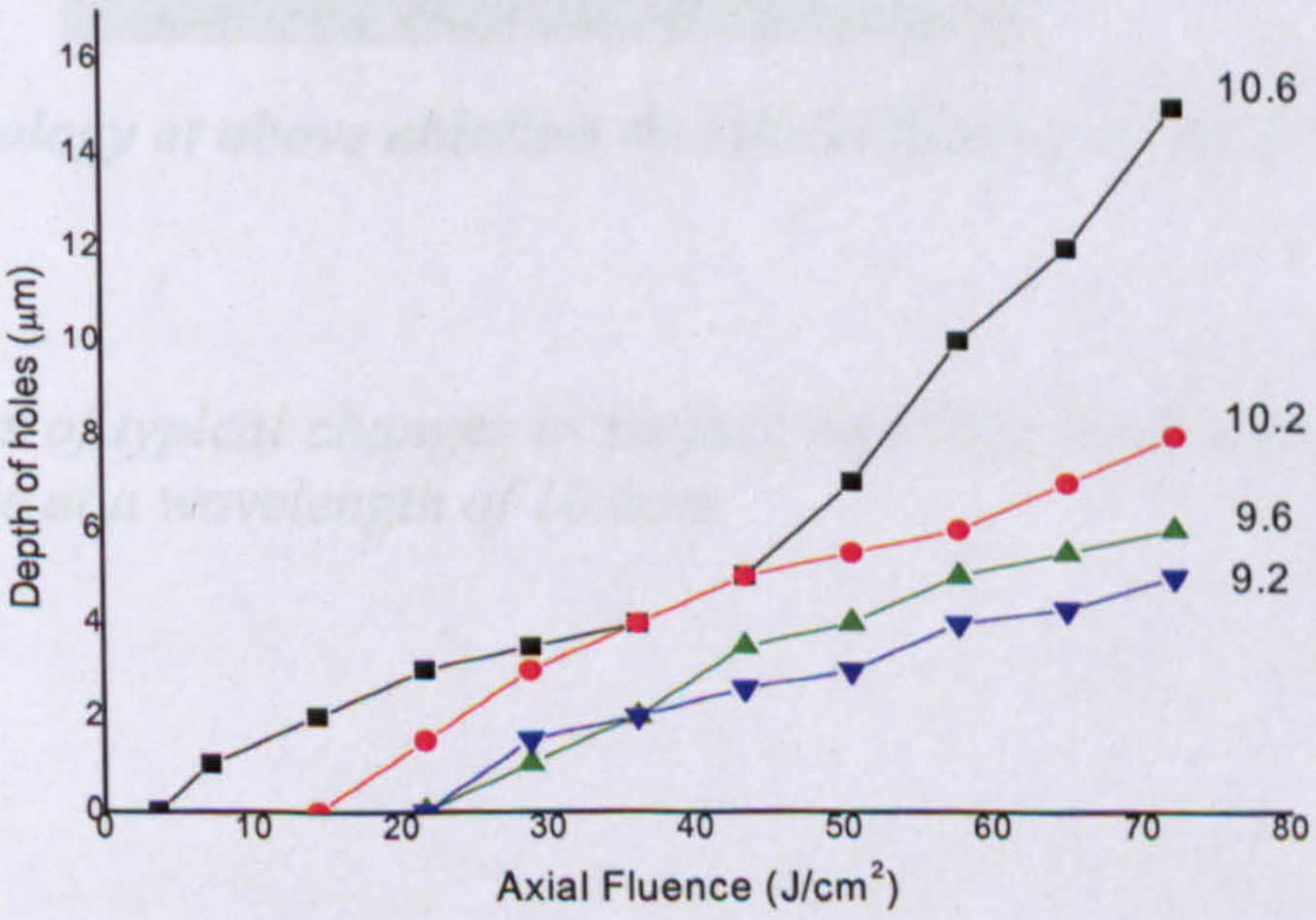

Figure 6.2: Ablation curves in alumina material in IR band

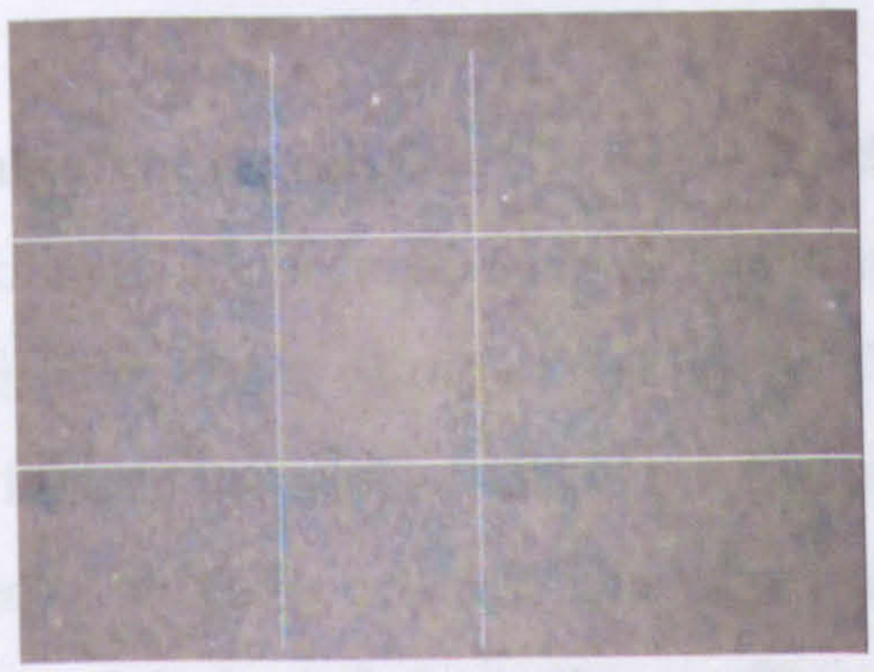

(a)Surface topology in alumina at fluence5.5J/cm^{2}showing melt /damage threshold

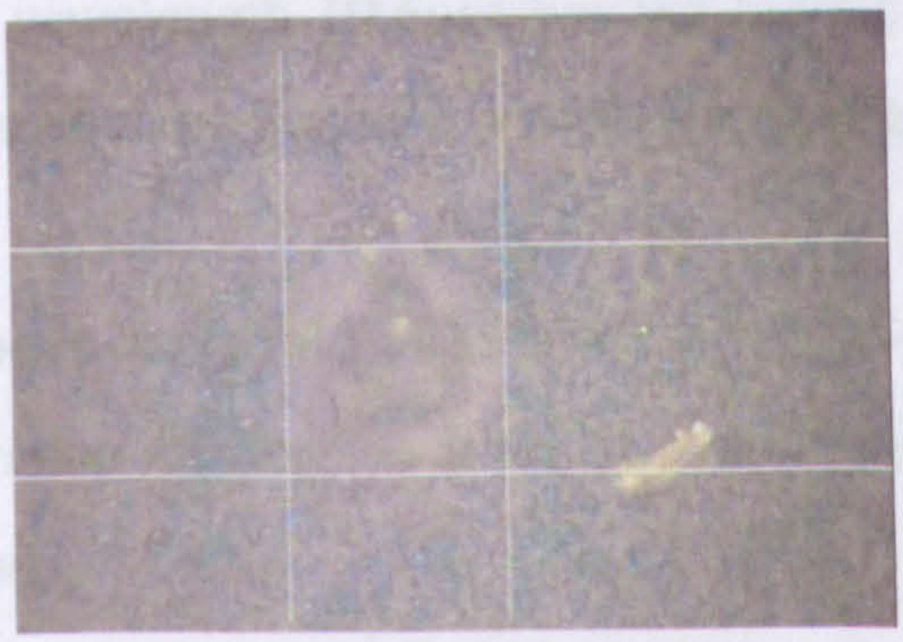

(b) Surface topology at ablation threshold fluence of 8.5 J/cm^2 in Alumina

(c) Surface topology at above ablation threshold fluence of 50 J/cm^2 in Alumina

Figure 6.3: Series of typical changes in surface topology in Alumina with changes in fluence at a wavelength of 10.6μm

absorption dependent, all the threshold fluences at each applied wavelength are presented in Table 6.1.

(b) Fluence at ablation threshold ($F = F_{th}$) – Section II:

The threshold for ablation is observed when the melt depth increases and the fluence is high enough to displace the melt out of the holes. The heat conduction is still one-dimensional at this fluence range. The threshold fluence for ablation for each selected wavelength is presented in Table 6.1. It is observed that this value also corresponds to the melt threshold as a function of absorption coefficient. It is clearly visible from the data table that the wavelength 10.6μm has the lowest threshold fluence for ablation and the values are seen to be increasing with decreasing wavelengths.

(c) Fluence above threshold of ablation ($F>F_{th}$) – Section III:

The initial observation of surface modification in alumina at each wavelength is discussed as follows:

- At 9.2 μm, the melt threshold fluence is 22J/cm^2 and the ablation threshold at 24 J/cm^2. With increase in pulse widths from 40 – 100 μs, the depth increases to only 2 – 5 μm. The rate of ablation is consistently slow, though the HAZ increases from 18 - 28 μm, which demonstrates that the heat conduction is two – dimensional, conducting the heat radially in the surface.
- At 9.6 μm the melt threshold fluence is 18 J/cm^2 and the ablation threshold is 21 J/cm^2. The HAZ increases from 17 – 23 μm with increase in pulse widths from 40 – 100 μs. Depth of holes is increased from 1 μm to 6μm. Again the rate of ablation is very slow and the heat conduction is two dimensional at this fluence range.
- At 10.2 μm, the melting threshold fluence is 10 J/cm^2 and the ablation threshold is 15 J/cm^2. HAZ increases from 11 - 22 μm with increasing pulse widths 30 – 100 μs. The depth of the hole increases from 1.5 μm at 30 μs pulse widths to 8 μm at 100 μs pulse widths. The rate of ablation is marginally increased with this wavelength.
- At 10.6 μm the melt threshold fluence is 5.5 J/cm^2. The ablation threshold is 8.5 J/cm^2. The heat affected zone is observed to be pretty constant between 14 – 19 μm, though the depth increases linearly till 15μm at 100μs.

Table 6.1: Threshold fluences at wavelengths in alumina

	Wavelength (μm)	Melt Threshold Fluence (J/cm^2)	Threshold Fluence (J/cm^2)
1	10.6	5.5	8.5
2	10.2	10	15
3	9.6	18	21
4	9.2	22	24

6.4.1 Ablation Curves of Alumina

The ablation curves of alumina illustrated in Figure 6.2 shows that the ablation rate in the fluence range studied varies from 1 micron/pulse to a more than 10 microns per pulse. There is a wide range of laser fluences (about two orders of magnitude) where for all applied pulse widths and wavelengths, the ablation rate rises fairly slowly but consistently. However, at fluence ($E< 10$ J/cm^2) the ablation rates become more sensitive to the irradiation conditions.

At 10.6μm, the ablation rate linearly increases with increasing fluence. This wavelength has the lowest melt threshold and hence uses lowest threshold fluence to ablate the material. The ablation rate is constant at 1μm/shot; however the ablation slows down between pulse widths 50 - 80μs but increases again at higher pulse durations. The value of hole depth measured does have standard deviation associated with it to take the measurement errors in to account. The ablation rate is dependent on two mechanisms here, liquid phase expulsion due to recoil pressure and the vaporisation due to higher fluence and longer pulse durations. Comparing the spectral absorptivity of this wavelength, there is a strong agreement. This is highest absorbed hence corresponds to lower fluence being required to melt and ablate the material.

Wavelength 10.2 μm is observed to have a relatively low threshold but somewhat higher than at 10.6μm. This again is in good agreement expectations from the absorption spectrum of the material. The ablation rate is constant with increasing fluence and the curve is smooth.

Wavelengths 9.6 and 9.2μm exhibit very similar behaviour. These wavelengths do not exhibit a remarkable difference in ablation threshold fluence. However, comparing the spectral absorptivity in Figure 6.1, there exists a high absorption peak at 9.6μm equivalent to wavelengths in 10μm band, though it does not correspond to the ablation curves. It is not clearly understood the reason for low absorption of the wavelength but it could be hypothesised that there is a deviation of 9μm band in higher absorption region due to change in temperature during phase change.

6.4.2 Comparison of ablation and absorption curves

In summary, a comparison of the absorption and ablation curves of alumina provides following information:

1 Pulses at a wavelength 10.6μm have the highest absorption and hence a strong coupling to the material. The fluence requirement to damage the surface and to ablate the material is low, which is in good agreement with high absorption coefficient.

2 Pulses at a wavelength of 10.2μm exhibits constant ablation rate in alumina. The absorption coefficient is less than 10.6μm, higher fluences are required to damage and ablate the material surface

3 Pulses at wavelengths of 9.6 and 9.2μm require higher fluences to damage the surface and do not display a significant difference in ablation rates even though 9.6μm has a high absorption peak.

4 10.6μm emerges as the choice of wavelength for machining the material. This is also used frequently to ablate the material in industrial applications.

5 Cracks are observed in the condensed melt layer due to the stress built up in the material due to cooling of the melt.

6.5 Ablation mechanism and surface modifications in Alumina

There are three mechanisms of material removal observed in ablation of alumina at different phases. These mechanisms are as follows:

1 At threshold fluences for each wavelength, the heat conducts linearly in to the surface and the depth of heat penetration is equivalent to melt pool created.

2 At increasing fluence, the melt depth increases. The increase in irradiance at the surface increases the surface tension or lower viscosity of the melt pool which consequently spatters the melt out of the holes. The melt than cools off and resolidifies as recast material outside the holes. It is understood that the cause of material removal at ablation threshold is recoil pressure and surface tension

3 At higher fluence, the peripheral spread of material around the hole after ablation suggests an explosive mechanism. According to Moorhouse et al [6.11], the plasma ignites at the irradiance level 1 -10MWcm^{-2}. The highest irradiance is 0.9 MWcm^{2} in the present experiments which is close to the range reported. This might induce a plasma plume at higher fluences hence affecting the ablation rate; however investigations using a fast camera have not been carried out to confirm if there is the occurrence of an incandescent glow indicating the presence of a plume or plasma.

4 Due to high values of latent heat of fusion and vaporisation for alumina, the material is removed in the molten state during laser drilling at the fluences used in the experiments [6.5-6.10]. The absorbed energy melts the material and heats it to the vaporisation temperature but there is a significant time delay whilst the thermal wave propagates into the material and evaporation occurs from the liquid material. Secondary effects include a heat-affected zone, a recast layer, micro cracks and surface damage caused by shockwaves and debris from ejected material. The result of high rate of ablation is hence consequently associated with surface tension and vaporization at this range of fluence in the material. The material removal in the experiments is summed up in Figure 6.4.

5 Effects caused by the temperature increase inside the sample become significant and hence, one obtains a transition to a strong ablation phase with

violent explosive thermal effect. The volumetric heating of alumina is explained with higher optical penetration length to heat diffusion length. Heat diffusion length at pulse duration 30μs for wavelength 9.2 is calculated to be 0.47 x 10^{-6} (m) which is slightly smaller than the optical penetration depth 0.52 x 10^{-6} (m). The absorption coefficient is calculated to be 1.8 x 10^{4} (cm^{-1}) at 9.2μm wavelength. The basic ablation mechanism responsible at higher fluences is summed up as a coulomb explosion followed by additional material removal due to shock wave expansion and thermal process. It is also important to mention that above the threshold fluence the alumina melt undergoes superheating that boils the thin layer of melt. This likely explains the bubbles that are observed in the cooled off melt on the surface of alumina.

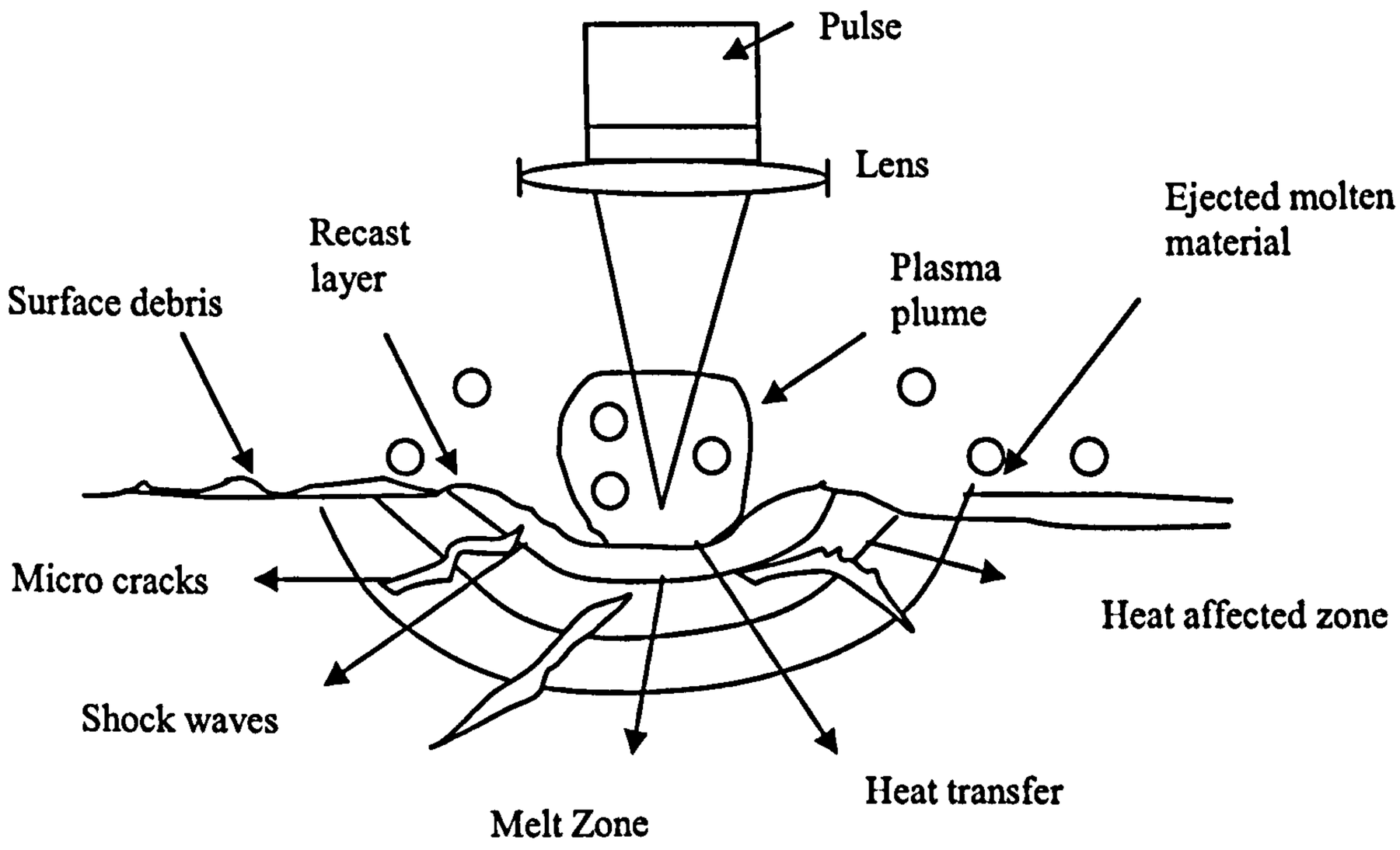

Figure 6.4.: Mechanism of ablation phenomenon and in Alumina in the operational regime.

6 If the fluence is further increased by applying even longer pulses, beyond the range applied in the experiments, the vaporised material is expected to form a hot plume from the leading edge of the pulse and this plume is sustained during the rest of the pulse. Due to the plasma shielding effect (the plume absorbs and defocuses the pulse energy) a higher fluence or irradiance for deeper penetration is required. Moorhouse et al [6.11] report studies, where high-speed videography combined with microscopic analysis confirm the onset of plasma and screening in ablation of alumina

6.6 Drilling of LTCCs (DuPont and Ferro)

The experimental investigations reported in this chapter are conducted on commercially available LTCC as follows:

(1) DuPont LTCC of thickness 0.547mm of blue colour

(2) Ferro LTCC substrate of thickness 0.765mm of characteristic white colour.

Information on the dopants used in the material during manufacturing that gives the LTCC samples their characteristic colour was unavailable.

(a) Fluence under and at threshold of ablation ($F \geq F_{th}$):

As with alumina, it is observed that LTCC also exhibits two thresholds: a damage threshold and an ablation threshold. The melt threshold and the ablation threshold fluence data for LTCC – blue DuPont is presented in Table 6.2 and for LTCC – White Ferro in Table 6.3. There is no remarkable disparity observed in the melt and ablation thresholds in both the LTCC samples. The surface change in both the samples is also fairly similar at this fluence range. The melt threshold creates a melt pool that resolidifies, and at the ablation threshold the melt is seen scattered out of holes as is observed in alumina, though, it is important to note that the fluence range needed to mark the LTCC surface is much lower than that required to damage the surface of alumina. Figure 6.5 (a) and (b) demonstrate the changes in surface in LTCC – Blue DuPont at wavelength 10.6μm.

(b) Fluence above threshold ($F>F_{th}$) in LTCC – Blue DuPont:

The ablation curves in LTCC Blue – DuPont is shown in Figure 6.6. The observations at each wavelength are as follows:

- At 9.2 μm, the melt threshold fluence is >3.5 J/cm^2 and the ablation threshold fluence is >3.5 J/cm^2. With an increase in pulse widths from 40 – 100 μs, the crater depth increases only from 4 – 8 μm
- At 9.6 μm the melt threshold fluence is 7 J/cm^2 and ablation threshold fluence is 11 J/cm^2. The depth of holes increases from 2 – 14 μm with increase in pulse widths from 40 – 100 μs.
- At 10.2 μm, the melting threshold fluence is 3.5J/cm^2 and ablation threshold fluence is 6J/cm^2. The depth of the hole increases from 5 μm at 20 μs pulse widths to 14 μm at 100 μs pulse widths.

At 10.6 μm the melt threshold exists at 3.5J/cm^2. The fluence threshold exists at 5 J/cm^2. The increase in depth of hole is observed to be pretty constant between 4 – 16 μm, though increasing linearly with pulse widths 20 - 100μs.

Table 6.2: Threshold fluences at wavelengths in LTCC – Blue DuPont

	Wavelength (μm)	Melt Threshold Fluence (J/cm^2)	Ablation Threshold Fluence (J/cm^2)
1	10.6	3.5	5
2	10.2	3.5	6
3	9.6	7	11
4	9.2	>3.5	>3.5

Table 6.3: Threshold fluences at wavelengths in LTCC-Ferro

	Wavelength (μm)	Melt Threshold Fluence (J/cm^2)	Ablation Threshold Fluence (J/cm^2)
1	10.6	3	4
2	10.2	3.5	6
3	9.6	3.5	6
4	9.2	>3.5	>3.5

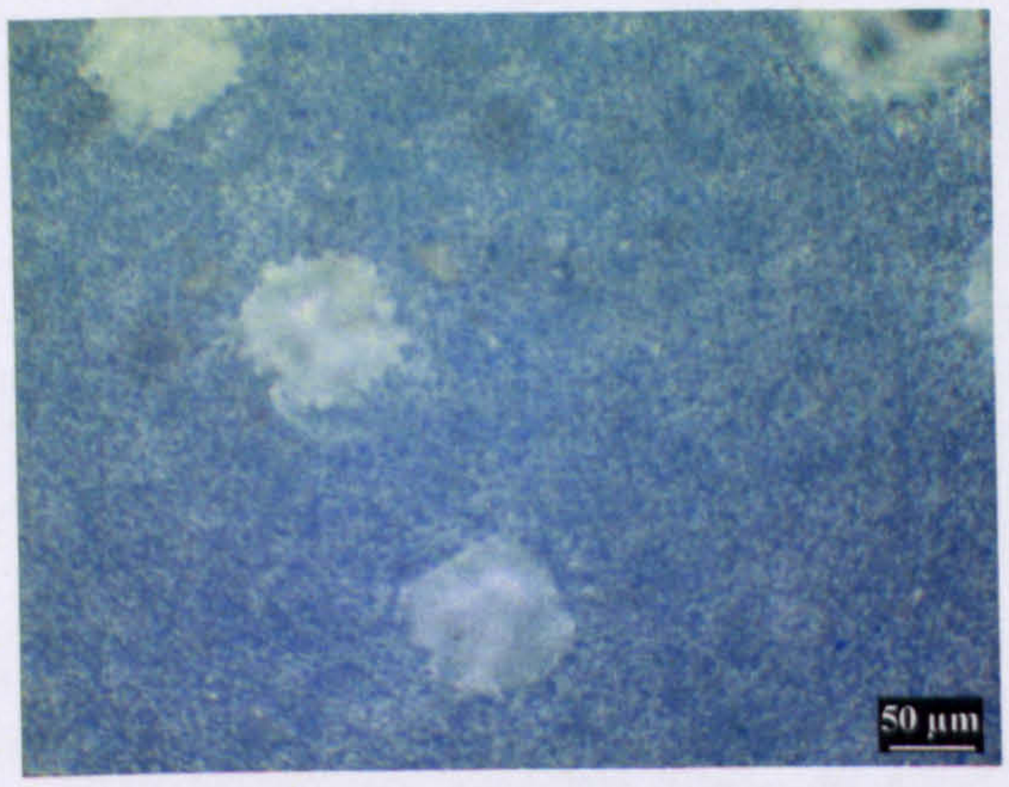

(a) Surface topology at melt/damage threshold in LTCC – DuPont (Blue)

(b) Surface topology at ablation threshold fluence

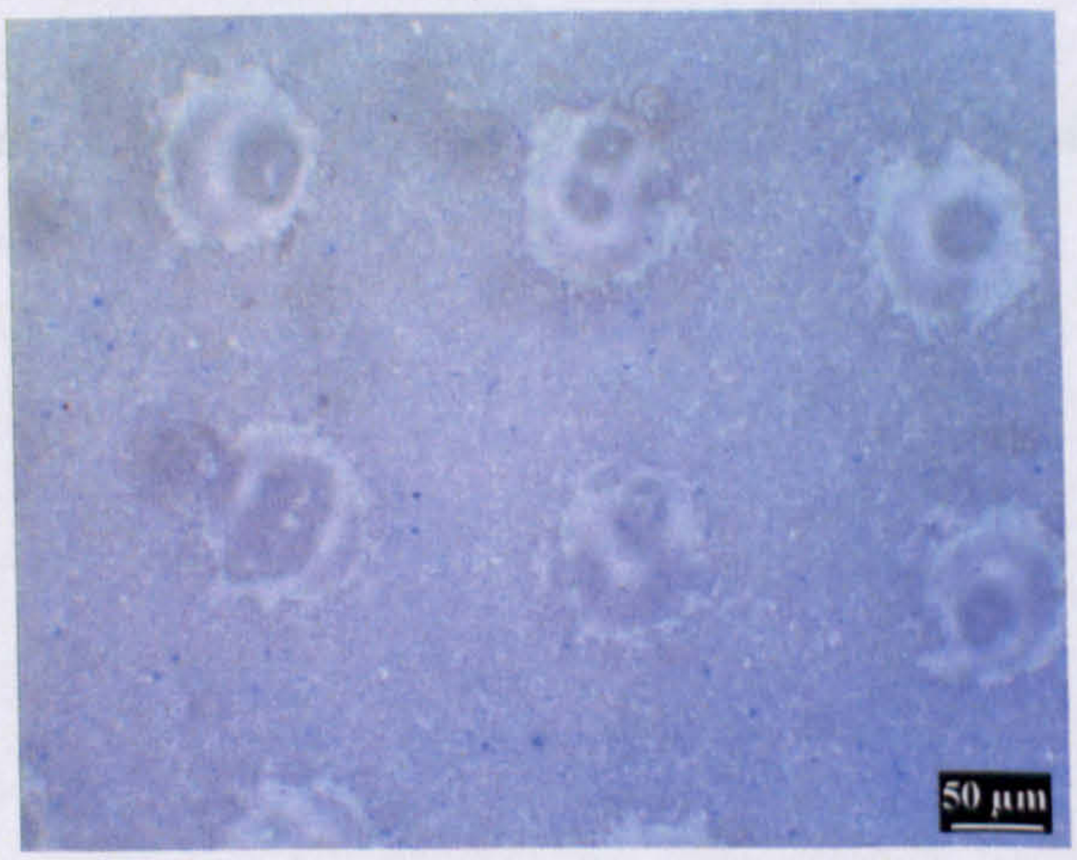

(c) Surface topology at fluence above threshold

Figure 6.5: *Typical surface changes at below ablation threshold, at threshold and above threshold in LTCC – DuPont at wavelength of 10.6 µm.*

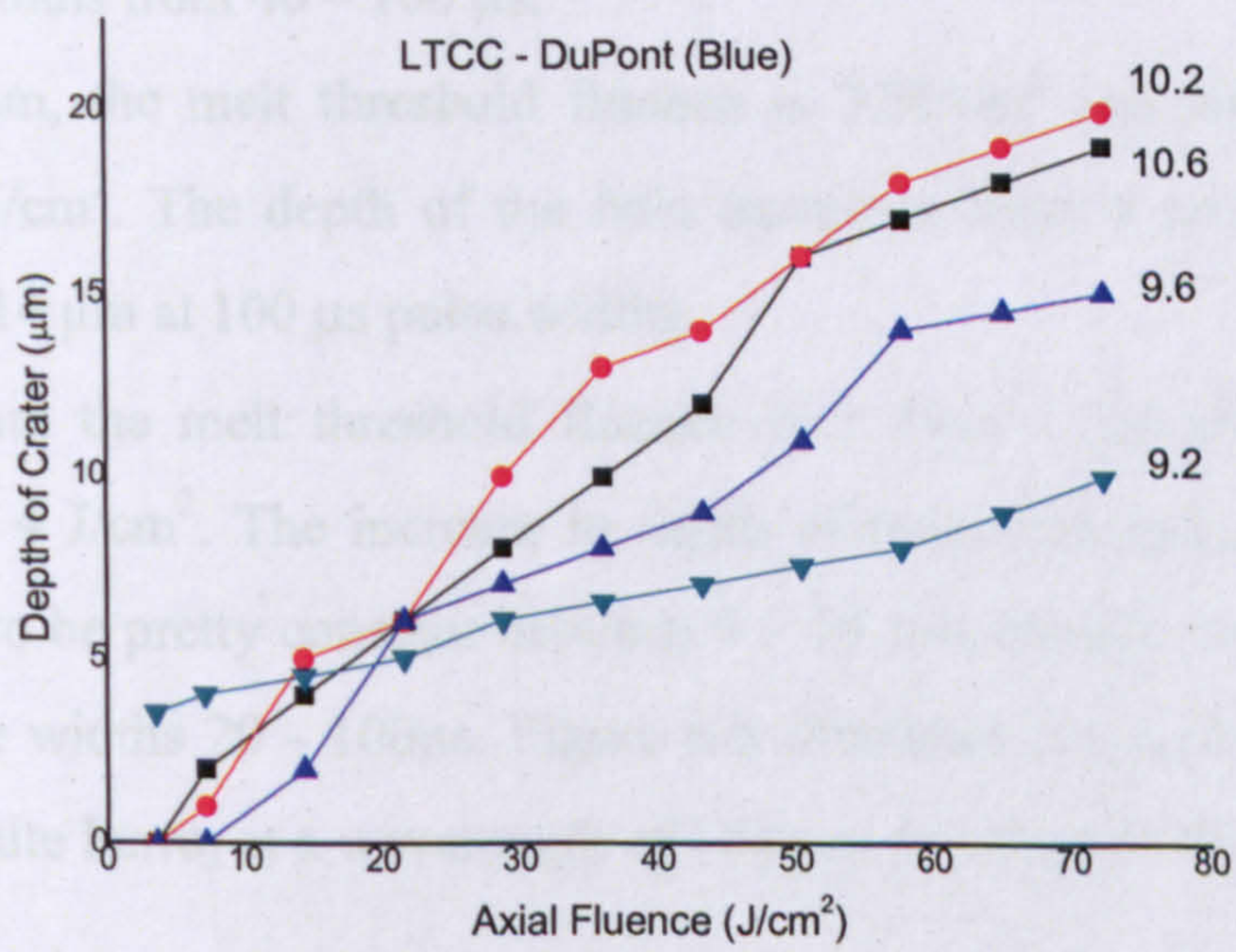

Fig 6.6: Ablation curves of LTCC (DuPont) in IR band

(c) Fluence above threshold ($F>F_{th}$) for LTCC White Ferro:

The machining curves in LTCC White Ferro are shown in Figure 6.7. The observations at each wavelength are presented as follows:

- At 9.2 μm, the melt threshold fluence is >3.5J/cm^2 and ablation threshold fluence is >3.5 J/cm^2. With increase in pulse widths from 40 – 100 μs, the depth increases only from 4 – 8 μm.
- At 9.6 μm the melt threshold fluence is 3.5 J/cm^2 and ablation threshold fluence is 6 J/cm^2. The depth of holes increases from 2 – 14 μm with increase in pulse widths from 40 – 100 μs.
- At 10.2 μm, the melt threshold fluence is 3.5J/cm^2 and ablation threshold fluence 6J/cm^2. The depth of the hole increases from 5 μm at 20 μs pulse widths to 14 μm at 100 μs pulse widths.
- At 10.6 μm the melt threshold fluence is 3 J/cm^2. The ablation threshold fluence is 4 J/cm^2. The increase in depth of hole with increasing fluence is observed to be pretty constant between 4 – 16 μm, though increasing linearly with pulse widths 20 - 100μs. Figure 6.8 illustrates a typical hole ablated in LTCC White Ferro, at a wavelength of 10.6μm and fluence 46 J/cm^2.

6.7 Ablation mechanism and surface modifications in LTCCs

As with alumina the material removal mechanisms observed in LTCC also exhibits three mechanisms of material removal, as follows:

1 At the damage threshold, the depth of heat penetration is calculated to be equivalent to the depth of the melt pool created.

2 At threshold fluence for ablation, the melt increases, due to a rise in the surface tension which causes spatter of the melt out of the holes. With increase fluence, the heat conduction extends radially causing HAZ, which is equivalent to depth of penetration. The melt than cools off and resolidifies as recast material outside the holes, creating a large rim at the edge of the holes. This is observed at all wavelengths in the fluence regime studied.

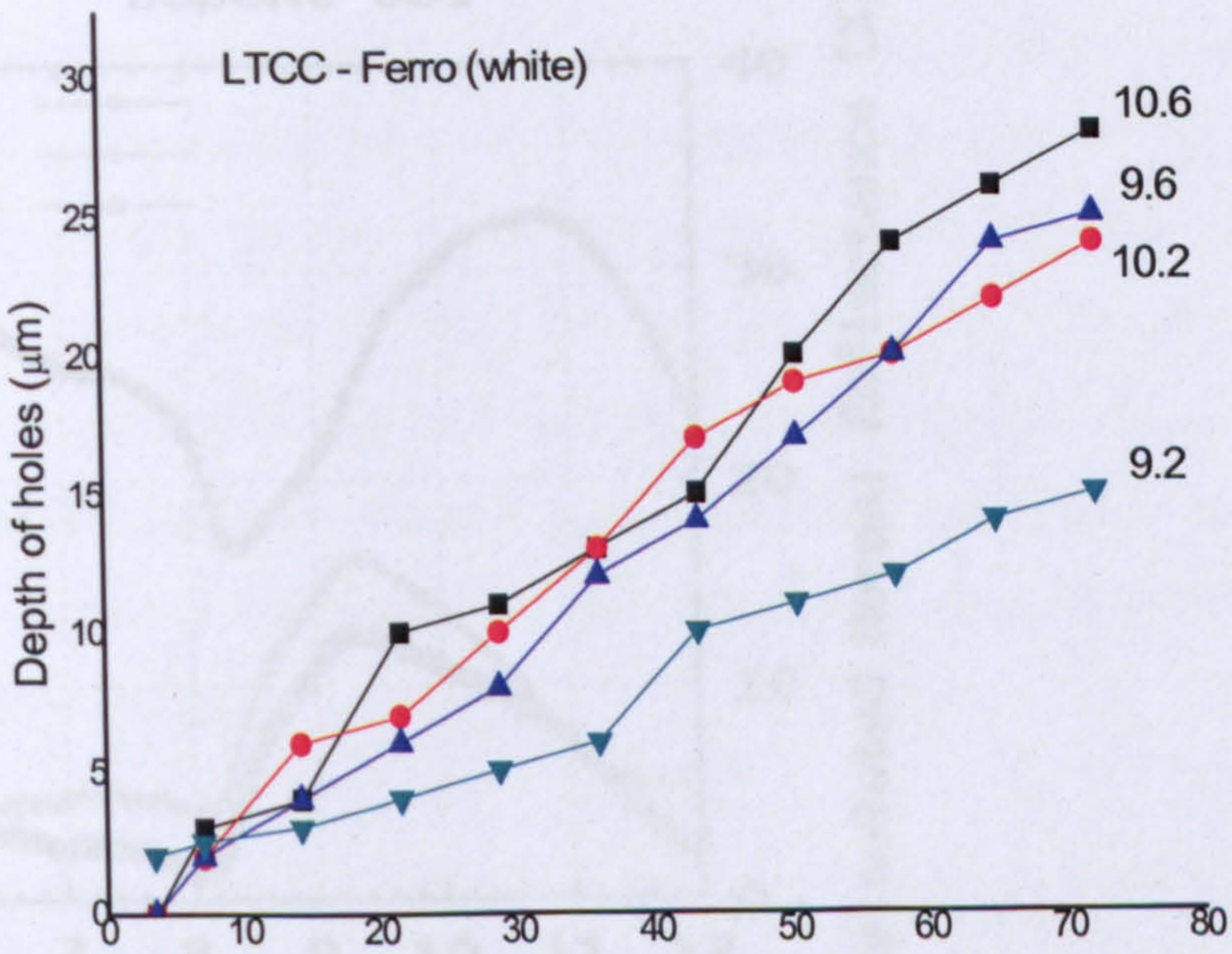

Figure 6.7: Ablation curves in LTCC (Ferro)

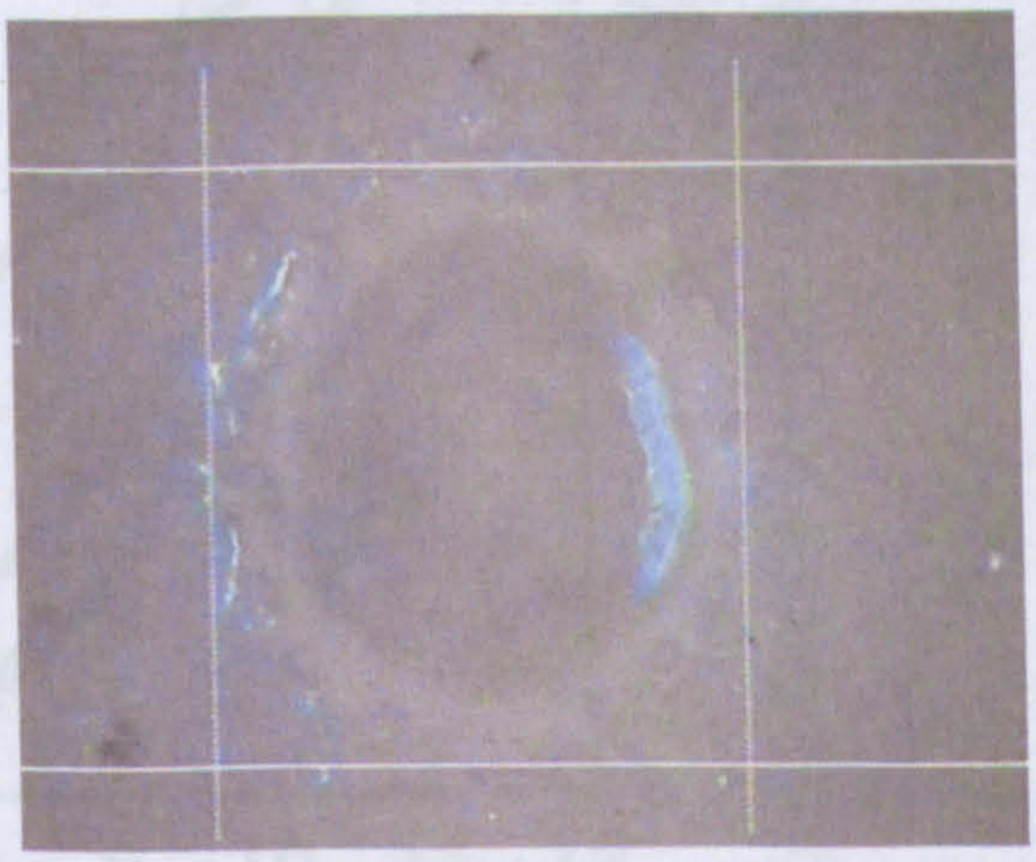

Figure 6.8: Typical ablated hole in LTCC Ferro – white. Example at wavelength 10.6μm at fluence 46 J/cm²

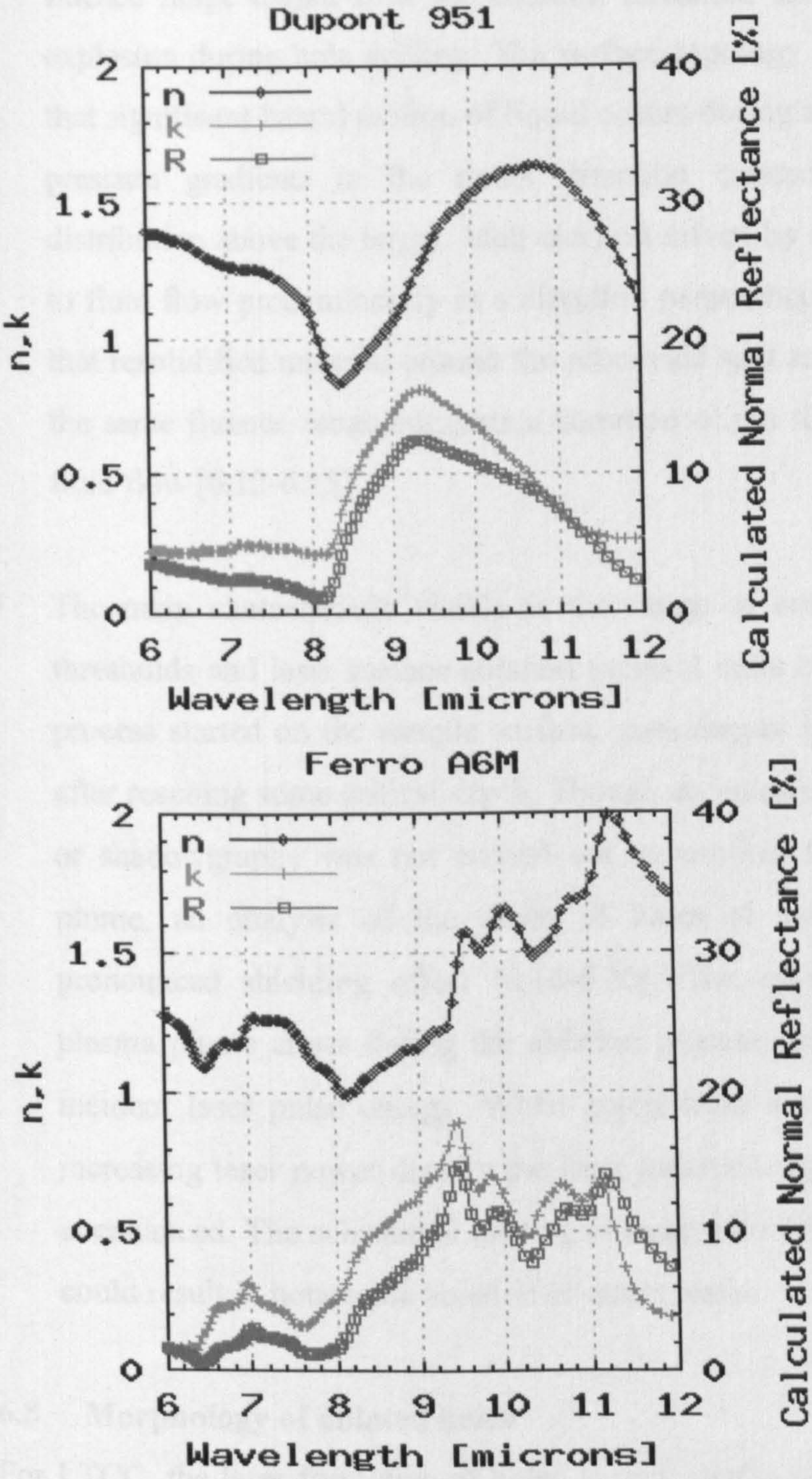

Figure 6.9: Spectral absorptivity of LTCCs (a) DuPont substrate (b) Ferro substrate. Data collected from IR ellipsometer

3 The distinctive character in LTCC is the observation of an incandescent glow during irradiation. An examination of the surfaces of both the LTCCs sample at a fluence range higher than the ablation threshold shows that there is melt and explosion during hole drilling. The surface topology of processed LTCC shows that significant lateral motion of liquid occurs during ablation. This flow is due to pressure gradients in the radial direction created by the plume pressure distribution above the target. Melt ejection driven by the expanding vapour leads to fluid flow predominantly in a direction perpendicular to the surface. The fact that resolidified material around the processed spot and particle ejection occur in the same fluence range suggests a common origin for both lateral and upwards fluid flow [6.12-6.15].

4 The main characteristic visible is the range of energy densities between the thresholds and laser surface ablation (several units of J/cm^2) where the ablation process started on the sample surface, goes deeper into the bulk and then stops after reaching some critical depth. Though an investigation using the fast camera or shadowgraphy was not carried out to confirm the presence of the plasma plume, an analysis of the depth of holes at increasing fluence suggest a pronounced shielding effect [6.16-6.20]. The explanation could be that the plasma plume arises during the ablation process causing a noticeable losses of incident laser pulse energy. When going from lower to higher pulse lengths, increasing laser power density the laser radiation shielding by the plasma plume is enhanced. The substantial heating of laser induced plasma filling a deep crater could result in noticeable ablation of crater walls.

6.8 Morphology of ablated holes

For LTCC, the laser formation of holes is very similar to the behaviour observed for alumina, but as mentioned in the previous section, a peculiar feature of deep channels/cave at the bottom of holes is observed, as is illustrated in Figure 6.10. This feature is observed to be wavelength dependent and is frequently observed at 9.2μm at fluences higher than the ablation threshold. As mentioned in the previous section the material ablates with an explosive mechanism and an incandescent plume is observed.

It is hypothesised that these deep channels at the bottom of holes is caused due to constructive interference of the laser beam.

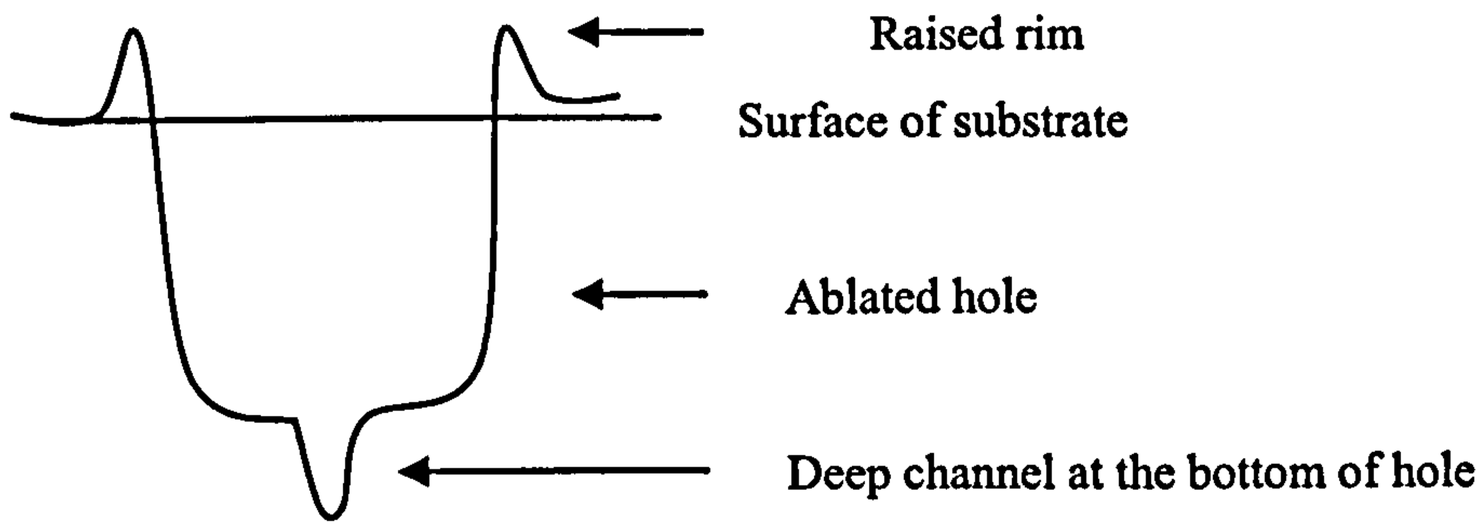

Figure 6.10: Formation of caves or deep channels in the centre of holes caused due to plume and explosive ablation in LTCCs.

In the region surrounding the processed area in samples of alumina and LTCC that are treated with fluences above threshold, spherical particles with diameters in the range 0.5 – 8 μm and a continuous film of material is observed. Furthermore the processed spot is surrounded by resolidified material as is visible in Figure 6.8 for a typical crater in LTCC white Ferro formed with the spot size of 90μm at fluence 46J/cm^2. The film is formed by an aggregation of particles a few tens of nanometre in diameter (debris) and debris is observed for entire range of fluences. The debris accumulates on a relatively large area around the laser-processed spot. The radial extension of that area increases with increasing fluence for all wavelengths studied. Clusters may also form by condensation of species emitted from the target in the ablation plume, and increasing species density and vapour pressure favour this condensation. The radial extension of debris relates to lateral extension of the incandescent plume, which may indicate that debris is formed by the collisions of ultra fine particles in the plume.

It is interesting to mention that if the LTCCs are ablated in the green state, the ablation phenomenon is very different from the mechanism seen in co – fired ceramics. As is mentioned in Chapter 2, a green state of LTCC consists of alumina and glass frit particles which is held together by an organic binder. The organic binder

acts as lower viscosity controller prior to sintering of green state LTCC. Therefore, the ablation mechanism in green state LTCC demonstrates a characteristic effect of the organic binder. Nowak et al [6.6] report a 'cold' ablation mechanism for green state LTCC with CO_2 laser. The cold ablation is so called because there is no incandescence observed at the ablation site. Additionally, there are no thermal effects like HAZ observed at the ablation site, whereas, in co-fired ceramics, the HAZ is observed with increasing fluence.

6.9 Summary and Conclusions

Interesting observations of ablation mechanism and ablation curves as a function of peak wavelengths emitted by CO_2 laser are presented in this chapter. These sets of experiments and hence the observations are reported for the first time. The absorption spectra of ceramics provide the basic criteria to choose the wavelengths that are highly absorbed to machine the substrates. The mechanism of ablation is discussed for each material as is observed with an increase in fluence. The morphology of holes also changes with fluence hence affecting the quality of the drilled holes. The material is removed effectively in the molten state in alumina and LTCC. The radial extension of scattered debris at higher fluences suggests the lateral movement of an incandescent plume. Though all the substrates are ceramics and the exact composition of the LTCCs are unknown, the ablation experiments allow the following interesting comparisons:

1 Pulses at 9.2μm require the lowest fluence to damage and ablate the material in both the LTCC samples. However, in both the cases, less material is ablated at higher fluences. The threshold fluences for ablation for wavelengths 9.6, 10.2, 10.6μm lie between the fluence 3.6 – 7.2 J/cm^2. These wavelengths show similar ablation behaviour in both the LTCCs.

2 In general, the wavelengths have high ablation rates in LTCC – white as compared to LTCC-blue.

3 10.6μm is the most strongly absorbed wavelength in LTCC - White.

4 10.2μm is the most strongly absorbed wavelength in LTCC – blue.

5 9.6μm exhibits the same ablation rate in both the LTCCs.

Now comparing the ablation curves of LTCCs with Alumina, suggest the following conclusions:

1 10.6 is the wavelength most strongly absorbed in alumina and LTCC- white but is not the case with LTCC blue where the wavelength 10.2μm is high absorbed that suggests that the doping of material in LTCC blue produces a different spectral absorptivity.

2 10.2 and 9.6μm in general have similar ablation behaviour in all the three materials.

3 9.2μm is least absorbed wavelength in all the three materials.

6.10 References

[6.1] S.Venkat,"*Processing ceramics with lasers"* in Ceramic Industry, (2001).

[6.2] J.H. Zhang, T.C. Lee, X.Ai, W.S. Lau "*Investigation of the surface integrity of laser – cut ceramic,"* Journal of Materials processing technology, Vol **57**, pp 304-310, (1996).

[6.3] J. Longfellow, "*High speed drilling in alumina substrates with a CO_2 Laser"* Ceramic Bulletin, Vol **50**, pp 251-253, (1971).

[6.4] M. Pabler, G. Lesch,"*Cutting and scribing of ceramic using a CO_2 laser"*, Proceedings SPIR, Vol **801**, pp 130-137, (1987).

[6.5] K.Imen and S.D.Allen,"*Pulse CO_2 Laser Drilling of Green Alumina Ceramic*" IEEE Trans advert Package **22**,620, (1999).

[6.6] K.M. Nowak, H.J. Baker, D.R. Hall,"*Cold processing of green state LTCC with a CO_2 laser."* Applied Physics, Vol **A 84**, pp267-270, (2006).

[6.7] H.Beyer, W. Ross, R. Rudolph, A. Michaelis, W. Viol *"Laser micromachining of Al_2O_3-TiC ceramics"* J. Appl. Phys.**70**, pp 75 (1991).

[6.8] S.K. Nikumb, M.U. Islam, G.R. Campbell, B.L. Mordike (Eds.) "*Laser Materials Processing"* Proc. ICALEO, Laser Institute of America, Orlando, **1194**, p.51, (1993).

[6.9] R. Dreyfus, R. Kelly, R.E. Walkup *"Laser induced fluorescence studies of excimer laser ablation of Al_2O_3"* Applied Physics Letter. pp 1478, **49** (1986).

[6.10] R.F. Haglund, N. Itoh, in " *J.C. Miller (Ed.), Laser Ablation: Principles and Applications*" Springer Series in Mater. Sci. Springer, Berlin, pp 11, (1994).

[6.11] Colin J. Moorhouse, Francisco Villarreal, Jozef J. Wendland, Howard J. Baker, Denis R. Hall, and Duncan P. Hand. "*CO_2 Laser Processing of Alumina (Al_2O_3) Printed Circuit Board Substrates*", IEEE Transactions on electronics packaging manufacturing, Vol. **28**, NO. 3, July (2005).

[6.12] H. Varel, D Ashkenasi, A. Rosenfeld, R. Herrmann, F. Noack, E.E.B. Campbell, "*Laser-induced damage in SiO_2 and CaF_2 with picosecond and femtosecond laser pulses*" Appl. Phys. A **62** pp 293 (1996).

[6.13] An-Chun Tien, Sterling Backus, Henry Kapteyn, Margaret Murnane, and Gérard Mourou. "*Short-Pulse Laser Damage in Transparent Materials as a Function of Pulse Duration*" Phys. Rev. Lett. **82**, pp3883 - 3886 (1999).

[6.14] A.C. Tien, S. Backus, H. Kapteyn, M. Murname, G. Mourou: *"Short pulse laser damage in transparent materials as a function of pulse duration"* Applied Physics Letter. **82** (19) pp 3883, (1999).

[6.15] A.C. Tam, J.L. Brand, D.C. Cheng, W. Zapka *"Nanosecond and femtosecond excimer laser ablation of fused silica"Applied Physics. Letters* **55920,** 2045, (1989).

[6.16] D.Ashkenasi et al: "*Laser processing of sapphire with picosecond and subpicosecond pulses"* Applied Surface Science **120**,65,(1997).

[6.17] A. Rosenfeld et al: "*Femtosecond laser ablation of sapphire with picosecond and subpicosecond pulses* "Applied Surface Science **76**,127-129 (1998).

[6.18] W.W. Duley, *UV lasers: Effect and Applications in Materials Science*, Cambridge Univ. Press, Cambridge, (1996).

[6.19] J. Ihlemann, A. Scholl, H. Schmidt, B. Wolff- Rottke: "*Nanosecond and Femtosecond excimer – laser ablation of oxide ceramics* "App. Phys. A Material Science Processing **60**, 41, (1995).

[6.20] D.Ashkenasi et al.*"Application of self –focussing of ps laser pulses for three dimensional microstructuring of transparent materials"* Appl. Phys. Letters. **72** ,pp 1442-1444 (1998).

Chapter 7

Conclusions and Future Work

7.1 Introduction

The principal objective of this research has been to investigate the wavelength dependence of the ablation characteristics of selected commercially-available dielectric substrate materials which are frequently used for PCBs and other applications in the electronics industry. Two categories of substrates have been studied, namely those based on organic and ceramic materials with the overall aim of generating the data necessary to optimise the laser machining (drilling)efficiency of vias and other structures in these materials. In the following section a summary of the main achievements and conclusions of the work are presented, followed by an outline of proposed future work designed to take the subject further forward.

7.2 Principal achievements and conclusions of the work

7.2.1 New laser hardware development

The main experimental investigation demanded the need of a versatile laser material processing work station that incorporated a laser source which provided both tuneable wavelengths and range of easily-selectable fluence values to enable the appropriate beam parameters to be selected. Since no commercial laser system with the required performance features was available, it was necessary to develop an in-house laser source for the experiments. The requirement was to produce adequate pulse peak power to enable a systematic investigation of ablation characteristics of the chosen materials over the full range of wavelengths available from the carbon dioxide laser in the 9-11μm region.

To fill the gap a versatile CO_2 laser machining system was designed and constructed based on the utilisation of a novel laser source design operating in a MOPA configuration using a multipass planar waveguide power amplifier, excited by a transverse RF discharge. This laser system involved the use of a line-tuneable CO_2 laser master oscillator operating in a cw mode which was used to inject a selected wavelength beam into a five-pass planar waveguide laser power amplifier. To attain adequate peak power at the output of the amplifier for the ablation experiments, it was necessary to operate the discharge in the so-called 'enhanced peak power' (or ultra-super-pulse - USP) mode of operation. In this mode the RF-excited amplifier gain was such that the amplifier was capable of generating peak power values which are four to five times the peak power values of conventional RF excited slab laser gain media. An acousto-optic modulator was placed in the optical beam train between the master oscillator and the power amplifier to provide digital control of the pulse amplitude and pulse duration at the input to the amplifier. The overall system was thereby capable of being tuned over 40 spectral lines in the 9-11μm region, with pulses in the range 5-100μs and delivered values of fluence as large as 50 J/cm^2.

This MOPA system is novel and may be useful (when suitably scaled up) for other applications – such as in lasers for EUV generation [7.1].

The system enabled wavelength dependent studies of the ablation characteristics (including the ablation threshold) to be carried out in a systematic manner for a range of important substrate materials to produce data which may be described as a kind of "ablation spectroscopy". The ablation spectrum was compared to the absorption spectrum and the conclusions have been derived as outlined below. It is believed that this data is perhaps the first to be reported over a broad range of laser parameters (wavelength and pulse duration) for this range of organic and ceramic dielectric materials.

7.2.2 Principal conclusions of research – ablation results

The principal outcomes of this work, which are significant to the knowledge base in laser ablation machining are summarised as follows:

1) In summary, the experimental investigations made advances over previously published work in providing data on the optimum wavelengths for efficient machining of the specified materials. This information is obtained by plotting ablation curves as a function of (selected) fluence and wavelength.

2) The Ellipsometry measurement technique was explored in an effort to collect the data on absorption of wavelengths for the selected materials, in 9-10μm IR spectral region. The aim was to select those wavelengths (from the > 40 lines available) that had high absorption in the room temperature absorption spectrum, collected from ellipsometer data. However, in practice, the room temperature absorption spectrum did not prove to be a good guide in assessing the optimum wavelength for machining the material. For example, in materials such as resin, Arlon and FR4, the absorption spectrum failed to demonstrate the absorption peak in the selected IR spectral range. Whereas, the ablation spectrum in each material and in all the materials in general, not only determined the optimum wavelength of machining but also provided the information on the requirement of fluence by the wavelength for attaining machining threshold and the fluence required to drill a crater of 30μm depth.

3) For Kapton, the fluence at the ablation threshold was observed to be between 1 J/cm^2 – $10J/cm^2$ depending on wavelength. In general, the wavelengths selected in 10μm emission band required less fluence for material removal as compared to the wavelengths selected in 9μm emission band. This agrees well with the room temperature absorption spectrum of Kapton where the high absorption peak is observed in 10μm band. Wavelength 10.24μm clearly emerged as a choice of wavelength for machining the material however, all the wavelengths including wavelength 10.24μm did not machine clean holes in the material. It may be concluded that Kapton has less spectral absorptivity in IR region (than other polymer materials) and hence IR wavelengths may not be suitable for machining the material.

4) The experimental results in proprietary resin from resin coated copper suggest high absorption of wavelength 9.55μm and have emerged as the choice of wavelength to drill resin. On comparing the ablation spectrum of the material

to the absorption spectrum, it was clear that the absorption spectrum failed to determine high absorbed peak in the selected IR region. Interestingly, the mechanism of material removal in resin is observed similar to silica [7.2], where at certain machining conditions the material is removed from the holes by melt ejection, which formed fibres that are rooted in the holes.

5) In the dielectric material Arlon, the ablation experiments showed high absorption efficiency at wavelengths of 9.27μm and 10.30μm wavelengths. 10.30μm requires less fluence to attain ablation threshold (4J/cm^2 as compared to 6J/cm^2 at 9.27μm). However, 9.27μm has clear advantage in removing more material at higher fluences. In conclusion, wavelength 9.27μm is selected the optimum wavelength for machining Arlon.

6) In FR4, the wavelength 10.59μm required less fluence for ablation threshold and removes more material at higher fluences as compared to other wavelengths selected in 9μm and 10μm emission region. The room temperature absorption spectrum of the material fails to detect any high absorption peak in the selected IR range. FR4 presented laser machining challenges for several reasons. First, the material is highly heterogeneous. Second, the disparity in fluence required to ablate the resin and glass. The goal was to address the disparity in vaporisation temperature between the glass fibers and the epoxy resin by delivering the energy very rapidly to the target material. Hence the optimum machining conditions are observed to be at fluences 7 – 57 J/cm^2 at 9.27 μm, 9.30 μm and 10.59μm but with higher pulse energy and small pulse widths which may avoid the 'wicking' problem encountered in industrial machining.

7) For alumina, it is experimentally determined that the wavelength 10.6μm has the advantage over the other wavelengths by using less fluence to attain ablation threshold and in removing more material at high fluences. This observation agrees well with room temperature absorption spectrum of the material.

8) The experimental investigations in LTCC samples from DuPont Inc and Ferro Inc suggest high spectral absorption in the 10μm region. In LTCC DuPont, wavelength 10.20μm is experimentally the optimum wavelength for efficient material removal and in LTCC Ferro 10.6μm has been experimentally determined as the optimum wavelength for efficient material removal.

9) Out of all the experiments done on the selected materials it is concluded that: the wavelength that requires least fluence in achieving threshold of ablation may not necessarily have high rate of material ablation at higher fluences. The absorption characteristic of the material may change at high temperature; therefore, the material that removes more material at high fluences is the optimum wavelength for machining the material.

7.3 Proposals for future work

Based on the observations during the experiments and from the conclusions, following proposals are made for future work.

1) In the present research, the energy per pulse is varied by varying the *duration of the pulse*. The effect of the pulse duration is not clearly understood from the experiments due to simultaneous change in fluence. Therefore, it is suggested that the investigations may be carried out by varying energy per pulse with the variation of *peak power*. This allows smaller interaction time of laser with the material hence, low heat escape losses during ablation. In principle, this will allow to investigate fluence variation impact without the effect of pulse duration impact.

2) CO_2 laser amplifiers are also being considered as a potential technology for creating trains of sub-microsecond pulses (e.g. 30-100ns) at multi-kilowatt average power levels for applications in EUV source generation [7.1], and for high speed environmentally friendly paint stripping of the exterior of aircraft and other high value structures [7.3]. The MOPA configuration is probably the only feasible architecture for the generation of such beams, and the planar waveguide architecture offers unique combination of high power density gain media, high pressure and high average power

capability and a planar folding geometry producing high beam quality. There is also the very real practical advantage that proven, reliable commercial planar waveguide laser oscillator technology is now well established as the basis for adaptation for use in a MOPA chain.

3) In Kapton, the quality of drilled holes is unacceptable industrially especially in high production of microvias in the material. The material requires post cleaning of holes to clear the debris from and around the holes. This adds to the post processing time and affects the economy of the rate of production of holes in the material. It is suggested that the spectral absorptivity of the material may be recorded in UV region to compare with the absorption of material in IR. The experiments can be performed similarly to find the optimum wavelength in UV spectral region.

4) Industrially, RCC is drilled with the copper layer intact on the resin layer. However, the investigation made here was to determine the wavelength dependent ablation characteristics in proprietary resin of RCC. The copper layer was etched off to expose the resin layer. It is suggested that the wavelength dependent experiments can be performed on RCC (with copper layer intact) to determine the optimum machining conditions in drilling both the metal and dielectric.

5) For industrial application, the LTCC machining is usually carried out in its 'green state'. Hence, it is suggested that the similar experiments with varying wavelengths and fluence may be carried out in the green state to determine the optimum wavelength and fluence conditions for efficient machining of the material. A precursor experiment has been carried out by the group, which reports interesting mechanism of material removal at 10.6μm [7.4]. The green state material is reported to ablate without melting and no HAZ is observed. The ablation process is termed as 'cold ablation'. The organic binder is removed due to explosive ablation of alumina grains. A further experimental investigation over wide range of

IR wavelengths and fluence can determine the *less* absorbed wavelengths by organic binder hence resulting in cleaner ablation mechanism.

6) The experimental investigation in fired LTCC substrates showed the presence of the so-called 'plasma plume'. It is suggested to use the techniques such as high speed videography along with the microscopic analysis of the samples to aid in understanding the screening effect of the 'plasma plume' during the machining of the material. The optimum machining conditions can be experimentally detected to avoid the generation and hence affect from the plasma plume.

7) The high melting point and latent heat of melting of alumina and LTCCs result in most of the material being removed in its molten form, which results in a considerable amount of spatter and re-deposited material. The laser machining system can be easily re-configured to respond rapidly to changes in pulsed RF-drive which can be exploited to generate a range of custom laser pulse shapes. The experiments can be performed with varying shapes of pulses for example flat top pulse which may effectively clear melt debris from the drilled holes.

8) The high peak power of the USP laser can also be utilised to drill many PCB boards simultaneously by splitting the beam into multiple beams. Due to the high absorption of organic dielectric materials, low peak power (~ 100W) is sufficient to drill holes. Hence, a USP laser with peak power of kilowatts (~5KW) can be split in up to ~40 beams to drill dielectric layers.

9) The high peak power of the USP laser can be utilised to drill many PCB boards that are reflective and highly conductive materials, such as metals. Though the metals reflect IR wavelengths, a high absorbing coating could be applied on the metal surfaces 'to reduce' reflection.

7.4 References

[7.1] Akira Endo, Masaki Nakano, Hiroshi Komori, Tatsuya Ariga, *"LPP architecture based on high average power gas laser for a commercial 115W EUV light source"* Sematech EUV Source Workshop, San Jose Convention Centre, San Jose, Ca, USA, (2005)

[7.2] G. Markillie, H. Baker, F. Villarreal, D. Hall:*" Effect of vaporisation and melt ejection on laser machining of silica glass micro – optical components."* Applied Optics, Vol 41, n 27, Sep (2002).

[7.3] Vivek Bakshi (Sematech Inc, USA), *"High power lasers for the generation of EUV light"*, Invited paper PThB4 at CLEO/QELS/PhAST Conference, Baltimore USA (2007)

[7.4] K.M. Nowak, H.J. Baker, D.R. Hall, *"Cold processing of green state LTCC with a CO_2 laser."* Applied Physics, Vol A 84, pp267-270, (2006).